UNIVERSITY OF THESSALY

DEPARTMENT OF MECHANICAL ENGINEERING

Effect of rotational and vibrational degrees of freedom in polyatomic gas heat transfer, flow and adsorption processes far from local equilibrium

by

Christos Tantos

M.Sc., Mechanical Engineer
Department of Mechanical Engineering
University of Thessaly

A Dissertation Submitted for the Partial Fulfillment of the
Requirements for the Degree of
Doctor of Philosophy

March, 2016

The approval of the current dissertation by the Department of Mechanical Engineering of the University of Thessaly does not imply acceptance of the author's opinions (Law 5343/32 number 202 paragraph 2). Also, the views and opinions expressed herein do not necessarily reflect those of the European Commission.

Certified by the members of the Dissertation Committee:

1st member
(Supervisor)

Professor Dimitris Valougeorgis
Professor in the Department of Mechanical Engineering
University of Thessaly

2nd member

Professor Vasilis Bontozoglou
Professor in the Department of Mechanical Engineering
University of Thessaly

3rd member

Associate Professor Theodoros Karakasidis
Associate Professor in the Department of Civil Engineering
University of Thessaly

4th member

Professor Nikos Andritsos
Professor in the Department of Mechanical Engineering
University of Thessaly

5th member

Professor Nikos Pelekasis
Professor in the Department of Mechanical Engineering
University of Thessaly

6th member

Associate Professor Dimitris Pandelis
Associate Professor in the Department of Mechanical Engineering
University of Thessaly

7th member

Professor Antonis Liakopoulos
Professor in the Department of Civil Engineering
University of Thessaly

Dedicated to my family

Acknowledgements

I would like to express my special appreciation and thanks to my advisor Prof. D. Valougeorgis, who has been a fantastic mentor to me. I would like to thank him for encouraging my research and helping me to grow as a research scientist. I could not have imagined having a better advisor and mentor for my Ph.D. study.

I would like to thank Prof. A. Frezzotti of Politecnico di Milano for his kindness and support as well as for stimulating discussions and numerous email exchanges on theoretical and computational issues on polyatomic gas heat transfer.

Professor G. L. Morini of the University of Bologna and Dr. C. Day of the Karlsruhe Institute of Technology (KIT) have supported the present work by providing and sharing their experimental data on the cylindrical heat transfer and adsorption configurations respectively. Also, the support of Dr. C. Day during the implementation of the VACU-TEC project is highly acknowledged and appreciated.

I would like to express my appreciation to the members of my Ph.D. committee, namely Prof. V. Bontozoglou, Assoc. Prof. T. Karakasidis, Prof. N. Andritsos, Prof. N. Pelekasis, Assoc. Prof. D. Pantelis and Prof. A. Liakopoulos for spending their time to read the manuscript and provide supportive revisions.

Many thanks to my colleagues and friends in the Laboratory of Transport Phenomena and Process Equipment: Mr. S. Misdanitis, Dr. S. Naris and Dr. J. Lyhnaropoulos as well as to Dr. S. Pantazis and Dr. S. Varoutis who now have departed from the lab. Thank you all for stimulating discussions and for the good times we had together in the past five years.

My deepest gratitude and love to Mrs. E. Anagnostopoulou, who spent sleepless nights with me, always being my support in moments of agony and frustration when there were no others to encourage me. Above all, I am grateful to my family: my parents and my sister for supporting me spiritually throughout writing this thesis and my life in general.

Effect of rotational and vibrational degrees of freedom in polyatomic gas heat transfer, flow and adsorption processes far from local equilibrium

Christos Tantos

University of Thessaly, Dept. Mechanical Engineering, 2016
Supervisor: Dr. D. Valougeorgis, Professor

Abstract

Gaseous transport phenomena far from local equilibrium, i.e. when the flow reference Knudsen number, defined as the ratio of the mean free path over a characteristic length, is larger than 10^{-3}, appear in several industrial processes and technological applications in vacuum technology and microsystems. Typical examples include the design and optimization of vacuum gas distribution systems with piping, vacuum pumps, sensors and leak detection equipment in high energy facilities (fusion reactors and accelerators) as well as condensation and adsorption/desorption processes (e.g. cryopumping and CD/DVD metallization), mass spectrometers, micro-filtering and porous media, micro-propulsion in satellite maneuvering and vehicle reentry. The flow behavior in these systems cannot be properly captured by the typical Navier-Stokes-Fourier approach and must be described based on kinetic theory of gases, as described by the integro-differential Boltzmann equation or reliable kinetic model equations. The most widely used and successfully implemented computational schemes in the solution of kinetic equations are the deterministic Discrete Velocity Method (DVM) and the stochastic Direct Simulation Monte Carlo (DSMC) scheme.

Non-equilibrium gas processes, also known as rarefied gas processes, in monatomic gases have been widely studied in the literature, while the corresponding work in polyatomic gases taking into consideration the internal degrees of freedom is rather limited. The present Ph.D. thesis is focused on the investigation of the effect of the rotational and vibrational degrees of freedom in polyatomic gas heat transfer, flow and adsorption processes in the whole range of the Knudsen number (or gas rarefaction) from the free molecular through the transition up to the slip and continuum regimes. The investigation is based on the numerical solution of typical heat transfer and flow problems which are modeled by kinetic model equations and simulated using both the DVM and the DSMC approaches.

More specifically, conductive heat transfer through rarefied polyatomic gases confined between parallel plates and coaxial cylinders maintained at different temperatures is investigated. It is assumed that gas molecules possess both rotational and vibrational degrees of freedom, described by the classical rigid rotator and quantum harmonic oscillator models, respectively. The approach is based on three kinetic models namely the Holway, Rykov and Andries models, as well as on the DSMC scheme supplemented by the Borgnakke-Larsen collision model. The total collision frequency is computed according to the Inverse Power Law intermolecular potential. Results are presented for the density as well as for the translational, rotational, vibrational and total parts of the heat flux and of the temperature fields in a wide range of the Knudsen number and for small, moderate and large temperature differences. All kinetic model results compare very well to each other and with corresponding DSMC results, as well as with experimental data verifying the validity of the simulations.

By considering in the beginning only the translational and rotational degrees of freedom, it has been found that the total heat fluxes of diatomic and polyatomic gases are higher about $30 - 50\%$ and $50 - 75\%$ respectively than the corresponding ones obtained by the monatomic modeling for both geometries. The influence of the type of gas-surface interaction has been also investigated finding out that in most cases as the gas-surface interaction becomes more diffusive the dimensionless total heat flux is increased. Then, the vibrational modes of the molecules have been included and results have been obtained for N_2, O_2, CO_2, CH_4 and SF_6 representing diatomic as well as linear and nonlinear polyatomic molecules with 1 up to 15 vibrational modes. The effect of the vibrational degrees of freedom is demonstrated. In diatomic gases the vibrational heat flux varies from 5% up to 25% of the total one. Corresponding results in polyatomic gases with a higher number of vibrational modes show that even at low reference temperatures the contribution of the vibrational heat flux may be considerably higher. For example in the case of SF_6 at 300 K and 500 K the vibrational heat flux is about 67% and 76% respectively of the total heat flux. Furthermore, it is numerically proved that the computed solutions are in agreement with the Chapman-Enskog approximation in a central strip of the computational domain even at moderately large values of the rarefaction parameter providing that the system Knudsen number is small. It is evident that modeling heat transfer configurations with polyatomic gases must consider, and in most cases include, the effect of the internal degrees of freedom even at ambient temperatures.

Next, the problem of polyatomic gas flow through circular tubes of various lengths has been considered. Pressure driven rarefied gas flow of polyatomic gases through short tubes in a wide range of the Knudsen number has been numerically investigated. The downstream

over the upstream pressure ratio is taken very close to zero. Such flows are characterized by low Reynolds numbers and high viscous losses and therefore short circular micro-tubes may be used, instead of typical micro-nozzles, as low-thrust propulsion systems. A parametric study on propulsion performance is performed based on the Holway kinetic model subject to diffuse boundary conditions and the main computed quantities include the flow rate, the discharge coefficient, the thrust and the impulse factor which are provided in terms of the gas rarefaction and the tube dimensionless length. Furthermore, a comparison between corresponding poly-atomic and monatomic results is performed and the effect of the internal degrees of freedom on the results is investigated. It has been found that the overall propulsion efficiency in the case of polyatomic gases compared to the one in monatomic gases is slightly improved. In general, the effect of the rotational degrees of freedom on the macroscopic quantities is small except of the temperature distribution, where the well-known observed minimum along the flow axis is less pronounced. Also, it has been demonstrated that this type of flows, which have been simulated so far only based on the DSMC method, can be also tackled by kinetic modeling.

This study has been extended in the case of flows through long tubes based on the infinite capillary theory (fully developed flow) driven by pressure and temperature gradients. Simulations are based on the Rykov model subject to diffuse-specular boundary conditions. In the pressure driven flow the polyatomic results are very close to the corresponding monatomic ones, while in the temperature driven flow, also known as thermal creep flow, there are significant discrepancies. More specifically, the fully developed thermal creep heat flow rates in the case of diatomic or linear polyatomic gases (e.g. N_2, CO_2) can be about $30-40\%$ higher than the corresponding monatmomic ones. This deviation is further increased in the case of nonlinear polyatomic gases (e.g. CH_4) and can be about $50-65\%$. It is noted that as the Knudsen number is increased the differences are also increased. The effect of the rotational degrees of freedom on the gas flow rate in Poiseuille flow is small for all values of the Knudsen number. However, the effect of the rotational degrees of freedom on the heat flow rate in Poiseuille flow is greater and can reach $20-30\%$ at moderate values of the rarefaction parameter.

The effect of the internal degrees of freedom has been also considered in adsorption pro-cesses. This investigation has been motivated by the design of multistage cryopumps and more specifically by the design of a three-stage cryopump which is recently under consideration within the EUROfusion programme. Since corresponding results in monatomic gases are not widely available the investigation includes both monatomic and polyatomic gases.

The steady half-space single gas flow driven by an adsorbing planar wall is investigated based on the solution of the BGK and Holway kinetic models. The mass and heat transfer

between the gas and the plate are characterized by the sticking and thermal accommodation coefficients, the surface temperature and the far upstream velocity and temperature. The work is focused on the influence of partial thermal gas-surface interaction on all flow quantities including the sticking coefficient. It has been found that as the gas thermal accommodation on the surface is reduced, for prescribed adsorbing flux and temperature difference, the sticking coefficient must be increased to sustain the prescribed flux or otherwise for the same sticking coefficient the adsorbing flux is reduced. This behavior is enhanced as the difference, between the surface and the far upstream temperatures, is increased. Overall, the effect of the thermal accommodation coefficient is significant in all flow quantities and must be accordingly taken into consideration. In general there is good agreement between monatomic and polyatomic results and therefore, it is stated that in general the effects of the internal degrees of freedom is small and does not exceed 10%. This is contributed to the low temperatures where these processes take place. The investigation of the partial thermal accommodation effect may provide a more clear interpretation of measurements of sticking coefficients, and conversely, improve performance calculations for cryopumps.

Further, the adsorption process has been simulated in a two-dimensional flow configuration in an effort to compare with corresponding experimental results and investigate the feasibility of designing a three stage cryopump for the main vacuum pumping system of the Demonstration Power Plant (DEMO) fusion facility. Based on inverse engineering procedures the sticking coefficients of gases contained in the exhaust mixture on charcoal surfaces maintained at different temperatures may be estimated. Simulations have been performed for different sets of parameters and numerical data have been recovered for H_2 and D_2. Following a comparison with experimental data, the values of the sticking coefficient for both gases have been provided. In addition, the detailed flow structure in terms of all macroscopic quantities of practical interest is viewed and the effect of the temperature of the adsorbing plate is reported. Most important a significant amount of back flow in the inlet slit is observed highly influencing the overall adsorption performance.

Overall, the theoretical/computational investigation performed in this thesis exhibits the importance of the rotational and vibrational degrees of freedom of polyatomic gases in non-equilibrium transport phenomena. It has been shown that ignoring the internal structure of the molecules may yield erroneous results and large deviations between measurements and calculations. The work provides some useful insight in the design and optimization of processes and devices with polyatomic gases operating under rarefied conditions in a wide temperature range.

Επίδραση των βαθμών ελευθερίας περιστροφής και δόνησης των πολυατομικών αερίων σε θέματα μεταφοράς θερμότητας, ροών και προσρόφησης εκτός θερμοδυναμικής ισορροπίας

Χρήστος Τάντος

Πανεπιστήμιο Θεσσαλίας, Τμήμα Μηχανολόγων Μηχανικών, 2016

Επιβλέπων: Δρ. Δημήτριος Βαλουγεώργης, Καθηγητής

Περίληψη

Φαινόμενα μεταφοράς εκτός θερμοδυναμικής ισορροπίας, όπου ο αριθμός Knudsen, ορισμένος ως ο λόγος της μέσης ελεύθερης διαδρομής προς ένα χαρακτηριστικό μήκος του εκάστοτε προβλήματος, είναι μεγαλύτερος από 10^{-3}, απαντώνται σε πολλές βιομηχανικές εφαρμογές όπως στη τεχνολογία κενού και σε μικροσυστήματα. Χαρακτηριστικά παραδείγματα αποτελούν ο σχεδιασμός και η βελτιστοποίηση των συστημάτων κενού, ανίχνευσης διαρροών σε μονάδες υψηλής ενέργειας (αντιδραστήρες σύντηξης και επιταχυντές), καθώς και σε διεργασίες συμπύκνωσης, προσρόφησης και εκρόφησης (κρυογενικές αντλίες και επίστρωση μετάλλου σε CD/DVD), στην κατασκευή φασματογράφων, στην χρήση πορωδών υλικών και σε μικροσυστήματα προώθησης διαστημικών οχημάτων. Η μελέτη των φαινομένων μεταφοράς στα προαναφερθέντα συστήματα δεν μπορεί να περιγραφεί επαρκώς μέσω της προσέγγισης Navier-Stokes-Fourier και απαιτείται η χρήση της κινητικής θεωρίας των αερίων, όπως αυτή περιγράφεται από την ολοκληροδιαφορική εξίσωση Boltzmann είτε εναλλακτικά με αξιόπιστα κινητικά μοντέλα. Οι πιο ευρέως διαδεδομένες και επιτυχώς εφαρμοσμένες υπολογιστικές μέθοδοι για την επίλυση των κινητικών εξισώσεων είναι η ντετερμινιστική μέθοδος των διακριτών ταχυτήτων (Discrete Velocity Method: DVM) και η στοχαστική μέθοδος Direct Simulation Monte Carlo (DSMC).

Διεργασίες μονατομικών αερίων εκτός θερμοδυναμικής ισορροπίας, γνωστές και ως διεργασίες αραιοποιημένων αερίων, έχουν μελετηθεί εκτενώς στην βιβλιογραφία. Αντίθετα, για την περίπτωση των πολυατομικών αερίων λαμβάνοντας υπόψη τους εσωτερικούς βαθμούς ελευθερίας των μορίων η επιστημονική έρευνα είναι αρκετά περιορισμένη. Η παρούσα διατριβή επικεντρώνεται στην μελέτη της επίδρασης των βαθμών ελευθερίας περιστροφής και δόνησης των πολυατομικών αερίων σε θέματα μεταφοράς θερμότητας, ροών και προσρόφησης εκτός θερμοδυναμικής ισορροπίας σε όλο το εύρος του αριθμού Knudsen (η αλλιώς της παραμέτρου αραιοποίησης), δηλαδή την

ελεύθερη μοριακή περιοχή, την μεταβατική περιοχή και την υδροδυναμική περιοχή έως το συνεχές όριο. Η μελέτη βασίζεται στην αριθμητική επίλυση τυπικών προβλημάτων μεταφοράς θερμότητας και ροών, τα οποία μοντελοποιούνται με την εφαρμογή κινητικών εξισώσεων χρησιμοποιώντας τις μεθόδους DVM και DSMC.

Πιο συγκεκριμένα, διερευνάται το πρόβλημα μεταφοράς θερμότητας σε πολυατομικά αέρια τα οποία εσωκλείονται σε παράλληλες πλάκες και σε ομόκεντρους κυλίνδρους, που διατηρούνται σε διαφορετικές θερμοκρασίες. Οι βαθμοί ελευθερίας περιστροφής και δόνησης των πολυατομικών αερίων περιγράφονται από το μοντέλο περιστροφής συμπαγών μαζών (rigid rotators) και το μοντέλο του απλού αρμονικού ταλαντωτή (quantum harmonic oscillator) αντίστοιχα. Η προσέγγιση βασίζεται στα εξής τρία κινητικά μοντέλα Holway, Rykov και Andries, καθώς και στη στοχαστική μέθοδο DSMC με χρήση του μοντέλου συγκρούσεων Borgnakke-Larsen. Η συχνότητα των συγκρούσεων υπολογίζεται σύμφωνα με το μοντέλο ενδομοριακών συγκρούσεων ¨Inverse Power Law¨. Αποτελέσματα παρουσιάζονται για την αριθμητική πυκνότητα καθώς και για την θερμοκρασία και την θερμοροή εξαιτίας της μεταφορικής, περιστροφικής και ταλαντωτικής κίνησης των μορίων σε ένα ευρύ φάσμα του αριθμού Knudsen όπως και για διάφορους λόγους θερμοκρασίας. Τα αποτελέσματα που προκύπτουν από τα τρία κινητικά μοντέλα συγκρίνονται με τα αντίστοιχα αποτελέσματα της μεθόδου DSMC, καθώς και με πειραματικά δεδομένα εδραιώνοντας την αξιοπιστία των προσομοιώσεων.

Θεωρώντας αρχικά μόνο τους μεταφορικούς και περιστροφικούς βαθμούς ελευθερίας των μορίων η συνολική θερμοροή των αερίων με γραμμικά και μη γραμμικά μόρια υπολογίστηκε υψηλότερη κατά $30 - 50\%$ και $50 - 75\%$ αντίστοιχα από εκείνη που υπολογίστηκε για μονατομικά αέρια. Επίσης μελετήθηκε η επίδραση των διαφορετικών τύπων αλληλεπίδρασης αερίου-τοιχώματος, αναδεικνύοντας στις περισσότερες περιπτώσεις ότι καθώς τα μόρια εκπέμπονται από το τοίχωμα πιο διαχυτικά η συνολική θερμοροή αυξάνεται. Η μελέτη επεκτάθηκε και στην περίπτωση των βαθμών ελευθερίας δόνησης, όπου εξετάζονται γραμμικά (N_2, CO_2, O_2) και μη γραμμικά (CH_4, SF_6) αέρια με βαθμούς δόνησης που να κυμαίνονται από 1 έως 15. Από αυτή την μελέτη αναδεικνύεται η επίδραση των βαθμών ελευθερίας δόνησης των μορίων. Πιο συγκεκριμένα στην περίπτωση των διατομικών αερίων η θερμοροή εξαιτίας της δόνησης των μορίων κυμαίνεται από 5% έως 25% της συνολικής. Αντίστοιχα αποτελέσματα στην περίπτωση των πολυατομικών αερίων με πολλούς βαθμούς δόνησης αποδεικνύουν ότι ακόμη και σε χαμηλές θερμοκρασίες αναφοράς η συνεισφορά της θερμοροής λόγω της δόνησης των μορίων είναι αρκετά υψηλή και εξαρτάται από το εξεταζόμενο αέριο. Για παράδειγμα στην περίπτωση του SF_6 στις θερμοκρασίες των 300 K και 500 K η θερμοροή λόγω δόνησης είναι περίπου 67% και 76% της συνολικής θερμοροής αντίστοιχα. Επιπρόσθετα αποδεικνύεται αριθμητικά ότι τα αποτελέσματα είναι σε συμφωνία με την

προσέγγιση Chapman-Enskog στο μέσο του υπολογιστικού πεδίου, ακόμη και σε μεγάλες τιμές της παραμέτρου αραιοποίησης του αερίου με την προυπόθεση ότι ο αριθμός Knudsen αναφοράς του όλου συστήματος λαμβάνει μικρές τιμές. Επομένως, η μοντελοποίηση του προβλήματος μεταφοράς θερμότητας σε πολυατομικά αέρια θα πρέπει σίγουρα να λαμβάνει υπόψη του την επίδραση των εσωτερικών βαθμών ελευθερίας ακόμη και σε θερμοκρασίες δωματίου.

Στη συνέχεια διερευνάται η ροή πολυατομικού αερίου διαμέσου αγωγού κυκλικής διατομής διαφόρων μηκών. Πιο συγκεκριμένα, επιλύεται αριθμητικά η ροή πολυατομικού αερίου διαμέσου αγωγών μικρού μήκους λόγω βαθμίδας πίεσης σε ένα ευρύ φάσμα του αριθμού Knudsen. Ο λόγος της πίεσης στο δοχείο εκτόνωσης προς την πίεση στο δοχείο που συνδέεται στην είσοδο του αγωγού λαμβάνει τιμή πολύ κοντά στο μηδέν. Τέτοιου είδους ροές χαρακτηρίζονται από μικρούς αριθμούς Reynolds και μεγάλες ιξώδεις απώλειες καθιστώντας εφικτή την αντικατάσταση των ακροφυσίων μικρών διαστάσεων με μικροαγωγούς πεπερασμένου μήκους στην περίπτωση των μικροπροωθητικών συστημάτων. Πραγματοποιείται μια παραμετρική μελέτη των χαρακτηριστικών της πρόωσης με βάση το κινητικό μοντέλο πολυατομικών αερίων Holway με την υπόθεση οριακών συνθηκών πλήρους διάχυσης και ποσότητες όπως η παροχή μάζας (flow rate), ο συντελεστής παροχής (discharge coefficient), η δύναμη ώθησης (thrust) και ο συντελεστής ώθησης (impulse factor) παρουσιάζονται ως συνάρτηση της αραιοποίησης του αερίου και του μήκους του αγωγού. Επιπρόσθετα πραγματοποιείται μια συστηματική σύγκριση μεταξύ πολυατομικών και μονατομικών αερίων με στόχο την μελέτη της επίδρασης των εσωτερικών βαθμών ελευθερίας των μορίων στις υπολογιζόμενες ποσότητες. Προέκυψε ότι η πρόωση επιτυγχάνεται ελαφρώς πιο αποτελεσματικά στην περίπτωση των πολυατομικών αερίων σε σχέση με τα μονατομικά αέρια. Εν γένει, η επίδραση των βαθμών ελευθερίας περιστροφής στις μακροσκοπικές ποσότητες είναι μικρή, εκτός από την περίπτωση της θερμοκρασίας όπου η γνωστή πτώση της κατά μήκος της κατεύθυνσης της ροής είναι λιγότερο έντονη. Επίσης αποδεικνύεται ότι αυτού του είδους οι ροές μπορούν να μοντελοποιηθούν και με τη χρήση κινητικών μοντέλων αντί της ευρέως διαδεδομένης μεθόδου DSMC.

Η εν λόγω μελέτη επεκτάθηκε και στην περίπτωση των ροών σε αγωγούς μεγάλου μήκους, λόγω βαθμίδας πίεσης και θερμοκρασίας κατά μήκος του πεδίου ροής, βασισμένη στη θεωρία της πλήρως αναπτυγμένης ροής. Οι προσομοιώσεις έχουν βασιστεί στο κινητικό μοντέλο του Rykov με την υπόθεση οριακών συνθηκών πλήρους διάχυσης. Στις ροές που οφείλονται σε βαθμίδες πίεσης, τα αποτελέσματα για τα πολυατομικά αέρια είναι πολύ κοντά με τα αντίστοιχα των μονατομικών, ενώ στην περίπτωση των ροών λόγω βαθμίδας θερμοκρασίας, γνωστές και ως ροές θερμικού ερπυσμού (thermal creep flow), υπάρχουν σημαντικές αποκλίσεις. Πιο συγκεκριμένα, η ροή θερμότητας στην περίπτωση των ροών θερμικού ερπυσμού για τα γραμμικά πολυατομικά αέρια (N_2, CO_2) είναι περίπου $30 - 40\%$ υψηλότερη από την αντίστοιχη των μονατομικών αερίων. Αυτή η απόκλιση

μπορεί να αυξηθεί περαιτέρω στην περίπτωση των μη γραμμικών πολυατομικών αερίων (π.χ. CH_4) σε $50 - 65\%$. Αξίζει να σημειωθεί πως αυτές οι διαφορές γίνονται πιο έντονες όσο ο αριθμός Knudsen αυξάνεται. Η επίδραση των βαθμών ελευθερίας λόγω περιστροφής στην παροχή μάζας ροής που οφείλεται σε βαθμίδα πίεσης είναι πολύ μικρή για όλες τις τιμές του αριθμού Knudsen, ενώ στην ροή θερμότητας η επίδραση τους είναι μεγαλύτερη και μπορεί να φτάσει το $20 - 30\%$ σε μέσες τιμές του αριθμού Knudsen.

Η επίδραση των εσωτερικών βαθμών ελευθερίας συνυπολογίζεται και στην περίπτωση διεργασιών προσρόφησης. Ερέθισμα για την εν λόγω μελέτη αποτέλεσε η σχεδίαση μιας κρυογενικής αντλίας πολλαπλών σταδίων και πιο συγκεκριμένα μιας κρυογενικής αντλίας τριών σταδίων η οποία πρόσφατα άρχισε να ερευνάται εντός του προγράμματος ελεγχόμενης θερμοπυρηνικής σύντηξης (EUROfusion). Καθώς σχετικά αποτελέσματα για την περίπτωση των μονατομικών αερίων δεν είναι ευρέως διαθέσιμα η έρευνα περιλαμβάνει τόσο μονατομικά όσο και πολυατομικά αέρια.

Η μόνιμη ροή αερίου σε ημιάπειρο χωρίο προκαλούμενη από μια προσροφητική επιφάνεια μελετάται με χρήση των κινητικών μοντέλων BGK και Holway. Η μεταφορά μάζας και θερμότητας μεταξύ του αερίου και της πλάκας χαρακτηρίζεται από τον θερμικό συντελεστή (thermal accommodation coefficient), τον συντελεστή προσρόφησης (sticking coefficient), την θερμοκρασία της επιφάνειας και τις συνθήκες θερμοκρασίας και ταχύτητας μακριά από την επιφάνεια προσρόφησης. Η παρούσα έρευνα επικεντρώνεται στην επίδραση που ασκεί η αλληλεπίδραση μεταξύ αερίου και τοιχώματος στις ποσότητες που εκφράζουν τη ροή, και ιδιαίτερα του θερμικού συντελεστή και του συντελεστή προσρόφησης. Έχει παρατηρηθεί πως όσο ο θερμικός συντελεστής του αερίου μειώνεται, για δεδομένη ροή προσρόφησης και θερμοκρασιακή διαφορά, ο συντελεστής προσρόφησης θα πρέπει να αυξάνεται προκειμένου η ροή προσρόφησης να παραμένει σταθερή. Η συμπεριφορά αυτή γίνεται πιο έντονη όσο η θερμοκρασιακή διαφορά μεταξύ της πλάκας και περιοχής μακριά από αυτή αυξάνεται. Καταλήγουμε στο γεγονός πως η επίδραση του θερμικού συντελεστή σε όλες τις ποσότητες που χαρακτηρίζουν τη ροή είναι πολύ σημαντική και συνεπώς πρέπει πάντοτε να λαμβάνεται υπόψη. Γενικά η σύγκριση των αποτελεσμάτων μεταξύ μονατομικών και πολυατομικών αερίων είναι καλή και εν γένει η επίδραση των εσωτερικών βαθμών ελευθερίας είναι σχετικά μικρή και δεν ξεπερνά το 10%. Σε αυτό συμβάλλουν οι χαμηλές θερμοκρασίες στις οποίες λαμβάνει χώρα η διεργασία της προσρόφησης. Η μελέτη του θερμικού συντελεστή θα μπορούσε να δώσει μια πιο αξιόπιστη ερμηνεία στις μετρήσεις του συντελεστή προσρόφησης και συνεπώς να βελτιώσει τους υπολογισμούς που έχουν γίνει για τις κρυογενικές αντλίες.

Επιπρόσθετα, η δισδιάστατη διεργασία προσρόφησης έχει μελετηθεί σε μια προσπάθεια σύγκρισης με διαθέσιμα πειραματικά δεδομένα και μελέτης του σχεδιασμού μιας κρυογενικής αντλίας τριών σταδίων για το κύριο σύστημα άντλησης του αντιδραστήρα DEMO (Demonstration Power

Plant). Επίσης έχουν πραγματοποιηθεί προσομοιώσεις για διαφορετικές αριθμητικές και φυσικές παραμέτρους για τα αέρια H_2 και D_2. Στη συνέχεια, μέσω μιας διαδικασίας σύγκρισης των αριθμητικών αποτελεσμάτων με τα πειραματικά δεδομένα, προκύπτουν οι τιμές του συντελεστή προσρόφησης για τα δυο αέρια. Επίσης παρουσιάζεται η λεπτομερής εικόνα της ροής για όλες τις μακροσκοπικές ποσότητες με πρακτικό ενδιαφέρον, όπως και η επίδραση της θερμοκρασίας της πλάκας προσρόφησης. Σημειώνεται ότι ένα σημαντικό ποσοστό ροής εξέρχεται από την επιφάνεια εισόδου επιδρώντας σημαντικά στην απόδοση της διαδικασίας προσρόφησης.

Η θεωρητική/υπολογιστική μελέτη που πραγματοποιείται στην παρούσα διδακτορική διατριβή αναδεικνύει τη σημαντικότητα των εσωτερικών βαθμών ελευθερίας περιστροφής και δόνησης σε φαινόμενα μεταφοράς εκτός θερμοδυναμικής ισορροπίας. Μη λαμβάνοντας υπόψη την εσωτερική δομή των αερίων προκύπτουν μεγάλες αποκλίσεις μεταξύ πειραματικών και υπολογιστικών αποτελεσμάτων. Η παρούσα διατριβή παρέχει χρήσιμες πληροφορίες για τον σχεδιασμό και την βελτιστοποίηση των διαδικασιών και συσκευών όπου εμπλέκονται πολυατομικά αέρια που λειτουργούν υπό συνθήκες αραιοποίησης σε μεγάλο εύρος θερμοκρασιακών διαφορών.

Contents

List of Figures

List of Tables

Chapter 1

Introduction

1.1 General concepts

The investigation of transport phenomena appearing in rarefied gas dynamics has attracted a lot of scientific attention during the last decade mainly due to the increasing number of technological applications. In general, rarefied gas dynamics is introduced in gaseous transport phenomena occurring at low density (or pressure) and/or in miniaturized systems. Typical examples include industrial processes and devices in high altitude aerodynamics, micro electromechanical systems (MEMS) and vacuum technology [1, 2]. In high altitude (i.e. low density) aerodynamics and aerospace technology a lot of scientific work is focused on atmospheric reentry of orbiting vehicles as well as satellite propulsion and maneuvering [3–5]. The design and optimization of gaseous MEMS, manufactured in sizes from millimeters down to micrometers, with components between 1 to 100 μm is an emerging technological field. There are plenty of applications encountered in personal consuming devices (computer peripherals, car and personal navigation devices, sports training devices, etc.), in automotive (airbag systems, vehicle security systems, automatic door locks, etc.), in biotechnology (polymerase chain reaction, microsystems for DNA amplification and identification, micromachined scanning tunneling microscopes, biochips for detection of hazardous chemical and biological agents, etc.) and in many other industrial and service domains (earthquake detection, leak detection, filters, coating of CDs / DVDs, etc.) [6–10]. Vacuum technology has always been an application

area for rarefied gas dynamics since in these systems and devices the pressure may range from rough vacuum down to ultra-high vacuum [11]. The design and optimization of vacuum gas distribution systems with piping, vacuum pumps, sensors and leak detection equipment in high energy facilities (fusion reactors and accelerators) is a very critical issue in the smooth operation of these facilities [12–14]. Also, condensation and adsorption/desorption processes in cryopumping, leak detection in refrigeration systems, sampling, mass spectrometers and sensors are typical applications in the wide field of vacuum technology and must be designed based on rarefied gas dynamics [11, 15].

The gaseous transport phenomena appearing in all aforementioned applications are far from local equilibrium and the hypothesis of continuum medium fails. In such situations, the average distance travelled by moving particles between intermolecular collisions become comparable to a characteristic length. As the flow departs from local equilibrium first the no velocity slip and temperature jump conditions at the walls fail and then, as the departure from local equilibrium is further increased, the well-known constitutive laws are not valid and as a result the typical Navier-Stokes-Fourier approach is not applicable.

To deal with this limitation of the continuum theory, concepts derived from statistical mechanics and the kinetic theory of gases, need to be involved. Then, the problem is described by the integro-differential Boltzmann equation, devised by Ludwig Boltzmann in 1872 [16]. This equation describes the evolution of the velocity distribution function of particles, which is a function of seven independent variables (time, position vector and molecular velocity vector). The Boltzmann equation, which is solved only numerically, at the right hand side, has the collision integral term with a complex mathematical structure, which is commonly replaced by suitable kinetic models. Several kinetic models have been proposed in the literature for monatomic gases, mixtures of monatomic gases and polyatomic gases. In order to properly define the problem, the Boltzmann equation is supplemented by boundary conditions describing the gas interaction with the boundaries. The most common one is the Maxwell diffuse-specular boundary condition [17], where a part of the incident particles is diffusely reflected according to a Maxwellian distribution, characterized by the conditions of the surface (velocity and temperature) and the remaining part is reflected specularly (the normal to the surface component of

2

the relative velocity reverses its direction, while the parallel to the surface components remain unchanged). Alternatively, more complicated models may be applied. Solving the Boltzmann equation for the unknown distribution function leads to the determination of the macroscopic quantities of practical interest (density, velocity, temperature, stress tensor, heat flux) which are obtained by the moments of the distribution function.

The solution of the Boltzmann equation in multidimensional problems is computationally very expensive. However, with the developments of numerical and computational techniques, this task has become computationally manageable. The most widely implemented computational schemes are the deterministic Discrete Velocity Method (DVM) [18] and the stochastic Direct Simulation Monte Carlo (DSMC) method [19]. In the deterministic approach (DVM) it is advisable to use kinetic model equations instead of the Boltzmann equation, applying discretization procedures in the physical, molecular velocity and time spaces. In the stochastic approach (DSMC) simulation particles are used to represent a large number of real molecules in a probabilistic manner following the collision rules and constrains of the Boltzmann equation. Nowadays, these mesoscale approaches, due to significant advancements in computational methods and mainly due to the availability of high speed parallel programming, may be applied in a computationally efficient manner even in the simulation of complex flow configurations in a wide range of the gas rarefaction from the free molecular through the transition up to the continuum regimes.

The above described modeling (Boltzmann equation, kinetic model equations, numerical approaches) has been widely applied in the literature to successively describe both flow and heat transfer problems with monatomic gases far from local equilibrium. However, in practice the working gas may be polyatomic and the internal structure of the molecules has an important effect on the macroscopic quantities. In this dissertation, the effects of the rotational and vibrational degrees of freedom in heat transfer, flow and adsorption processes are investigated based on the microscopic description of the gas, as described by the Boltzmann equation. The approach is based on the Holway [20], Rykov [21] and Andries [22] kinetic models as well as on the DSMC method supplemented by the Borgnakke-Larsen collision model [23]. The validity of the simulations is confirmed by comparisons between the various kinetic models and the DSMC

method as well as between simulations and experiments. A detailed description on the thesis contents and structure is provided in the next section.

1.2   Dissertation content and structure

The thesis aims to the computational study of the effects of rotational and vibrational degrees of freedom of polyatomic gases in heat transfer, flow and adsorption processes far from local equilibrium in the whole range of the gas rarefaction. It is structured as follows:

In Chapter 2 the literature review is presented. It includes the basic concepts of kinetic theory related to polyatomic gases (Boltzmann equation, kinetic models, boundary conditions), the implemented computational approaches and an overview of the published work in heat transfer between plates and cylinders, flow through capillaries and adsorption flows in rarefied polyatomic gases.

In Chapters 3 and 4 the conductive heat transfer through rarefied polyatomic gases with translational and rotational degrees of freedom, confined between parallel plates and coaxial cylinders respectively maintained at different temperatures is investigated. The approach is based on three kinetic models namely the Holway, Rykov and Andries models, as well as on the DSMC scheme supplemented by the Borgnakke-Larsen collision model. The influence of boundary conditions on the distribution of macroscopic parameters of various types is also studied. Comparisons between results obtained by kinetic models and DSMC method as well as between simulations and experimental data are performed. Results are presented for all the heat fluxes and also for the density and temperatures fields in a wide range of the Knudsen number subject to small, moderate and large temperature differences.

In Chapter 5 the effects of the vibrational modes on the heat transfer in polyatomic gases confined between parallel plates are studied. The approach is based on the Holway model. Results are presented for N_2, O_2, CO_2, CH_4 and SF_6 representing diatomic as well as linear and nonlinear polyatomic molecules with 1 up to 15 vibrational modes. The results include the heat fluxes and the temperature and density distributions in a wide range of the rarefaction parameter and for various ratios of the hot over the cold plate temperatures. Comparisons with the DSMC method and experimental data are performed. Furthermore, it is numerically proved

that the computed solutions are in agreement with the Chapman-Enskog approximation in a central strip of the computational domain even at moderately large values of the rarefaction parameter.

In Chapter 6 the polyatomic gas flows through circular tubes of various length are examined. The investigation includes pressure driven flows in short channels as well as pressure and temperature driven flows in long channels in a wide range of the Knudsen number. In the former case a parametric study on the propulsion characteristics is performed and the computed quantities include the flow rate, the discharge coefficient, the thrust and the impulse factor are provided in terms of the gas rarefaction and the tube dimensionless length. In the latter case the flow is fully developed and the Poiseuille and thermal creep flows are studied. The effect of the internal degrees of freedom on the results is investigated. The influence of the tangential momentum accommodation coefficient on the flow rates is discussed. Comparisons with experiments are also reported.

In Chapter 7 the adsorption process is investigated. A steady-state half-space gas flow driven by an adsorbing planar wall is considered. The work is focused on the influence of the internal degrees of freedom and the partial thermal gas-surface interaction on all flow quantities including the sticking coefficient. Also comparisons with available numerical data in literature are included. The work is extended in two dimensions in an effort to study the feasibility of multistage cryopumps including a comparison with experimental data.

In Chapter 8 a summary with the associate main results plus some comments on future work are provided.

1.3 Novelty and scientific contributions of the thesis

As discussed in Section 1.1, the dissertation is focused on the effect of the rotational and vibrational degrees of freedom in polyatomic gas heat transfer, flow and adsorption processes in the whole range of the Knudsen number. The investigation is based on the numerical solution of typical heat transfer and flow problems which are modeled by kinetic model equations and simulated using both the DVM and the DSMC approaches. The novel scientific contributions of the dissertation are outlined:

- Based on a detailed comparison with DSMC computational results and available in the literature experimental data, the validity of the Holway, Rykov and Andries models to simulate the specific polyatomic heat transfer, flow and adsorption configurations has been verified.

- The Holway kinetic model has been accordingly adjusted to be applied in polyatomic gases with molecules having more than two atoms in heat flow simulations.

- In conductive plane and cylindrical polyatomic heat transfer the portions of the rotational and vibrational heat fluxes with regard to the total heat flux for various temperatures differences in the whole range of the Knudsen number are reported (similarly for the density and temperature distributions).

- In the case of conductive polyatomic heat transfer in coaxial cylinders the effect of the radius ratio is examined.

- Following the detailed investigation of the effect of the vibrational degrees of freedom, the major importance of the excited vibrational modes in certain polyatomic gases even at ambient temperatures is clearly demonstrated (e.g. SF_6).

- A detailed parametric study on the performance of micro-tubes as low-thrust propulsion systems is performed finding out that the overall propulsion efficiency in polyatomic gases compared to the one in monatomic gases is slightly improved.

- In pressure and temperature driven flows through long tubes, results are reported for polyatomic gases with molecules having more than two atoms.

- Adsorption flow in one and two dimensions has been simulated based on kinetic modeling (instead of the DSMC method).

- In adsorption processes the effect of the internal degrees of freedom is small mainly due to the low temperatures where these processes take place.

- Based on inverse engineering procedures the sticking coefficients of H_2 and D_2 on charcoal surfaces maintained at different temperatures have been estimated.

6

All above scientific contributions in the field of rarefied polyatomic gas processes are reported for first time in the literature and are considered as novel.

Chapter 2

Literature review

2.1 The Knudsen number and flow regimes

In non-equilibrium or rarefied gas flows the main flow parameter is the Knudsen number Kn, introduced by Knudsen around 1909 [24], defined as

$$Kn = \frac{\lambda}{D}, \tag{2.1}$$

where the mean free path λ is defined as the average distance a particle travels between successive collisions and D is a characteristic length of the problem or a length scale of macroscopic gradient, given by $D = \rho/(\partial\rho/\partial x)$, where ρ is the fluid density. For the hard sphere molecules the mean free path can be written as [17]

$$\lambda = \frac{8}{5}\sqrt{\frac{2k_B T}{\pi m}}\frac{\mu}{\hat{P}}, \tag{2.2}$$

with μ being the dynamic viscosity of the gas in temperature T, $\hat{P}$ is the pressure, k_B is the Boltzmann constant and m is the molecular mass. The Knudsen number can thus be interpreted based on the ratio between the Mach number Ma and the Reynolds number Re as,

$$Kn = \sqrt{\frac{\pi\gamma}{2}}\frac{Ma}{Re}, \tag{2.3}$$

9

where γ is the specific heat ratio, while Ma and Re are the Mach and Reynolds numbers. Alternatively, the rarefaction parameter δ is also commonly used, given by

$$\delta = \frac{\hat{P}D\sqrt{m}}{\mu\sqrt{2k_B T}} \sim \frac{1}{Kn}. \tag{2.4}$$

According to the range of the properly chosen Knudsen number the flow regimes can be classified as the continuum regime, slip regime, transition regime, and the free molecular regime. Generally, when $Kn < 0.001$, the Navier-Stokes equations and the continuum model are valid giving accurate results. When Kn is less than 0.1 but is larger than 0.01, some rarefied effects such as the velocity slip and temperature jump appear, although the continuum model is still valid applying a proper modification of the boundary conditions at the solid walls. For values of Knudsen number lie between 0.1 and 100 a kinetic description of the gas is necessary, since intermolecular collisions are reduced and the distribution function is not of Maxwellian type and the use of the Boltzmann equation is needed. The Boltzmann equation describes the time-evolution of the particle distribution function of a simple gas, and is the basic mathematical model in rarefied gas dynamics. It is valid in all flow regimes and the macroscopic fluid dynamic equations, such as the Navier-stokes, Burnett and Super-Burnett, can be derived from it.

2.2 The Boltzmann equation of polyatomic gases

In 1859 Maxwell [25] abandoned the idea that all gaseous molecules move with the same speed and introduced the statistical approach to gaseous medium. Also, he introduced the velocity distribution function and obtained its expression in the equilibrium state. Thus, Maxwell gave the origin to the kinetic theory of gases. Then, in 1872 Boltzmann [26] introduced the kinetic equation which determines the evolution of the distribution function for gaseous systems being out of equilibrium. The first attempt for the kinetic description in polyatomic gas was done by Wang Chang and Uhlenbeck [27] in 1951 utilizing a semi-classical approach. A completely classical treatment was given later by Taxman in 1958 [28]. Usually at small and moderate temperatures, the gas rotation of the gas molecules is modelled by rigid rotators [29], while in some situations depending on the working gas and the temperature the vibration

degrees of freedom are additionally included and described by the quantum harmonic oscillator model [29]. When, as in the case considered in this thesis, intrinsic molecular angular momenta (spin) have no preferential alignment, it is reasonable to describe molecular internal states through a single variable, the internal energy $\hat{I}$. Then, a dilute gas of classical rigid rotators undergoing binary collisions can be described by a kinetic equation having the following general form [30]:

$$\frac{\partial \hat{f}}{\partial t} + \boldsymbol{v} \cdot \frac{\partial \hat{f}}{\partial \hat{\boldsymbol{r}}} + \hat{\boldsymbol{F}}_{\boldsymbol{ex}} \cdot \frac{\partial \hat{f}}{\partial \boldsymbol{v}} = Q\left(\hat{f}, \hat{f}\right), \tag{2.5}$$

where $\hat{f}(t, \hat{\boldsymbol{r}}, \boldsymbol{v}, \hat{I})$ is the spin orientation averaged distribution function, t denotes the time, $\boldsymbol{v} = (\xi_x, \xi_y, \xi_z)$ is the velocity vector, $\hat{\boldsymbol{r}} = (\hat{x}, \hat{y}, \hat{z})$ is the position vector and $\hat{\boldsymbol{F}}_{\boldsymbol{ex}} = (\hat{F}_{ex,x}, \hat{F}_{ex,y}, \hat{F}_{ex,z})$ is the field of the external forces, while the collision operator Q is given by

$$Q = \int\limits_{-\infty}^{\infty} \int\limits_{0}^{\infty} \left[\hat{f}\left(\hat{\boldsymbol{r}}, \boldsymbol{v'}_1, \hat{I}'_1, t\right) \hat{f}\left(\hat{\boldsymbol{r}}, \boldsymbol{v'}, \hat{I}', t\right) - \hat{f}\left(\hat{\boldsymbol{r}}, \boldsymbol{v}_1, \hat{I}_1, t\right) \hat{f}\left(\hat{r}, \boldsymbol{v}, \hat{I}, t\right) \right] \Omega \hat{I}_1^{\mu} d\hat{I}_1 d^3 v_1, \tag{2.6}$$

where Ω is defined as

$$\Omega = \int\limits_{S} d^2 \hat{e}' \int\limits_{0}^{\hat{E}} \left(\hat{I}'\right)^{\mu} d\hat{I}' \int\limits_{0}^{\hat{E}-\hat{I}'_1} \left(\hat{I}'_1\right)^{\mu} d\hat{I}'_1 \frac{v_r'^2}{v_r} \sigma\left(\hat{E}; \hat{\boldsymbol{e}}' \cdot \hat{\boldsymbol{e}}; \hat{I}', \hat{I}'_1 \to \hat{I}, \hat{I}_1\right). \tag{2.7}$$

Here, $\sigma(\hat{E}; \hat{\boldsymbol{e}}' \cdot \hat{\boldsymbol{e}}; \hat{I}', \hat{I}'_1 \to \hat{I}, \hat{I}_1)$ is the differential cross-section associated with a binary collision which produces a pair of molecules in the final states $(\boldsymbol{v}, \hat{I})$, $(\boldsymbol{v}_1, \hat{I}_1)$ from a pair of molecules in the initial states $(\boldsymbol{v'}, \hat{I}')$, $(\boldsymbol{v'}_1, \hat{I}'_1)$. The argument $\hat{E}$ denotes the conserved total energy in the center of mass reference frame:

$$\hat{E} = \frac{1}{4} m\, v_r^2 + \hat{I} + \hat{I}_1 = \frac{1}{4} m\, (v_r')^2 + \hat{I}' + \hat{I}'_1. \tag{2.8}$$

The unit vectors $\hat{\boldsymbol{e}}' = \boldsymbol{v'}_r/v'_r$ and $\hat{\boldsymbol{e}} = \boldsymbol{v}_r/v_r$ have the directions of the relative velocities $\boldsymbol{v'}_r = \boldsymbol{v'}_1 - \boldsymbol{v'}$ and $\boldsymbol{v}_r = \boldsymbol{v}_1 - \boldsymbol{v}$ before and after a collision, respectively. The exponent μ takes the values 0 for $j = 2$ and $1/2$ for $j = 3$, with j being the number of rotational degrees of freedom. In Eq. (2.5) the left part of the equation describes the free flight of the particles

11

under the influence of external forces $\hat{\boldsymbol{F}}_{\boldsymbol{ex}}$. The right hand of the equation is the collision term and its complexity makes the solution of the Boltzmann equation a very difficult and challenging task. An alternative definition of the Boltzmann equation in polyatomic gases with several degrees of freedom (inducing rotational and vibrational states) can be found in [31]. All the details related to the vibrational degrees of freedom are discussed in Chapter 5. The distribution function $\hat{f}(t, \hat{\boldsymbol{r}}, \boldsymbol{v}, \hat{I})$ of the polyatomic Boltzmann equation satisfies the H-theorem [1], introduced by Ludwig Boltzmann in 1872, which is a more general statement of the second thermodynamic law and is a quantity that on the kinetic time scale measures the approach to equilibrium.

Solving the Boltzmann equation for the unknown distribution function leads to the determination of any quantity of practical interest. In particular, the macroscopic quantities are found by appropriate moments of the distribution function, such as the following:

- Number density

$$n(\hat{\boldsymbol{r}}, t) = \int\limits_{-\infty}^{\infty} \int\limits_{0}^{\infty} \hat{f} d\hat{I} d\boldsymbol{v} \tag{2.9}$$

- Bulk velocity vector

$$\hat{\boldsymbol{u}}(\hat{\boldsymbol{r}}, t) = \frac{1}{n(\hat{\boldsymbol{r}}, t)} \int\limits_{-\infty}^{\infty} \int\limits_{0}^{\infty} \boldsymbol{v} \hat{f} d\hat{I} d\boldsymbol{v} \tag{2.10}$$

- Stress tensor

$$\hat{P}_{ij}(\hat{\boldsymbol{r}}, t) = m \int\limits_{-\infty}^{\infty} \int\limits_{0}^{\infty} (\xi_i - \hat{u}_i)(\xi_j - \hat{u}_j) \hat{f} d\hat{I} d\boldsymbol{v} \tag{2.11}$$

- Translational temperature

$$T_{tr}(\hat{\boldsymbol{r}}, , t) = \frac{m}{3k_B n(\hat{\boldsymbol{r}}, t)} \int\limits_{-\infty}^{\infty} \int\limits_{0}^{\infty} (\boldsymbol{v} - \hat{\boldsymbol{u}})^2 \hat{f} d\hat{I} d\boldsymbol{v} \tag{2.12}$$

- Rotational temperature

$$T_{rot}(\hat{\boldsymbol{r}}, t) = \frac{2}{jk_B n(\hat{\boldsymbol{r}}, t)} \int\limits_{-\infty}^{\infty} \int\limits_{0}^{\infty} \hat{f} \hat{I} d\hat{I} d\boldsymbol{v} \tag{2.13}$$

12

- Total temperature

$$T\left(\hat{\boldsymbol{r}},t\right)=\frac{3T_{tr}\left(\hat{\boldsymbol{r}},t\right)+jT_{rot}\left(\hat{\boldsymbol{r}},t\right)}{3+j} \tag{2.14}$$

- Translational heat flux vector

$$\boldsymbol{Q}_{tr}\left(\hat{\boldsymbol{r}},t\right)=\frac{m}{2}\int\limits_{-\infty}^{\infty}\int\limits_{0}^{\infty}\left(\boldsymbol{v}-\hat{\boldsymbol{u}}\right)\left(\boldsymbol{v}-\hat{\boldsymbol{u}}\right)^2\hat{f}d\hat{I}d\boldsymbol{v} \tag{2.15}$$

- Rotational heat flux vector

$$\boldsymbol{Q}_{rot}\left(\hat{\boldsymbol{r}},t\right)=\int\limits_{-\infty}^{\infty}\int\limits_{0}^{\infty}\left(\boldsymbol{v}-\hat{\boldsymbol{u}}\right)\hat{f}\hat{I}d\hat{I}d\boldsymbol{v} \tag{2.16}$$

- Total heat flux vector

$$\boldsymbol{Q}\left(\hat{\boldsymbol{r}},t\right)=\boldsymbol{Q}_{tr}\left(\hat{\boldsymbol{r}},t\right)+\boldsymbol{Q}_{rot}\left(\hat{\boldsymbol{r}},t\right) \tag{2.17}$$

- Total pressure

$$\hat{P}\left(\hat{\boldsymbol{r}},t\right)=n\left(\hat{\boldsymbol{r}},t\right)k_BT\left(\hat{\boldsymbol{r}},t\right) \tag{2.18}$$

In Eqs. (2.9)-(2.17) the quantities with subscripts tr and rot are related to the translational and rotational degrees of freedom respectively.

Due to the complexity of the collision term of the Boltzmann equation and immense computational requirements associated with the solution of the Boltzmann equation, several polyatomic kinetic models have been proposed to substitute the collision term. Alternatively, the polyatomic Boltzmann equation can be solved using the stochastic method Direct Simulation Monte Carlo which has been thoroughly tested in high Knudsen-number flows over the past 25 years [33, 34]. An important issue is the interaction of rarefied gases with solid surfaces and significant effort has been made in the modelling of the boundary conditions. The polyatomic kinetic models, the boundary conditions and the numerical methods widely used in literature are presented in the next sections.

2.3   Polyatomic kinetic models

The mathematical complexity in dealing directly with the collision integrals appearing in the formal kinetic theory of the Boltzmann equation for polyatomic gases compelled the introduction of a great number of kinetic model equations. More specifically, the complicated collision term eplaced by the kinetic models causing a remarkable reduction in the computational solving effort. The kinetic models must satisfy the collision invariants of mass, momentum and energy as well as the H-theorem. Moreover, the Chapman-Enskog analysis of those models must lead to the correct calculation of transport coefficients such as bulk viscosity, viscosity and thermal conductivity for translational and internal degrees of freedom.

In 1964, Morse [35] proposed an extension of the Bhatnagar-Gross-Krook model (BGK) [36] for monatomic gases to polyatomic gases in which the internal degrees of freedom of the molecules are represented by an additional energy variable in the distribution function, and both elastic and inelastic collisions (the latter providing the coupling between translational and internal energies) are characterized by constant collision frequencies. More elaborate kinetic model equations for polyatomic gases can also be found in the literature, e.g., the works of Holway [20], Hanson and Morse [37], Brau [38], Wood [39], McCormack [40], Rykov [21], Andries [22], Marques [41] and Fernandes and Marques [42]. In the work of Hanson and Morse, kinetic model equations for diatomic gases have been obtained by employing a diagonal approximation in the linear operator of the Boltzmann equation. In Braus work, the inelastic collisions are treated by a FokkerPlanck term whereas the elastic collisions are described by a single relaxationtime term. The kinetic model equation proposed by Wood uses the ellipsoidal statistical model (formulated by Cercignani and Tironi [43] for the elastic collisions) which retains the essential simplicity of the BGK model and allows the calculation of the correct value of the Prandtl number. The McCormack model is an extension of the Hanson and Morse diatomic gas model to a polyatomic gas. In the work of Marques, a classical kinetic model equation for polyatomic gases is derived by replacing the Boltzmann collision operator by a single relaxation-time term and keeping some of the main physical properties of the usual Navier-Stokes-Fourier description. The model proposed by Fernandes and Marques replaces the Boltzmann collision

operator by a single relaxation-time term which is compatible with Grads 6-moment approximation and valid for the limiting case that the energy exchange between translational and internal degrees of freedom is slow, but not negligible. It is noted that most of the aforementioned kinetic models belong to linearized kinetic theory, except from those proposed by Morse, Holway, Brau, Rykov and Andries. The Holway, Rykov and Andries models have been applied in the past to solve high speed flows providing very good agreement between simulations and available experimental data [44, 45]. For this reason, these models are used in this thesis and are presented in more detail below.

The Holway model [20] was established in 1966. This model was one of the first approaches for polyatomic gases. In this model the collision term consists of two components corresponding to elastic and inelastic collisions. The Holway model is similar to Morse model but there are some differences. The elastic collision term used by Holway is different and satisfies the requirement for conservation of particles in any state and not over all the states at it is in the Morse model. Also, in the Morse model the definition of the heat capacity at constant volume used in the temperature over all degrees of freedom is independent of the temperature, something which is true only at very high temperatures [37]. The Holway model can be written by

$$Q\left(\hat{f}, \hat{f}\right) = \nu_{tr}\left(n, T_{tr}\right)\left(\hat{f}_{tr} - \hat{f}\right) + \nu_{rot}\left(n, T_{tr}\right)\left(\hat{f}_{rot} - \hat{f}\right), \qquad (2.19)$$

where ν_{tr} and ν_{rot} are the elastic and inelastic collision frequencies, while the elastic and inelastic equilibrium distribution functions $\hat{f}_{tr}$ and $\hat{f}_{rot}$ are given by

$$\hat{f}_{rot} = n\left(\frac{m}{2\pi k_B T}\right)^{3/2} \exp\left[\frac{-m(\boldsymbol{v} - \hat{\boldsymbol{u}})^2}{2k_B T}\right] \frac{\hat{I}^{j/2-1}}{\Gamma\left(j/2\right)\left(k_B T\right)^{j/2}} \exp\left(\frac{-\hat{I}}{k_B T}\right) \qquad (2.20)$$

and

$$\hat{f}_{tr} = \hat{n}(\hat{I}|\hat{y})\left(\frac{m}{2\pi k_B T_{tr}}\right)^{3/2} \exp\left[\frac{-m(\boldsymbol{v} - \hat{\boldsymbol{u}})^2}{2k_B T_{tr}}\right], \qquad (2.21)$$

respectively, where Γ is the gamma function, $\hat{n}(\hat{I}|\hat{y})$ is the number density of molecules having internal energy $\hat{I}$, n is the total number density, T_{tr} is the translational temperature and T is the total temperature, as well as $\hat{\boldsymbol{u}} = (\hat{u}_x, \hat{u}_y, \hat{u}_z)$ and $\hat{\boldsymbol{v}} = (\xi_x, \xi_y, \xi_z)$ are the bulk and molecular

velocity vectors respectively. It is noted that as $\nu_{rot} \to 0$ the Holway model is reduced to BGK model for monatomic gases [36]. The main disadvantage of this model is that cannot recover the shear viscosity and the thermal conductivity simultaneously. Thus depending on the problem which is under question, the proper elastic and inelastic collision frequencies must be chosen. The H-theorem for this model can be proved in a straightforward manner following the arguments leading to analogous proof of the BGK model and the corresponding analysis is presented in Appendix B.

Another model, the Rykov model [21], appeared in 1975. Although its first version was only for diatomic gases, recently in [46] the model has been extended to polyatomic gases. The Rykov model consists of two components, one for the elastic collisions and the other for the inelastic collisions, and can be written in the same way as the Holway model described by the Eq. (2.19). The elastic and inelastic equilibrium distribution functions $\hat{f}_{tr}$ and $\hat{f}_{rot}$ for the Rykov model read such that

$$
\hat{f}_{rot} = n \left(\frac{m}{2\pi k_B T} \right)^{3/2} \exp\left[\frac{-m(\boldsymbol{v} - \hat{\boldsymbol{u}})^2}{2 k_B T} \right] \frac{\hat{I}^{j/2-1}}{\Gamma\left(j/2\right) \left(k_B T\right)^{j/2}} \exp\left(\frac{-\hat{I}}{k_B T} \right) \times
$$
$$
\left[1 + \frac{2\varpi_0 m \boldsymbol{Q}_{tr} \left(\boldsymbol{v} - \hat{\boldsymbol{u}}\right)}{15 n (k_B T)^2} \left(\frac{m(\boldsymbol{v} - \hat{\boldsymbol{u}})^2}{2 k_B T} - \frac{5}{2} \right) + \frac{2\varpi_1 \left(1 - \kappa\right)}{j} \frac{m \boldsymbol{Q}_{rot} \left(\boldsymbol{v} - \hat{\boldsymbol{u}}\right)}{n(k_B T)^2} \left(\frac{\hat{I}}{k_B T} - \frac{j}{2} \right) \right] \quad (2.22)
$$

and

$$
\hat{f}_{tr} = n \left(\frac{m}{2\pi k_B T_{tr}} \right)^{3/2} \exp\left[\frac{-m(\boldsymbol{v} - \hat{\boldsymbol{u}})^2}{2 k_B T_{tr}} \right] \frac{\hat{I}^{j/2-1}}{\Gamma\left(j/2\right) \left(k_B T_{rot}\right)^{j/2}} \exp\left(\frac{-\hat{I}}{k_B T_{rot}} \right) \times
$$
$$
\left[1 + \frac{2 m \boldsymbol{Q}_{tr} \left(\boldsymbol{v} - \hat{\boldsymbol{u}}\right)}{15 n (k_B T_{tr})^2} \left(\frac{m(\boldsymbol{v} - \hat{\boldsymbol{u}})^2}{2 k_B T_{tr}} - \frac{5}{2} \right) + \frac{2 \left(1 - \kappa\right)}{j} \frac{m \boldsymbol{Q}_{rot} \left(\boldsymbol{v} - \hat{\boldsymbol{u}}\right)}{n k_B^2 T_{tr} T_{rot}} \left(\frac{\hat{I}}{k_B T_{rot}} - \frac{j}{2} \right) \right], \quad (2.23)
$$

where n is the number density, T is the temperature and $\boldsymbol{Q}$ is the heat flux vector. The quantities with subscripts tr and rot are related to the translational and rotational degrees of freedom. It is stated in [46] that the parameters ϖ_0 and ϖ_1 are chosen so that the thermal conductivity obtained from the model equation is close to the experimental data in [47]. It is also pointed that the parameter κ for a power intermolecular potential is constant. The Rykov model recovers simultaneously both the viscosity and thermal conductivity coefficients, while

in the limit case $\nu_{rot} \to 0$ is transformed to the Shakhov model [48] for monatomic gases. A shortcoming of the Rykov model is that the H-theorem has not been proved for it yet.

Finally, the model proposed by Andries in 2000 [22] is presented. This model holds the entropy inequality and provides correct expressions simultaneously for the viscosity and thermal conductivity coefficients. In addition, preliminary calculations indicate good agreement with corresponding results based on the Boltzmann equation. This model for monatomic gas is reduced to the ES model [20]. Contrary to the aforementioned models, the collision term of the Andries model is kept in compact form as it is in ES model, introducing a new "artificial" temperature which is accordingly decomposed into translational and rotational parts. The model is written by

$$Q(\hat{f}, \hat{f}) = \left(\frac{1}{1 - \nu + \theta\nu} \right) \frac{\hat{P}_{tr}}{\mu(T_{tr})} \left(\hat{f}_{mod} - \hat{f} \right), \tag{2.24}$$

where

$$\hat{f}_{mod} = \frac{n\hat{I}^{j/2-1}}{\Gamma(j/2)\pi^{3/2}\sqrt{\det \hat{K}_{ij}}(kT_{rel})^{j/2}} \exp\left[-\sum_{i,j}^{3} (\xi_i - \hat{u}_i)\hat{K}_{ij}^{-1}(\xi_j - \hat{u}_j) - \frac{\hat{I}}{k_B T_{rel}} \right], \tag{2.25}$$

with

$$\hat{K}_{ij} = (1 - \theta)\left[(1 - \nu)\frac{2k_B T_{tr}}{m}\delta_{ij} + 2\nu\frac{\hat{P}_{ij}}{nm} \right] + \theta\frac{2k_B T}{m}\delta_{ij}. \tag{2.26}$$

The quantity T_{rel} in Eq. (2.25) is a new artificial temperature which is defined as

$$T_{rel} = \theta T + (1 - \theta)T_{rot}. \tag{2.27}$$

In Eqs. (2.24)-(2.27), T_{rot} is the rotational temperature, T is the total temperature, $\hat{P}_{ij}$ are the components of the pressure tensor, $\hat{P}_{tr} = nk_B T_{tr}$ is the translational pressure, $\mu(T_{tr})$ is the viscosity at translational temperature T_{tr} and δ_{ij} is the Kronecker delta. The Andries model is transformed to the ES monatomic model by taking $\theta = 0$ and $\nu = -1/2$. It is noted that the entropy inequality (H-theorem) has been proved for this polyatomic kinetic model with $-1/2 \leq \nu < 1$ and $0 \leq \theta < 1$ in [22].

The model kinetic equations obtained allow further simplification by averaging of the distribution function over the variable $\hat{I}$. We introduce the functions $\hat{g}$ and $\hat{h}$, described by

$$\hat{g} = \int_0^\infty \hat{f} d\hat{I}, \qquad \hat{h} = \int_0^\infty \hat{f} \hat{I} d\hat{I}, \tag{2.28}$$

in order to eliminate the rotational energy variable to save computational memory and cost. Multiplying the each kinetic model equation by 1 and $\hat{I}$ and integrating the resulting equations with respect to $\hat{I}$ from zero to infinity, the kinetic equations can be transformed into two coupled equations. The equilibrium distribution functions for the elastic and inelastic collisions for each model are written as

- *Holway model*

$$\hat{g}_{rot} = n \left(\frac{m}{2\pi k_B T} \right)^{3/2} \exp \left[\frac{-m(\boldsymbol{v} - \hat{\boldsymbol{u}})^2}{2 k_B T} \right], \quad \hat{h}_{rot} = \frac{j k_B T}{2} \hat{g}_{rot},$$

$$\hat{g}_{tr} = n \left(\frac{m}{2\pi k_B T_{tr}} \right)^{3/2} \exp \left[\frac{-m(\boldsymbol{v} - \hat{\boldsymbol{u}})^2}{2 k_B T_{tr}} \right], \quad \hat{h}_{tr} = \frac{j k_B T_{rot}}{2} \hat{g}_{tr}. \tag{2.29}$$

- *Rykov model*

$$\hat{g}_{rot} = n \left(\frac{m}{2\pi k_B T} \right)^{3/2} \exp \left[\frac{-m(\boldsymbol{v} - \hat{\boldsymbol{u}})^2}{2 k_B T} \right] \left[1 + \frac{2\varpi_0 m \boldsymbol{Q}_{tr} (\boldsymbol{v} - \hat{\boldsymbol{u}})}{15 n (k_B T)^2} \left(\frac{m(\boldsymbol{v} - \hat{\boldsymbol{u}})^2}{2 k_B T} - \frac{5}{2} \right) \right],$$

$$\hat{g}_{tr} = n \left(\frac{m}{2\pi k_B T_{tr}} \right)^{3/2} \exp \left[\frac{-m(\boldsymbol{v} - \hat{\boldsymbol{u}})^2}{2 k_B T_{tr}} \right] \left[1 + \frac{2 m \boldsymbol{Q}_{tr} (\boldsymbol{v} - \hat{\boldsymbol{u}})}{15 n (k_B T_{tr})^2} \left(\frac{m(\boldsymbol{v} - \hat{\boldsymbol{u}})^2}{2 k_B T_{tr}} - \frac{5}{2} \right) \right],$$

$$\hat{h}_{rot} = \frac{j k_B T}{2} \hat{g}_{rot} + \left(\frac{m}{2\pi k_B T} \right)^{3/2} \exp \left[\frac{-m(\boldsymbol{v} - \hat{\boldsymbol{u}})^2}{2 k_B T} \right] \varpi_1 \left(1 - \kappa \right) \frac{m \boldsymbol{Q}_{rot} (\boldsymbol{v} - \hat{\boldsymbol{u}})}{k_B T},$$

$$\hat{h}_{tr} = \frac{j k_B T_{rot}}{2} \hat{g}_{tr} + \left(\frac{m}{2\pi k_B T_{tr}} \right)^{3/2} \exp \left[\frac{-m(\boldsymbol{v} - \hat{\boldsymbol{u}})^2}{2 k_B T_{tr}} \right] \left(1 - \kappa \right) \frac{m \boldsymbol{Q}_{rot} (\boldsymbol{v} - \hat{\boldsymbol{u}})}{k_B T_{tr}}. \tag{2.30}$$

18

- *Andries model*

$$\hat{g}_{mod} = \frac{n}{\pi^{3/2}\sqrt{\det \hat{K}_{ij}}} \exp\left[-\sum_{i,j}^{3}\left(\xi_i - \hat{u}_i\right)\hat{K}_{ij}^{-1}\left(\xi_j - \hat{u}_j\right)\right],$$

$$\hat{h}_{mod} = \frac{jk_B T_{rel} n}{2\pi^{3/2}\sqrt{\det \hat{K}_{ij}}} \exp\left[-\sum_{i,j}^{3}\left(\xi_i - \hat{u}_i\right)\hat{K}_{ij}^{-1}\left(\xi_j - \hat{u}_j\right)\right]. \tag{2.31}$$

The above kinetic equations are used in the next chapters for the modeling of the heat transfer, flow and adsorption processes. Also, comprehensive analysis showing the advantages and disadvantages of each model is performed.

2.4 Boundary conditions for polyatomic gases

The Boltzmann equation must be accompanied by the boundary conditions which describe the interaction between molecules and solid walls. The gap between solid state physics and the kinetic theory of gases is bridged with the definition of the boundary conditions. The limited knowledge on the interaction potential of the gas molecules with molecules of the solid makes the theoretical investigation of the gas-surface interaction a very difficult task. In the description of the interaction of the gas molecules with solid surface there are two simple models proposed by Maxwell [49] in 1879: the diffuse reflection model and the specular reflection model.

On a boundary surface the velocity distribution function of incident particles $\hat{f}^{-}$ is related to that of reflected molecules $\hat{f}^{-}$ in the polyatomic gases as [17]

$$\xi_n \hat{f}^{+}\left(\boldsymbol{v}, \hat{I}\right) = -\int_{\xi'_n \leq 0}\int_{0}^{\infty}\xi'_n \hat{f}^{-}\left(\boldsymbol{v}', \hat{I}'\right) R\left(\boldsymbol{v}', \boldsymbol{v}, \hat{I}, \hat{I}'\right) d\hat{I}'d\boldsymbol{v}', \quad \xi_n \geq 0, \tag{2.32}$$

where $\xi_n = \boldsymbol{\xi} \cdot \boldsymbol{n}$ is a normal velocity component, $\boldsymbol{n}$ is the unit vector normal to the surface directed to the gas. In Eq. (2.32) the velocity and the energy before and after the collision with the solid wall are denoted by $\left(\boldsymbol{v}', \hat{I}'\right)$ and $\left(\boldsymbol{v}, \hat{I}\right)$ respectively. The explicit expression of the scattering kernel $R\left(\boldsymbol{v}', \boldsymbol{v}, \hat{I}, \hat{I}'\right)$ depends on the gas-surface interaction law. The well known

19

diffuse scattering corresponds to the following kernel [1]

$$R_d\left(\boldsymbol{v}', \boldsymbol{v}, \hat{I}, \hat{I}'\right) = \frac{m^2}{2\pi(k_B T_{tr}^\alpha)^2} \exp\left(-\frac{mv^2}{2k_B T_{tr}^\alpha}\right) \frac{\hat{I}^{j/2-1}}{\Gamma\left(j/2\right)(k_B T_{rot}^\alpha)^{j/2}} \exp\left(-\frac{\hat{I}}{k_B T_{rot}^\alpha}\right), \quad (2.33)$$

where T_{tr}^α and T_{rot}^α are two temperatures. Physically, it means that a particle can be reflected to any direction independently of its velocity before the collision with a surface. The two temperatures T_{tr}^α and T_{rot}^α can be determined from the balance equations for the translational and rotational energies of the gas when it interacts with the wall. In [50] different models have been proposed for the determination of T_{tr}^α and T_{rot}^α and are examined in Chapter 2. The simplest is that the T_{tr}^α and T_{rot}^α are equal to the temperature of the wall T^w ($T_{tr}^\alpha = T_{rot}^\alpha = T^w$). Such an interaction is frequently called as the complete accommodation. In many practical applications the diffuse scattering is well justified and provides reliable results. The final form of the outgoing distribution from the wall is obtained by substituting Eq. (2.33) into Eq. (2.32) as

$$\hat{f}_d^+ = n_w \left(\frac{m}{2\pi k_B T_{tr}^\alpha}\right)^{3/2} \exp\left(-\frac{mv^2}{2k_B T_{tr}^\alpha}\right) \frac{\hat{I}^{j/2-1}}{(k_B T_{rot}^\alpha)^{j/2} \Gamma\left(j/2\right)} \exp\left(-\frac{\hat{I}}{k_B T_{rot}^\alpha}\right). \quad (2.34)$$

The specular reflection model assumes that the incident molecules reflect on the body surface as the elastic spheres reflect on the entirely elastic surface, i.e., the normal to the surface component of the relative velocity reverses its direction while the parallel to the surface components remain unchanged. Thus the normal pressure originated from the reflected mofecules equals to that originated from the incident molecules; the sheer stress subjected by the surface from the reflected molecules has the opposite sign to that from the incident molecules and the net sheer stress is zero; the total energy exchange with the surface is zero. An other widely used boundary condition is the diffuse-specular boundary conditions defined as [1]

$$\hat{f}_{ds}^+ = \alpha_M \hat{f}_d^+ + (1 - \alpha_M) \hat{f}^-, \quad (2.35)$$

where $\hat{f}^-$ is the velocity distribution functions of molecules incident at the surface and α_M is the tangential momentum accommodation coefficient. This boundary condition allows to

eliminate the discrepancy between simulations and experiments which is observed for some noble gases, e.g. helium, neon etc. Experimental data on the accommodation coefficient of the noble gases on various surfaces reported in [51]. However, some experimental data contradict to theoretical results based on the boundary condition Eq. (2.35), hence more physical scattering kernels should be used, e.g. that proposed by Cercignani and Lampis [52]. Some of the facts that establish the superiority of this model are the distinction between the accommodation of energy and momentum introducing two coefficients and the possibility of adjusting them to obtain diffuse, specular or backscattering reflection which can occur on a rough surface. Recently, the model has been extended to polyatomic gases [53]. A serious shortcoming of the model is its inability to include the case of completely diffuse scattering with partial or zero energy accommodation. Also, the model is purely classical and thus cannot realistically describe energy exchange to and from vibrational states, where the separation of energy levels is typically of the same order as, or larger than, $k_B T^w$.

2.5 Numerical methods

The area of numerical simulation of rarefied gas flows is rapidly expanding due to the applicability of the rarefied gas dynamics theory in several practical applications (micromachines, deposition techniques, fusion technology, etc.), requiring more and more computer simulations. The numerical solution of the integral-differential Boltzmann equation in the case of polyatomic gases, with the collision term and an unknown function having as many as eight arguments is so difficult that many researchers envisaged various methods to solve the problems in transitional regime, making them readily tackled. Some of these methods are characterized as analytical, for instance the Moment method [54, 56] or the Method of elementary solutions [17, 54], and some other as semi-analytical, for example the Integro-moment method [17, 55, 57]. Due to limitations related to applicability range, generality, accuracy or complexity, two numerical methods have prevailed: the Discrete Velocity Method (DVM) and the Direct Simulation Monte Carlo (DSMC).

After the innovated work of Carleman [58], Broadwell [59], Huang et al. [60] and Cabanes [61], the deterministic DVM method has been developed into one of the most common

techniques for solving the Boltzmann equation [1, 62] and simplified kinetic model equations [17, 63] in the area of rarefied gas dynamics. The method has also been applied to solve mixture problems [64, 65]. An extensive review article on internal rarefied gas flows including DVM applications has been given lately by Sharipov [17]. Recently, new models of discrete velocity gases [66] and mixtures [67] have been introduced indicating that the method can be extended into more general models including polyatomic gases [68]. Also, recent work shows that the DVM method can also be employed when the form of kinetic models is non-linear producing accurate results. The method is based on a discretization of the velocity and space variables by choosing a suitable set of discrete velocities and by applying a consistent finite difference scheme, respectively. Then, the collision integral term is approximated by an appropriate quadrature, and the resulting discrete system of equations is solved in an iterative manner. It is noted that the number of the iterations is rapidly increased as the Knudsen number is decreased, although the results are considered valid in the whole range of the Knudsen number. The accuracy of the results depends on the number of the chosen discrete velocities, as the number of the velocities is increased more and more accurate results are provided.

The stochastic DSMC method, proposed by Bird [69] in the 1960s, is an alternative method to DVM for simulation of rarefied gas flows, in which the mean free path of a molecule is of the same order (or greater) of a representative physical length scale. Later, it was revealed that the DSMC solves the Boltzmann equation [70]. Currently the DSMC method has been applied to the solution of flows ranging from estimation of the space shuttle re-entry aerodynamics, to the modeling micro-electro-mechanical systems (MEMS) [71–73]. In the DSMC method simulation molecules which represent a large number of real molecules are used. Simulation molecules are moved through a simulation of physical space in a realistic manner that is directly coupled to physical time such that unsteady flow characteristics can be modeled. Intermolecular collisions and molecule-surface collisions are calculated using probabilistic, phenomenological models. Common collision models include the Hard Sphere model, the Variable Hard Sphere (VHS) model [71], and the Variable Soft Sphere (VSS) model [71]. In the DSMC method the anelastic collisions are dealt by Borgnakke-Larsen (BL) model [23] and by its quantum extension [75] to describe collisions involving vibrational energy transfer when the vibrational

degrees of freedom must be taken into account. The BL model describes energy transfer between internal and translational energies by assuming that a fraction of the total number of collisions is elastic, i.e. no exchange between internal and translational energy occurs, whereas the remaining fraction is composed by collisions in which rotational and/or vibrational energy is exchanged according to prescribed probabilistic rules. Recently the quantum-kinetic (Q-K) model proposed by Bird for study of chemically reacting gas [76]. The main drawback of the method is the frequent occurrence of noisy results. Numerous parameters (i.e. size of cells, number of representative molecules, number of samples) must be adjusted to obtain a good representation of the gas.

The main numerical method used in this thesis is the DVM method, while the DSMC method is used as an alternative technique for benchmarking purposes.

2.6   Polyatomic heat transfer

Heat transfer through stationary rarefied gases confined between solid surfaces continues to be an active area of research. This is well justified since this heat transfer problem is met in several technological applications including vacuum pressure gauges [78], vacuum solar collectors [79], multilayer insulation blankets in space and cryogenic equipment [15], micro heat exchangers and microsensors [80, 81]. It is also commonly used as a prototype set-up in order to determine the thermal conductivity of gases [82] the temperature jump coefficient [83] and the energy accommodation at the cold and hot surfaces, combining modeling and measurements [84–86]. The case of the heat transfer through a monatomic gas has been extensively investigated. The literature survey on this topic is very long and only some very recent papers for linear and nonlinear kinetic treatment of single monatomic gases or mixtures of monatomic gases are cited here [86–90]. However, the research work is not as extensive in the case of polyatomic gases, where the contribution of the internal degrees of freedom to thermal effects is expected to be important, leading to deviations from the corresponding monatomic results.

The polyatomic kinetic models by Morse [35], Holway [20] and Hanson and Morse [37] have been implemented to solve the plane heat transfer and temperature jumps problems. Most of the work refers to small temperature differences and the applied linearized kinetic model equations

are solved via semi-analytical techniques and variational methods [91–94] as well as by an early version of the discrete ordinates (velocity) method [95]. The model proposed by Rykov [21] has also been implemented to solve heat transfer in diatomic gases confined between parallel plates in a wide range of temperatures providing good agreement with experimental data [50]. Also, experimental work in polyatomic gases between parallel plates has been performed in [96, 97] and [85] measuring heat flow rates and thermal accommodation coefficients respectively.

The available research work of cylindrical heat conduction in rarefied polyatomic gases is rather limited. There are only the early works of Lees and Liu [98] applying the two-sided Maxwellian associated with the 4th order moment method and of Cipolla and Morse [99] solving the Morse model by the Knudsen iteration scheme for small temperature differences. Experimental work has been performed for very small temperature differences in [84] and for larger differences in [79, 80]. The two latter works have direct relevance to the design of evacuated solar collectors and Pirani micro sensors respectively. In [79], the DSMC method [19] subject to the Borgnakke-Larsen collision scheme [23] has also been applied to provide satisfactory data for desorbable gases which are difficult to obtain experimentally.

Similar work in the case of large temperature differences is very limited. Nonlinear heat transfer in diatomic gases confined between two parallel plates has been solved based on the Rykov model in [50] focusing on the influence of the boundary conditions on the density and temperature distributions. The solution is based on the discrete ordinates (velocity) method, while good agreement with experimental results [96, 97] has been observed. Thus, a detailed investigation of the nonlinear conductive heat transfer through rarefied polyatomic gases confined between two coaxial cylinders and two infinite parallel pates is needed. These heat transfer configurations are investigated here, based on both deterministic and stochastic methodologies. The deterministic modeling includes the direct solution of the Holway, Rykov and Andries models, whereas the stochastic DSMC scheme is adopted to solve the Boltzmann equation in combination with the Larsen-Borgnakke collision model.

2.7   Polyatomic flows through capillaries

Rarefied gaseous flows in micro devices can be found almost everywhere in technological applications, i.e. micro-electromechanical devices (MEMS), micro-sensors, pressure gauges, vacuum pumps, pipe networks etc. It is noted that in all these applications the operation of the system may be under low, medium, or high vacuum conditions. The majority of the studies was made for monatomic gases based on the DSMC method [73, 100] as well as on the kinetic models [101, 102]. However, the research work in polyatomic gas flow is limited and is referred mainly to linear polyatomic gases. In [103–106] the Hanson-Morse and Rykov models have been implemented to solve the fully developed diatomic flows under temperature and pressure gradients through parallel plates and cylindrical tubes. The analysis shows that the calculated quantities in the case of temperature driven flows can differ from the corresponding ones in the monatomic gas by 30 to 40%.

The available research in the case of short channels is not as extensive in the case of the long channels where the flow is fully developed. The study of short channels is more difficult since the distribution function is four- or five-dimensional and the complete flow field, including part of the upstream/downstream containers, must be included in the simulation. In [107, 108] numerical investigation of the rarefied nitrogen gas flow through parallel plates into vacuum is performed. Also, the dependence of the gas flow rate through the channel on the Knudsen number, the wall temperature, the thermal accommodation coefficients and the channel length is determined, showing that when a diatomic gas flow is computed with the boundary conditions proposed in [50], which take into account the physics of the interaction between diatomic molecules and the solid surface, the flow rates for diatomic and monatomic gases differ. Also in [109] the temperature driven gas flows in both a two-dimensional finite length microchannel and a cylindrical tube have been studied numerically, based on the DSMC method supplemented with the Larsen-Borgnakke collision model, while in [110] experimental data for nitrogen flow in channels are presented.

Since in many practical applications the working gas is polyatomic, and the available work on flows with nonlinear molecules is limited, a part of this thesis deals with polyatomic gas flows through long and short tubes.

2.8   Polyatomic gas adsorption on solid surfaces

Gas adsorption processes are present in many natural, physical, biological, and chemical systems and are widely used in industrial applications such as water purification, air conditioning (adsorption chillers), vapor deposition [111] and vacuum pumping (getters and cryogenic pumps) [112]. At the gas-surface interface a Knudsen layer is developed and therefore, modeling of such flows is commonly based on kinetic equations or on the DSMC method. In [113], the authors have studied one-dimensional steady flows of binary monatomic gas mixtures in contact with an infinite planar wall which absorbs the two gas components at different rates based on the DSMC method. Recently in [114], a 2D geometry, met in vacuum technology devices like Nonevaporable getters (NEG) or cryogenic pumps [112], has been simulated. In such devices the absorbing surfaces are organized in more or less densely packed arrays. An other application area of the adsorption processes is the cryopumping. The cryopumps, where the main operational mechanism is based on the adsorption process, have been proposed for use in fusion reactors and their modelling is an attractive area for many researchers. In [115] a numerical modeling, including comparisons with experimental data, of a high-performance large-scale prototype cryopump of ITER (International Thermonuclear Experimental Reactor) is performed based on the Test Particle Monte Carlo (TPMC), which is a simulation tool in the collisionless flow regime. Next, the same configuration is modelled combining both DSMC and TPMC methods in [116] providing detailed information of the gas flow field such as pressure and temperature distributions, number of particles absorbed by each cryopanel, etc. In [117] a three-stage compound cryopump for use in fusion reactors such as DEMO (DEMOnstration Power Plant) is modelled based on the DSMC method.

All the aforementioned works are based on the DSMC method due to the geometry complexity, while the corresponding work using kinetic models is rather limited. Moreover, the main available work has been done for monatomic gases and the corresponding work in polyatomic gases remained an open issue, that is studied in this thesis.

Chapter 3

Conductive heat transfer in rarefied polyatomic gases confined between parallel plates

3.1 Introduction

A detailed computational investigation of conductive heat transfer through rarefied polyatomic gases confined between parallel plates is performed providing a complete description of the heat flux, temperature and density distributions in terms of all involved parameters. The formulation is based on the kinetic models proposed by Holway [20] and Rykov [21] as well as on the more recently introduced model by Andries et al. [22]. In addition, the solution is also obtained by the Boltzmann equation via the DSMC scheme supplemented by the Borgnakke-Larsen collision model [23]. A systematic comparison between the results obtained by the three kinetic models and the DSMC method, by ensuring equivalent translational and rotational relaxation rates, is performed. The effect of the thermal accommodation at the boundaries is also examined for various diffuse-specular reflection scenarios at the walls and comparisons with corresponding experimental work are included. Overall, the influence of the number of rotational degrees of freedom is investigated and the differences (and similarities) compared to the corresponding monatomic gas heat transfer problem are pointed out.

In the next section, the kinetic formulation of the three kinetic models with the associated boundary conditions as well as the alternative stochastic DSMC method are described in detail. Finally, the most important results are provided in the last section, where the effect of each parameter is discussed.

3.2 The plane heat flow configuration

Consider a stationary polyatomic gas confined between two infinite parallel plates, fixed at $\hat{y} = \pm H/2$ and maintained at constant temperatures T_H and T_C respectively, with $T_H > T_C$, as it is seen in Fig. 3.1. Then, due to the temperature difference, a steady one-dimensional heat flow is established in the direction normal to the plates and directed from the hot towards the cold plate. The present analysis treats only the translational and rotational energy modes ignoring the vibrational ones. A detailed analysis of the effects of the vibrational modes on present heat transfer configuration is presented in Chapter 5.
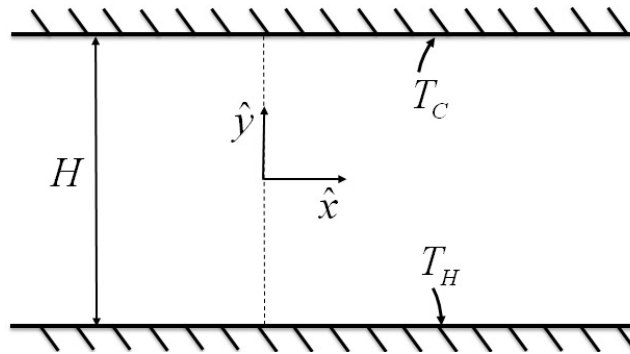
Figure 3.1: The heat transfer configuration.

In the temperature range where the effects of vibrational degrees of freedom can be neglected, the problem may be modelled by the Boltzmann equation for a gas of rigid rotators. When intrinsic molecular angular momenta (spin) has no preferential alignment, the gas may be described by a spin orientation averaged distribution function $\hat{f}\left(\hat{y}, \boldsymbol{v}, \hat{I}\right)$, where $\boldsymbol{v} = (\xi_x, \xi_y, \xi_z)$ is the molecular velocity vector and $\hat{I}$ is the internal energy, describing the molecular internal states through a single variable [30]. In polyatomic gases the internal energy can be divided in two parts, the energy of the translational motion and the energy associated to the internal

structure. These energies are related to the corresponding so-called translational and rotational temperatures and heat fluxes. Then, the macroscopic quantities of practical interest are obtained by the moments of $\hat{f}$ as

$$n\left(\hat{y}\right) = \int\limits_{-\infty}^{\infty}\int\limits_{-\infty}^{\infty}\int\limits_{-\infty}^{\infty}\int\limits_{0}^{\infty} \hat{f}d\hat{I}d\xi_x d\xi_y d\xi_z, \tag{3.1}$$

$$T_{tr}\left(\hat{y}\right) = \frac{m}{3k_B n}\int\limits_{-\infty}^{\infty}\int\limits_{-\infty}^{\infty}\int\limits_{-\infty}^{\infty}\int\limits_{0}^{\infty} \upsilon^2\hat{f}d\hat{I}d\xi_x d\xi_y d\xi_z, \tag{3.2}$$

$$T_{rot}\left(\hat{y}\right) = \frac{2}{jk_B n}\int\limits_{-\infty}^{\infty}\int\limits_{-\infty}^{\infty}\int\limits_{-\infty}^{\infty}\int\limits_{0}^{\infty} \hat{I}\hat{f}d\hat{I}d\xi_x d\xi_y d\xi_z, \tag{3.3}$$

$$T\left(\hat{y}\right) = \frac{3T_{tr}\left(\hat{y}\right) + jT_{rot}\left(\hat{y}\right)}{3+j}, \tag{3.4}$$

$$Q_{tr}\left(\hat{y}\right) = \frac{m}{2}\int\limits_{-\infty}^{\infty}\int\limits_{-\infty}^{\infty}\int\limits_{-\infty}^{\infty}\int\limits_{0}^{\infty} \xi_y\upsilon^2\hat{f}d\hat{I}d\xi_x d\xi_y d\xi_z, \tag{3.5}$$

$$Q_{rot}\left(\hat{y}\right) = \int\limits_{-\infty}^{\infty}\int\limits_{-\infty}^{\infty}\int\limits_{-\infty}^{\infty}\int\limits_{0}^{\infty} \xi_y\hat{I}\hat{f}d\hat{I}d\xi_x d\xi_y d\xi_z, \tag{3.6}$$

$$Q\left(\hat{y}\right) = Q_{tr}\left(\hat{y}\right) + Q_{rot}\left(\hat{y}\right), \tag{3.7}$$

$$\hat{P}_{ii}\left(\hat{y}\right) = m\int\limits_{-\infty}^{\infty}\int\limits_{-\infty}^{\infty}\int\limits_{-\infty}^{\infty}\int\limits_{0}^{\infty} \xi_i^2\hat{f}d\hat{I}d\xi_x d\xi_y d\xi_z, \quad i = x, y, z \tag{3.8}$$

where n, T, Q and $\hat{P}_{ii}$, with k_B being the Boltzmann constant and m the molecular mass, are the number density, total (thermodynamic) temperature, total heat flux and normal stresses respectively. The subscripts tr and rot denote the translational and rotational parts, while the parameter j is the number of rotational degrees of freedom, with $j = 2$ for diatomic and linear molecules and $j = 3$ in all other cases ($j = 0$ refers to monoatomic molecules).

The main two parameters characterizing the problem are the normalized temperature difference

$$\beta = \frac{T_H - T_C}{2T_0}, \tag{3.9}$$

where $T_0 = (T_H + T_C)/2$ is the reference temperature and the reference gas rarefaction parameter

$$\delta_0 = \frac{\hat{P}_0 H}{\mu_0 \upsilon_0}, \tag{3.10}$$

where, μ_0 is the gas viscosity at reference temperature T_0, $\upsilon_0 = \sqrt{2k_B T_0/m}$ is the most probable molecular speed and $\hat{P}_0 = n_0 k_B T_0$ is a reference pressure. The average number density

$$n_0 = \frac{1}{H} \int_{-H/2}^{H/2} n(\hat{y}) \, d\hat{y}, \tag{3.11}$$

has been used to specify the density level. It is noted that $\delta_0 \in [0, \infty)$ and it is proportional to the inverse Knudsen number, with the limiting values of $\delta_0 = 0$ and $\delta_0 \to \infty$ corresponding to the free molecular and hydrodynamic limits respectively. In addition to the parameters β and δ_0 the problem is also characterized by the type of wall-gas interaction, which is defined in Subsection 3.3.3. Here, the effect of all parameters on the translational and rotational heat fluxes and temperature distributions as well as on the density distribution for polyatomic gases is examined. This is achieved both in a deterministic and stochastic manner described in Sections 3.3 - 3.4 respectively.

3.3 Polyatomic kinetic modeling

The effort of solving the Boltzmann equation either analytically or numerically, is significantly reduced by substituting its collision term with reliable kinetic models. The two well-known models introduced by Holway and Rykov as well as the more recently introduced model by Andries, are implemented. All three models may be considered as BGK type models and, for monatomic gases they are reduced to the BGK [36], Shakhov [48] and ES [20] models respectively. The models by Holway and Rykov, where the collision integral consists of two components corresponding to the elastic and inelastic collisions are described in Subsection 3.3.1. The model by Andries, where the collision term is kept in compact form as it is in the ES model with a new artificial temperature which is accordingly decomposed into translational and rotational parts, is provided in Subsection 3.3.2. The associated boundary conditions are given

in Subsection 3.3.3, while the translational and rotational relaxation rates of all models are formulated in the Appendix A. The H-theorem has been proved in [22] for the Andries model and following the arguments leading to analogous proof of the BGK model can be proved in a straightforward manner for the Holway model as it is shown in Appendix B.

3.3.1 Models with elastic and inelastic collision terms

The Holway and Rykov models, which have been commonly applied with considerable success in rarefied polyatomic gas flows and heat transfer configurations [45, 50, 118], are formulated. Applying the projection process in energy space as it is shown in Chapter 2, for the present one-dimensional heat transfer problem, both models may be written in a similar compact form as

$$\xi_y \frac{\partial \hat{\boldsymbol{L}}}{\partial \hat{y}} = \frac{\hat{P}_{tr}}{\mu_{tr}} \text{Pr}^\chi \left[\left(1 - \frac{1}{Z^{(i)}}\right) \left(\hat{\boldsymbol{L}}_{tr}^{(i)} - \hat{\boldsymbol{L}}\right) + \frac{1}{Z^{(i)}} \left(\hat{\boldsymbol{L}}_{rot}^{(i)} - \hat{\boldsymbol{L}}\right) \right], \qquad (3.12)$$

where $i = H, R$ for the Holway and the Rykov model respectively, Pr is the Prandtl number of the gas, with the parameter $\chi = 1$ in the Holway model and $\chi = 0$ in the Rykov model, $\hat{P}_{tr} = n k_B T_{tr}$ is the pressure defined by the translational temperature, $\mu_{tr} = \mu(\text{T}_{tr})$ is the gas viscosity based on the translational temperature of the gas, while the parameter $0 \le (Z^{(i)})^{-1} \le 1$ indicates the fraction of rotational collisions of their total number. In Eq. (3.12) the first and the second terms on the right hand side of equation describe elastic and inelastic collisions respectively. The elastic collision conserves the translational energy, while the inelastic collision exchanges the translational and rotational energies. Here, the vector of the unknown distributions $\hat{\boldsymbol{L}} = \left[\hat{g}, \hat{h}\right]^T$ depends on the spatial variable $\hat{y}$ and the molecular velocity vector $\boldsymbol{v} = (\xi_x, \xi_y, \xi_z)$. The reference translational and rotational distribution functions in Eq. (3.12) are given by $\hat{\boldsymbol{L}}_{tr}^{(i)} = \left[\hat{g}_{tr}^{(i)}, \hat{h}_{tr}^{(i)}\right]^T$ and $\hat{\boldsymbol{L}}_{rot}^{(i)} = \left[\hat{g}_{rot}^{(i)}, \hat{h}_{rot}^{(i)}\right]^T$, where the components of these vectors for each kinetic model are as follows

- *Holway model*

$$\hat{g}_{tr}^{(H)} = n\left(\frac{m}{2\pi k_B T_{tr}}\right)^{3/2} \exp\left(\frac{-mv^2}{2k_B T_{tr}}\right), \quad \hat{h}_{tr}^{(H)} = \frac{j k_B T_{rot}}{2}\hat{g}_{tr}^{(H)},$$

$$\hat{g}_{rot}^{(H)} = n\left(\frac{m}{2\pi k_B T}\right)^{3/2} \exp\left(\frac{-mv^2}{2k_B T}\right), \quad \hat{h}_{rot}^{(H)} = \frac{j k_B T}{2}\hat{g}_{rot}^{(H)}. \tag{3.13}$$

- *Rykov model*

$$\hat{g}_{tr}^{(R)} = \hat{g}_{tr}^{(H)}\left[1 + \frac{2}{15}\frac{mQ_{tr}\xi_y}{n(kT_{tr})^2}\left(\frac{mv^2}{2k_B T_{tr}} - \frac{5}{2}\right)\right],$$

$$\hat{h}_{tr}^{(R)} = \hat{g}_{tr}^{(H)}k_B T_{rot}\left[1 + \frac{2}{15}\frac{mQ_{tr}\xi_y}{n(k_B T_{tr})^2}\left(\frac{mv^2}{2k_B T_{tr}} - \frac{5}{2}\right) + (1-\kappa)\frac{mQ_{rot}\xi_y}{nk_B^2 T_{tr}T_{rot}}\right],$$

$$\hat{g}_{rot}^{(R)} = \hat{g}_{rot}^{(H)}\left[1 + \varpi_0\frac{2}{15}\frac{mQ_{tr}\xi_y}{n(k_B T)^2}\left(\frac{mv^2}{2k_B T} - \frac{5}{2}\right)\right], \tag{3.14}$$

$$\hat{h}_{rot}^{(R)} = \hat{g}_{rot}^{(H)}k_B T\left[1 + \varpi_0\frac{2}{15}\frac{mQ_{tr}\xi_y}{n(k_B T)^2}\left(\frac{mv^2}{2k_B T} - \frac{5}{2}\right) + \varpi_1(1-\kappa)\frac{mQ_{rot}\xi_y}{n(k_B T)^2}\right].$$

The parameter $\kappa = \mu/(mnD)$, where D is the gas self-diffusion coefficient, is a constant which for a power intermolecular potential is varying between the values of $1/1.2$ for hard spheres and $1/1.543$ for Maxwell molecules [120]. The parameters ϖ_0 and ϖ_1 can be chosen so that the thermal conductivity obtained from the model equation is close to the experimental data in [119]. Alternatively, following the theory in [47], once the constant κ and the rotational collision number $Z^{(R)}$ are defined, the parameters ϖ_0 and ϖ_1 may be determined in order to obtain the correct translational and rotational thermal conductivity coefficients from the equations [47, 121]

$$\left(1 + \frac{1-\varpi_0}{2Z^{(R)}}\right)^{-1} = 1 - \frac{1}{2Z^{(R)}}\left(1 - \frac{2}{5\kappa}\right), \tag{3.15}$$

$$\left(1 + \frac{(1-\kappa)(1-\varpi_1)}{Z^{(R)}\kappa}\right)^{-1} = 1 + \frac{3}{4Z^{(R)}}\left(1 - \frac{2}{5\kappa}\right). \tag{3.16}$$

Then, based on Eq. (3.15) and Eq. (3.16), the Prandtl number is given by [121]

$$\text{Pr} = \frac{7}{5Z^{(R)}} \left[\frac{3}{2Z^{(R)} + 1 - \varpi_0} + \frac{0.4}{\kappa Z^{(R)} + (1 - \kappa)(1 - \varpi_1)} \right]^{-1}. \tag{3.17}$$

In cases where the Pr number, along with the constant κ and the collision number $Z^{(R)}$, are given, Eq. (3.17) and either of Eq. (3.15) and (3.16) may be used to define ϖ_0 and ϖ_1. At this stage it is convenient to introduce the dimensionless quantities

$$y = \hat{y}/H, \quad \boldsymbol{c} = \boldsymbol{v}/v_0, \quad g = (\hat{g}\, v_0^3)/n_0, \quad h = (\hat{h}\, v_0^3)\Big/\hat{P}_0,$$

$$\rho = n/n_0, \quad P_{ii} = \hat{P}_{ii}\Big/(2n_0 k_B T_0),$$

$$\tau_{tr} = T_{tr}/T_0, \quad \tau_{rot} = T_{rot}/T_0, \quad \tau = (3\tau_{tr} + j\tau_{rot})/(3 + j), \tag{3.18}$$

$$q_{tr} = Q_{tr}/(n_0 k_B T_0 v_0), \quad q_{rot} = Q_{rot}/(n_0 k_B T_0 v_0), \quad q = q_{tr} + q_{rot},$$

where H is the distance between the plates and $g = g(y, \boldsymbol{c})$, $h = h(y, \boldsymbol{c})$ are the dimensionless distribution functions. Employing the Inverse power law model (IPL), where the repulsive force between two molecules is proportional to the inverse of the nth power of the distance between their centers, for the dependence of viscosity on temperature [19]

$$\frac{\mu}{\mu_0} = \left(\frac{T}{T_0}\right)^{\omega}, \tag{3.19}$$

where $\omega = 1/2 + [2/(n - 1)]$ is the viscosity index, which for the limiting cases of hard sphere (HS) and Maxwell Molecules (MM) takes the values $1/2$ $(n \rightarrow \infty)$ and 1 $(n = 5)$ respectively, and based on the definition of the rarefaction parameter, Eq. (3.10) becomes

$$c_y \frac{\partial \boldsymbol{L}}{\partial y} = \delta_0 \rho(\tau_{tr})^{1-\omega} \text{Pr}^{\chi} \left[\left(1 - \frac{1}{Z^{(i)}}\right) \left(\boldsymbol{L}_{tr}^{(i)} - \boldsymbol{L}\right) + \frac{1}{Z^{(i)}} \left(\boldsymbol{L}_{rot}^{(i)} - \boldsymbol{L}\right) \right], \tag{3.20}$$

where $\boldsymbol{L}$ is the vector of the unknown dimensionless distribution functions g and h, while components of the reference vectors $\boldsymbol{L}_{tr}^{(i)} = \left[g_{tr}^{(i)}, h_{tr}^{(i)}\right]^T$ and $\boldsymbol{L}_{rot}^{(i)} = \left[g_{rot}^{(i)}, h_{rot}^{(i)}\right]^T$ for each model are given in dimensionless form as

33

- *Holway model*

$$g_{tr}^{(H)} = \frac{\rho}{(\pi\tau_{tr})^{3/2}} \exp\left(-\frac{c^2}{\tau_{tr}}\right), \quad h_{tr}^{(H)} = \frac{j\rho\tau_{rot}}{2(\pi\tau_{tr})^{3/2}} \exp\left(-\frac{c^2}{\tau_{tr}}\right),$$

$$g_{rot}^{(H)} = \frac{\rho}{(\pi\tau)^{3/2}} \exp\left(-\frac{c^2}{\tau}\right), \quad h_{rot}^{(H)} = \frac{j\rho\tau}{2(\pi\tau)^{3/2}} \exp\left(-\frac{c^2}{\tau}\right). \tag{3.21}$$

- *Rykov model*

$$g_{tr}^{(R)} = g_{tr}^{(H)} \left[1 + \frac{4}{15} \frac{q_{tr}c_y}{\rho\tau_{tr}^2} \left(\frac{c^2}{\tau_{tr}} - \frac{5}{2}\right)\right],$$

$$h_{tr}^{(R)} = g_{tr}^{(H)} \tau_{rot} \left[1 + \frac{4}{15} \frac{q_{tr}c_y}{\rho\tau_{tr}^2} \left(\frac{c^2}{\tau_{tr}} - \frac{5}{2}\right) + 2(1-\kappa)\frac{q_{rot}c_y}{\rho\tau_{tr}\tau_{rot}}\right],$$

$$g_{rot}^{(R)} = g_{rot}^{(H)} \left[1 + \varpi_0 \frac{4}{15} \frac{q_{tr}c_y}{\rho\tau^2} \left(\frac{c^2}{\tau} - \frac{5}{2}\right)\right], \tag{3.22}$$

$$h_{rot}^{(R)} = g_{rot}^{(H)} \tau \left[1 + \varpi_0 \frac{4}{15} \frac{q_{tr}c_y}{\rho\tau^2} \left(\frac{c^2}{\tau} - \frac{5}{2}\right) + 2\varpi_1(1-\kappa)\frac{q_{rot}c_y}{\rho\tau^2}\right].$$

Furthermore, for the specific problem under consideration the computational effort is further reduced by eliminating, based on the so-called projection procedure, the c_x and c_z components of the molecular velocity by introducing the following reduced distributions:

$$F(y, c_y) = \int\limits_{-\infty}^{\infty} \int\limits_{-\infty}^{\infty} g\, dc_z dc_x,$$

$$G(y, c_y) = \int\limits_{-\infty}^{\infty} \int\limits_{-\infty}^{\infty} g\left(c_z^2 + c_x^2\right) dc_z dc_x, \tag{3.23}$$

$$S(y, c_y) = \int\limits_{-\infty}^{\infty} \int\limits_{-\infty}^{\infty} h\, dc_z dc_x,$$

and operate accordingly on Eq. (3.20) to reduce after some routine manipulation the final coupled set of non-linear integro-differential equations

$$c_y \frac{\partial \boldsymbol{\Psi}}{\partial y} = \delta_0 \rho (\tau_{tr})^{1-\omega} \mathrm{Pr}^\chi \left[\left(1 - \frac{1}{Z^{(i)}} \right) \left(\boldsymbol{\Psi}_{tr}^{(i)} - \boldsymbol{\Psi} \right) + \frac{1}{Z^{(i)}} \left(\boldsymbol{\Psi}_{rot}^{(i)} - \boldsymbol{\Psi} \right) \right], \qquad (3.24)$$

where δ_0 is the rarefaction parameter given by Eq. (3.10). Here, the vector of the unknown distributions $\boldsymbol{\Psi} = [F, G, S]^T$ depends on two independent variables, namely y and c_y. The translational and rotational relaxing distributions in Eq. (3.24) are given by $\boldsymbol{\Psi}_{tr}^{(i)} = \left[F_{tr}^{(i)}, G_{tr}^{(i)}, S_{tr}^{(i)} \right]^T$ and $\boldsymbol{\Psi}_{rot}^{(i)} = \left[F_{rot}^{(i)}, G_{rot}^{(i)}, S_{rot}^{(i)} \right]^T$ respectively, where the components of these vectors for each kinetic model are as follows:

- *Holway model*

$$F_{tr}^{(H)} = \frac{\rho}{\sqrt{\pi \tau_{tr}}} \exp \left(-\frac{c_y^2}{\tau_{tr}} \right), \quad G_{tr}^{(H)} = \tau_{tr} F_{tr}^{(H)}, \quad S_{tr}^{(H)} = \frac{j}{2} \tau_{rot} F_{tr}^{(H)},$$

$$ \tag{3.25}$$

$$F_{rot}^{(H)} = \frac{\rho}{\sqrt{\pi \tau}} \exp \left(-\frac{c_y^2}{\tau} \right), \quad G_{rot}^{(H)} = \tau F_{rot}^{(H)}, \quad S_{rot}^{(H)} = \frac{j}{2} \tau F_{rot}^{(H)}.$$

- *Rykov model*

$$F_{tr}^{(R)} = F_{tr}^{(H)} \left[1 + \frac{4}{15} \frac{q_{tr} c_y}{\rho \tau_{tr}^2} \left(\frac{c_y^2}{\tau_{tr}} - \frac{3}{2} \right) \right],$$

$$G_{tr}^{(R)} = \tau_{tr} F_{tr}^{(H)} \left[1 + \frac{4}{15} \frac{q_{tr} c_y}{\rho \tau_{tr}^2} \left(\frac{c_y^2}{\tau_{tr}} - \frac{1}{2} \right) \right],$$

$$S_{tr}^{(R)} = \tau_{rot} F_{tr}^{(H)} \left[1 + \frac{4}{15} \frac{q_{tr} c_y}{\rho \tau_{tr}^2} \left(\frac{c_y^2}{\tau_{tr}} - \frac{3}{2} \right) + 2 \left(1 - \kappa \right) \frac{q_{rot} c_y}{\rho \tau_{tr} \tau_{rot}} \right],$$

$$ \tag{3.26}$$

$$F_{rot}^{(R)} = F_{rot}^{(H)} \left[1 + \varpi_0 \frac{4}{15} \frac{q_{tr} c_y}{\rho \tau^2} \left(\frac{c_y^2}{\tau} - \frac{3}{2} \right) \right],$$

$$G_{rot}^{(R)} = \tau F_{rot}^{(H)} \left[1 + \varpi_0 \frac{4}{15} \frac{q_{tr} c_y}{\rho \tau^2} \left(\frac{c_y^2}{\tau} - \frac{1}{2} \right) \right],$$

$$S_{rot}^{(R)} = \tau F_{rot}^{(H)} \left[1 + \varpi_0 \frac{4}{15} \frac{q_{tr} c_y}{\rho \tau^2} \left(\frac{c_y^2}{\tau} - \frac{3}{2} \right) + 2 \varpi_1 \left(1 - \kappa \right) \frac{q_{rot} c_y}{\rho \tau^2} \right].$$

Applying the same non-dimensionalization and projection procedures in energy and velocity spaces to the moments in Eqs. (3.1)-(3.8) and after some similar manipulation to the one applied in the governing equations the macroscopic quantities are given in terms of F, G and S, according to

$$\rho = \int\limits_{-\infty}^{\infty} F dc_y, \tag{3.27}$$

$$\tau_{tr} = \frac{2}{3\rho} \int\limits_{-\infty}^{\infty} \left(c_y^2 F + G \right) dc_y, \quad \tau_{rot} = \frac{2}{j\rho} \int\limits_{-\infty}^{\infty} S dc_y, \quad \tau = \frac{3\tau_{tr} + j\tau_{rot}}{3 + j}, \tag{3.28}$$

$$q_{tr} = \int\limits_{-\infty}^{\infty} \left(c_y^2 F + G \right) c_y dc_y, \quad q_{rot} = \int\limits_{-\infty}^{\infty} S c_y dc_y, \quad q = q_{tr} + q_{rot}. \tag{3.29}$$

The Holway model cannot recover the shear viscosity and thermal conductivity simultaneously and since here a purely heat transfer configuration is investigated the collision frequency has been set to properly recover the property of thermal conductivity. The Rykov model, as the Shakhov model for monatomic gases, recovers both coefficients. The Rykov model at its present form is applicable only to diatomic gases ($j = 2$), while the Holway model is applicable to polyatomic gases ($j = 2, 3$).

3.3.2 The ES-BGK model for polyatomic gases

The ES-BGK model for polyatomic gases proposed by Andries et al., has received less attention since it has been proposed more recently. Its applicability is demonstrated in [44] where some typical rarefied gas flows are solved and a comparison with corresponding results based on the Boltzmann equation is provided. The ES-BGK model in terms of the unknown distribution functions $\hat{g}$ and $\hat{h}$ is written as [22, 44]

$$\xi_y \frac{\partial \hat{\boldsymbol{L}}}{\partial \hat{y}} = \frac{\hat{P}_{tr}}{\mu_{tr}} \left(\frac{1}{1 - \nu + \theta\nu} \right) \left(\hat{\boldsymbol{L}}_{eq}^{(A)} - \hat{\boldsymbol{L}} \right), \tag{3.30}$$

where the superscript (A) denotes the Andries model and $\hat{\boldsymbol{L}} = \left[\hat{g}, \hat{h}\right]^T$ is the vector of the unknown distribution functions. For the problem under question,in this model the reduced equilibrium distributions in Eqs. (3.30) are kept in a compact form $\hat{\boldsymbol{L}}_{eq}^{(i)} = \left[\hat{g}_{eq}^{(A)}, \hat{h}_{eq}^{(A)}\right]^T$, where

$$\hat{g}_{eq}^{(A)} = \frac{n}{\pi^{3/2}\sqrt{\hat{K}_{xx}\hat{K}_{yy}\hat{K}_{zz}}} \exp\left(-\xi_x^2\hat{K}_{xx}^{-1} - \xi_y^2\hat{K}_{yy}^{-1} - \xi_z^2\hat{K}_{zz}^{-1}\right), \tag{3.31}$$

$$\hat{h}_{eq}^{(A)} = \frac{jnk_BT_{rel}}{2\pi^{3/2}\sqrt{\hat{K}_{xx}\hat{K}_{yy}\hat{K}_{zz}}} \exp\left(-\xi_x^2\hat{K}_{xx}^{-1} - \xi_y^2\hat{K}_{yy}^{-1} - \xi_z^2\hat{K}_{zz}^{-1}\right), \tag{3.32}$$

with

$$\hat{K}_{ii} = (1-\theta)\left[(1-\nu)\frac{2k_BT_{tr}}{m} + 2\nu\frac{\hat{P}_{ii}}{nm}\right] + \theta\frac{2k_BT}{m}, \quad i = \hat{x}, \hat{y}, \hat{z}. \tag{3.33}$$

The quantity T_{rel} in Eq. (3.32) is a new artificial temperature, which is accordingly decomposed as

$$T_{rel} = \theta T + (1-\theta)T_{rot}, \tag{3.34}$$

where T and T_{rot} are the total and rotational temperatures respectively. The relaxation parameters $-1/2 \leq \nu < 1$ and $0 \leq \theta \leq 1$ are chosen to recover the correct Prandtl number of diatomic and polyatomic gases according to

$$\frac{2}{3} \leq \mathrm{Pr} = \frac{1}{1-\nu+\theta\nu} < \infty. \tag{3.35}$$

For a monatomic gas a Prandtl of 2/3 is obtained by taking $\theta = 0$ and $\nu = -1/2$. In that case the ES model kinetic model for monatomic gases is recovered. Furthermore, the same processes of the non-dimensionalization and projection mentioned in Subsection 3.3.1 are applied. More specifically, an additional reduced distribution added to the aforementioned set of Eq. (3.23), which is defined by

$$R = \int\limits_{-\infty}^{\infty}\int\limits_{-\infty}^{\infty} gc_x^2 dc_z dc_x. \tag{3.36}$$

In terms of the reduced dimensionless distribution functions the model, for the present heat transfer problem is written as

$$c_y \frac{\partial \boldsymbol{\Psi}}{\partial y} = \delta_0 \rho (\tau_{tr})^{1-\omega} \left(\frac{1}{1 - \nu + \theta \nu} \right) \left[\boldsymbol{\Psi}_{eq}^{(A)} - \boldsymbol{\Psi} \right], \tag{3.37}$$

where $\boldsymbol{\Psi} = [F, G, S, R]^T$ is the vector of the unknown reduced distributions, while the reduced equilibrium functions in Eq. (3.37) are kept in compact form $\boldsymbol{\Psi}_{eq}^{(A)} = \left[F_{eq}^{(A)}, G_{eq}^{(A)}, S_{eq}^{(A)}, R_{eq}^{(A)} \right]^T$, where

$$\begin{aligned}
F_{eq}^{(A)} &= \frac{\rho}{\sqrt{\pi K_{yy}}} \exp \left[-c_y^2 K_{yy}^{-1} \right], \\[2mm]
G_{eq}^{(A)} &= \frac{\rho \left(K_{xx} + K_{zz} \right)}{2 \sqrt{\pi K_{yy}}} \exp \left[-c_y^2 K_{yy}^{-1} \right], \\[2mm]
S_{eq}^{(A)} &= \frac{j \rho \tau_{rel}}{2 \sqrt{\pi K_{yy}}} \exp \left[-c_y^2 K_{yy}^{-1} \right], \\[2mm]
R_{eq}^{(A)} &= \frac{\rho K_{xx}}{2 \sqrt{\pi K_{yy}}} \exp \left[-c_y^2 K_{yy}^{-1} \right],
\end{aligned} \tag{3.38}$$

with the tensor K_{ii}, $i = x, y, z$, written as

$$K_{ii} = (1 - \theta) \left[(1 - \nu) \tau_{tr} + 2\nu \frac{P_{ii}}{\rho} \right] + \theta \tau. \tag{3.39}$$

The dimensionless artificial temperature temperature in Eq. (3.38) is given as $\tau_{rel} = \theta \tau + (1 - \theta) \tau_{rot}$. It is noted that the scales of the pressure $\hat{P}_{ii}$ and the tensor $\hat{K}_{ii}$ are set to $2P_0$ and v_0^2 respectively. The macroscopic quantities of number density ρ, translational, rotational and total temperatures τ_{tr}, τ_{rot} and τ respectively as well as the corresponding heat fluxes q_{tr}, q_{rot} and q are given by Eqs. (3.27)-(3.29), while the normal stresses in Eq. (3.39) are

$$P_{xx} = \int\limits_{-\infty}^{\infty} R dc_y, \quad P_{yy} = \int\limits_{-\infty}^{\infty} F c_y^2 dc_y, \quad P_{zz} = \int\limits_{-\infty}^{\infty} (G - R) \, dc_y. \tag{3.40}$$

It is noted that the entropy inequality (H-theorem) has been proved for this polyatomic kinetic model with $-1/2 \leq \nu < 1$ and $0 \leq \theta < 1$ in [22]. Also, for all aforementioned models

namely Holway, Rykov and Andries the conservation equation $\partial q\left(y\right)/\partial y=0$ is readily deduced, which implies that the total heat flux $q\left(y\right)$ remains constant along $-1/2\leq y\leq 1/2$.

3.3.3 Boundary conditions

To close the problem the formulation of the boundary conditions at $\hat{y}=\pm H/2$ for the reflected distributions is provided. The classical Maxwell wall model is applied [122]. Hereby, to distinguish between incident and reflected quantities the superscripts $(-)$ and $(+)$ are introduced. In the investigation of gas flows with rotational degrees of freedom, the distribution function of the particles reflected from the solid surfaces is taken in the form [123]

$$\hat{f}^+ = n_w\left(\frac{m}{2\pi k_B T_{tr}^\alpha}\right)^{3/2}\exp\left(-\frac{mv^2}{2k_B T_{tr}^\alpha}\right)\frac{\hat{I}^{j/2-1}}{(k_B T_{rot}^\alpha)^{j/2}\Gamma\left(j/2\right)}\exp\left(-\frac{\hat{I}}{k_B T_{rot}^\alpha}\right).\qquad(3.41)$$

Introducing in Eq. (3.41), the same projection process in energy space as for the kinetic equations, leads to the following reflected reduced distributions at the boundaries $\hat{y}=\pm H/2$

$$\hat{g}^+ = n_w\left(\frac{m}{2\pi k_B T_{tr}^\alpha}\right)^{3/2}\exp\left(-\frac{mv^2}{2k_B T_{tr}^\alpha}\right),\quad \hat{h}^+ = \frac{jk_B T_{rot}^\alpha}{2}\hat{g}^+,\qquad(3.42)$$

where n_w is a parameter found from the no-flow condition as

$$n_w = 2\hat{N}\sqrt{\frac{\pi m}{2k_B T_{tr}^\alpha}},\quad \hat{N} = -\int\limits_{\xi_y<0}\xi_y\hat{g}^-\,d\boldsymbol{\xi},\qquad(3.43)$$

where, $\hat{N}$ is the incident particle flux which is equal with the reflected particle flux. The parameters T_{tr}^α and T_{rot}^α are obtained as part of the solution from the energy balances at the surface. The following three possible types of boundary conditions for determining the parameters T_{tr}^α and T_{rot}^α are considered [50]

- *Boundary condition model I*

  In most occasions, experimental studies report only one energy accommodation coefficient defined as

  $$\hat{E}^+ = \hat{E}^- - \alpha \left(\hat{E}^- - \hat{E}^w \right). \tag{3.44}$$

  The energy fluxes in Eq. (3.44) are obtained by adding the corresponding translational and rotational parts, i.e. $\hat{E}^- = \hat{E}_{tr}^- + \hat{E}_{rot}^-$, $\hat{E}^+ = (2 + j/2) \hat{N} k_B T^\alpha$ and $\hat{E}^w = (2 + j/2)\hat{N}k_B T^w$, while $T^\alpha = T_{tr}^\alpha = T_{rot}^\alpha$. Introducing in Eqs. (3.42), the same normalization and projection process in velocity space as for the kinetic equations, lead to the following reflected reduced distributions at the boundaries $y = \pm 1/2$

  $$F^+ = \frac{\rho_w}{\sqrt{\pi \tau^\alpha}} \exp\left(-\frac{c_y^2}{\tau^\alpha} \right), \quad G^+ = \tau^\alpha F^+, \quad S^+ = \frac{j}{2}\tau^\alpha F^+, \quad R^+ = \frac{1}{2}\tau^\alpha F^+, \tag{3.45}$$

  where $\tau^\alpha = T^\alpha/T_0$ based on Eq. (3.44) is given by

  $$\tau^\alpha = \alpha \tau^w + (1 - \alpha)\frac{2E^-}{(4 + j) N} \tag{3.46}$$

  while

  $$\frac{E^-}{N} = \frac{\int\limits_0^\infty \left(c_y^2 F^- + G^- + S^- \right)c_y dc_y}{\int\limits_0^\infty F^- c_y dc_y}. \tag{3.47}$$

  The parameter ρ_w in Eq. (3.45) is computed as

  $$\rho_w = \frac{2\sqrt{\pi}}{\sqrt{\tau^\alpha}} \int\limits_0^\infty F^- c_y dc_y, \tag{3.48}$$

  with $\tau^w = T^w/T_0$. This approach with the one thermal accommodation coefficient has been widely used in literature [50, 124] and the modelling remains efficient.

- *Boundary condition model II*

  A more detailed description of the energy transfer between the gas and the plates includes two energy accommodation coefficients one for the translational and one for rotational

degrees of freedom defined as [50, 94, 124]

$$\hat{E}_{tr}^{+} = \hat{E}_{tr}^{-} - \alpha_{tr}\left(\hat{E}_{tr}^{-} - \hat{E}_{tr}^{w}\right), \quad \hat{E}_{rot}^{+} = \hat{E}_{rot}^{-} - \alpha_{rot}\left(\hat{E}_{rot}^{-} - \hat{E}_{rot}^{w}\right), \quad (3.49)$$

where $\hat{E}_{tr}^{-}$ and $\hat{E}_{rot}^{-}$ are the incident translational and rotational energy fluxes, $\hat{E}_{tr}^{+} = 2\hat{N}k_{B}T_{tr}^{\alpha}$ and $\hat{E}_{rot}^{+} = (j/2)\hat{N}k_{B}T_{rot}^{\alpha}$ are the reflected translational and rotational energy fluxes, while $\hat{E}_{tr}^{w} = 2\hat{N}k_{B}T^{w}$ and $\hat{E}_{rot}^{w} = (j/2)\hat{N}k_{B}T^{w}$ are the translational and rotational energy fluxes that would have been achieved if the reflected molecules were emitted in thermal equilibrium at the surface. Adding the two reflected energy fluxes of the Eq. (3.49) the total energy balance equation is given as

$$\hat{E}^{+} = \hat{E}^{-} - \alpha_{tr}\left(\hat{E}_{tr}^{-} - \hat{E}_{tr}^{w}\right) - \alpha_{rot}\left(\hat{E}_{rot}^{-} - \hat{E}_{rot}^{w}\right), \quad (3.50)$$

where $\hat{E}^{+}$ and $\hat{E}^{-}$ are the total reflected and incident energy fluxes respectively. The reflected dimensionless reduced distributions at the boundaries $y = \pm 1/2$ are given as

$$F^{+} = \frac{\rho_{w}}{\sqrt{\pi\tau_{tr}^{\alpha}}}\exp\left(-\frac{c_{y}^{2}}{\tau_{tr}^{\alpha}}\right), \quad G^{+} = \tau_{tr}^{\alpha}F^{+}, \quad S^{+} = \frac{j}{2}\tau_{rot}^{\alpha}F^{+}, \quad R^{+} = \frac{1}{2}\tau_{tr}^{\alpha}F^{+}, \quad (3.51)$$

where the parameter ρ_{w} is given by the Eq. (3.48). Also, based on the definition of the two accommodation coefficients given in Eq. (3.49), the parameters $\tau_{tr}^{\alpha} = T_{tr}^{\alpha}/T_{0}$ and $\tau_{rot}^{\alpha} = T_{rot}^{\alpha}/T_{0}$ are defined as

$$\tau_{tr}^{\alpha} = \alpha_{tr}\tau^{w} + (1 - \alpha_{tr})\frac{E_{tr}^{-}}{2N}, \quad \tau_{rot}^{\alpha} = \alpha_{rot}\tau^{w} + (1 - \alpha_{rot})\frac{2E_{rot}^{-}}{jN}, \quad (3.52)$$

with

$$\frac{E_{tr}^{-}}{N} = \frac{\int_{0}^{\infty}\left(c_{y}^{2}F^{-} + G^{-}\right)c_{y}dc_{y}}{\int_{0}^{\infty}F^{-}c_{y}dc_{y}}, \quad \frac{E_{rot}^{-}}{N} = \frac{\int_{0}^{\infty}S^{-}c_{y}dc_{y}}{\int_{0}^{\infty}F^{-}c_{y}dc_{y}}. \quad (3.53)$$

It is noted that for $\alpha = \alpha_{tr} = \alpha_{rot}$ the boundary condition model II is not the same with the boundary condition model I, since in model I the two parameters T_{tr}^{α} and T_{rot}^{α} are assumed to be equal, whereas in model II these two parameters are different in the general

case. Furthermore, the boundary condition model II with the two thermal accommodation coefficients, separate contributions from the different energy modes and provide a detailed description of the energy transfer between the gas and the surface.

- *Boundary condition model III*

Furthermore, to take into account the cross energy transfer between the translational and rotational modes two additional energy accommodations may be introduced into the two thermal accommodation coefficients model resulting to a total of four coefficients, namely α_{tr}, α_{rot}, α_{tr}^{rot} and α_{rot}^{tr} [50]. Transfer of such a type is considered if two terms added into two expressions for the translational and rotational reflected energy fluxes of Eq. (3.49) according to

$$
\begin{aligned}
\hat{E}_{tr}^{+} &= \hat{E}_{tr}^{-} - \alpha_{tr} \left(\hat{E}_{tr}^{-} - \hat{E}_{tr}^{w} \right) - \alpha_{tr}^{rot} \left(\hat{E}_{tr}^{-} - \hat{E}_{tr}^{w} \right) + \alpha_{rot}^{tr} \left(\hat{E}_{rot}^{-} - \hat{E}_{rot}^{w} \right), \\
\hat{E}_{rot}^{+} &= \hat{E}_{rot}^{-} - \alpha_{rot} \left(\hat{E}_{rot}^{-} - \hat{E}_{rot}^{w} \right) - \alpha_{rot}^{tr} \left(\hat{E}_{rot}^{-} - \hat{E}_{rot}^{w} \right) + \alpha_{tr}^{rot} \left(\hat{E}_{tr}^{-} - \hat{E}_{tr}^{w} \right).
\end{aligned}
\tag{3.54}
$$

The two Eqs. (3.54) are the equations of translational and rotational energy balance on the plates. The energies of the translational and rotational degrees of freedom of the reflected molecules are denoted by $\hat{E}_{tr}^{+}$ and $\hat{E}_{rot}^{+}$ as well as the translational $\hat{E}_{tr}^{w}$ and rotational $\hat{E}_{rot}^{w}$ energy fluxes of the molecules which are in thermal equilibrium with the wall are the same with those given for the boundary condition model II. It is noted that by adding the two reflected energy fluxes of the Eq. (3.54) the total energy balance describing by Eq. (3.50) is obtained. The coefficients α_{tr} and α_{rot} determine the fraction of the rotational and translational energy transferred to the surface while the coefficients α_{tr}^{rot} and α_{rot}^{tr} determine the transition rates of translational to rotational energy and vice versa respectively. The values of the four thermal accommodation coefficients can be determined experimentally [50, 125]. The reflected reduced distributions at the boundaries in terms of F, G, S, R are described by the Eqs. (3.51), while the parameter ρ_w is given by the Eq. (3.48). Based on the rotational and translational energy balance on the wall of Eqs. (3.54), the two

42

dimensionless parameters $\tau_{tr}^\alpha = T_{tr}^\alpha/T_0$ and $\tau_{rot}^\alpha = T_{rot}^\alpha/T_0$ in Eq. (3.51) are given as

$$\tau_{tr}^\alpha = \frac{E_{tr}^-}{2N} - (\alpha_{tr} + \alpha_{tr}^{rot})\left(\frac{E_{tr}^-}{2N} - \tau^w\right) + \frac{\alpha_{rot}^{tr}}{2}\left(\frac{E_{rot}^-}{N} - \frac{j}{2}\tau^w\right),$$

$$\tau_{rot}^\alpha = \frac{2E_{rot}^-}{jN} - (\alpha_{rot} + \alpha_{rot}^{tr})\left(\frac{2E_{rot}^-}{jN} - \tau^w\right) + \frac{4\alpha_{tr}^{rot}}{j}\left(\frac{E_{tr}^-}{2N} - \tau^w\right),$$

$$\tag{3.55}$$

where the ratios E_{tr}^-/N and E_{rot}^-/N are given in Eqs. (3.53). The boundary condition model III allows a better adjustment to experimental results, but since the number of parameters to be examined is increased this type of boundary conditions seems to be more useful in investigations focused on specific comparisons between simulations and experiments.

It is noted that in the manipulation of Eqs. (3.46), (3.52) and (3.55) the scales of the incident energy flux and incident particle flux are set to $\hat{P}_0 v_0$ and $n_0 v_0$ respectively. Moreover, the thermal accommodation coefficients α, α_{tr}, α_{rot}, α_{tr}^{rot} and α_{rot}^{tr} vary between zero and unity. The thermal accommodation coefficient α of the model I is related to the thermal accommodation coefficients of the translational α_{tr} and rotational degrees of freedom α_{rot} of model II and III according to

$$\alpha = \frac{\alpha_{tr}\left(E_{tr}^- - 2N\tau^w\right) + \alpha_{rot}\left(E_{rot}^- - \frac{j}{2}N\tau^w\right)}{E_{tr}^- + E_{rot}^- - \left(2 + \frac{j}{2}\right)N\tau^w}. \tag{3.56}$$

Furthermore, in accordance with the experimental and theoretical papers [126, 127] it is obtained that $\alpha_{tr} \geq \alpha_{rot}$. The nonlinear set of Equations presented in Subsections 3.3.1 and 3.3.2 along with the different model boundary conditions presented in Subsection 3.3.3 provide a theoretically well-established kinetic formulation for the heat transfer problem under consideration.

3.4 DSMC solution of the Boltzmann equation

In order to increase confidence into the predictions of the kinetic models described in the previous section, the problem has also been studied by a DSMC particle scheme [19]. In general,

the determination of the form of the collision cross section for polyatomic gases is not easy. As it is well known, the dynamics of a binary *molecular* collision is much more complicated than a binary *atomic* collision which is largely amenable to analytical treatment. Simple mechanical models of translational-rotational coupling (rough spheres, loaded spheres, spherocylinders) [128] are not flexible enough to fit experimental data on polyatomic species. Hence, the collision dynamics and cross-sections have been obtained from the well-known phenomenological model proposed by Borgnakke and Larsen [23]. The model can be easily adapted to reproduce experimental translational-rotational relaxation rates with good accuracy [129]. Moreover, its collision algorithm is very well suited to particle schemes used to obtain numerical solutions of the Boltzmann equation [19].

In the particular form of the Borgnakke-Larsen model adopted here, collision dynamics is organized as follows:

- The collision probability of two molecules in the pre-collision state $\left(\boldsymbol{v}', \hat{I}'\right)$, $\left(\boldsymbol{v}_1', \hat{I}_1'\right)$ is proportional to $\sigma_{HS} v_r'$, where $\sigma_{HS} = \pi d^2$ is the integral cross-section of hard sphere molecules of diameter d and $v_r' = \|\boldsymbol{v}_1' - \boldsymbol{v}'\|$ is the relative velocity modulus.

- An individual collision is inelastic with probability $1/Z^{(DSMC)}$ or elastic with probability $1 - 1/Z^{(DSMC)}$. An inelastic collision gives rise to an exchange between translational and rotational energies, as explained below. In an elastic collision pre- and post-collision rotational energies do not change, i.e. $\hat{I} = \hat{I}'$, $\hat{I}_1 = \hat{I}_1'$. Conservation of total energy then implies $v_r = v_r'$ and, according to hard sphere impact dynamics, post-collision relative velocity is written as $\boldsymbol{v}_r = v_r \hat{\boldsymbol{e}}$, being $\hat{\boldsymbol{e}}$ a random vector uniformly distributed on the unit sphere S.

- In an inelastic collision conserved total energy $\hat{E}$ of the center of mass reference frame:

$$\hat{E} = \frac{1}{4} m \, v_r^2 + \hat{I} + \hat{I}_1 = \frac{1}{4} m \, v_r'^2 + \hat{I}' + \hat{I}_1' \tag{3.57}$$

is randomly partitioned between translational and rotational motion by sampling the translational energy fraction $\hat{E}_{tr}/E$ from a given probability density function $P_1\left(\hat{E}_{tr}/\hat{E}\,\middle|\,j\right)$. The available total rotational energy $\hat{E}_{rot} = \hat{I} + \hat{I}_1 = \hat{E} - \hat{E}_{tr}$ is then randomly distributed

44

between the collision partners by sampling the fraction $\hat{I}/\hat{E}_{rot}$ from a given probability density function $P_2\left(\hat{I}/\hat{E}_{rot}\Big| j\right)$. The relative velocity after a collision is again written as $v_r = v_r \hat{\boldsymbol{e}}$, where $\hat{\boldsymbol{e}}$ is a random unit vector and $v_r = \sqrt{4\hat{E}_{tr}/m}$. The specific form of the probability densities $P_1\left(\hat{E}_{tr}/\hat{E}\Big| j\right)$ and $P_2\left(I/\hat{E}_{rot}\Big| j\right)$ depends both on the number of internal degrees of freedom and on the assumed intermolecular interaction [19]. In the case of hard sphere interaction and $j = 2$ they take a particularly simple form [19, 30]

$$P_1\left(\hat{E}_{tr}/E\Big| 2\right) = 6\frac{\hat{E}_{tr}}{\hat{E}}\left(1 - \frac{\hat{E}_{tr}}{\hat{E}}\right), \tag{3.58}$$

$$P_2\left(I/\hat{E}_{rot}\Big| 2\right) = 1. \tag{3.59}$$

The strength of translational-rotational coupling is determined by the mixing parameter $Z^{(DSMC)}$ which can be made to depend on the local flow field temperature to fit experimental relaxation rates [129]. As mentioned above, the hard sphere collision cross section has been used in the DSMC simulations presented in this work. The choice is suggested by the limited temperature range of the experimental measurements which allow to assume a constant value of the total collision cross section. For the same reason, a similar choice has been made about the rotational collision number, $Z^{(DSMC)}$, whose value has been assumed not to depend on temperature, neglecting its weak temperature dependence in the case of air species [129]. In the DSMC algorithm, the main hypothesis is that at each discrete time interval, particle motion and intermolecular collisions are considered as two independent, uncoupled steps. The physical space domain is discretized into cells, which are used to track model particles and calculate the bulk properties. Each model particle in the simulation represents a large number of real molecules in the physical system and is characterized by spatial position $\hat{\boldsymbol{r}}(\hat{t})$, velocity $\boldsymbol{v}(\hat{t})$ and internal energy $\hat{I}(\hat{t})$ associated with j rotational degrees of freedom. The particles states are advanced from time $\hat{t}$ to time $\hat{t} + \Delta\hat{t}$ in two stages. In the first stage gas-gas collisions are neglected and particles move along straight lines with the constant velocity and rotational energy they had at time $\hat{t}$. In this free flight stage wall boundary conditions are applied to change the velocity and internal energy of molecules hitting a wall. In the second stage, particle

positions are kept fixed and equal to the final values resulting from the free flight. Particles belonging to the same cell of the spatial grid are allowed to collide according to the rule described above. Finally, macroscopic quantities are obtained by sampling and time averaging particles microscopic states after the onset of steady flow conditions.

3.5 Results and discussion

In this section, results for the heat fluxes and the distributions of temperature and density obtained by the Holway, Rykov and Andries models as well as by the DSMC method in a wide range of all involved parameters are presented in tabulated and graphical form. The temperature ratio of the hot over the cold plate takes the values of $T_H/T_C = (1 + \beta)/(1 - \beta) = [1.1, 3, 7, 10]$ covering the cases of small, moderate and large temperature differences, while the reference gas rarefaction parameter $\delta_0 \in [0, 100]$ varies in a wide range of the gas rarefaction from the free molecular up to the slip regime. Three types of gas-surface interaction are considered and comparisons with measurements under various conditions are included.

The results are organized as follows: In Subsection 3.5.1 the numerical parameters used in the simulations are given. Subsection 3.5.2 presents results of the heat fluxes for diatomic and polyatomic gases as well as a comparison between kinetic and DSMC results including density and temperature fields. Subsection 3.5.3 describes the dependency of the heat fluxes on the accommodation coefficients and finally, Subsection 3.5.4 is focused on comparison with experiments. The computational results always coincide in the free molecular limit ($\delta_0 = 0$) with the corresponding analytical results of the translational and rotational temperatures and heat fluxes. Also, as δ_0 is increased, the computed heat flux gradually tends to the analytical one in the hydrodynamic limit. The analytical solutions in the two limits are provided in the Appendix C.

3.5.1 Numerical parameters and the computing quantities

The kinetic model equations of Holway, Rykov and Andries with the associated moments applying the three types of boundary conditions described above are solved numerically in

a deterministic manner. The discretization is based on the discrete velocity method in the molecular velocity space and on a second order control volume approach in the physical space. The macroscopic quantities are computed by Gauss-Legendre quadrature. The implemented algorithm is parallel in the velocity space and has been extensively applied in previous works to solve with considerable success heat transfer configurations [89, 124]. The iteration process between the kinetic equations and the corresponding moments of the distribution functions is terminated when the convergence criteria

$$\frac{1}{3K} \sum_{i=1}^{K} \left[\left| \rho_i^{(t+1)} - \rho_i^{(t)} \right| + \left| \tau_i^{(t+1)} - \tau_i^{(t)} \right| + \left| q_i^{(t+1)} - q_i^{(t)} \right| \right] < \varepsilon, \qquad (3.60)$$

with t denoting the iteration index and K the number of nodes in the physical space, is fulfilled. The kinetic results presented here have been obtained with 4001 equally spaced nodes and 96 molecular velocities being the roots of the corresponding Legendre polynomial, while the tolerance parameter is set to $\varepsilon = 10^{-8}$. Computations have been performed with a parallel version of the code parallelizing in the molecular velocity space on 3 Intel® Core™ i5-3570 cpus at 3.40 GHz (total of 12 cores). The computational times per iteration for the BGK, Shakhov, Holway, Andries and Rykov models are roughly speaking in the ratio 1:2:3:4:6, i.e. the computational time of the polyatomic models is approximately three times higher than the corresponding monatomic ones. It is noted that the total number of iterations for convergence depends only on the reference rarefaction parameter and is independent of the model. To have an idea of the required computational times, it is stated indicatively that the simulation of the case $\delta_0 = 50$, $T_H/T_C = 3$ with the above defined parallelization and numerical parameters, based on the Holway model, takes about 3.2min (*serial* execution time about 32 min).

The reported DSMC results have been obtained from simulations using not less than 1250 particles per cell. The spatial cell size $\Delta \hat{y}$ does not exceed $1/20$ of the reference mean free path. The time step $\Delta \hat{t}$ has been set equal to the minimum between the estimated time a particle takes to cross a cell, $\left(\Delta \hat{t} \right)_{adv} = \left(\Delta \hat{y} \sqrt{m} \right) / \left(\sqrt{k_B T_H} \right)$, and a small fraction $\left(\Delta \hat{t} \right)_{col}$ of the minimum mean free time, based on the maximum value of the collision frequency in the domain. Macroscopic quantities have been obtained by sampling microscopic particles states

for $20 - 40 \times 10^4$ time steps after the estimated onset of steady conditions. The heat fluxes dispersion within each sample allows estimating the statistical error associated with the Monte Carlo method. In most of the cases the relative statistical error is well below 1%. Larger relative standard deviations (around 2%) are found for the largest value of the rarefaction parameter and the smallest temperature ratio. The computing time associated to a *serial* DSMC simulation amounts to about 5×10^{-8} per time step, per particle, on a workstation equipped with Intel® Xeon® E5-2630 cpus, running at 2.3 GHz. For instance, the simulation of the case $\delta_0 = 50$, $T_H/T_C = 3$ with 1000 spatial cells and particles, takes about 40 min to execute 3×10^5 time steps and produce an accurate solution.

3.5.2 Comparison between kinetic and DSMC results

In Tables 3.1 and 3.2 the dimensionless translational and rotational heat fluxes respectively obtained by all three kinetic models are compared for a diatomic gas ($j = 2$, Pr $= 0.72$) with HS molecules. The temperature ratio and the reference gas rarefaction parameter take the values of $T_H/T_C = [1.1, 3, 10]$ and $\delta_0 \in [0, 100]$ respectively. Since the translational and rotational heat fluxes vary between the plates the tabulated results are at the hot plate $y = -1/2$. Of course the total heat flux remains constant. The gas molecules are fully accommodated at the two plates. Furthermore, in order to ensure comparison compatibility between the various kinetic models and according to the Appendix A (Eq. (A.4)), where the relaxation rates are discussed, the rotational collision numbers are set as $Z^{(R)} = Z^{(A)} = 6.50$ and $Z^{(H)} = Z^{(A)} \times \text{Pr} = 4.67$. Based on these values and $\kappa = 1/1.2$ (HS molecules) it is deduced that $\varpi_o = 0.458$, $\varpi_1 = 2.840$ in the Rykov model and $\nu = -0.50$, $\theta = 0.21$ in the Andries model. It is clearly seen that for both heat fluxes the agreement between the corresponding results obtained by all three models is excellent (within two or even three significant figures for all values of δ_0 and T_H/T_C). The rotational heat flux is always about one-half of the corresponding translational one, while in the free molecular limit, is exactly one-half. The results for $\delta_0 = 0$ coincide with the corresponding analytical ones estimated by Eqs. (C.5)-(C.6) in Appendix C.

It is noted that the dependency of the results on the values of $Z^{(i)}$ for the present heat transfer configuration and for all values of δ_0 and T_H/T_C tested, in all three models, is small,

with the Holway model being the less sensitive one. Also, as $Z^{(i)}$ is increased the translational heat flux tends to the heat flux of a monatomic gas, while the rotational heat flux remains always about one-half of the translational one. To clearly demonstrate that, in Table 3.3, the monatomic heat fluxes obtained by the BGK and Shakhov models are tabulated for the same temperature ratios T_H/T_C and rarefaction gas parameter δ_0 [130]. It is seen that the monoatomic heat fluxes are close to and always a little bit higher than the translational part of the corresponding diatomic heat flux, shown in Table 3.1, while the total diatomic heat fluxes $q = q_{tr} + q_{rot}$ are higher compared to the corresponding monatomic ones of Table 3.3 about $30 - 50\%$.

A comparison between the dimensionless total heat fluxes obtained by the Andries model and the DSMC method for a diatomic gas with $Z^{(DSMC)} = Z^{(A)} = 5$ ($\nu = -0.5$, $\theta = 0.27$) is presented in Table 3.4. The particles reflection is purely diffuse at the walls. The temperature ratio and the reference gas rarefaction parameter take the values of $T_H/T_C = [1.1, 3, 7, 10]$ and $\delta_0 \in [0, 100]$ respectively. In all cases the agreement between the results is very good with the relative error being less than 3%. Furthermore, the comparison is extended to the number density distributions plotted in Fig. 3.2 as well as to the translational and rotational temperature distributions plotted in Fig. 3.3 for various typical values of δ_0 and T_H/T_C demonstrating excellent agreement between the deterministic and stochastic approaches. It is also seen that the translational and rotational distributions are very close to each other and through Eq. (3.20) it is deduced that $\tau \simeq \tau_{tr} \simeq \tau_{rot}$, with the larger deviations occurring at larger temperature differences and intermediate values of the gas rarefaction. Overall, the effectiveness of the Andries as well as of the Holway and Rykov models to simulate this heat transfer configuration is clearly demonstrated.

In Table 3.5 the translational and rotational heat fluxes of a polyatomic gas ($j = 3$) based on the Andries model with $Z^{(A)} = 6.50$, $\nu = -0.50$, $\theta = 0.21$ and purely diffuse reflection at the walls are tabulated. The results are at the hot plate for $T_H/T_C = [1.1, 3, 7, 10]$ and $\delta_0 \in [0, 100]$. Overall, the qualitative variation of the polyatomic heat fluxes in terms of T_H/T_C and δ_0 is similar to the diatomic ones. More specifically, the translational parts of the polyatomic and diatomic heat fluxes are close, while the rotational part of the polyatomic heat

flux is always higher than the corresponding one of the diatomic gas. Comparing the total polyatomic heat fluxes with those in Tables 3.3, it is deduced that they are about $50 - 75\%$ higher than the corresponding monatomic ones. The analytical free molecular solutions are fully recovered with the rotational part being 75% of the translational one.

3.5.3   Effect of accommodation coefficients

The effect of partial accommodation at the walls on the heat fluxes is investigated based on the two types of boundary conditions presented in Subsection 3.3.3. Results are provided for the typical values $T_H/T_C = [1.1, \ 3, \ 10]$, $\delta_0 \in [0, 100]$ and they are based on the Holway kinetic model.

First the boundary condition Eqs. (3.45)-(3.47) with the one energy accommodation co-efficient $\alpha \in [0, 1]$, defined by Eq. (3.44), is considered. In Fig. 3.4, the dimensionless total heat flux q of a diatomic gas ($j = 2$, Pr $= 0.71$, $Z^{(H)} = 5$) with HS molecules in terms of α is plotted. As expected the effect of α on the total heat flux becomes more significant as δ_0 is decreased, i.e. as the gas becomes more rarefied, while at $\delta_0 = 100$ the total heat flux is practi-cally independent of α. Also, in almost all cases as α is increased the dimensionless total heat flux is monotonically increased, which is physically justified since a larger portion of particles is reflected with temperatures closer to the wall temperatures. However, for large temperature differences this is true only at large δ_0, while as δ_0 is decreased a maximum heat flux is observed at some $\alpha < 1$. This is clearly shown at $T_H/T_C = 10$ and $\delta_0 \leq 0.1$, where the maximum heat flux is reached at about $\alpha = 0.95$. It has been found that as the temperature ratio is further increased the value of α where the maximum heat flux occurs is decreased. The behavior of both the translational and rotational parts of the heat flux with respect to α is similar to the one described here for the total heat flux and therefore is not shown separately. These findings have also been confirmed by simulations with the other kinetic models and the DSMC approach. In addition, the results for $\delta_0 = 0$ are in excellent agreement with the corresponding analytical ones given in the Appendix C, where the detailed dependence of q_{fm} on the parameters α and β is shown in Fig. C.1.

Next, the boundary condition Eqs. (3.51)-(3.53) with the two energy accommodation coefficients $\alpha_{tr} \in [0,1]$ and $\alpha_{rot} \in [0,1]$, defined by Eq. (3.49), is considered and the effect of the accommodation coefficients on each of the translational and rotational parts of the heat flux is investigated. In Fig. 3.5, the dimensionless translational heat flux q_{tr} at the hot plate of a diatomic gas ($j = 2$, Pr $= 0.71$, $Z = 5$) with HS molecules in terms of with $\alpha_{tr} = 1$ with α_{rot} as well as in terms of α_{tr} with $\alpha_{rot} = 1$ is plotted. It is seen that the dependency of q_{tr} on α_{tr} is very similar to the one observed before of $q^{(H)}$ on α . On the contrary q_{tr} is actually independent of α_{rot}.

In Fig. 3.6, the corresponding plots for q_{rot} are provided. The rotational heat flux depends on both α_{tr} and α_{rot}. With regard to α_{tr} the dependency is in general weak in small temperature differences but becomes stronger as the temperature difference is increased and the gas becomes more rarefied. It is interesting to observe that in these latter conditions as α_{tr} is increased q_{rot} is decreased. With regard to α_{rot} the dependency of the rotational heat flux is strong and as α_{rot} is increased, q_{rot} is also increased.

The effect of the two thermal accommodation coefficients on the density and temperature distributions is shown in Figs. 3.7 and 3.8 for a diatomic HS gas ($j = 2$, Pr $= 0.71$, $Z = 5$) in the case of $T_H/T_C = 10$ and $\delta_0 = 1$. The dimensionless wall temperatures are $\tau_H = 1.82$ and $\tau_C = 0.18$. More specifically, in Fig. 3.7 the distributions of density and translational temperature are plotted for various values of α_{tr} with $\alpha_{rot} = 1$. It is seen that at small values of α_{tr} both distributions, even at this large temperature ratio, are almost anti-symmetric about $y = 0$ (typical of a linear configuration) and then as is increased the anti-symmetry is vanished (typical of a nonlinear configuration). The effect of the variation of α_{tr} on the wall temperature jump is more dominant at the cold rather than at the hot wall. The coefficient α_{rot} has always a very small effect or no effect at all on these distributions and therefore its effect is not plotted. On the contrary, both α_{tr} and α_{rot} have an important effect on the rotational temperature shown in Fig. 3.8. It is seen that as α_{tr} is increased, $\tau_{rot}(y)$ is decreased in a uniform manner along the distance y (the curves are almost parallel to each other). Also, at large values of α_{rot}, the $\tau_{rot}(y)$ distribution is symmetric and as α_{rot} is decreased it becomes antisymmetric. In addition, as T_H/T_C is decreased the effect of α_{tr} and α_{rot} on $\tau_{rot}(y)$ is drastically decreased.

Furthermore, comparing the translational and rotational temperatures in Figs. 3.7 and 3.8 respectively with $\alpha_{tr} \leq 1$ and $\alpha_{rot} = 1$ it is seen that $\tau_{tr} \simeq \tau_{rot}$ only when $\alpha_{tr} = 1$ while as α_{tr} is reduced the translational and rotational temperatures start to depart from each other. To clearly demonstrate that the two temperatures are plotted for $\alpha_{tr} = 1$, $\alpha_{rot} = 0.2$ and $\alpha_{tr} = 0.2$, $\alpha_{rot} = 1$ at two different values of the reference gas rarefaction parameter in Fig. 3.9. It is seen that for $\alpha_{tr} \neq \alpha_{rot}$, i.e., when translational and rotational energies are differently accommodated at the walls, then the corresponding temperatures vary significantly ($\tau_{tr} \neq \tau_{rot}$) and this difference becomes larger as δ_0 is increased. Also, at $\delta_0 = 0.1$ the departure between τ_{tr} and τ_{rot} is larger with the variation of α_{rot} rather than of α_{tr}. It is expected that similar results will be obtained performing molecular dynamics simulations.

3.5.4 Comparison with experiments

A comparison with the early experimental results in [96, 97] and the more recent ones in [85] is performed based on the kinetic Holway model and the DSMC method. In experiments [85, 96] the temperature difference between the plates is small, while in [97] the temperature difference is large, the gas is nitrogen (N_2) and the associated energy accommodation coefficient has been experimentally determined from heat transfer measurements at low pressures where the Knudsen formula is valid, to be about $\alpha = 0.75 - 0.8$. The simulations have been performed for a diatomic HS gas with Pr = 0.71, while the rotational collision number for the DSMC approach is taken to be $Z^{(DSMC)} = 5$.

The comparison with [96] is shown in Fig. 3.10 in terms of the total heat flux normalized with the corresponding free molecular heat flux versus the inverse of the reference Knudsen number. The measured temperature of the hot plate and the temperature ratio are $T_H = 301.96$ K and $T_H/T_C = 1.0291$ respectively, while the experimentally determined thermal accommodation coefficient is $\alpha = 0.76$. The Holway model simulations have been performed for these data with $Z^{(H)} = 5$ as well as with Z obtained by the Landau-Teller (L-T) expression [19] based on the Lordi and Mates [131] experimental data. As it is seen the computed results are in very good agreement with the experimental ones in the whole range of the inverse Knudsen number. It is noted however, that the implemented gas-surface interaction model is not capable

to capture both the heat flux and density variations presented in [96] simultaneously and to achieve that more complex boundary conditions, as the ones in [50], are needed.

The comparison with [85] is shown in Fig. 3.11 in terms of the dimensionless total heat flux q versus the inverse measured pressure. The measured temperatures of the hot and cold plates are $T_H = 308.3$ K and $T_C = 288.3$ K respectively ($T_H/T_C = 1.069$), while the associated experimentally estimated thermal accommodation coefficients are $\alpha_H = 0.795$ and $\alpha_C = 0.808$ [85]. Simulations have been performed for these data with the Holway model ($Z^{(H)} = 5$). Excellent agreement between the kinetic results and measurements is observed in the whole range of measured pressures.

The comparison with [97] is shown in Fig. 3.12 in terms of the dimensionless density distribution between the parallel plates. The temperatures of the hot and cold plates are $T_H = 294$ K and $T_C = 79$ K respectively ($T_H/T_C = 3.72$). In this case the temperature difference is large, while in the former comparisons it was small. The comparison covers a wide range of the rarefaction parameter (1.52, 3.08, 4.64, 16.72), while the experimentally determined thermal accommodation coefficient is $\alpha = 0.82$. It is noted that in order to perform the comparison the experimental rarefaction parameters have been accordingly converted having as the reference number density the mean number density and not the number density at the center plane as it is taken in [97]. Simulations have been performed for these data with the Holway model and $Z^{(H)} = 5$. The influence of the different models of boundary conditions described in Subsection 3.3.3 on the density distribution between the plates is investigated. In the boundary condition model I the accommodation coefficient is taken equal to experimental value ($\alpha = 0.82$). In [50] the range of the parameters $\alpha_{tr} = [0.7, 0.9]$ and $\alpha_{rot} = [0.3, 0.8]$ for the heat transfer problem through N_2 is given. Moreover, in [126, 127] it is found that $\alpha_{rot} \leq \alpha_{tr}$. Taking into consideration the aforementioned and due to the fact that the coefficients α_{tr} and α_{rot} must have a value equal to that measured experimentally ($\alpha = 0.82$) according to Eq. (3.56) the values $\alpha_{tr} = 0.9$ and $\alpha_{rot} = 0.65$ are chosen in the case of boundary condition model II. For the boundary condition model III the values $\alpha_{tr} = \alpha_{rot} = 0.82$, $\alpha_{tr}^{rot} = 0.18$ and $\alpha_{rot}^{tr} = 0.01$ are used based on all the above information related to the coefficients α_{tr} and α_{rot}. The values of the α_{tr} and α_{rot} are different in boundary condition model II and model III, since from all

the available combinations these values of α_{tr} and α_{rot} for each model achieve the best fitting with experimental data in [97]. As it is seen very good agreement between all three boundary condition models and experiments is observed at large values of the rarefaction parameter, since in this case the effects of the boundary conditions is small. However, at $\delta_0 = 1.52$ the comparison between the density profiles obtained by the boundary condition model I and II with the corresponding experimental data is not as good as for higher values of δ_0. This is due to the fact that the boundary condition model I and II do not take into account the energy transfer between the translational and rotational degrees of freedom of the molecules as they collide with the plates. As it is seen the boundary condition model III makes it possible to obtain very good agreement in the whole examined range of the rarefaction parameter.

In order to obtain a more physical understanding of the heat transfer in monatomic and polyatomic gases and to facilitate comparisons with experiments, in Fig. 3.13, some dimensional total heat fluxes [W/m^2] in terms of the reference pressure $\hat{P}_0$ [Pa] are given for the monatomic gases of He and Ar ($j = 0$, Pr $= 0.67$), the diatomic gases of H$_2$ and N$_2$ ($j = 2$, Pr $= 0.71$) and for the polyatomic gases of CO$_2$ ($j = 2$, Pr $= 0.75$) and CH$_4$ ($j = 3$, Pr $= 0.75$). The distance between the plates is $H = 5$ mm with the temperature of the cold plate to be set at $T_C = 293$ K and temperature ratio $T_H/T_C = 3$. The reference pressure $\hat{P}_0 \in \left[10^{-3}, 5 \times 10^2\right]$ Pa is easily connected to the rarefaction parameter δ_0, via Eq. (3.10) once the viscosity and the most probable velocity of each gas is specified. All computations are based on the Holway model and the IPL interaction law with $\omega = [0.66, 0.81, 0.67, 0.74, 0.93, 0.84]$ for He, Ar, H$_2$, N$_2$, CO$_2$, CH$_4$ respectively. It is noted that the experimentally estimated rotational collision number of these gases may vary between one and five [47]. However, the dependency of the results on Z is small and therefore in all cases $Z^{(H)} = 5$ is introduced. It is seen that, as expected, the heat flux is monotonically increased with pressure. At highly rarefied atmospheres the heat flux is proportional to gas pressure, then, in the transition regime the relation becomes more complex and at dense atmospheres the heat flux depends weakly and finally is independent of pressure.

More importantly, it is observed in Fig. 3.13, that under the same conditions the heat flux of different gases varies significantly. The largest heat fluxes are achieved for H$_2$ followed successively by the heat fluxes of He, CH$_4$, N$_2$, CO$_2$ and Ar. This trend is valid in the whole

range of pressure except for the curves of CO_2 and Ar, which cross each other at some relatively large pressure $\hat{P}_0 > 1$ Pa. In monatomic gases confined between surfaces the heat transfer is increased as the molar mass of the gas is decreased and the molecular velocities are increased. However, this remark cannot be generalized in the case of polyatomic gases since the additional degrees of freedom result to additional heat transfer, as seen in Fig. 3.13, where in a wide range of pressure the heat flux of CO_2 is larger than that of Ar, while its molar mass is larger.

3.6 Concluding remarks

The problem of heat transfer through rarefied polyatomic gases confined between two parallel plates maintained at different temperatures is solved based on three kinetic models namely the ones proposed by Holway, Rykov and Andries as well as on the DSMC scheme supplemented by the Borgnakke-Larsen collision model. Results for the heat fluxes and the distributions of density and temperature are provided for small, moderate and large temperature differences in a wide range of the gas rarefaction from the free molecular limit up to the slip regime with full and partial energy accommodation at the boundaries. The three kinetic models and the DSMC method provide very close values of the computed macroscopic quantities as well as very good agreement with corresponding experimental data available in the literature. In addition, the computational results perfectly match the analytical ones in the free molecular limit and tend to the analytical ones in the hydrodynamic regime.

Based on the above, the validity of the implemented modeling approaches is demonstrated. All kinetic models provide accurate results for the specific problem. The H-theorem has been proved for the Andries model and can be readily obtained for the Holway model, while no such proof exists for the Rykov model. Surely, the Holway model is the simplest to use since it depends only on one parameter, the Prandtl number, but probably not accurate enough to treat problems with combined heat transfer and flow phenomena. The Rykov model remains a solid alternative for diatomic gases, while very recently has been extended to polyatomic gases [46]. It is noted that for this specific heat transfer problem the dependency of the results on the parameter indicating the strength of translational-rotational coupling is very small for all kinetic models and the DSMC method (the Holway model is the less sensitive one).

The total heat fluxes of diatomic and polyatomic gases have been found to be higher about $30 - 50\%$ and $50 - 75\%$ respectively than the corresponding monatomic ones, with the highest differences occurring in the free molecular limit. Furthermore, as the amount of elastic compared to inelastic collisions is increased, the translational heat fluxes are slightly increased and they tend to the monatomic ones, while the rotational heat fluxes are always about 50% and 75% of the translational ones for diatomic and polyatomic gases respectively. Also, the translational and rotational temperature distributions (as well as the total temperature) are very close to each other for each set of parameters examined and they are similar to the corresponding monatomic ones when the translational and rotational accommodation coefficients are the same. On the contrary they depart from each other when the two coefficients are different. In most cases as the thermal accommodation coefficient α is increased, i.e. the gas-surface interaction becomes more diffusive, the dimensionless total heat flux is monotonically increased. However, for adequately large temperature differences and efficiently high gas rarefaction levels a non-monotonic behavior, with a maximum total heat flux at some $\alpha < 1$, has been observed. A detailed description of the behavior of the translational and rotational heat fluxes and temperatures on the partial energy accommodation at the walls is provided. Finally, providing some dimensional results, it has been found that while in monatomic gases the heat flux is always increased as the molar mass is decreased, this is not necessarily the case in polyatomic gases since the additional degrees of freedom result to additional heat transfer.

Overall, it is noted that the present work may be useful in the heat transfer design and optimization of MEMS, vacuum sensors and other technological devices with polyatomic gases. It is also noted that the presented results are in a range of heat transfer parameters where the assumption of a gas of rigid rotators is justified.

Table 3.1: Dimensionless translational heat fluxes q_{tr} for a diatomic gas ($j = 2$, $\mathrm{Pr} = 0.72$) with HS molecules ($\omega = 0.5$) at the hot plate ($y = -1/2$) and various values of δ_0 and T_H/T_C ($Z^{(R)} = Z^{(A)} = 6.50$, $\nu = -0.50$, $\theta = 0.21$, $\varpi_o = 0.458$, $\varpi_1 = 2.840$, $Z^{(H)} = 4.67$).

δ_0	$T_H/T_C = (1 + \beta)/(1 - \beta)$								
	1.1			3.0			10.0		
	Andries	Holway	Rykov	Andries	Holway	Rykov	Andries	Holway	Rykov
0	5.37(-2)	5.37(-2)	5.37(-2)	5.06(-1)	5.06(-1)	5.06(-1)	5.98(-1)	5.98(-1)	5.98(-1)
0.1	5.11(-2)	5.11(-2)	5.09(-2)	4.84(-1)	4.84(-1)	4.83(-1)	5.83(-1)	5.83(-1)	5.88(-1)
1	3.79(-2)	3.79(-2)	3.77(-2)	3.65(-1)	3.65(-1)	3.66(-1)	4.68(-1)	4.67(-1)	4.82(-1)
5	1.92(-2)	1.92(-2)	1.95(-2)	1.92(-1)	1.92(-1)	1.95(-1)	2.75(-1)	2.75(-1)	2.85(-1)
10	1.21(-2)	1.21(-2)	1.23(-2)	1.22(-1)	1.22(-1)	1.25(-1)	1.84(-1)	1.84(-1)	1.90(-1)
50	3.03(-3)	3.03(-3)	3.10(-3)	3.13(-2)	3.13(-2)	3.20(-2)	4.96(-2)	4.96(-2)	5.07(-2)
100	1.56(-3)	1.57(-3)	1.60(-3)	1.62(-2)	1.62(-2)	1.66(-2)	2.58(-2)	2.58(-2)	2.64(-2)

Table 3.2: Dimensionless rotational heat fluxes q_{rot} for a diatomic gas ($j = 2$, $\mathrm{Pr} = 0.72$) with HS molecules ($\omega = 0.5$) at the hot plate ($y = -1/2$) and various values of δ_0 and T_H/T_C ($Z^{(R)} = Z^{(A)} = 6.50$, $\nu = -0.50$, $\theta = 0.21$, $\varpi_o = 0.458$, $\varpi_1 = 2.840$, $Z^{(H)} = 4.67$).

δ_0	$T_H/T_C = (1 + \beta)/(1 - \beta)$								
	1.1			3.0			10.0		
	Andries	Holway	Rykov	Andries	Holway	Rykov	Andries	Holway	Rykov
0	2.68(-2)	2.68(-2)	2.68(-2)	2.53(-1)	2.53(-1)	2.53(-1)	2.99(-1)	2.99(-1)	2.99(-1)
0.1	2.54(-2)	2.54(-2)	2.51(-2)	2.40(-1)	2.40(-1)	2.39(-1)	2.90(-1)	2.90(-1)	2.91(-1)
1	1.80(-2)	1.80(-2)	1.74(-2)	1.74(-1)	1.74(-1)	1.69(-1)	2.24(-1)	2.24(-1)	2.24(-1)
5	8.55(-3)	8.55(-3)	8.11(-3)	8.59(-2)	8.59(-2)	8.20(-2)	1.25(-1)	1.24(-1)	1.21(-1)
10	5.27(-3)	5.27(-3)	4.98(-3)	5.39(-2)	5.38(-2)	5.12(-2)	8.18(-2)	8.18(-2)	7.85(-2)
50	1.31(-3)	1.31(-3)	1.25(-3)	1.36(-2)	1.36(-2)	1.29(-2)	2.17(-2)	2.16(-2)	2.05(-2)
100	6.79(-4)	6.79(-4)	6.44(-4)	7.05(-3)	7.04(-3)	6.68(-3)	1.12(-2)	1.12(-2)	1.07(-2)

Table 3.3: Dimensionless heat flux for a monatomic gas with HS molecules ($\omega = 0.5$) for various values of δ_0 and T_H/T_C based on the BGK and Shakhov models.

δ_0	$T_H/T_C = (1+\beta)/(1-\beta)$					
	1.1		3.0		10.0	
	BGK	Shakhov	BGK	Shakhov	BGK	Shakhov
0	5.37(-2)	5.37(-2)	5.06(-1)	5.06(-1)	5.98(-1)	5.98(-1)
0.1	5.13(-2)	5.09(-2)	4.86(-1)	4.84(-1)	5.85(-1)	5.89(-1)
1	3.86(-2)	3.81(-2)	3.72(-1)	3.70(-1)	4.74(-1)	4.88(-1)
5	2.02(-2)	2.01(-2)	2.01(-1)	2.02(-1)	2.86(-1)	2.94(-1)
10	1.28(-2)	1.28(-2)	1.30(-1)	1.31(-1)	1.95(-1)	1.98(-1)
50	3.31(-3)	3.31(-3)	3.43(-2)	3.43(-2)	5.42(-2)	5.43(-2)
100	1.72(-3)	1.72(-3)	1.78(-2)	1.78(-2)	2.84(-2)	2.84(-2)

Table 3.4: Comparison between the dimensionless total heat fluxes q of the Andries model and the DSMC method for a diatomic gas ($j = 2$, Pr = 0.73) with HS molecules ($\omega = 0.5$) and various values of δ_0 and T_H/T_C ($Z^{(DSMC)} = Z^{(A)} = 5$, $\nu = -0.5$, $\theta = 0.27$).

δ_0	$T_H/T_C = (1+\beta)/(1-\beta)$							
	1.1		3.0		7.0		10.0	
	Andries	DSMC	Andries	DSMC	Andries	DSMC	Andries	DSMC
0.1	7.64(-2)	7.55(-2)	7.24(-1)	7.21(-1)	8.90(-1)	8.87(-1)	8.73(-1)	8.70(-1)
1	5.56(-2)	5.57(-2)	5.36(-1)	5.35(-1)	6.86(-1)	6.81(-1)	6.89(-1)	6.81(-1)
5	2.74(-2)	2.80(-2)	2.74(-1)	2.80(-1)	3.77(-1)	3.82(-1)	3.95(-1)	3.99(-1)
10	1.71(-2)	1.75(-2)	1.73(-1)	1.78(-1)	2.46(-1)	2.52(-1)	2.62(-1)	2.68(-1)
50	4.26(-3)	4.38(-3)	4.41(-2)	4.55(-2)	6.47(-2)	6.68(-2)	6.99(-2)	7.23(-2)
100	2.20(-3)	2.28(-3)	2.28(-2)	2.38(-2)	3.36(-2)	3.50(-2)	3.63(-2)	3.78(-2)

Table 3.5: Dimensionless translational and rotational heat fluxes for a polyatomic gas ($j = 3$, Pr = 0.72) with HS molecules ($\omega = 0.5$) at the hot plate ($y = -1/2$) and various values of δ_0 and T_H/T_C based on the Andries model ($Z^{(A)} = 6.50$, $\nu = -0.50$, $\theta = 0.21$).

δ_0	$T_H/T_C = (1 + \beta)/(1 - \beta)$							
	1.1		3.0		7.0		10.0	
	q_{tr}	q_{rot}	q_{tr}	q_{rot}	q_{tr}	q_{rot}	q_{tr}	q_{rot}
0	5.37(-2)	4.03(-2)	5.06(-1)	3.79(-1)	6.14(-1)	4.61(-1)	5.98(-1)	4.49(-1)
0.1	5.11(-2)	3.80(-2)	4.84(-1)	3.61(-1)	5.95(-1)	4.43(-1)	5.83(-1)	4.35(-1)
1	3.79(-2)	2.70(-2)	3.65(-1)	2.61(-1)	4.66(-1)	3.34(-1)	4.68(-1)	3.36(-1)
5	1.92(-2)	1.28(-2)	1.91(-1)	1.29(-1)	2.62(-1)	1.78(-1)	2.75(-1)	1.86(-1)
10	1.20(-2)	7.88(-3)	1.22(-1)	8.05(-2)	1.73(-1)	1.15(-1)	1.83(-1)	1.22(-1)
50	3.01(-3)	1.96(-3)	3.11(-2)	2.03(-2)	4.57(-2)	2.98(-2)	4.93(-2)	3.23(-2)
100	1.56(-3)	1.01(-3)	1.61(-2)	1.05(-2)	2.37(-2)	1.55(-2)	2.57(-2)	1.67(-2)
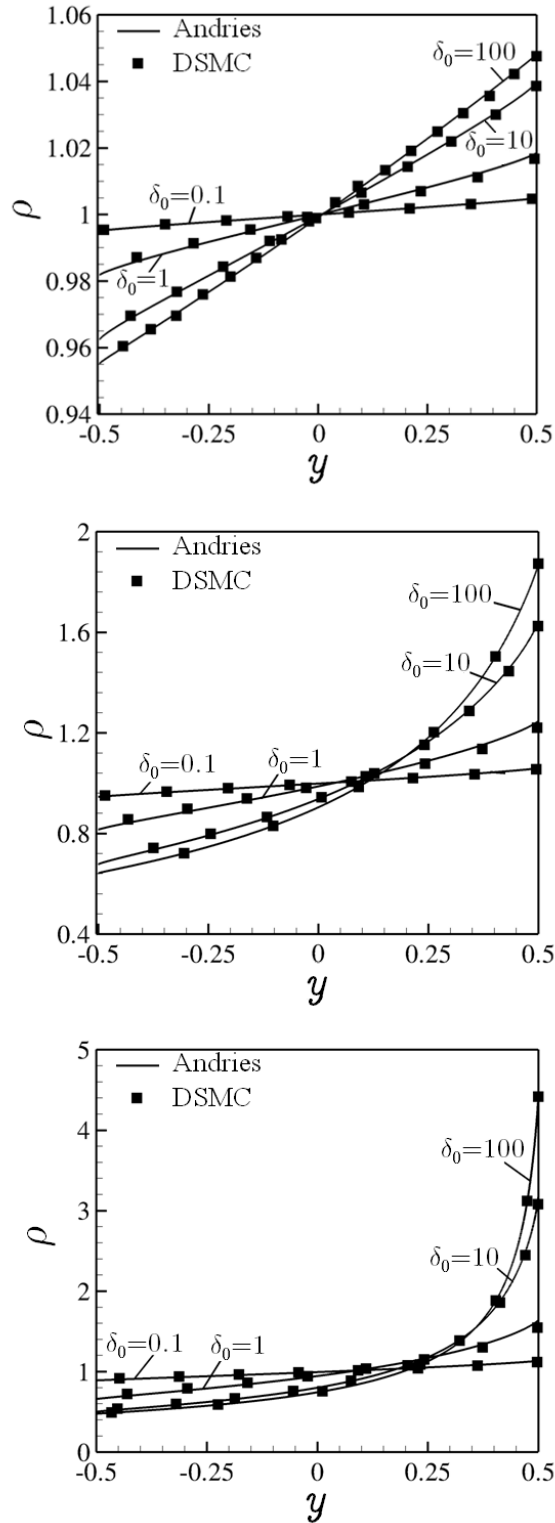
Figure 3.2: Comparison between the dimensionless number density distributions $\rho(y)$ of the Andries model and the DSMC method for a diatomic HS gas ($j = 2$, $\text{Pr} = 0.73$, $Z^{(DSMC)} = Z^{(A)} = 5$, $\nu = -0.5$, $\theta = 0.27$) and various values of δ_0 with $T_H/T_C = 1.1$ (up), $T_H/T_C = 3$ (middle) and $T_H/T_C = 10$ (down).
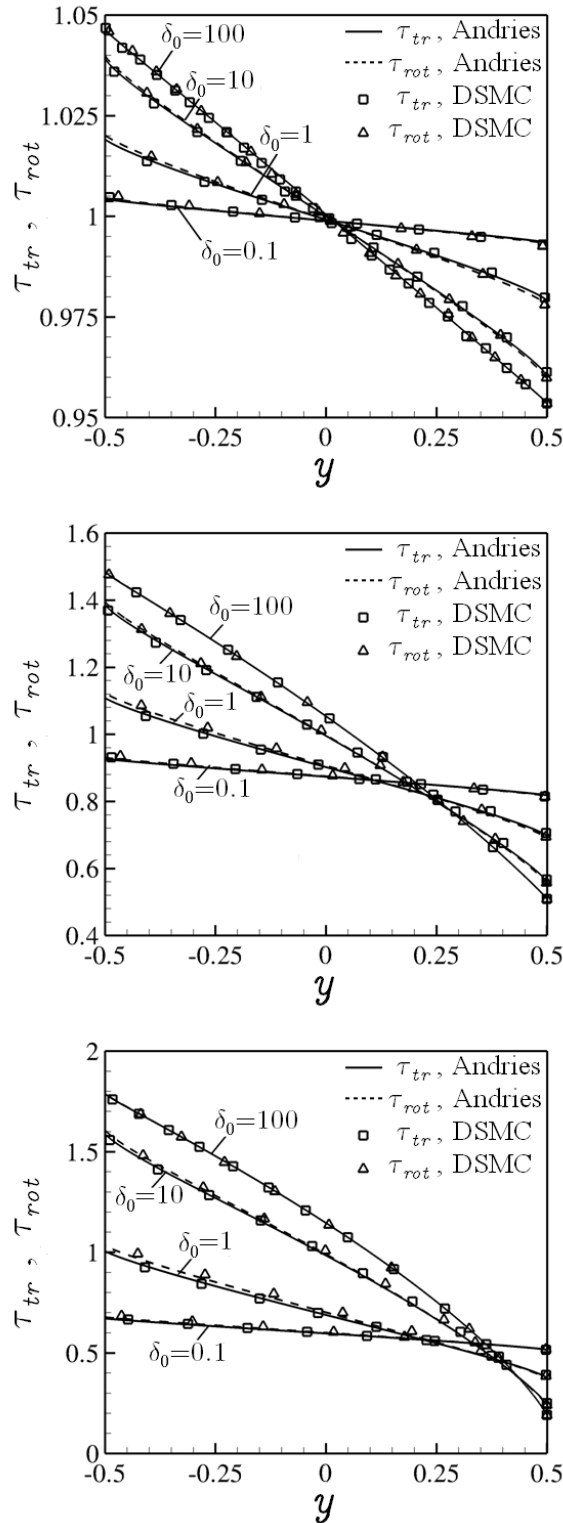
Figure 3.3: Comparison between the dimensionless translational $\tau_{tr}(y)$ and rotational $\tau_{rot}(y)$ temperature distributions of the Andries model and the DSMC method for a diatomic HS gas ($j = 2$, Pr $= 0.73$, $Z^{(DSMC)} = Z^{(A)} = 5$, $\nu = -0.5$, $\theta = 0.27$) and various values of δ_0 with $T_H/T_C = 1.1$ (up), $T_H/T_C = 3$ (middle) and $T_H/T_C = 10$ (down).

61
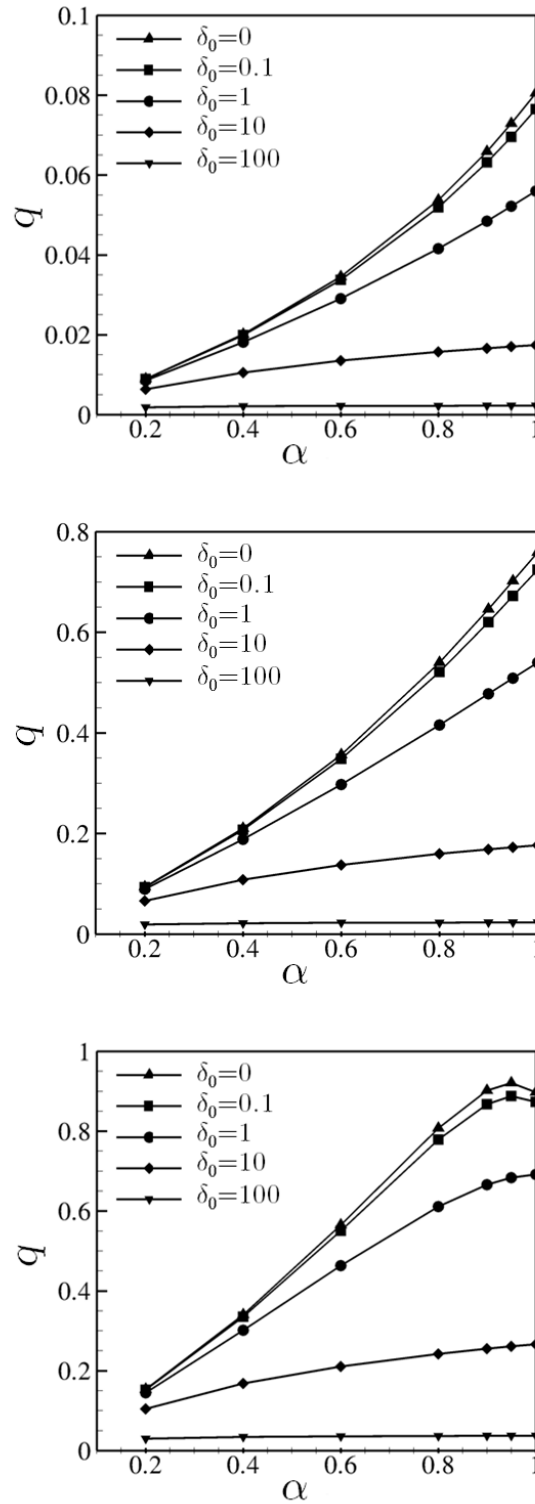
Figure 3.4: Dimensionless total heat flux q of a diatomic HS gas ($j = 2$, $\mathrm{Pr} = 0.71$, $Z^{(H)} = 5$) in terms of thermal accommodation coefficient α for various values of δ_0 with $T_H/T_C = 1.1$ (up), $T_H/T_C = 3$ (middle) and $T_H/T_C = 10$ (down) based on the Holway model.

62
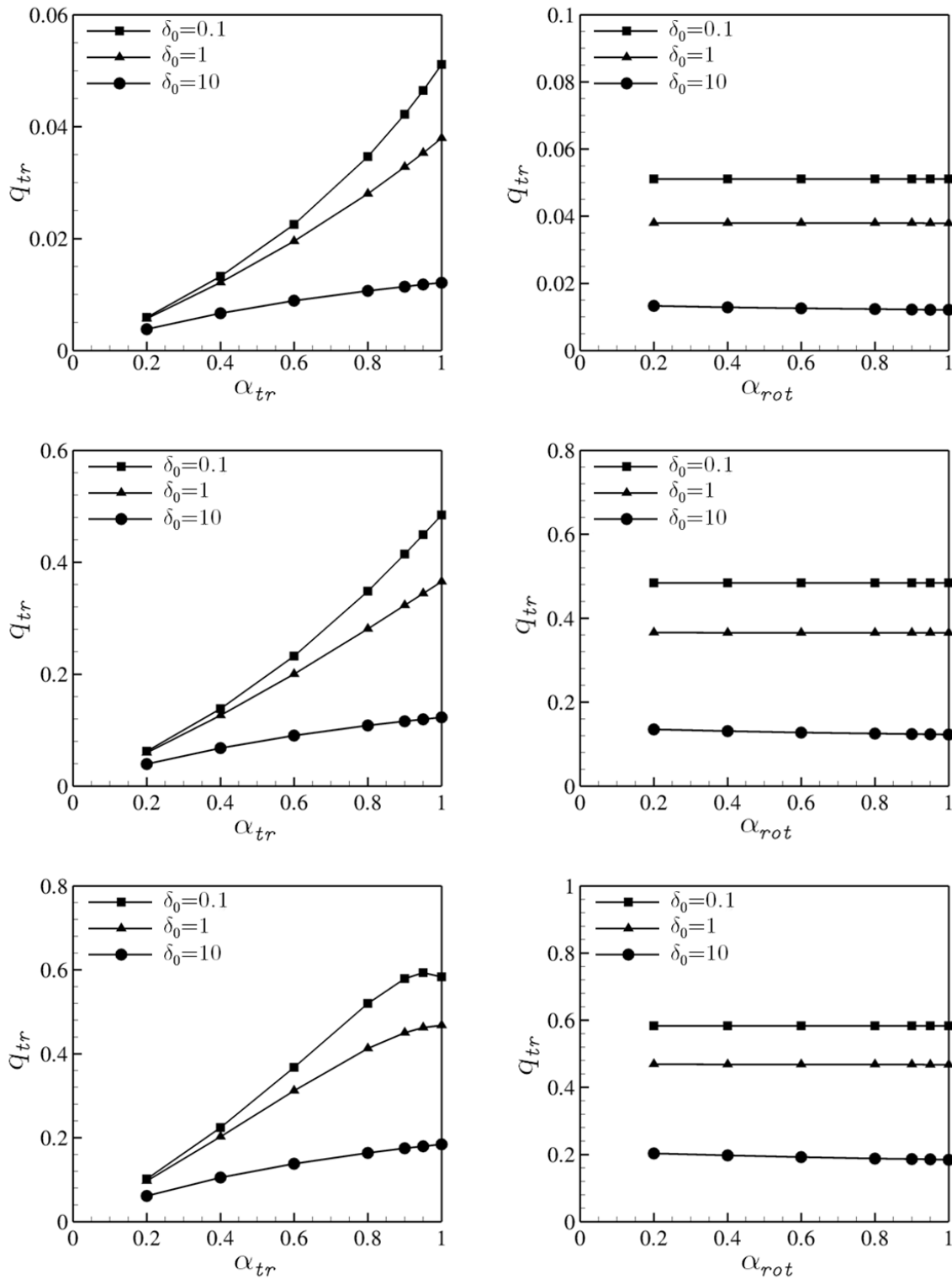
Figure 3.5: Dimensionless translational heat flux q_{tr} at the hot plate of a diatomic HS gas ($j = 2$, $\text{Pr} = 0.71$, $Z^{(H)} = 5$) in terms of α_{tr} (left) and α_{rot} (right) for $\delta_0 = [0.1, 1, 10]$ and $T_H/T_C = 1.1$ (up), $T_H/T_C = 3$ (middle), $T_H/T_C = 10$ (down) based on the Holway model.

63
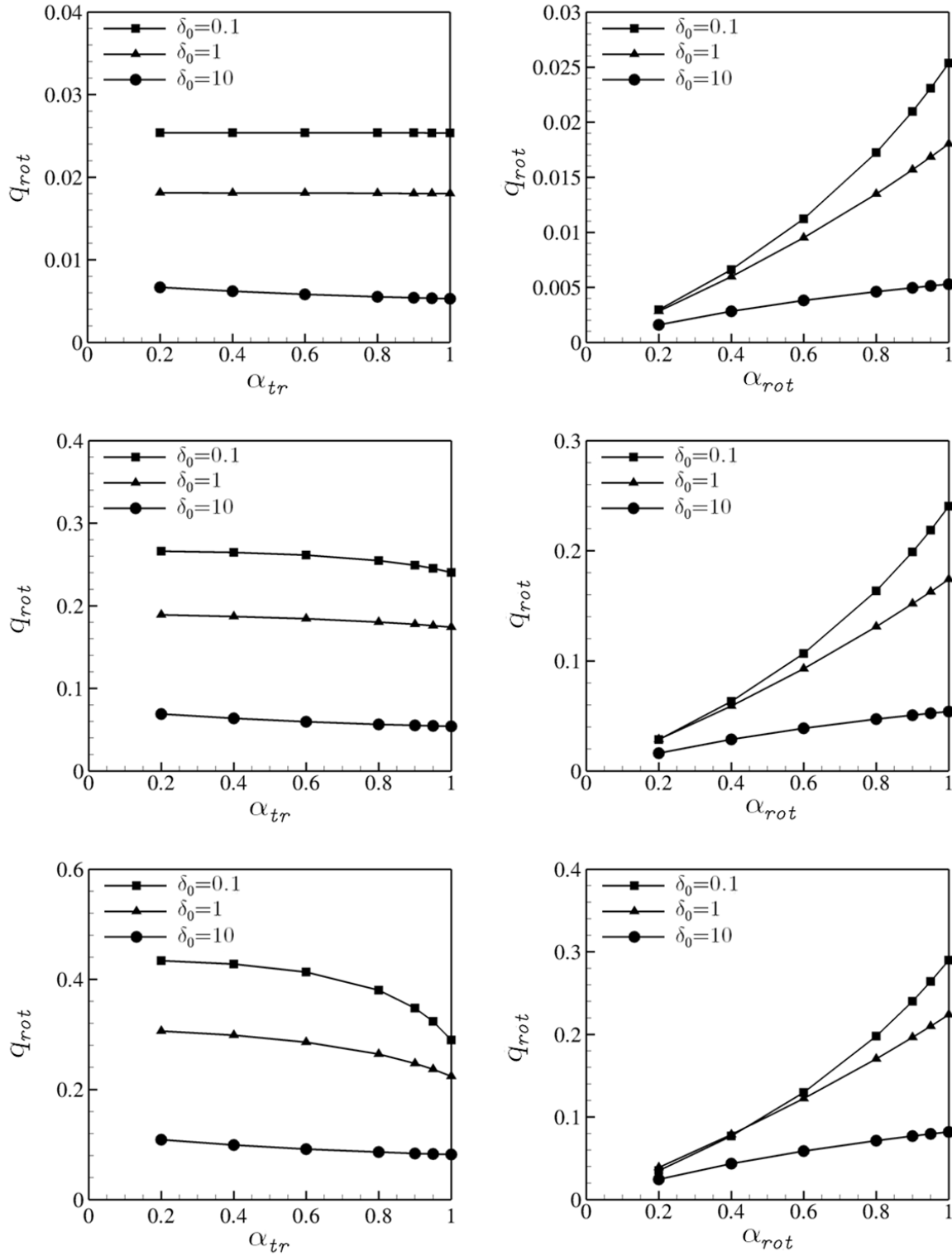
Figure 3.6: Dimensionless rotational heat flux q_{rot} at the hot plate of a diatomic HS gas ($j = 2$, $\text{Pr} = 0.71$, $Z^{(H)} = 5$) in terms of α_{tr} (left) and α_{rot} (right) for $\delta_0 = [0.1, 1, 10]$ and $T_H/T_C = 1.1$ (up), $T_H/T_C = 3$ (middle), $T_H/T_C = 10$ (down) based on the Holway model.
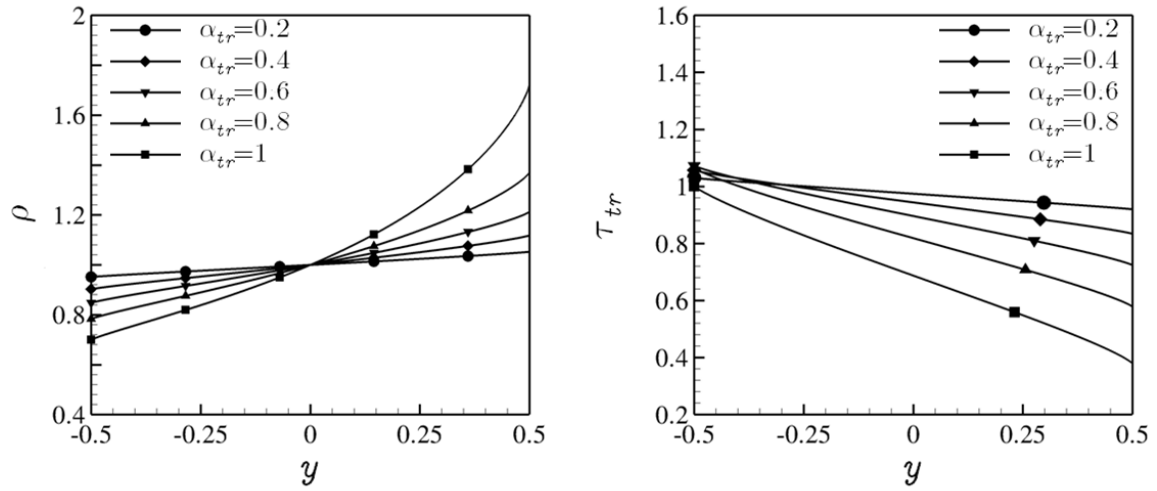
Figure 3.7: Dimensionless distributions of number density $\rho(y)$ (left) and translational temperature $\tau_{tr}(y)$ (right) of a diatomic HS gas ($j = 2$, Pr = 0.71, $Z = 5$) with $T_H/T_C = 10$ and $\delta_0 = 1$ for various values of α_{tr} with $\alpha_{rot} = 1$, based on the Holway model.
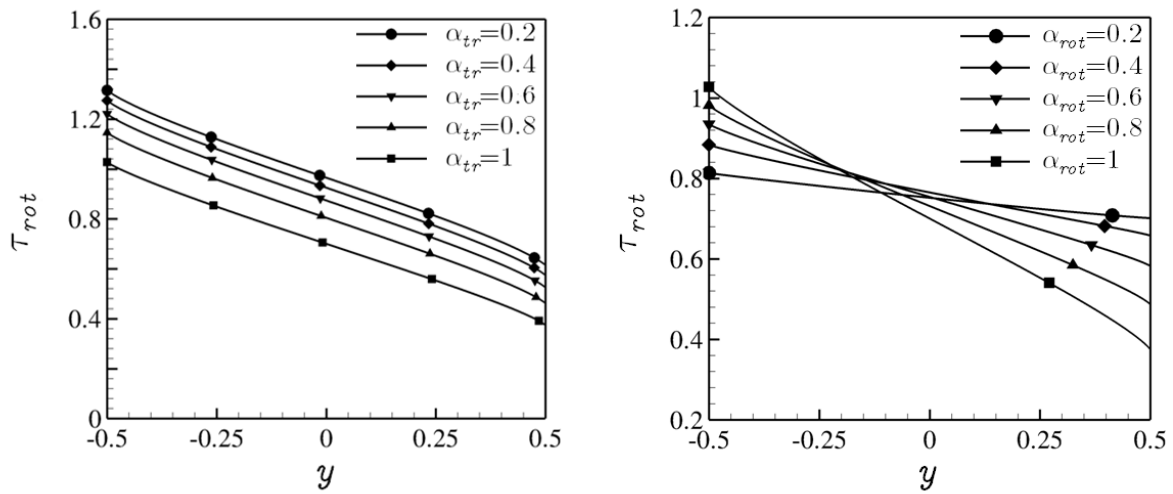
Figure 3.8: Dimensionless distributions of rotational temperature $\tau_{rot}(y)$ of a diatomic HS gas ($j = 2$, Pr = 0.71, $Z = 5$) with $T_H/T_C = 10$ and $\delta_0 = 1$ for various values of α_{tr} with $\alpha_{rot} = 1$ (left) and α_{rot} with $\alpha_{tr} = 1$ (right), based on the Holway model.
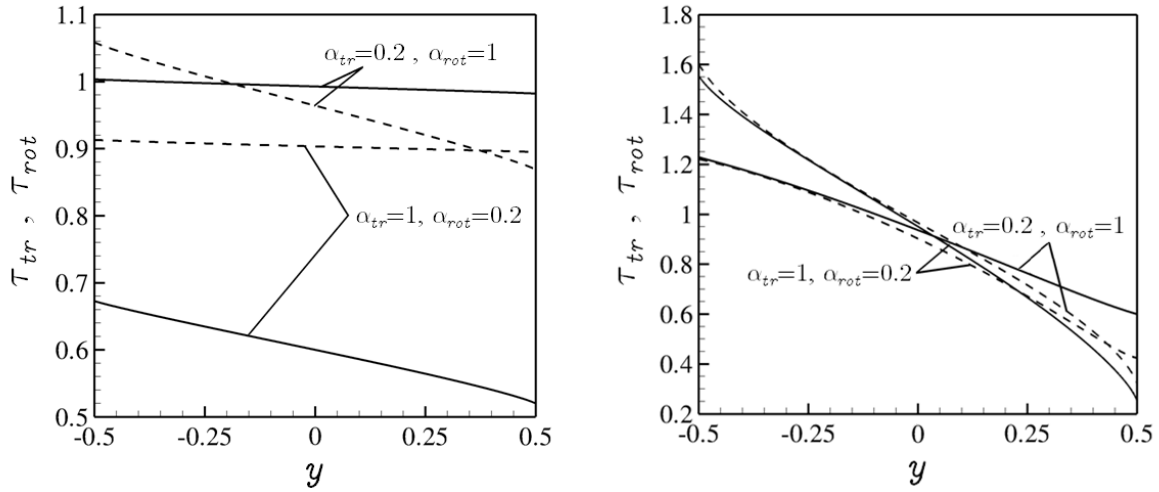
Figure 3.9: Dimensionless distributions of translational τ_{tr} (solid lines) and rotational τ_{rot} (dashed lines) of a diatomic HS gas ($j = 2$, Pr = 0.71, $Z = 5$) with $\alpha_{tr} \neq \alpha_{rot}$ for $T_H/T_C = 10$ and $\delta_0 = 0.1$ (left) and $\delta_0 = 10$ (right), based on the Holway model.
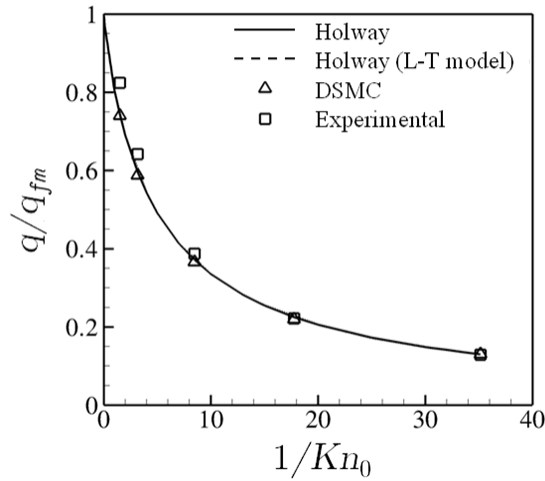
Figure 3.10: Comparison between the experimental data in [96] and the computational results obtained by the Holway model and the DSMC method (gas: N_2, $Pr = 0.71$, $Z^{(DSMC)} = 5$, $T_H/T_C = 1.0291$, $T_H = 301.96$ K, $\alpha = 0.76$, HS molecules).
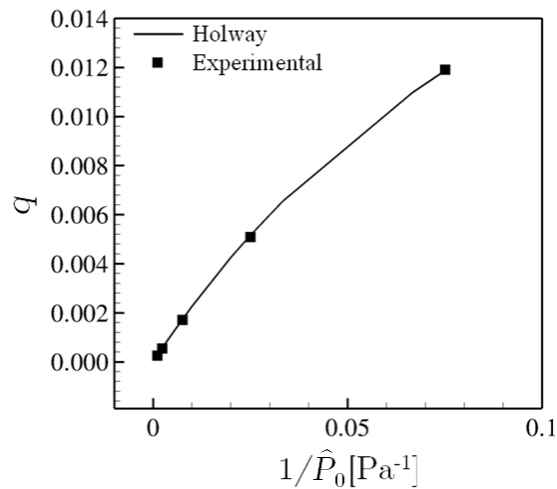
Figure 3.11: Comparison between the experimental data in [85] and the computational results obtained by the Holway model (gas: N_2, $Pr = 0.71$, $Z^{(H)} = 5$, $T_H = 308.3$ K, $T_H/T_C = 1.069$, $\alpha_H = 0.795$, $\alpha_C = 0.808$, HS molecules).

67
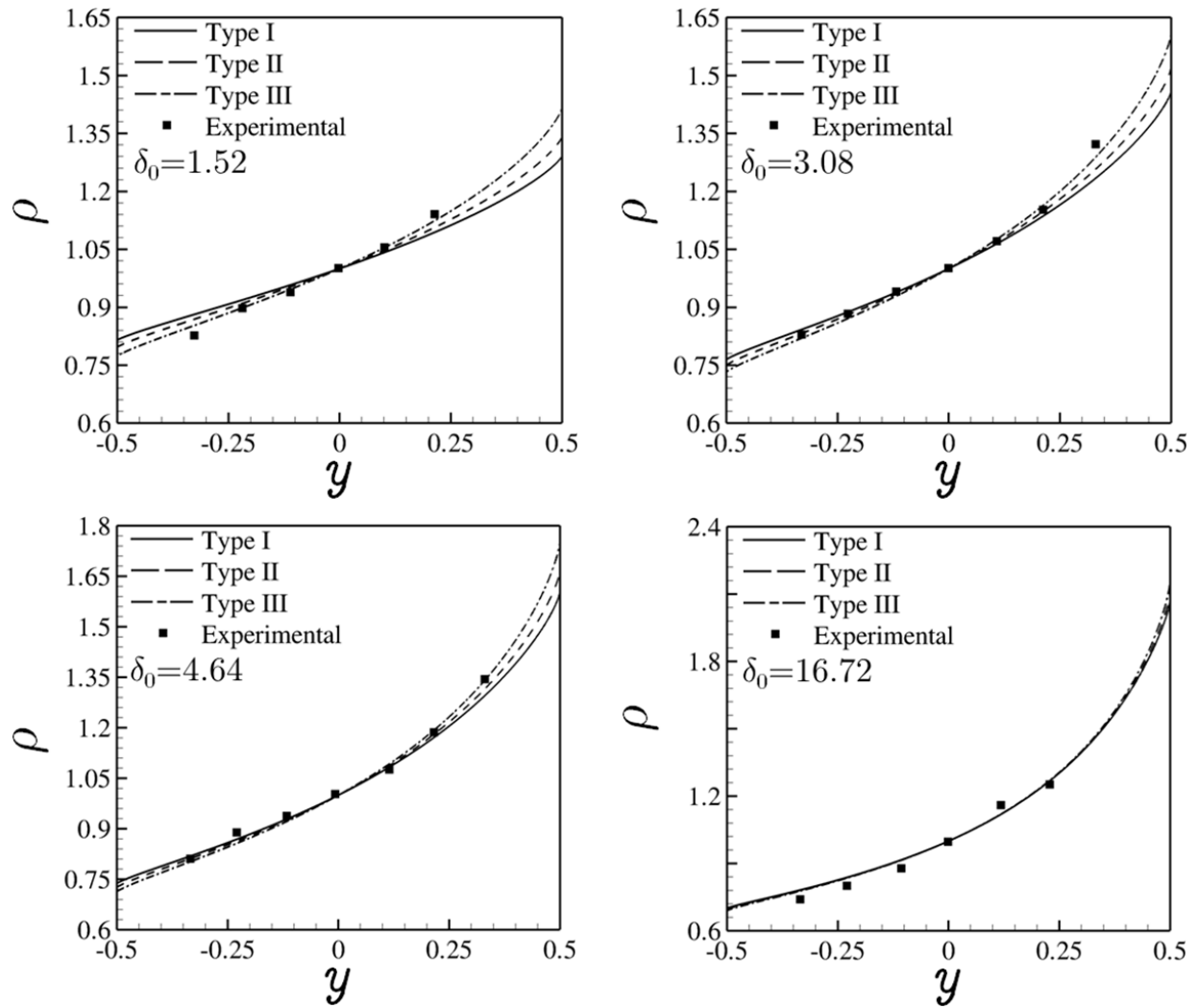
Figure 3.12: Comparison between the experimental data in [97] and the computational results obtained by the Holway model (gas: N_2, Pr = 0.71, $Z^{(H)} = 5$, $T_H = 294$ K, $T_H/T_C = 3.72$, $\alpha_H = \alpha_C = 0.82$, HS molecules).

68
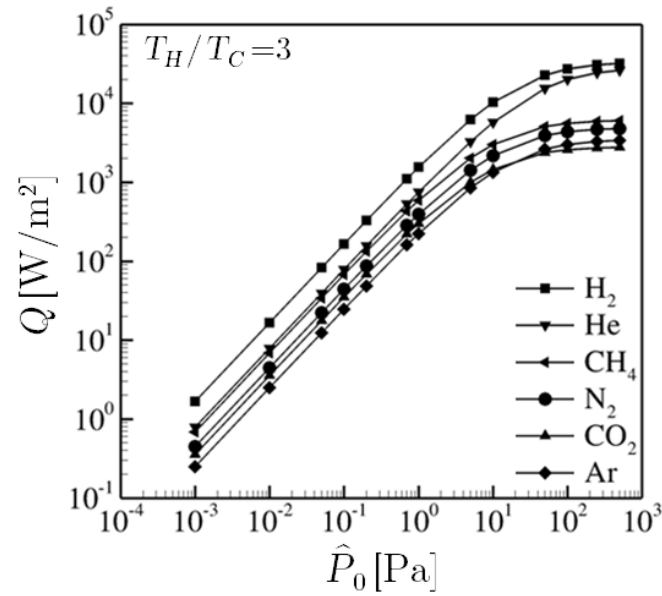
Figure 3.13: Dimensional heat flux through various gases enclosed between two plates with distance $H = 5$ mm for $T_C = 293$ K and $T_H/T_C = 3$ in terms of the reference pressure obtained by the Holway model ($Z^{(H)} = 5$, IPL model).

69

Chapter 4

Conductive heat transfer in a rarefied polyatomic gases confined between coaxial cylinders

4.1 Introduction

The available research work of cylindrical heat conduction in rarefied polyatomic gases is very limited and is mainly for small temperature differences. Thus, a detailed investigation of the conductive heat transfer through rarefied polyatomic gases confined between two coaxial cylinders is needed and it is tackled in this chapter considering only rotational degrees of freedom. This heat transfer configuration is investigated here, based on the Holway [20] and Rykov [21] models. Macroscopic quantities are provided for various radii ratios in a wide range of the rarefaction parameter number and for small, moderate and large temperature differences. Comparisons between kinetic models and DSMC results as well as between simulations and available in the literature experimental data are presented and discussed. The validity of the results is confirmed and the effects of all involved parameters on the heat flux and on the temperature as well as on the density distributions are examined. Moreover, the influence of the gas-surface interaction, as well as the influence of the number of rotational degrees of freedom on the computed quantities are investigated.

71

4.2 The cylindrical heat flow configuration

Consider two concentric stationary cylinders with radii R_A, R_B and the annular gap $\Re = \{(x, y) : R_A^2 < x^2 + y^2 < R_B^2\}$ filled with a polyatomic gas at rest and arbitrary density level. The temperatures of the inner and outer cylinder are maintained constant at T_A and T_B respectively with $T_A > T_B$. The cylinders are assumed to be very long and variations in the axial direction (end effects) are neglected. Then, due to the temperature difference there is an axisymmetric conductive heat flow through the gas from the inner hot cylinder towards the cold outer cylinder. The problem configuration is shown in Fig. 4.1. In the temperature range where the effects of vibrational degrees of freedom can be neglected, and the gas temperature is neither too high nor too low, so that the rotational degrees of freedom may be considered classically the problem may be modeled by rigid rotators model [29].
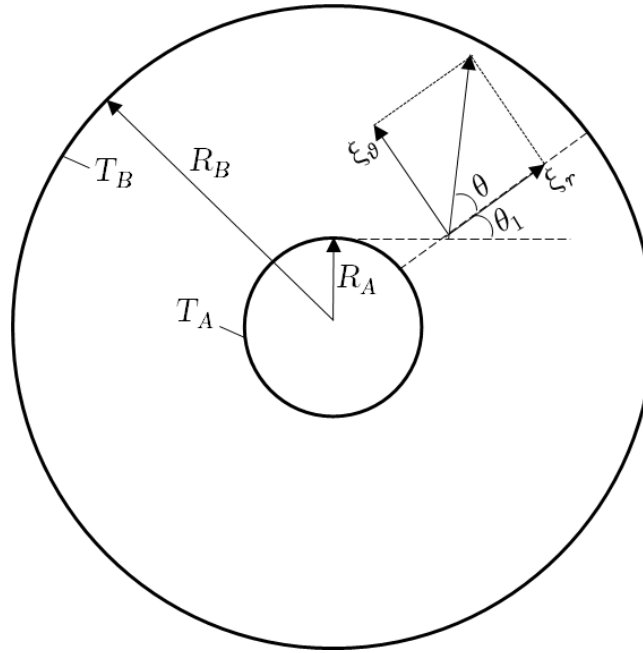
Figure 4.1: Cross-sectional schema of the heat transfer between coaxial cylinders.

The investigation is based on the description of the state of a polyatomic gas using the distribution function $\hat{f}\left(\hat{\boldsymbol{r}}, \boldsymbol{v}, \hat{I}\right)$ dependent on $\boldsymbol{v} = (\xi_r, \xi_\vartheta, \xi_z) = (\xi \cos\theta, \xi \sin\theta, \xi_z)$, with $v^2 = \xi^2 + \xi_z^2$ being the molecular velocity, the position vector $\hat{\boldsymbol{r}}$ and the rotational motion energy $\hat{I}$. The objective is to estimate all macroscopic distributions in terms of the three parameters

72

governing this heat transfer problem, namely the temperature difference between the cylindrical walls, the ratio of the two cylindrical radii and the degree of gas rarefaction.

It is convenient to introduce these three parameters in dimensionless form, taking the quantities at the outer cylinder as reference quantities. In particular

$$\beta = \frac{T_A - T_B}{T_B} = \frac{\Delta T}{T_B} \tag{4.1}$$

is the normalized temperature difference

$$\gamma = \frac{R_A}{R_B} \tag{4.2}$$

is the ratio of the inner over the outer radius and

$$\delta_B = \frac{R_B \hat{P}_B}{\mu_B \upsilon_B} \tag{4.3}$$

is the reference gas rarefaction parameter. In the latter expression $\hat{P}_B$ is a reference gas pressure, measured when the system is in equilibrium ($T_A = T_B$), μ_B is the gas viscosity at reference temperature T_B and $\upsilon_B = \sqrt{2k_B T_B/m}$, with k_B being the Boltzmann constant and m the molecular mass, is the most probable molecular speed. The problem is axially symmetric and one-dimensional in the physical space $R_A < \hat{r} < R_B$. The macroscopic quantities of practical interest are the number density distribution

$$n(\hat{r}) = \int\limits_{0}^{2\pi} \int\limits_{0}^{\infty} \int\limits_{-\infty}^{\infty} \int\limits_{0}^{\infty} \hat{f} d\hat{I} d\xi_z \xi d\xi d\theta \tag{4.4}$$

as well as the temperature and heat flux distributions denoted by $T(\hat{r})$ and $Q(\hat{r})$ respectively. In polyatomic gases the internal energy can by divided in two parts, the energy of the translational motion and the energy associated to the internal structure. These energies are related to the corresponding temperatures and heat fluxes. Then, the translational, rotational and total

(thermodynamic) temperatures are:

$$T_{tr}(\hat{r}) = \frac{m}{3k_B n} \int\limits_{0}^{2\pi} \int\limits_{0}^{\infty} \int\limits_{-\infty}^{\infty} \int\limits_{0}^{\infty} \left(\xi^2 + \xi_z^2\right) \hat{f} d\hat{I} d\xi_z \xi d\xi d\theta, \tag{4.5}$$

$$T_{rot}(\hat{r}) = \frac{2}{jk_B n} \int\limits_{0}^{2\pi} \int\limits_{0}^{\infty} \int\limits_{-\infty}^{\infty} \int\limits_{0}^{\infty} \hat{f}\hat{I} d\hat{I} d\xi_z \xi d\xi d\theta, \tag{4.6}$$

$$T(\hat{r}) = \frac{3T_{tr}(\hat{r}) + jT_{rot}(\hat{r})}{3 + j}. \tag{4.7}$$

The subscripts *tr* and *rot* refer to translational and rotational parts respectively, with $j = 2$ for diatomic and linear molecules and $j = 3$ in all other cases (nonlinear molecules). The corresponding heat fluxes are:

$$Q_{tr}(\hat{r}) = \frac{m}{2} \int\limits_{0}^{2\pi} \int\limits_{0}^{\infty} \int\limits_{-\infty}^{\infty} \int\limits_{0}^{\infty} \left(\xi^2 + \xi_z^2\right) (\xi\cos\theta)\, \hat{f} d\hat{I} d\xi_z \xi d\xi d\theta, \tag{4.8}$$

$$Q_{rot}(\hat{r}) = \int\limits_{0}^{2\pi} \int\limits_{0}^{\infty} \int\limits_{-\infty}^{\infty} \int\limits_{0}^{\infty} (\xi\cos\theta)\, \hat{f}\hat{I} d\hat{I} d\xi_z \xi d\xi d\theta, \tag{4.9}$$

$$Q(\hat{r}) = Q_{tr}(\hat{r}) + Q_{rot}(\hat{r}). \tag{4.10}$$

Here, the effect of all involved parameters, namely of β, γ and δ_B on the heat flux, temperature and density distributions for diatomic and polyatomic gases is examined. This is achieved in a deterministic manner described in Section 4.3. The approach includes the replacement of the rather complex collision term of Eq. (2.5) by the Holway and Rykov kinetic models.

4.3   Kinetic formulation in cylindrical geometry

The effort of solving the Boltzmann either analytically or numerically, is significantly reduced by substituting its collision term with reliable kinetic models. Here, for purposes related mainly to benchmarking and validation of results the Holway and Rykov models are

applied. The Rykov model at its present form is applicable only to diatomic gases ($j = 2$), while the Holway model is more general and is applicable to polyatomic gases ($j = 2, 3$). Applying the described projection process in energy space in Chapter 2, both models for the present steady-state heat transfer configuration can be written in a similar form as [124, 132]

$$\xi \cos\theta \frac{\partial \hat{g}}{\partial \hat{r}} - \frac{\xi \sin\theta}{\hat{r}} \frac{\partial \hat{g}}{\partial \theta} = \nu_{rot}^{(i)} \left(\hat{g}_{rot}^{(i)} - \hat{g} \right) + \nu_{tr}^{(i)} \left(\hat{g}_{tr}^{(i)} - \hat{g} \right), \tag{4.11}$$

$$\xi \cos\theta \frac{\partial \hat{h}}{\partial \hat{r}} - \frac{\xi \sin\theta}{\hat{r}} \frac{\partial \hat{h}}{\partial \theta} = \nu_{rot}^{(i)} \left(\hat{h}_{rot}^{(i)} - \hat{h} \right) + \nu_{tr}^{(i)} \left(\hat{h}_{tr}^{(i)} - \hat{h} \right), \tag{4.12}$$

where the superscript $i = H, R$ denotes the Holway (H) and Rykov (R) models respectively. Here, the collision term consists of the elastic and inelastic collision parts, with the subscripts tr referring to elastic and rot to inelastic, while $\hat{g}_{tr}^{(i)}$, $\hat{h}_{tr}^{(i)}$, $\hat{g}_{rot}^{(i)}$ and $\hat{h}_{rot}^{(i)}$ are the corresponding relaxing distributions given by Eqs. (3.13) and (3.14) for the Holway and the Rykov models respectively. The quantities $\nu_{tr}^{(i)}$ and $\nu_{rot}^{(i)}$ denote the frequency of the elastic and inelastic collisions respectively. The collision frequencies $\nu_{tr}^{(i)}$ and $\nu_{rot}^{(i)}$ are specified as

$$\nu_{tr}^{(i)} = \left(1 - \frac{1}{Z^{(i)}} \right) \frac{\hat{P}_{tr}}{\mu_{tr}} \mathrm{Pr}^\chi, \quad \nu_{rot}^{(i)} = \frac{1}{Z^{(i)}} \frac{\hat{P}_{tr}}{\mu_{tr}} \mathrm{Pr}^\chi, \tag{4.13}$$

where Pr is the Prandtl number of the gas, with the parameter $\chi = 1$ in the Holway model ($i = H$) and $\chi = 0$ in the Rykov model ($i = R$), while the parameter $1 \le Z < \infty$ indicates how many collisions occur per single rotational collision. Also in Eqs. (4.13), $\hat{P}_{tr} = n k_B T_{tr}$ is the pressure defined by the translational temperature and $\mu_{tr} = \mu(\mathrm{T}_{tr})$ is the gas viscosity based on the translational temperature of the gas. At this stage the following dimensionless quantities are introduced

$$r = \frac{\hat{r}}{R_B}, \quad \zeta = \frac{\xi}{\upsilon_B}, \quad c_z = \frac{\xi_z}{\upsilon_B}, \quad g = \frac{\hat{g}\upsilon_B^3}{n_B}, \quad h = \frac{\hat{h}\upsilon_B^3}{\hat{P}_B},$$

$$\rho = \frac{n}{n_B}, \quad \tau_{tr} = \frac{T_{tr}}{T_B}, \quad \tau_{rot} = \frac{T_{rot}}{T_B}, \quad \tau = \frac{3\tau_{tr} + j\tau_{rot}}{3 + j}, \tag{4.14}$$

$$q_{tr} = \frac{Q_{tr}}{\hat{P}_B \upsilon_B}, \quad q_{rot} = \frac{Q_{rot}}{\hat{P}_B \upsilon_B}, \quad q = q_{tr} + q_{rot}.$$

All quantities with the subscript B are considered as reference quantities ($\hat{P}_B = n_B k_B T_B$). Here, $g = g(r, \zeta, \theta, c_z)$ and $h = h(r, \zeta, \theta, c_z)$ are the dimensionless distributions, with $\gamma \leq r \leq 1$ while $\mathbf{c} = (\zeta \cos \theta, \zeta \sin \theta, c_z)$ is the dimensionless molecular velocity vector. Furthermore, ρ, τ and q are the dimensionless distributions of number density, temperature and radial heat flux respectively, with τ_{tr}, τ_{rot}, q_{tr}, q_{rot} denoting the corresponding dimensionless translational and rotational parts. Next, the computational effort is further reduced by eliminating the c_z component of the molecular velocity by introducing the reduced distributions

$$F(r, \zeta, \theta) = \int\limits_{-\infty}^{\infty} g \, dc_z, \quad G(r, \zeta, \theta) = \int\limits_{-\infty}^{\infty} g c_z^2 \, dc_z, \quad S(r, \zeta, \theta) = \int\limits_{-\infty}^{\infty} h \, dc_z. \qquad (4.15)$$

By operating successively on Eq. (4.11) with the integral operators $\int (.) dc_z$ and $\int (.) c_z^2 dc_z$ as well as on Eq. (4.12) with $\int (.) dc_z$, a system of three integro-differential equations is obtained, which in compact vector form is written as

$$\zeta \cos \theta \frac{\partial \mathbf{\Psi}}{\partial r} - \frac{\zeta \sin \theta}{r} \frac{\partial \mathbf{\Psi}}{\partial \theta} = \delta_B \rho (\tau_{tr})^{1-\omega} \text{Pr}^\chi \left[\left(1 - \frac{1}{Z^{(i)}} \right) \left(\mathbf{\Psi}_{tr}^{(i)} - \mathbf{\Psi} \right) + \frac{1}{Z^{(i)}} \left(\mathbf{\Psi}_{rot}^{(i)} - \mathbf{\Psi} \right) \right]. \qquad (4.16)$$

Here, the vector of the unknown distributions $\mathbf{\Psi} = [F, G, S]^T$ depends on three independent variables, namely ρ, ζ and θ. Also, the reference gas rarefaction δ_B is given by Eq. (4.3). As $Z^{(i)} \to \infty$, the first two equations in Eq. (4.16) for $i = H, R$ are transformed to the corresponding reduced BGK and Shakhov equations for monatomic gas. In the derivation of Eq. (4.16) the Inverse Power Law (IPL) interaction between particles has been introduced with $\omega \in [0.5, 1]$. In addition, the translational and rotational relaxing distributions in Eq. (4.16) are given by $\mathbf{\Psi}_{tr}^{(i)} = \left[F_{tr}^{(i)}, G_{tr}^{(i)}, S_{tr}^{(i)} \right]^T$ and $\mathbf{\Psi}_{rot}^{(i)} = \left[F_{rot}^{(i)}, G_{rot}^{(i)}, S_{rot}^{(i)} \right]^T$ respectively, where the components of these vectors for each kinetic model are as follows

- *Holway model*

$$F_{tr}^{(H)} = \frac{\rho}{\pi \tau_{tr}} \exp \left(-\frac{\zeta^2}{\tau_{tr}} \right), \quad G_{tr}^{(H)} = \frac{1}{2} \tau_{tr} F_{tr}^{(H)}, \quad S_{tr}^{(H)} = \frac{j}{2} \tau_{rot} F_{tr}^{(H)},$$

$$F_{rot}^{(H)} = \frac{\rho}{\pi \tau} \exp \left(-\frac{\zeta^2}{\tau} \right), \quad G_{rot}^{(H)} = \frac{1}{2} \tau F_{rot}^{(H)}, \quad S_{rot}^{(H)} = \frac{j}{2} \tau F_{rot}^{(H)}. \qquad (4.17)$$

- *Rykov model*

$$F_{tr}^{(R)} = F_{tr}^{(H)} \left[1 + \frac{4}{15} \frac{q_{tr}\zeta\cos\theta}{\rho\tau_{tr}^2} \left(\frac{\zeta^2}{\tau_{tr}} - 2 \right) \right],$$

$$G_{tr}^{(R)} = \frac{1}{2}\tau_{tr}F_{tr}^{(H)} \left[1 + \frac{4}{15} \frac{q_{tr}\zeta\cos\theta}{\rho\tau_{tr}^2} \left(\frac{\zeta^2}{\tau_{tr}} - 1 \right) \right],$$

$$S_{tr}^{(R)} = \tau_{rot}F_{tr}^{(H)} \left[1 + \frac{4}{15} \frac{q_{tr}\zeta\cos\theta}{\rho\tau_{tr}^2} \left(\frac{\zeta^2}{\tau_{tr}} - 2 \right) + 2\left(1 - \kappa\right) \frac{q_{rot}\zeta\cos\theta}{\rho\tau_{tr}\tau_{rot}} \right],$$

$$F_{rot}^{(R)} = F_{rot}^{(H)} \left[1 + \varpi_0\frac{4}{15} \frac{q_{tr}\zeta\cos\theta}{\rho\tau^2} \left(\frac{\zeta^2}{\tau} - 2 \right) \right], \tag{4.18}$$

$$G_{rot}^{(R)} = \frac{1}{2}\tau F_{rot}^{(H)} \left[1 + \varpi_0\frac{4}{15} \frac{q_{tr}\zeta\cos\theta}{\rho\tau^2} \left(\frac{\zeta^2}{\tau} - 1 \right) \right],$$

$$S_{rot}^{(R)} = \tau F_{rot}^{(H)} \left[1 + \varpi_0\frac{4}{15} \frac{q_{tr}\zeta\cos\theta}{\rho\tau^2} \left(\frac{\zeta^2}{\tau} - 2 \right) + 2\varpi_1\left(1 - \kappa\right) \frac{q_{rot}\zeta\cos\theta}{\rho\tau^2} \right].$$

The parameters ϖ_0 and ϖ_1 are chosen so that the thermal conductivity obtained from the model equation is close to the experimental data in [119], while the parameter κ for a power intermolecular potential is constant. The parameters ϖ_0, ϖ_1 and κ are discussed in detail in Chapter 3. The macroscopic quantities in Eqs. (4.16)-(4.18) in terms of the reduced distributions F, G and S are obtained by operating accordingly on Eqs. (4.4)-(4.10). A similar manipulation to the one applied in the governing equations is applied to deduce the following moments

$$\rho = \int\limits_0^{2\pi} \int\limits_0^{\infty} F\zeta d\zeta d\theta, \tag{4.19}$$

$$\tau_{tr} = \frac{2}{3\rho} \int\limits_0^{2\pi} \int\limits_0^{\infty} \left(\zeta^2 F + G \right) \zeta d\zeta d\theta, \quad \tau_{rot} = \frac{2}{j\rho} \int\limits_0^{2\pi} \int\limits_0^{\infty} S\zeta d\zeta d\theta, \quad \tau = \frac{3\tau_{tr} + j\tau_{rot}}{3 + j}, \tag{4.20}$$

$$q_{tr} = \int\limits_0^{2\pi} \int\limits_0^{\infty} \left(\zeta^2 F + G \right) \left(\zeta\cos\theta \right) \zeta d\zeta d\theta, \quad q_{rot} = \int\limits_0^{2\pi} \int\limits_0^{\infty} S \left(\zeta\cos\theta \right) \zeta d\zeta d\theta, \quad q = q_{tr} + q_{rot}. \tag{4.21}$$

It is noted that by operating accordingly on Eq. (4.16) the conservation equation

$$\frac{\partial\left[rq\left(r\right)\right]}{\partial r} = 0 \tag{4.22}$$

is readily deduced, which implies that the product $rq\left(r\right)$ remain constant along $\gamma \leq r \leq 1$. Therefore in the Section 4.5, results for the heat fluxes are presented only at the inner hot cylinder where $r = \gamma$. In addition, this conservation equation is used for benchmarking purposes. Furthermore, it is noted that upon convergence the conservation equation Eq. (4.22) is accordingly satisfied in several significant figures. In addition, the numerical solutions at the free molecular ($\delta_B = 0$) and continuum ($\delta_B \to \infty$) limits have an excellent agreement with the corresponding analytical ones presented in Appendix C.

To close the problem formulation boundary conditions have to be assigned. The problem is axially symmetric and therefore becomes one-dimensional in physical space. Thus, the boundary conditions are only imposed in two points. Since, in many practical applications [80] the radius ratio is characterized by large values the influence of the gas-surface interaction on the external cylinder is so small that we may neglect it. Thus, the diffuse scattering is assumed on the outer cylinder, while the boundary condition model I with one thermal accommodation coefficient described in Chapter 3 is applied at the inner cylinder. Then, the outgoing distributions (+) associated to Eq. (4.16) are at the inner wall ($r = \gamma$)

$$F^+ = \frac{\rho_w}{\pi\tau^\alpha}\exp\left(-\frac{\zeta^2}{\tau^\alpha}\right), \quad G^+ = \frac{1}{2}\tau^\alpha F^+, \quad S^+ = \frac{j}{2}\tau^\alpha F^+, \tag{4.23}$$

where $\tau^\alpha = T^\alpha/T_B$ is given by

$$\tau^\alpha = \alpha\left(1+\beta\right) + \left(1-\alpha\right)\frac{2E^-}{\left(4+j\right)N}, \tag{4.24}$$

while

$$\frac{E^-}{N} = \frac{\int\limits_{\pi/2}^{3\pi/2}\int\limits_{0}^{\infty}\left(\zeta\cos\theta\right)\left(\zeta^2 F^- + G^- + S^-\right)\zeta d\zeta d\theta}{\int\limits_{\pi/2}^{3\pi/2}\int\limits_{0}^{\infty}\left(\zeta\cos\theta\right)F^-\zeta d\zeta d\theta}. \tag{4.25}$$

The parameter ρ_w is obtained by the no penetration condition according to

$$\rho_w = -\frac{2\sqrt{\pi}}{\sqrt{\tau^\alpha}} \int\limits_{\pi/2}^{3\pi/2} \int\limits_{0}^{\infty} (\zeta \cos\theta) \, F^- \zeta d\zeta d\theta. \tag{4.26}$$

In the Eqs. (4.24)-(4.26) the superscript (-) denotes the incoming fluxes on the wall. At the outer wall ($r = 1$) the following boundary conditions are applied

$$F^+ = \frac{1}{\pi} \exp\left(-\zeta^2\right), \quad G^+ = \frac{1}{2} F^+, \quad S^+ = \frac{j}{2} F^+. \tag{4.27}$$

Boundary conditions Eqs. (4.23)-(4.26) and Eq. (4.27) are valid for $\theta \in [-\pi/2, \pi/2]$ and $\theta \in [\pi/2, 3\pi/2]$ respectively. The nonlinear vector Eq. (4.16) along with the associated expressions Eqs. (4.17)-(4.18), the moments Eqs. (4.19)-(4.21) and the boundary conditions Eqs. (4.23)-(4.27) provide a theoretically well-established closed kinetic formulation for the heat transfer problem under consideration, which is solved numerically both for the Holway and Rykov models in a deterministic manner.

4.4 Results and discussion

4.4.1 Numerical parameters and computing quantities

The molecular velocity space (ζ, θ), with $\zeta \in [0, \infty)$, $\theta \in [0, 2\pi]$, and the physical space $r \in [\gamma, 1]$ are discretized. The continuum spectrum of magnitudes of the molecular velocity vector is replaced by a set of discrete magnitudes $\zeta_m \in [0, \zeta_{\max}]$, $m = 1, 2, ..., M$, which are taken to be the roots of the Legendre polynomial of order M accordingly mapped from $[-1, 1]$ to $[0, \zeta_{\max}]$. Also, by using a uniform grid, the angular space is divided into N intervals. Each of the angular intervals is defined by its angle θ_n, $n = 1, 2, ..., N$. Finally, the distance between the two cylinders is divided into K equal segments, defined by r_k, $k = 1, 2, ..., K + 1$.

The integro-differential equations Eq. (4.16) are first discretized in the variable ζ and the resulting equations are integrated over each spatial and angular intervals $\left[r_{k-1/2}, \, r_{k+1/2}\right]$ and $\left[\theta_{n-1/2}, \, \theta_{n+1/2}\right]$. The moments Eq. (4.4)-(4.10) are numerically integrated by applying the

trapezoidal rule and Gauss-Legendre quadrature in the polar angle θ and the velocity magnitude ζ respectively. The resulting discretized equations for $\boldsymbol{\Psi}_{k,m,n} = [F_{k,m,n}, G_{k,m,n}, S_{k,m,n}]^T$ with the associated discretized moments are solved in an iterative manner which is concluded when the convergence criteria

$$\frac{1}{3\,(K+1)} \sum_{i=1}^{K+1} \left[\left| \rho_i^{(t+1)} - \rho_i^{(t)} \right| + \left| \tau_i^{(t+1)} - \tau_i^{(t)} \right| + \left| q_i^{(t+1)}{}_i - q_i^{(t)} \right| \right] < \varepsilon, \qquad (4.28)$$

with t denoting the iteration index, is fulfilled. The results presented in Section 5 have been obtained with $M = 24$, $N = 400$ and $K = 800$ for $\gamma \geq 0.1$ and $K = 2000$ for $\gamma < 0.1$, while the termination parameter is set to $\varepsilon = 10^{-8}$. Recently, the implemented numerical scheme has been applied to solve with considerable success heat transfer configurations [124, 132].

Results in graphical and tabulated form are presented for the macroscopic quantities in terms of all parameters involved in the problem. In particular, in Subsection 4.4.2 the macroscopic quantities obtained by the Holway and Rykov kinetic models as well as by the DSMC method in a wide range of all parameters involved in the problem are presented for linear ($j = 2$) and nonlinear ($j = 3$) polyatomic molecules in tabulated and graphical form. The influence of the rotational degrees of freedom on the translational, rotational and total heat fluxes in the case of the cylindrical geometry is investigated in Subsection 4.4.3. More specifically, heat fluxes distributions are provided for diatomic and polyatomic gases enclosed between cylinders with the normalized temperature difference $\beta = [0.1, 1, 10]$, the radii ratio $\gamma = [1/2, 1/10, 1/65]$ and the gas rarefaction parameter δ_B varying from the free molecular limit up to the hydrodynamic regime. Finally, in Subsection 4.4.4 comparisons between computational results and experimental data available in literature are performed.

4.4.2 Comparison between kinetic models and DSMC

In Table 4.1, the dimensionless translational and rotational heat fluxes computed by the Holway and Rykov models ($j = 2$) are given for various β and δ_B with $\gamma = 1/2$. The tabulated results are at the surface $r = \gamma$ of the inner cylinder. The enclosed gas is nitrogen (N_2) and the inverse power law (IPL) model with $\omega = 0.74$ has been applied. In the case

of the Rykov model, the parameters in Eq. (4.18) are set to $\varpi_0 = 0.2354$, $\varpi_1 = 0.3049$ and $\kappa = 0.645$ [45, 106]. Results are provided for $Z = 1$ and 5, which are indicative for this type of simulations since, $Z = 1$ means that only inelastic collisions occur, while $Z = 5$ refers to the situation where the amount of inelastic collisions is small compared to the elastic ones. In the last column the corresponding heat fluxes obtained by the Shakhov model for a monatomic gas are given. It is observed that the agreement between the results of the Holway and Rykov models is, in general, very good. As expected, at $\delta_B = 0$ identical results are provided and then as δ_B is increased the deviation between the Holway and Rykov heat fluxes is increased. Also, in terms of the parameter Z the agreement is better as Z is increased. The largest discrepancies are about 10% and they are occurring at $Z = 1$ and $\delta_B = 10$ (independent of β). According to Eq. (3.17) for fixed values of the parameters $\varpi_0 = 0.2354$, $\varpi_1 = 0.3049$ and $\kappa = 0.645$ the Prandtl number of the Rykov model is a function of the parameter Z taking the values $\mathrm{Pr} = 0.71$ and 0.91 for $Z = 1$ and 5 respectively. In order to achieve a consistent comparison for $Z = 1$ between the Holway and Rykov models the Prandtl number used in the Holway model is taken equal to the Prandtl number obtained by the Rykov model. Thus, in Table 4.2 the corresponding comparison performed in Table 4.1 for $Z = 1$ is presented for $\mathrm{Pr} = 0.91$. As it is seen the comparison is very good with the maximum relative error being less than 2%. In both models the rotational heat fluxes are about half of the corresponding translational ones (at $\delta_B = 0$, q_{rot} is exactly one-half of q_{tr}). It is clearly seen that the Rykov model is more sensitive to the variation of Z, compared to the Holway model which, at least for this set of parameters, is slightly affected and only at large values of δ_B. In both models as Z is increased, the translational heat fluxes are increased approaching those of the Shakhov model ($Z \to \infty$). The values of q_{tr}, at $Z = 5$, are already close enough to the corresponding q of the Shakhov model. The total heat fluxes $q = q_{tr} + q_{rot}$ of N_2 for the Rykov and Holway models are higher about $22 - 50\%$ and $36 - 50\%$ respectively than the corresponding monatomic heat fluxes. It is noted that the analytical free molecular results in Appendix C are recovered to all significant figures, while the conservation Eq. (4.22) is fully satisfied. The heat flux distributions between the cylinders are readily reduced by multiplying the tabulated values by the ratio γ/r.

81

In Table 4.3, a comparison between the results obtained by the Holway model and the DSMC method [132] for a diatomic gas ($j = 2$) enclosed between cylinders with $\gamma = 1/2$ and various values of β and δ_0 is performed. Based on the hard sphere (HS) model the dimensionless translational and rotational heat fluxes for $Z = 1$ and 5 at $r = \gamma$ are provided. It is important to note that in order to facilitate comparisons between the DSMC and kinetic results, the gas rarefaction parameter δ_0 is defined in terms of a reference pressure $\hat{P}_0$ given by $\hat{P}_0 = n_0 k_B T_B$ (instead of $\hat{P}_B = n_B k_B T_B$), where n_0 is an average reference number density defined as

$$n_0 = \frac{2}{R_B^2 - R_A^2} \int_{R_A}^{R_B} n(\hat{r}) \, \hat{r} d\hat{r}. \tag{4.29}$$

Therefore, the Holway kinetic heat fluxes presented in Table 4.3 are not directly compatible with the ones in Table 4.1. The variation of the DSMC heat fluxes in terms of the problem parameters (β, δ_0, Z) is exactly the same as for the kinetic models. More importantly, in all cases the quantitative agreement between the Holway and DSMC results is excellent with the largest discrepancies not exceeding 5%. For completeness purposes the monatomic modelling results based on the Shakhov model are also included.

The comparison is continued in Figs. 4.2 and 4.3, where the distributions of density and temperatures respectively, obtained by the Holway and DSMC approaches, are plotted for the indicative values of $\beta = 0.1$, 1, 10 and $\delta_0 = 0.2$, 2, 20. As it is observed in Fig. 4.2, the corresponding density distributions are in excellent agreement for all β and δ_0, with the relative plots actually coinciding on each other. Furthermore, in Fig. 4.3 the agreement between the corresponding translational and rotational temperature distributions is again very good in all cases with an exception at $\beta = 10$ and $\delta_0 = 20$, where a small deviation between the relative plots is observed. It is also seen that the translational and rotational temperatures for the same set of parameters are almost identical. Therefore, Eq. (4.20) yields $\tau \approx \tau_{tr} \approx \tau_{rot}$. Observing the results presented so far (Tables 4.1, 4.2 and 4.3 and Figs. 4.2 and 4.3) it is deduced that the deterministic modeling based on two different kinetic model equations namely the Holway and Rykov models and the stochastic modeling based on the DSMC method provide similar results in simulating polyatomic gas heat transfer between coaxial cylinders in a wide range of problem parameters.

4.4.3 Effects of cylindrical geometry on heat fluxes

In this subsection the study is focused on the dependency of the translational, rotational and total heat fluxes on $0 \leq \delta_B \leq 10$, γ and β. The presented results are for $\delta_B = [0, 0.1, 1, 4, 10]$, $\gamma = [1/2, 1/10, 1/65]$ and $\beta = [0.1, 1, 10]$. Also, the influence of the thermal accommodation coefficient α on the heat transfer characteristics is studied by providing numerical results for $q(r = \gamma)$ in terms of the parameter $0 \leq \alpha \leq 1$ of the boundary condition model I with one thermal accommodation coefficient, which is applied at inner cylinder. Furthermore, the simple approximate expression for the heat flux proposed in [98] is tested for different values of the parameters δ_0, γ and β. The simulations have been performed for diatomic ($j = 2$) and polyatomic ($j = 3$) hard sphere gases ($\omega = 1/2$) with Pr = 0.71 and $Z = [1, 3, 5]$.

In Table 4.4, the translational, rotational and total heat fluxes of a diatomic gas ($j = 2$) are presented for $\delta_B = [0, 0.1, 1, 4, 10]$, $\gamma = [1/2, 1/10, 1/65]$ and $\beta = [0.1, 1, 10]$. These dimensionless results demonstrate the effect of all parameters on the heat fluxes including the effect of the radius ratio, which has not been shown before. Furthermore, they may be used for reference purposes in future computational and experimental studies. Therefore, in order to be as general as possible for diatomic gases, they are obtained based on the Holway model, which depends only on the parameter Z. Also, based on the literature, the value of $Z = 3$ used in the simulations is the most suitable one covering a wide range of diatomic gases. The behaviour of the polyatomic heat fluxes in terms of δ_B, γ and β, qualitatively is similar to that of the monatomic ones (are also included for comparison purposes), i.e., they are increased slowly as γ is decreased, they are increased almost proportionally to β and they are decreased as δ_B is increased. Quantitatively however, they vary significantly, with the diatomic heat fluxes being $36 - 50\%$ higher. Also, q_{rot} is about one-half of q_{tr}, with the latter one being close and always smaller to the heat flux of the Shakhov model.

In Table 4.5, the translational, rotational and total heat fluxes for a polyatomic gas ($j = 3$) are presented for $\delta_B = [0, 0.1, 1, 4, 10]$, $\gamma = 1/2$ and $\beta = [0.1, 1, 10]$. The results are based on the Holway model and since no results for $j = 3$ have been presented so far, the parameter Z is set to $Z = 1$ and 5. The variation of all heat fluxes in terms of δ_B and β, as well as of Z is similar to the one for a diatomic gas (see Tables 4.1 and 4.3). The numerical solutions at

$\delta_B = 0$ are exactly the same to all tabulated significant figures with the ones obtained by the analytical expressions given in Appendix C with $j = 3$. Also, at $\delta_B = 0$, q_{rot} is 75% (instead of 50% in diatomic gases) of q_{tr}. This relation applies approximately to all $\delta_B > 0$ independent of β, with rotational heat fluxes being about 75% of the translational ones, while the latter ones are close to the translational heat fluxes of a diatomic (and monatomic) gas. As a result, the dimensionless total heat fluxes of polyatomic gases are about $58 - 75\%$ higher than the corresponding monatomic ones.

In Fig. 4.4 the dimensionless total heat flux q of a diatomic gas ($j = 2$, Pr = 0.71, $Z = 5$) with HS molecules in terms of α is plotted. Results are given for $\delta_B = [0.1, 1, 10]$, $\gamma = [1/2, 1/10]$ and $\beta = [0.1, 1, 10]$. As expected the effect of the thermal accommodation coefficient α on the total heat flux is increased as the rarefaction parameter is decreased. Also, in all cases as α is increased the dimensionless total heat flux is also increased, which is physically justified since as α is increased the temperature of the particles leave from the inner cylinder is increased approaches the temperature of the cylinder. Moreover, it is seen that the behaviour of the total heat flux in terms of α is independent of the radius ratio γ. Qualitatively similar behaviour is observed for the translational and rotational heat fluxes and therefore is not shown separately.

It has been proposed in [98] that the heat flux between confined coaxial cylinders may be computed in the whole range of the rarefaction parameter, assuming small temperature differences and large radius ratios, according to

$$\frac{1}{q} = \frac{1}{q_{fm}} + \frac{1}{q_c}, \tag{4.30}$$

where q_{fm} and q_c are the corresponding free molecular and continuum heat fluxes, which are given for the cylindrical geometry in Appendix C. It has been observed in [86] that in monatomic gases this expression remains valid well beyond the introduced assumptions providing easy-to-go results. Here, this investigation is extended to N_2 and in Fig. 4.5, a comparison is made between the computed heat fluxes based on the Rykov model for the large temperature difference of $\beta = 10$, $\gamma = [1/2, 1/10, 1/65]$ and in a wide range of δ_B, with the corresponding ones obtained by the empirical Eq. (4.30). It is seen that the agreement is excellent for $\delta_B < 10$ and then as δ_B is further increased there are some discrepancies which are increased as γ is decreased. However,

84

the overall agreement remains good and becomes even better as β is decreased. Therefore this expression may also be implemented in polyatomic gases for engineering purposes when the temperature distributions are not needed.

4.4.4 Comparison with experiments

A comparison with experimental data available in the literature is performed in terms of the total heat fluxes. In [84], in an effort to estimate the energy accommodation coefficient of various gases, a detailed experimental investigation has been performed for heat transfer in rarefied gases between coaxial cylinders maintained at a very small temperature difference. It has been found that in the case of N_2 the interaction with the wall is almost purely diffusive. These dimensionless experimental data for N_2 with $\gamma = 1/65$ and $T_B = 300$ K (see Tables 2 and 3 in [84]) are compared, in Fig. 4.6, with the corresponding computational ones, based on the Rykov model. Since the temperature difference is very small and in order to avoid introducing a specific temperature difference, the linearized Rykov model has been applied. The linearized formulation of the Rykov model for the problem under question is described in Appendix D. It is noted that the nonlinear Rykov model with $\beta < 0.1$ provides very similar results with those of its linearized version. Simulations are performed with $\varpi_0 = 0.2354$, $\varpi_1 = 0.3049$ and $\kappa = 0.645$ [106] for N_2 while the parameter Z is chosen equal to 3 in order to obtain a Prandtl number equal to 0.73, which is a good estimation for the Prandtl number of N_2 [133]. The results obtained by the Rykov model are in very good agreement with the experimental results in a wide range of the gas rarefaction $\delta_B \in \left[1, 10^2\right]$. On the contrary, the heat fluxes obtained by the linearized Shakhov kinetic model, also shown in Fig. 4.6, are erroneous underestimating the experimental ones about 50%. In [84] experimental data for D_2 are also reported. In Fig. 4.7 the results obtained from the Holway kinetic model with $\beta = 0.01$, $\alpha = 0.479$, $j = 2$, Pr $= 0.66$, $\omega = 0.67$ [84, 134] are compared with the corresponding experimental data in [84] for D_2. Very good agreement is observed in a wide range of the rarefaction parameter δ_B between simulations and experiments. In the same comparison the numerical results obtained with $\alpha = 1$ are shown for completeness purposes. For small values of the rarefaction parameter δ_B the total heat flux with $\alpha = 1$ is about two times higher than the corresponding one with $\alpha = 0.479$.

Next, a comparison with the experimental data in [80] is also performed in Fig. 4.8, in dimensional form. Now, the inner diameter is $R_A = 75$ μm, the radius ratio $\gamma = 1/667$, the temperature of the outer cylinder $T_B = 298$ K and the temperature difference ΔT ($\beta = 0.336$). The computational total heat fluxes, based on the DSMC method and the Rykov model, with $Z = 3$, are in very good agreement with the experimental ones, while once again the heat fluxes based on the Shakhov model for monatomic gases are significantly smaller than the experimental ones. As it is seen the comparison is in a wide range of the reference pressure $\hat{P}_B$ varying from 1 Pa up to 10^3 Pa, with the corresponding gas rarefaction parameter δ_B varying from 6 up to 2600. It is noted that as δ_B is increased the computational results tend to the analytical ones obtained by Eq. (C.21). Overall, the comparison studies in Figs. 4.6, 4.7 and 4.8 with the experimental data in [84] and [80] respectively, validate the simulation results.

In order to obtain a more physical understanding of the heat transfer in monatomic and polyatomic gases and to facilitate comparisons with experiments, in Fig. 4.9, some dimensional total heat fluxes [W/m^2] in terms of the reference pressure $\hat{P}_B$ [Pa] are given for the monatomic gases of He and Ar, the diatomic gases of H_2 and N_2 and for the polyatomic gas of CO_2. The inner diameter is $R_A = 1$ cm with $\gamma = [1/2, 1/10]$, while the reference temperature is $T_B = 293$ K with $\beta = [0.1, 1]$. The reference pressure $\hat{P}_B \in [10^{-3}, 10]$ Pa and is easily connected to the rarefaction parameter δ_B, via Eq. (4.3) once the viscosity and the most probable velocity of each gas is specified. All computations are based on the Holway model with $Z = 3$ and the IPL model ($\omega = [0.66, 0.81, 0.67, 0.74, 0.93]$ for He, Ar, H_2, N_2, CO_2 respectively). In all cases, as expected, the heat flux is monotonically increased with pressure. At highly rarefied atmospheres the heat flux is proportional to gas pressure, then, in the transition regime the relation becomes more complex and at dense atmospheres the heat flux depends weakly and finally is independent of pressure. Also, the heat fluxes for $\beta = 1$ are about one order magnitude higher than the corresponding ones for $\beta = 0.1$, while the effect of γ is not that important with the heat fluxes being slightly decreased as the gap between the cylinders is increased.

More importantly, it is observed in Fig. 4.9, that under the same conditions the heat flux of different gases varies significantly. The largest heat fluxes are achieved for H_2 followed successively by the heat fluxes of He, N_2, CO_2 and Ar. This trend is valid in the whole range of

pressure except for the curves of CO_2 and Ar, which cross each other at some relatively large pressure $\hat{P}_B > 1$Pa. It is well known that in heat transfer through monatomic gases confined between coaxial cylinders, the dimensional heat flux is increased as the molar mass of the gas is decreased (see Fig. 9 in [89]). However, this remark cannot be generalized in the case of polyatomic gases since, as seen in Fig. 4.9, in a wide range of pressure the heat flux of CO_2 is larger than that of Ar, while its molar mass is larger.

4.5 Concluding remarks

The problem of heat transfer through rarefied polyatomic gases confined between two coaxial cylindrical surfaces maintained at different temperatures is solved based on the Holway and Rykov kinetic models. The quantitative behavior of the radial heat flux is examined in a wide range of the gas rarefaction parameter, small, moderate and large normalized temperature differences and various radius ratios. The deduced density and temperature (translational, rotational, total) distributions are also provided. The results obtained by the two kinetic models are in good agreement, with the Rykov model being more sensitive, compared to the Holway model, in the variation of the mixing parameter indicating the strength of translational-rotational coupling. Very good agreement between the Holway model and DSMC results for HS molecules has also been observed. In addition, the computational results match perfectly the analytical ones in the free molecular and continuum limits. These findings along with the successful comparison between simulations and available experimental data for polyatomic gases associated to small and large temperature differences demonstrate the validity of the implemented modeling approaches.

The translational and rotational as well as the total temperatures are very close to each other for all parameters examined here and they are similar to the corresponding monatomic ones. In contrary, the total heat fluxes for polyatomic gases are significantly higher than those for monatomic gases. More specifically, the heat fluxes of diatomic and polyatomic gases, obtained by the Holway model, are higher about $36 - 50\%$ and $58 - 75\%$ respectively than the corresponding ones obtained by the Shakhov model, with the highest differences occurring in the free molecular limit. As the amount of elastic compared to inelastic collisions is increased,

the translational heat fluxes are increased and they tend to the monatomic ones, while always the rotational heat fluxes are about 50% and 75% of the translational ones for diatomic and polyatomic gases respectively. Furthermore, it has been found that the simple expression in Eq. (4.30), proposed in [98], provides reasonably accurate results in a wide range of parameters, while another observation of practical interest is that, while in monatomic the dimensional heat flux is increased as the molar mass is decreased, this is not necessarily the case in polyatomic gases.

Overall, it may be stated that the implementation of the Holway model is more flexible to polyatomic gases, while the Rykov model, although seems to be more accurate, is limited to additional experimental data for the specific gas under consideration. It is hoped that the present work may be useful in engineering purposes as well as in comparisons with experimental results.

Table 4.1: Heat fluxes at the inner hot cylinder ($r = \gamma$) with $\gamma = 1/2$ for N$_2$ ($\omega = 0.74$, $j = 2$, Pr = 0.71) based on the Holway and Rykov models.

β	δ_B	$Z = 1$				$Z = 5$				q
		q_{tr}		q_{rot}		q_{tr}		q_{rot}		
		Rykov	Holway	Rykov	Holway	Rykov	Holway	Rykov	Holway	Shakhov
0.1	0	5.64(-2)	5.64(-2)	2.82(-2)	2.82(-2)	5.64(-2)	5.64(-2)	2.82(-2)	2.82(-2)	5.64(-2)
	0.1	5.57(-2)	5.58(-2)	2.78(-2)	2.79(-2)	5.58(-2)	5.58(-2)	2.79(-2)	2.79(-2)	5.59(-2)
	1	4.97(-2)	5.10(-2)	2.46(-2)	2.52(-2)	5.12(-2)	5.11(-2)	2.54(-2)	2.52(-2)	5.15(-2)
	4	3.65(-2)	3.96(-2)	1.75(-2)	1.90(-2)	3.98(-2)	3.97(-2)	1.92(-2)	1.89(-2)	4.08(-2)
	10	2.37(-2)	2.72(-2)	1.11(-2)	1.27(-2)	2.75(-2)	2.74(-2)	1.28(-2)	1.25(-2)	2.87(-2)
1	0	5.64(-1)	5.64(-1)	2.82(-1)	2.82(-1)	5.64(-1)	5.64(-1)	2.82(-1)	2.82(-1)	5.64(-1)
	0.1	5.57(-1)	5.58(-1)	2.78(-1)	2.79(-1)	5.59(-1)	5.58(-1)	2.79(-1)	2.79(-1)	5.60(-1)
	1	4.98(-1)	5.11(-1)	2.47(-1)	2.53(-1)	5.14(-1)	5.11(-1)	2.56(-1)	2.53(-1)	5.18(-1)
	4	3.73(-1)	4.01(-1)	1.81(-1)	1.94(-1)	4.05(-1)	4.02(-1)	1.97(-1)	1.93(-1)	4.15(-1)
	10	2.53(-1)	2.86(-1)	1.20(-1)	1.35(-1)	2.90(-1)	2.88(-1)	1.37(-1)	1.34(-1)	3.02(-1)
10	0	5.64	5.64	2.82	2.82	5.64	5.64	2.82	2.82	5.64
	0.1	5.57	5.58	2.79	2.79	5.61	5.58	2.81	2.79	5.62
	1	5.00	5.10	2.49	2.53	5.24	5.10	2.62	2.53	5.31
	4	3.86	4.08	1.91	2.00	4.25	4.08	2.11	2.00	4.37
	10	2.86	3.10	1.40	1.51	3.24	3.11	1.59	1.50	3.37

Table 4.2: Heat fluxes at the inner hot cylinder ($r = \gamma$) with ($\gamma = 1/2$) for N_2 ($\omega = 0.74$, $j = 2$, $Pr = 0.91$) based on the Holway and Rykov models.

| β | δ_B | $Z = 1$ | | | |
| | | q_{tr} | | q_{rot} | |
		Rykov	Holway	Rykov	Holway
0.1	0	5.64(-2)	5.64(-2)	2.82(-2)	2.82(-2)
	0.1	5.57(-2)	5.57(-2)	2.78(-2)	2.78(-2)
	1	4.97(-2)	4.97(-2)	2.46(-2)	2.44(-2)
	4	3.65(-2)	3.65(-2)	1.75(-2)	1.74(-2)
	10	2.37(-2)	2.38(-2)	1.11(-2)	1.10(-2)
1	0	5.64(-1)	5.64(-1)	2.82(-1)	2.82(-1)
	0.1	5.57(-1)	5.57(-1)	2.78(-1)	2.78(-1)
	1	4.98(-1)	4.98(-1)	2.47(-1)	2.46(-1)
	4	3.73(-1)	3.73(-1)	1.81(-1)	1.79(-1))
	10	2.53(-1)	2.54(-1)	1.20(-1)	1.19(-1)
10	0	5.64	5.64	2.82	2.82
	0.1	5.57	5.56	2.79	2.78
	1	5.00	4.97	2.49	2.47
	4	3.86	3.83	1.91	1.88
	10	2.86	2.84	1.40	1.37

Table 4.3: Heat fluxes at the inner hot cylinder ($r = \gamma$) with $\gamma = 1/2$ for a diatomic gas ($j = 2$, $\mathrm{Pr} = 0.71$) with HS molecules, based on the Holway model and the DSMC method.

| β | δ_0 | $Z = 1$ | | | | $Z = 5$ | | | | q |
| | | q_{tr} | | q_{rot} | | q_{tr} | | q_{rot} | | |
		Holway	DSMC	Holway	DSMC	Holway	DSMC	Holway	DSMC	Shakhov
0.1	0.2	5.59(-2)	5.61(-2)	2.79(-2)	2.80(-2)	5.59(-2)	5.62(-2)	2.79(-2)	2.79(-2)	5.61(-2)
	2	4.73(-2)	4.81(-2)	2.30(-2)	2.36(-2)	4.73(-2)	4.89(-2)	2.30(-2)	2.30(-2)	4.81(-2)
	8	3.08(-2)	3.09(-2)	1.44(-2)	1.49(-2)	3.09(-2)	3.26(-2)	1.42(-2)	1.40(-2)	3.23(-2)
	20	1.79(-2)	1.76(-2)	8.18(-3)	8.30(-3)	1.81(-2)	1.89(-2)	8.03(-3)	7.76(-3)	1.93(-2)
1	0.2	5.98(-1)	6.01(-1)	2.98(-1)	3.00(-1)	5.98(-1)	6.02(-1)	2.98(-1)	2.99(-1)	6.01(-1)
	2	5.16(-1)	5.26(-1)	2.52(-1)	2.59(-1)	5.17(-1)	5.35(-1)	2.52(-1)	2.53(-1)	5.30(-1)
	8	3.42(-1)	3.45(-1)	1.61(-1)	1.66(-1)	3.44(-1)	3.62(-1)	1.59(-1)	1.57(-1)	3.60(-1)
	20	2.03(-1)	2.01(-1)	9.35(-2)	9.53(-2)	2.05(-1)	2.14(-1)	9.18(-2)	8.94(-2)	2.18(-1)
10	0.2	6.85	6.85	3.42	3.42	6.85	6.85	3.42	3.41	7.00
	2	6.48	6.64	3.19	3.26	6.48	6.65	3.17	3.17	6.99
	8	4.85	4.94	2.32	2.38	4.86	5.06	2.29	2.24	5.27
	20	3.26	3.27	1.53	1.56	3.29	3.43	1.50	1.46	3.54

Table 4.4: Heat fluxes at the inner hot cylinder ($r = \gamma$) for a diatomic gas ($j = 2$, Pr = 0.71) with HS molecules.

γ	β	δ_B	Holway ($Z = 3$)			Shakhov
			q_{tr}	q_{rot}	q	q
1/2	0.1	0	5.64(-2)	2.82(-2)	8.46(-2)	5.64(-2)
		0.1	5.58(-2)	2.79(-2)	8.37(-2)	5.59(-2)
		1	5.10(-2)	2.51(-2)	7.62(-2)	5.15(-2)
		4	3.95(-2)	1.88(-2)	5.84(-2)	4.07(-2)
		10	2.72(-2)	1.25(-2)	3.97(-2)	2.86(-2)
	1	0	5.64(-1)	2.82(-1)	8.46(-1)	5.64(-1)
		0.1	5.58(-1)	2.79(-1)	8.37(-1)	5.59(-1)
		1	5.09(-1)	2.51(-1)	7.60(-1)	5.15(-1)
		4	3.95(-1)	1.90(-1)	5.84(-1)	4.08(-1)
		10	2.77(-1)	1.29(-1)	4.06(-1)	2.91(-1)
	10	0	5.64	2.82	8.46	5.64
		0.1	5.57	2.78	8.35	5.62
		1	4.99	2.48	7.47	5.22
		4	3.84	1.87	5.71	4.11
		10	2.81	1.35	4.15	3.04
1/10	0.1	0	5.64(-2)	2.82(-2)	8.46(-2)	5.64(-2)
		0.1	5.61(-2)	2.80(-2)	8.41(-2)	5.61(-2)
		1	5.32(-2)	2.64(-2)	7.96(-2)	5.38(-2)
		4	4.51(-2)	2.19(-2)	6.70(-2)	4.66(-2)
		10	3.41(-2)	1.62(-2)	5.04(-2)	3.62(-2)
	1	0	5.64(-1)	2.82(-1)	8.46(-1)	5.64(-1)
		0.1	5.61(-1)	2.80(-1)	8.41(-1)	5.62(-1)
		1	5.30(-1)	2.63(-1)	7.93(-1)	5.39(-1)
		4	4.45(-1)	2.17(-1)	6.62(-1)	4.63(-1)
		10	3.37(-1)	1.61(-1)	4.98(-1)	3.57(-1)
	10	0	5.64	2.82	8.46	5.64
		0.1	5.60	2.80	8.40	5.66
		1	5.22	2.60	7.82	5.61
		4	4.21	2.08	6.29	4.70
		10	3.17	1.55	4.72	3.50
1/65	0.1	0	5.64(-2)	2.82(-2)	8.46(-2)	5.64(-2)
		0.1	5.63(-2)	2.82(-2)	8.45(-2)	5.63(-2)
		1	5.55(-2)	2.77(-2)	8.32(-2)	5.57(-2)
		4	5.29(-2)	2.62(-2)	7.91(-2)	5.35(-2)
		10	4.80(-2)	2.36(-2)	7.17(-2)	4.94(-2)
	1	0	5.64(-1)	2.82(-1)	8.46(-1)	5.64(-1)
		0.1	5.63(-1)	2.82(-1)	8.45(-1)	5.64(-1)
		1	5.55(-1)	2.77(-1)	8.31(-1)	5.58(-1)
		4	5.25(-1)	2.60(-1)	7.85(-1)	5.34(-1)
		10	4.70(-1)	2.32(-1)	7.02(-1)	4.87(-1)
	10	0	5.64	2.82	8.46	5.64
		0.1	5.63	2.82	8.45	5.65
		1	5.52	2.76	8.27	5.70
		4	5.07	2.52	7.59	5.50
		10	4.32	2.14	6.47	4.75

Table 4.5: Heat fluxes at the inner hot cylinder ($r = \gamma$) with $\gamma = 1/2$ for a polyatomic gas ($j = 3$, Pr = 0.71) with HS molecules based on the Holway model.

β	δ_B	$Z = 1$			$Z = 5$		
		q_{tr}	q_{rot}	q	q_{tr}	q_{rot}	q
0.1	0	5.64(-2)	4.23(-2)	9.87(-2)	5.64(-2)	4.23(-2)	9.87(-2)
	0.1	5.58(-2)	4.18(-2)	9.76(-2)	5.58(-2)	4.18(-2)	9.76(-2)
	1	5.10(-2)	3.77(-2)	8.87(-2)	5.10(-2)	3.77(-2)	8.87(-2)
	4	3.94(-2)	2.83(-2)	6.77(-2)	3.96(-2)	2.82(-2)	6.78(-2)
	10	2.70(-2)	1.88(-2)	4.58(-2)	2.72(-2)	1.86(-2)	4.58(-2)
1	0	5.64(-1)	4.23(-1)	9.87(-1)	5.64(-1)	4.23(-1)	9.87(-1)
	0.1	5.58(-1)	4.18(-1)	9.76(-1)	5.58(-1)	4.18(-1)	9.76(-1)
	1	5.08(-1)	3.77(-1)	8.86(-1)	5.09(-1)	3.77(-1)	8.86(-1)
	4	3.94(-1)	2.85(-1)	6.79(-1)	3.95(-1)	2.84(-1)	6.79(-1)
	10	2.76(-1)	1.94(-1)	4.70(-1)	2.77(-1)	1.92(-1)	4.69(-1)
10	0	5.64	4.23	9.87	5.64	4.23	9.87
	0.1	5.57	4.17	9.74	5.57	4.17	9.74
	1	4.99	3.72	8.71	4.99	3.72	8.71
	4	3.82	2.82	6.64	3.84	2.81	6.65
	10	2.79	2.03	4.82	2.81	2.01	4.82
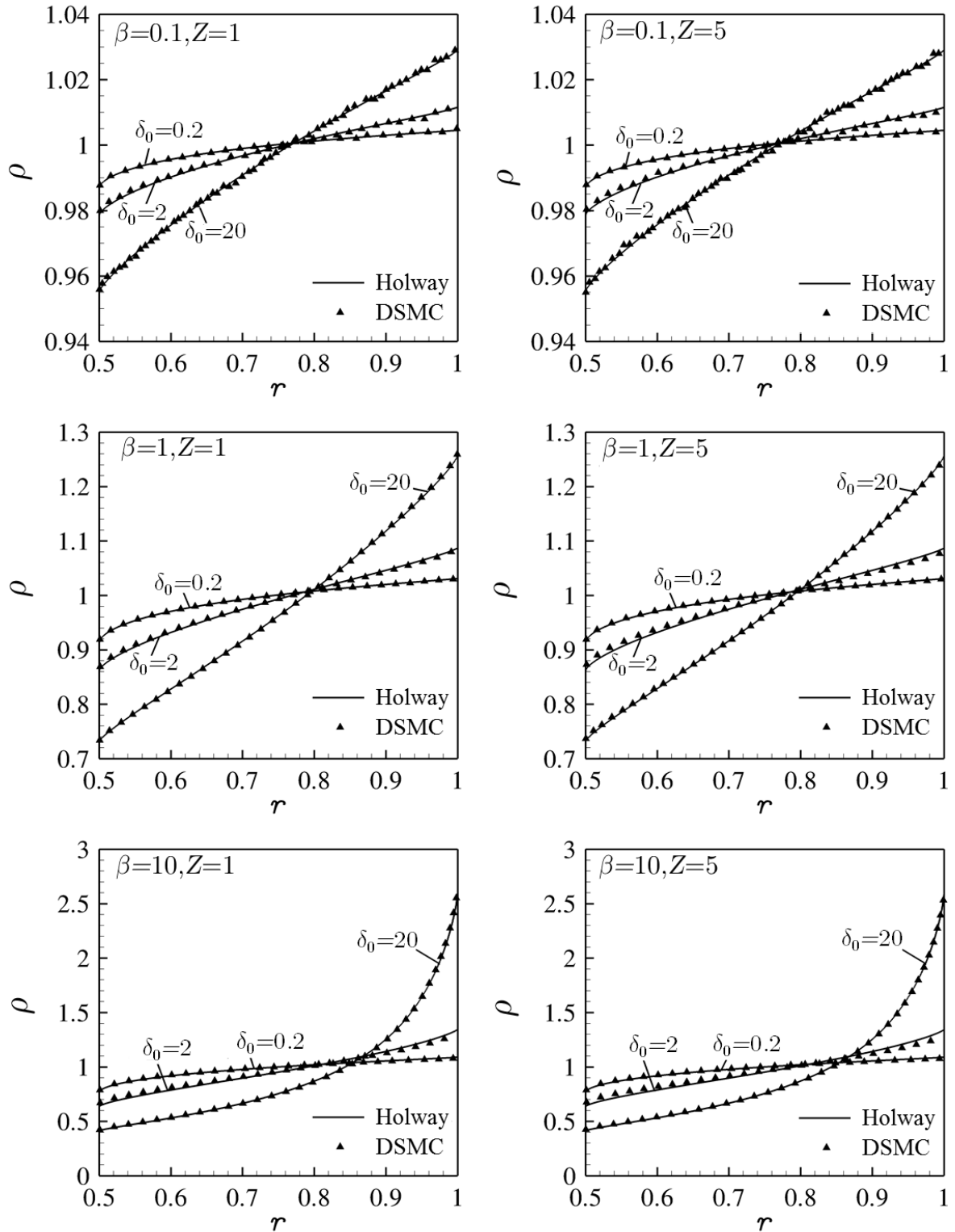
Figure 4.2: Dimensionless density distributions with $\gamma = 1/2$ for a diatomic gas ($j = 2$, Pr = 0.71) with HS molecules, based on the Holway model and the DSMC method.

94
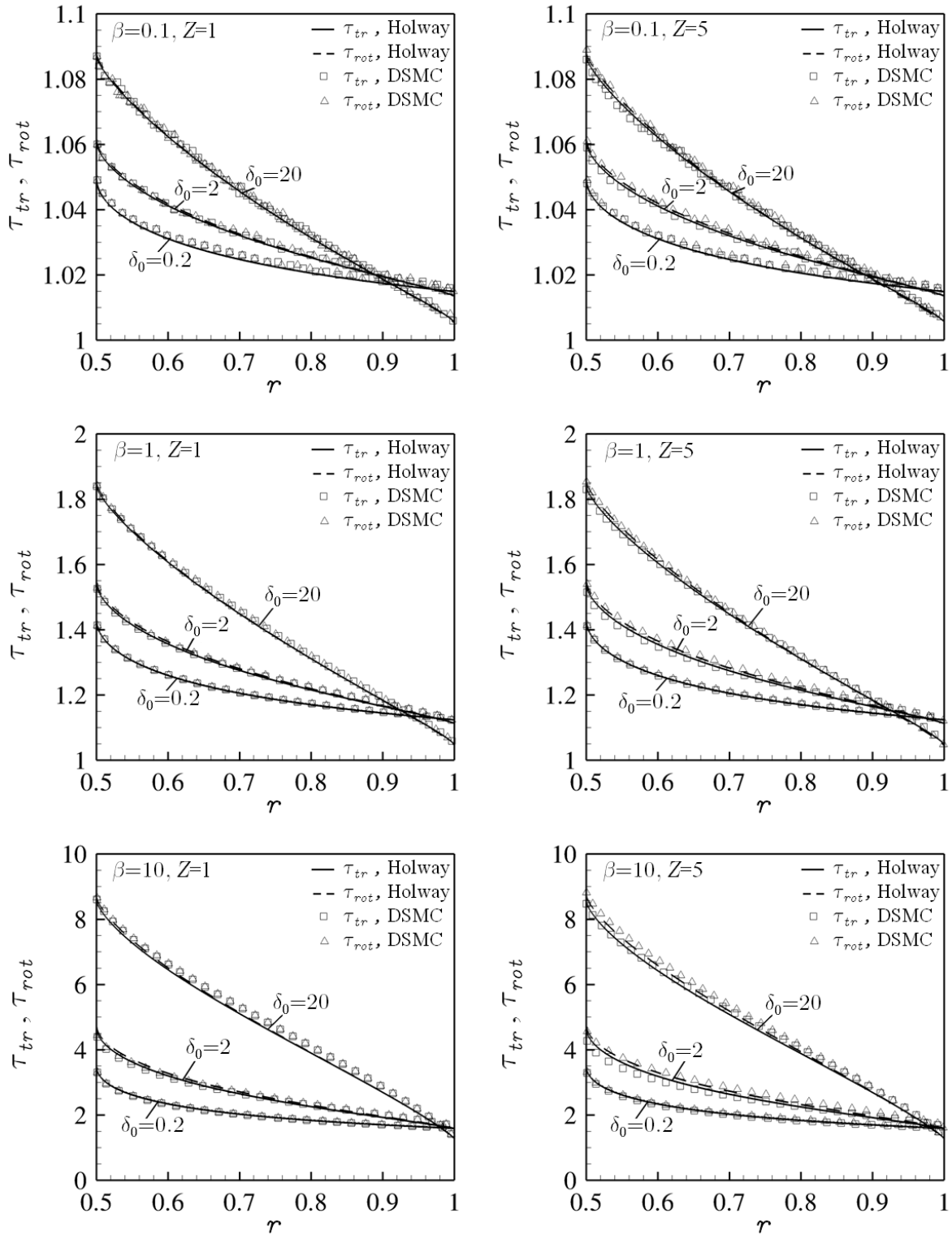
Figure 4.3: Dimensionless translational and rotational temperature distributions with $\gamma = 1/2$ for a diatomic gas ($j = 2$, $\mathrm{Pr} = 0.71$) with HS molecules, based on the Holway model and the DSMC method.

95
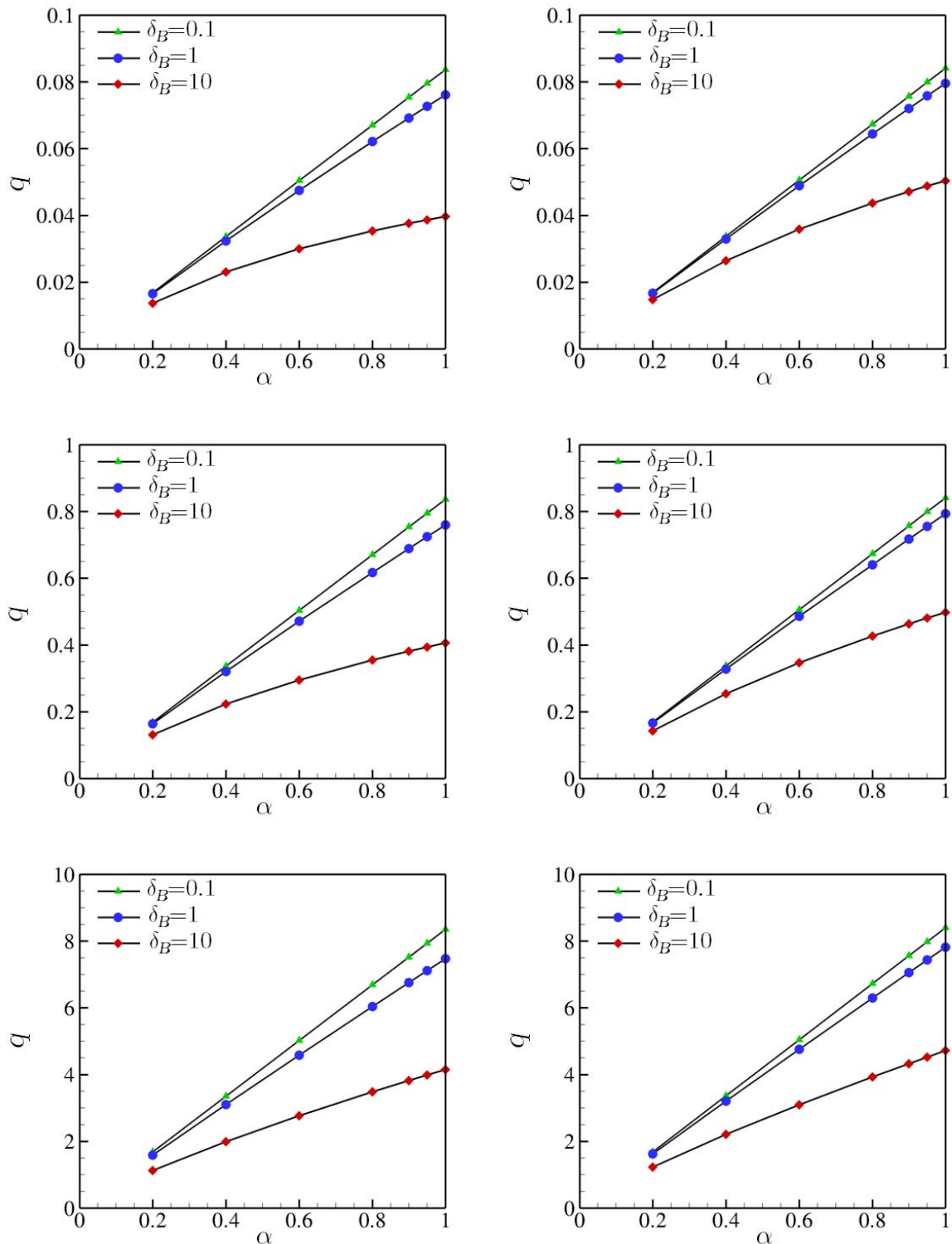
Figure 4.4: Dimensionless total heat flux q of a diatomic HS gas ($j = 2$, $\mathrm{Pr} = 0.71$, $Z = 5$) in terms of thermal accommodation coefficient α for various values of δ_B and $\beta = 0.1$ (up), $\beta = 1$ (middle), $\beta = 10$ (down) with $\gamma = 1/2$ (left) and $\gamma = 1/10$ (right) based on the Holway model.

96
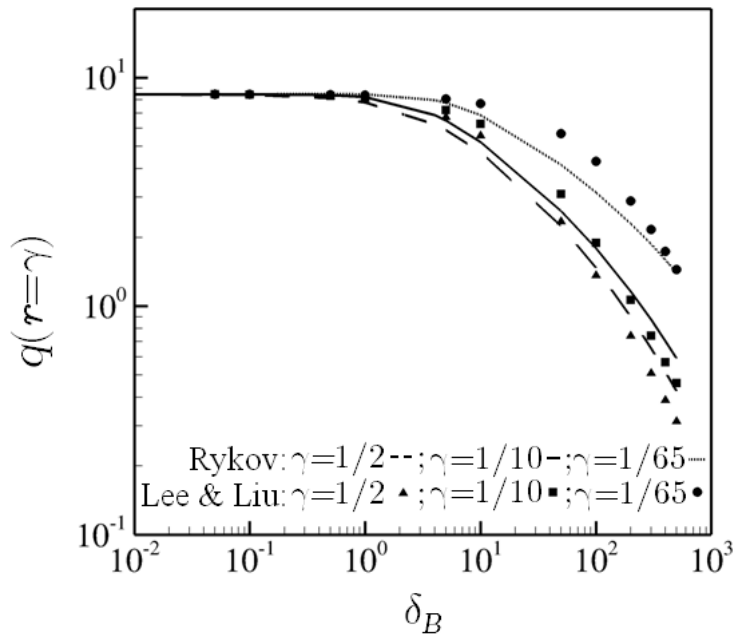
Figure 4.5: Comparison of the radial heat flux at the inner hot cylinder $q\,(r = \gamma)$ for N_2 and $\beta = 10$ with corresponding results of Eq. (4.30).
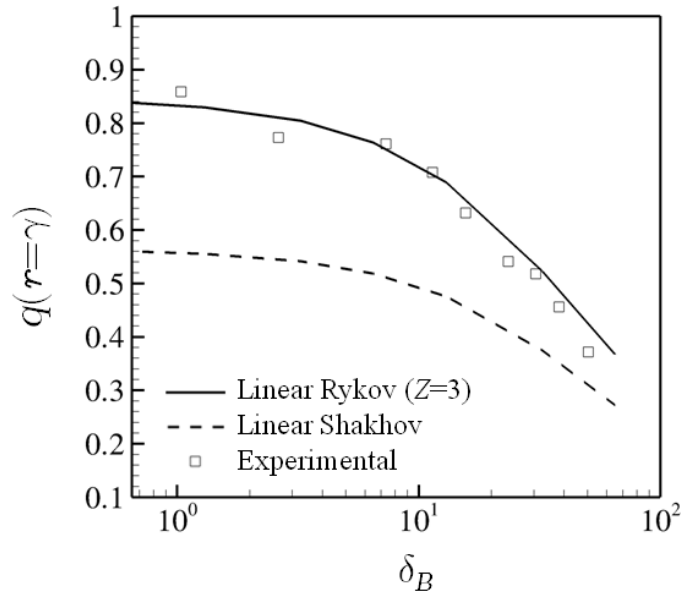
Figure 4.6: Comparison between computational and experimental [84] dimensionless heat fluxes $q(r = \gamma)$ for N_2 confined between two cylinders with $R_A = 100$ μm, $\gamma = 1/65$ and maintained at a very small temperature difference with $T_B = 300$ K.
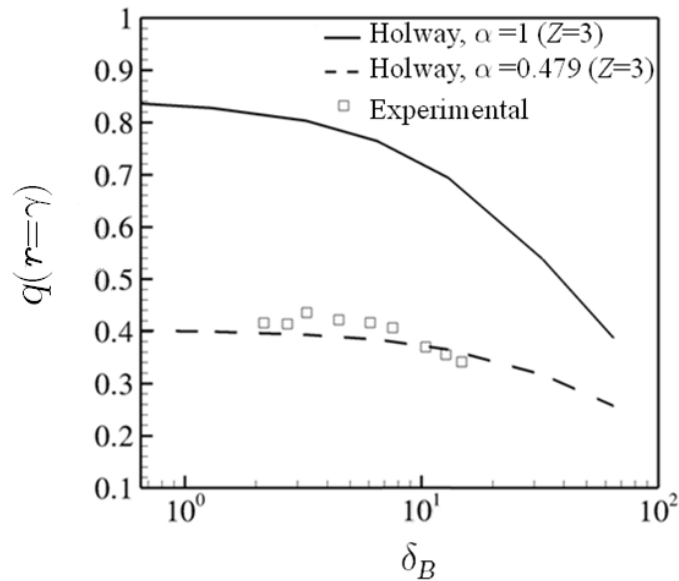
Figure 4.7: Comparison between computational and experimental [84] dimensionless heat fluxes $q(r = \gamma)$ for D_2 confined between two cylinders with $R_A = 100$ μm, $\gamma = 1/65$ and maintained at a very small temperature difference with $T_B = 300$ K.

98
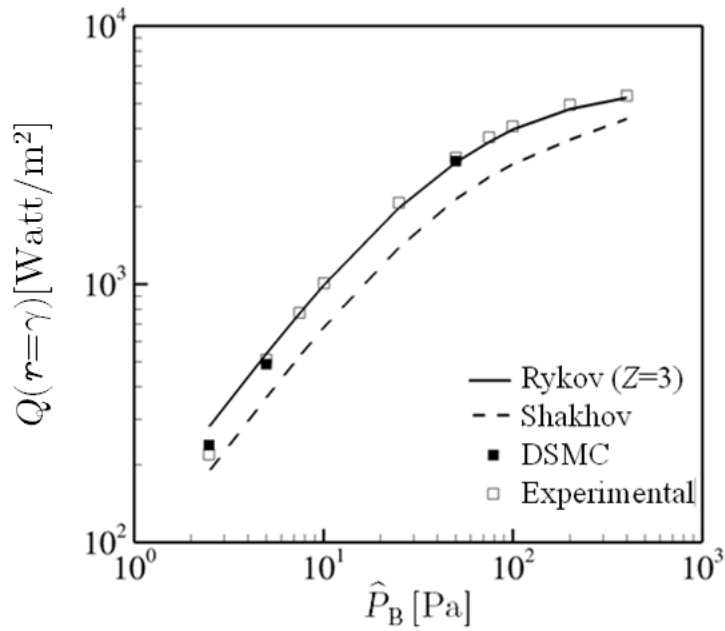
Figure 4.8: Comparison between computational and experimental [80] dimensional heat fluxes $Q\left(r=\gamma\right)$ for N_2 and air respectively, confined between two cylinders with $R_A = 75\ \mu$m, $\gamma = 1/667$ and maintained at a temperature difference of $\Delta T = 100$ K, with $T_B = 298$ K.
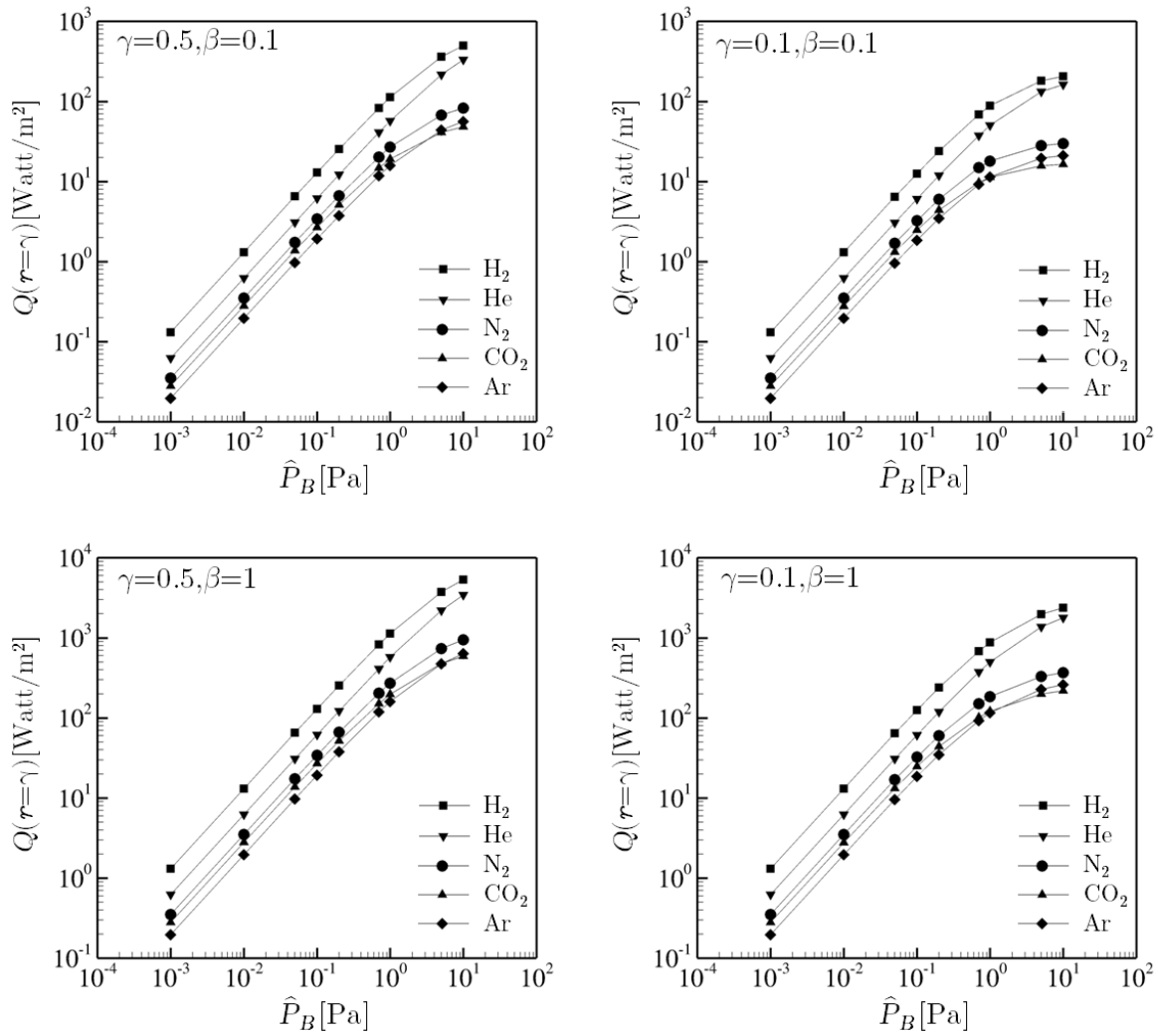
Figure 4.9: Dimensional heat flux $Q\,(r = \gamma)$ through various gases enclosed between two cylinders with $R_A = 1$ cm and $\gamma = [1/2, 1/10]$, maintained at $T_B = 293$ K and $\beta = [0.1, 1]$, in terms of the reference pressure $\hat{P}_B$ obtained by the Holway model ($Z = 3$, IPL model).

Chapter 5

Effects of vibrational degrees of freedom on the heat transfer in polyatomic gases confined between parallel plates

5.1 Properties of polyatomic gases

In general, it is advisable to consider vibrational excitation when the problem characteristic temperature exceeds $25-30\%$ of the gas characteristic vibrational temperature which varies significantly for each gas. For instance, for O_2 and N_2 the characteristic vibrational temperatures are 2256 K and 3371 K respectively, whereas for CO_2 and SF_6 the lowest ones are 960 K and 520 K respectively [19, 135].

Polyatomic gases with relatively low and moderate characteristic vibrational temperatures are very common in several industrial processes and technological applications running in a wide range of operating temperatures. A typical example of low excitation temperature gases is SF_6, which is used in the electronics industry (plasma etching and chemical vapor deposition), in the magnesium production (die casting), in the fusion technology (as insulating gas into neutral beam injector high voltage towers and transmission lines) and in other applications including

101

gas-air tracing, leak detection, soundproof windows, etc. [136–138]. Other gases with moderate excitation temperatures may be involved in piezoelectric sensing technologies [139] for use at high temperatures (> 800 °C), in the automotive industry and in micro-electro-mechanical systems for aeronautics and space applications (e.g. micro rocket engines) [140], as well as in natural and environmental processes. Modeling of these processes should include the effect of the excited vibrational modes, if agreement between measurements and calculations is to be obtained.

Here, the same simple heat transfer configuration as in Chapter 3 is considered taking into account however the vibrational degrees of freedom. The whole approach is based on the Holway kinetic model [20]. The translational, rotational, vibrational and total temperature distributions and the corresponding heat fluxes are presented for a wide range of the involved parameters. Comparisons between the simulations based on the Holway kinetic model and the DSMC method [173] as well as between simulations and experimental data [141] are shown and discussed. The influence of the vibrational degrees of freedom on the heat fluxes for CO_2, CH_4 and SF_6 at low reference temperatures is investigated, while corresponding high temperature calculations with N_2 and O_2 are mainly performed for model testing and results validation. The properties including the characteristic vibrational temperatures of all gases examined here are given in Table 5.1. Furthermore, thermal conductivities predicted by the considered gas models have been estimated exploiting the good agreement between the kinetic solutions and their hydrodynamic (Chapman-Enskog) approximations, which occurs for moderately high values of the rarefaction parameter, in a central strip of the domain [142, 143].

Table 5.1: Properties of working gases (in the 3$^{\text{rd}}$ column the numbers in parenthesis indicate degeneracy)

Gas	Θ_v [K]	$m \times 10^{-26}$ [Kg]	μ_0 [μPa s]	ω	j
N$_2$	3371	4.65	61.40	0.69	
O$_2$	2256	5.31	72.51	0.66	2
CO$_2$	960(2)	7.31	62.01	0.7	
	1930(1)				
	3390(1)				
CH$_4$	1880(3)	2.66	41.12	0.68	
	2200(2)				
	4200(1)				
	4350(3)				
SF$_6$	520(3)	24.3	59.82	0.69	3
	760(3)				
	890(3)				
	930(2)				
	1120(1)				
	1390(3)				

5.2   Basic definitions

Consider the state of a stationary nonpolar polyatomic gas confined between two infinite parallel plates fixed at $\hat{y} = \pm H/2$ and maintained at constant temperatures T_H and T_C respectively, with $T_H > T_C$. Then, due to temperature difference a conductive heat flow through the gas from the hot plate to the cold plate is induced.

The adopted models include translational, rotational and vibrational energy modes of the molecules assuming that the translational and the rotational energies are continuous, while the vibrational energy is discrete. The rotation and vibration of the gas molecules are described by the rigid rotator and quantum the harmonic oscillator models respectively. The rotational mode can be described as having a constant number of degrees of freedom at all temperatures which is $j = 2$ for linear molecules and $j = 3$ for non-linear molecules.

On the contrary, the effective number of vibrational degrees of freedom varies with temperature. For the simple quantum harmonic oscillator assumed here they are defined as [29]

$$\zeta_v\left(T\right) = \frac{2}{T}\sum_{i=1}^{N}\frac{\Theta_{v,i}}{\exp\left(\Theta_{v,i}/T\right)-1}, \tag{5.1}$$

where N is the total number of vibrational modes given by $N = 3M - 5$ for linear molecules and $N = 3M - 6$ for nonlinear molecules with M being the number of atoms in the molecule. Also, $\Theta_{v,i}$ is the characteristic vibrational temperature of vibrational mode i given by

$$\Theta_{v,i} = \frac{\hbar\varpi_i}{k_B}, \tag{5.2}$$

where $\hbar = 1.05457 \times 10^{-34}$ J s is the reduced Planck constant, ϖ_i is the vibrational frequency of the gas molecules and $k_{\mathrm{B}} = 1.38065 \times 10^{-23}$ J/K is the Boltzmann constant. At very high temperature each vibrational mode is linked to 2 degrees of freedom, from which one describes the linear distance between the two atoms and the other describes the speed of vibration. In diatomic gases at high temperature $\zeta_v \to 2$, while in polyatomic gases ζ_v takes higher values depending on the specific gas and the applied temperature.

Depending on the accuracy desired level, the presence of the dissociation must be included when the characteristic temperature exceeds $3 - 6\%$ of the gas characteristic dissociation temperature. It is noted that for most of the diatomic gases at these temperatures the atom mass fraction is less than 10% [135]. For instance the dissociation temperatures of N_2 and O_2 are 113500 K and 59500 K respectively.

In the absence of dissociation the state of a polyatomic gas is determined by its distribution function $\hat{f}_S\left(\hat{y}, \boldsymbol{v}, \hat{I}\right)$, where $S = \{S_1, S_2, \ldots S_N\}$, with $S_i = 0, 1, 2, \ldots$, represents the vibrational quantum states, that depends on the space coordinate $\hat{y}$, the molecular translational velocity $\boldsymbol{v} = (\xi_x, \xi_y, \xi_z)$ and the energy of rotational motion $\hat{I}$ [20, 29]. Then, the macroscopic quantities of practical interest are obtained by the moments of $\hat{f}_S$ as [20, 144]

$$n\left(\hat{y}\right) = \sum_{S=0}^{\infty}\int_{-\infty}^{\infty}\int_{0}^{\infty}\hat{f}_S d\hat{I} d\boldsymbol{v}, \tag{5.3}$$

$$E_{tr}\left(\hat{y}\right) = \frac{3k_B T_{tr}\left(\hat{y}\right)}{2} = \frac{m}{2n}\sum_{S=0}^{\infty}\int_{-\infty}^{\infty}\int_{0}^{\infty}\upsilon^2\hat{f}_S d\hat{I}d\boldsymbol{v}, \tag{5.4}$$

$$E_{rot}\left(\hat{y}\right) = \frac{jk_B T_{rot}\left(\hat{y}\right)}{2} = \frac{1}{n}\sum_{S=0}^{\infty}\int_{-\infty}^{\infty}\int_{0}^{\infty}\hat{I}\hat{f}_S d\hat{I}d\boldsymbol{v}, \tag{5.5}$$

$$E_{vib}\left(\hat{y}\right) = \frac{\zeta_v\left(T_{vib}\left(\hat{y}\right)\right)k_B T_{vib}\left(\hat{y}\right)}{2} = \frac{1}{n}\sum_{S=0}^{\infty}\int_{-\infty}^{\infty}\int_{0}^{\infty}\left(\sum_{i=1}^{N}\hbar\varpi_i S_i\right)\hat{f}_S d\hat{I}d\boldsymbol{v}, \tag{5.6}$$

$$T_{tot}\left(\hat{y}\right) = \frac{3\,T_{tr}\left(\hat{y}\right) + j\,T_{rot}\left(\hat{y}\right) + \zeta_v\left(T_{vib}\left(\hat{y}\right)\right)T_{vib}\left(\hat{y}\right)}{3 + j + \zeta_v\left(T_{tot}\left(\hat{y}\right)\right)}, \tag{5.7}$$

$$Q_{tr}\left(\hat{y}\right) = \frac{m}{2}\sum_{S=0}^{\infty}\int_{-\infty}^{\infty}\int_{0}^{\infty}\xi_y\upsilon^2\hat{f}_S d\hat{I}d\boldsymbol{v}, \tag{5.8}$$

$$Q_{rot}\left(\hat{y}\right) = \sum_{S=0}^{\infty}\int_{-\infty}^{\infty}\int_{0}^{\infty}\xi_y\hat{I}\hat{f}_S d\hat{I}d\boldsymbol{v}, \tag{5.9}$$

$$Q_{vib}\left(\hat{y}\right) = \sum_{S=0}^{\infty}\int_{-\infty}^{\infty}\int_{0}^{\infty}\xi_y\left(\sum_{i=1}^{N}\hbar\varpi_i S_i\right)\hat{f}_S d\hat{I}d\boldsymbol{v}, \tag{5.10}$$

$$Q_{tot}\left(\hat{y}\right) = Q_{tr}\left(\hat{y}\right) + Q_{rot}\left(\hat{y}\right) + Q_{vib}\left(\hat{y}\right). \tag{5.11}$$

In Eqs. (5.3)-(5.11), $n\left(\hat{y}\right)$ is the number density, $E_{tr}\left(\hat{y}\right)$, $E_{rot}\left(\hat{y}\right)$, $E_{vib}\left(\hat{y}\right)$ are the mean particle energies and $Q_{tr}\left(\hat{y}\right)$, $Q_{rot}\left(\hat{y}\right)$, $Q_{vib}\left(\hat{y}\right)$ are the heat fluxes related to the translational, rotational and vibrational motion of the molecules respectively, with $T_{tr}\left(\hat{y}\right)$, $T_{rot}\left(\hat{y}\right)$, $T_{vib}\left(\hat{y}\right)$ denoting the corresponding temperatures. Also $T_{tot}\left(\hat{y}\right)$ is the total temperature and $Q_{tot}\left(\hat{y}\right)$ is the total heat flux of all degrees of freedom.

The problem in dimensionless form is prescribed by the ratio of the high over the low plate temperatures

$$\beta = \frac{T_H}{T_C} \tag{5.12}$$

and the reference gas rarefaction parameter

$$\delta_0 = \frac{\hat{P}_0 H}{\mu_0 \upsilon_0}, \tag{5.13}$$

where μ_0 is the gas viscosity at reference temperature $T_0 = (T_H + T_C)/2$, $\hat{P}_0 = n_0 k_B T_0$ is the reference pressure and $\upsilon_0 = \sqrt{2k_B T_0/m}$, with m denoting the molecular mass, is the most probable molecular speed at T_0. The reference number density n_0 is given by Eq. (3.11). The cases of $\delta_0 = 0$ and $\delta_0 \to \infty$ correspond to the free molecular and hydrodynamic limits respectively. In addition, the dimensionless vibrational temperatures

$$\theta_{v,i} = \frac{\Theta_{v,i}}{T_0}, \tag{5.14}$$

depending upon the working gas under consideration, are specified.

The effect of all involved parameters on the heat transfer problem is investigated focusing of course on the effect of $\theta_{v,i}$ since it is the parameter which characterizes the importance of the vibrational degrees of freedom. This is achieved via the Holway kinetic model described in Section 5.3.

5.3 Holway kinetic model with vibrational degrees of freedom

As it has been shown in Chapter 3 the Holway kinetic model has been applied with considerable success in the present heat transfer configuration providing good agreement with the DSMC method and the experimental data. Since here a purely heat transfer configuration is investigated the collision frequency has been set to properly recover the thermal conductivity coefficient and for the present heat transfer configuration the Holway model taking into consideration the translational, rotational and vibrational degrees of freedom can be written as

$$\xi_y \frac{\partial \hat{f}_S}{\partial \hat{y}} = \hat{\nu}_{tot} \left[\left(1 - \frac{1}{Z_r} - \frac{1}{Z_v} \right) \left(\hat{f}_S^{(t)} - \hat{f}_S \right) + \frac{1}{Z_r} \left(\hat{f}_S^{(t,r)} - \hat{f}_S \right) + \frac{1}{Z_v} \left(\hat{f}_S^{(t,r,v)} - \hat{f}_S \right) \right], \tag{5.15}$$

where

$$\hat{f}_S^{(t)} = n_S(\hat{I}|\hat{y})\left(\frac{m}{2\pi k_B T_{tr}}\right)^{3/2} \exp\left(-\frac{m\upsilon^2}{2k_B T_{tr}}\right),$$

$$\hat{f}_S^{(t,r)} = \hat{n}_S(\hat{y})\left(\frac{m}{2\pi k_B T^r}\right)^{3/2} \exp\left(-\frac{m\upsilon^2}{2k_B T^r}\right) \frac{\hat{I}^{j/2-1}}{(k_B T^r)^{j/2}\Gamma(j/2)} \exp\left(-\frac{\hat{I}}{k_B T^r}\right),$$

$$\hat{f}_S^{(t,r,v)} = n\left(\frac{m}{2\pi k_B T_{tot}}\right)^{3/2} \exp\left(-\frac{m\upsilon^2}{2k_B T_{tot}}\right) \frac{\hat{I}^{j/2-1}}{(k_B T_{tot})^{j/2}\Gamma(j/2)} \exp\left(-\frac{\hat{I}}{k_B T_{tot}}\right) \tag{5.16}$$

$$\times \prod_{i=1}^{N}\left[1 - \exp\left(-\frac{\hbar\varpi_i}{k_B T_{tot}}\right)\right] \exp\left(-\frac{\sum_{i=1}^{N}\hbar\varpi_i S_i}{k_B T_{tot}}\right).$$

Here, $\hat{\nu}_{tot} = [\Pr(T_{tr})nk_B T_{tr}]/\mu(T_{tr})$ is the total collision frequency where $\Pr(T_{tr})$ is the Prandtl number and $\mu(T_{tr})$ is the viscosity both depending on the translational temperature. The parameters $1 \leq Z_r, Z_v < \infty$ define how many collisions occur per single rotational and vibrational collisions respectively. It is noted that Z_r, Z_v must be chosen in such a way that the rotational and vibrational relaxations governed by the Holway model match the corresponding relaxations obtained by the DSMC method when these approaches are compared. This task is performed in Appendix A. Also n is the total number density defined by Eq. (5.3), $\hat{n}_S$ is the total number density in vibrational state S and n_S is the number density of molecules having rotational energy $\hat{I}$ in vibrational state S. Finally, $T^r(\hat{y})$ is the common temperature of the rotational and translational modes given by $T^r(\hat{y}) = [3T_{tr}(\hat{y}) + jT_{rot}(\hat{y})]/(3+j)$.

In order to reduce the computational cost the following three reduced density distributions one for the mass and two for the internal energy (rotational and vibrational) are introduced

$$\hat{g} = \sum_{S=0}^{\infty}\int_0^{\infty}\hat{f}_S d\hat{I}, \quad \hat{h} = \sum_{S=0}^{\infty}\int_0^{\infty}\hat{I}\,\hat{f}_S d\hat{I}, \quad \hat{w} = \sum_{S=0}^{\infty}\int_0^{\infty}\left(\sum_{i=1}^{N}\hbar\varpi_i S_i\right)\hat{f}_S d\hat{I}. \tag{5.17}$$

For the specific problem under consideration the computational effort is further reduced by eliminating the ξ_x and ξ_z components of the molecular velocity by introducing the reduced

107

distributions

$$\hat{F} = \int\limits_{-\infty}^{\infty} \int\limits_{-\infty}^{\infty} \hat{g} \, d\xi_z d\xi_x, \quad \hat{G} = \int\limits_{-\infty}^{\infty} \int\limits_{-\infty}^{\infty} \hat{g} \, \left(\xi_z^2 + \xi_x^2\right) d\xi_z d\xi_x,$$

$$\hat{K} = \int\limits_{-\infty}^{\infty} \int\limits_{-\infty}^{\infty} \hat{h} \, d\xi_z d\xi_x, \quad \hat{L} = \int\limits_{-\infty}^{\infty} \int\limits_{-\infty}^{\infty} \hat{w} \, d\xi_z d\xi_x. \tag{5.18}$$

Operating accordingly with the appropriate summation and integral operators, defined by Eqs. (5.17) and (5.18), on Eq. (5.15) and introducing the following dimensionless quantities

$$y = \hat{y}/H, \quad \boldsymbol{c} = \boldsymbol{v}/v_0, \quad I = \hat{I}\big/ k_B T_0, \quad \rho = n/n_0,$$

$$F = v_0 \hat{F}\big/ n_0, \quad G = \hat{G}\big/ (n_0 v_0), \quad K = v_0 \hat{K}\big/ \hat{P}_0, \quad L = v_0 \hat{L}\big/ \hat{P}_0, \tag{5.19}$$

$$\tau_i = T_i/T_0, \quad q_i = Q_i\big/ \left(\hat{P}_0 v_0\right), \quad e_i = E_i/(k_B T_0),$$

where the subscript $i = tr$, rot, vib, tot refers to translational, rotational, vibrational or total quantities, the following system of kinetic equations may be obtained in vector form

$$c_y \frac{\partial \boldsymbol{\Psi}}{\partial y} = \nu_{tot} \left[\left(1 - \frac{1}{Z_r} - \frac{1}{Z_v}\right) \left(\boldsymbol{\Psi}^{(t)} - \boldsymbol{\Psi}\right) + \frac{1}{Z_r} \left(\boldsymbol{\Psi}^{(t,r)} - \boldsymbol{\Psi}\right) + \frac{1}{Z_v} \left(\boldsymbol{\Psi}^{(t,r,v)} - \boldsymbol{\Psi}\right) \right]. \tag{5.20}$$

Here, $\boldsymbol{\Psi} = [F, \ G, \ K, \ L]^T$ are the unknown reduced distributions, which depend on the dimensionless space and molecular velocity independent variables y and c_y. Also, δ_0 is the reference gas rarefaction given by Eq. (5.13) and $\nu_{tot} = \delta_0 \rho (\tau_{tr})^{1-\omega} \mathrm{Pr}\,(\tau_{tr})$ is the dimensionless collision frequency. The relaxing distributions in Eq. (5.20) are given by $\boldsymbol{\Psi}^{(i)} = \left[F^{(i)}, \ G^{(i)}, \ K^{(i)}, \ L^{(i)}\right]^T$, with $i = (t)$, (t,r), (t,r,v), where

$$F^{(t)} = \frac{\rho}{\sqrt{\pi \tau_{tr}}} \exp\left(-\frac{c_y^2}{\tau_{tr}}\right), \ F^{(t,r)} = \frac{\rho}{\sqrt{\pi \tau^r}} \exp\left(-\frac{c_y^2}{\tau^r}\right), \ F^{(t,r,v)} = \frac{\rho}{\sqrt{\pi \tau_{tot}}} \exp\left(-\frac{c_y^2}{\tau_{tot}}\right),$$

$$G^{(t)} = \tau_{tr} F^{(t)}, \quad G^{(t,r)} = \tau^r F^{(t,r)}, \quad G^{(t,r,v)} = \tau_{tot} F^{(t,r,v)},$$

$$K^{(t)} = \frac{j}{2}\tau_{rot}F^{(t)}, \quad K^{(t,r)} = \frac{j}{2}\tau^r F^{(t,r)}, \quad K^{(t,r,v)} = \frac{j}{2}\tau_{tot}F^{(t,r,v)},$$

$$L^{(t)} = \frac{\zeta_v\left(\tau_{vib}\right)}{2}\tau_{vib}F^{(t)}, \quad L^{(t,r)} = \frac{\zeta_v\left(\tau_{vib}\right)}{2}\tau_{vib}F^{(t,r)}, \quad L^{(t,r,v)} = \frac{\zeta_v\left(\tau_{tot}\right)}{2}\tau_{tot}F^{(t,r,v)}. \tag{5.21}$$

In the derivation of Eq. (5.20) the Inverse Power Law (IPL) interaction between particles has been introduced with the parameter ω taking the values of $1/2$ and 1 for hard sphere (HS) and Maxwell (MM) interactions respectively.

The same non-dimensionalization and projection procedures are applied to the moments in Eqs. (5.3)-(5.11), to find that the macroscopic quantities are given in terms of F, G, K and L according to

$$\rho = \int_{-\infty}^{\infty} F dc_y, \quad e_{tr} = \frac{3\,\tau_{tr}}{2} = \frac{1}{\rho}\int_{-\infty}^{\infty}\left(c_y^2 F + G\right)dc_y,$$

$$e_{rot} = \frac{j\,\tau_{rot}}{2} = \frac{1}{\rho}\int_{-\infty}^{\infty} K dc_y, \quad e_{vib} = \frac{\zeta_v\left(\tau_{vib}\right)\tau_{vib}}{2} = \frac{1}{\rho}\int_{-\infty}^{\infty} L dc_y,$$

$$q_{tr} = \int_{-\infty}^{\infty}\left(c_y^2 F + G\right)c_y dc_y, \quad q_{rot} = \int_{-\infty}^{\infty} K c_y dc_y, \quad q_{vib} = \int_{-\infty}^{\infty} L c_y dc_y, \tag{5.22}$$

$$q_{tot} = q_{vib} + q_{rot} + q_{tr}, \quad \tau^r = \frac{3\,\tau_{tr} + j\,\tau_{rot}}{3 + j}, \quad \tau_{tot} = \frac{3\,\tau_{tr} + j\,\tau_{rot} + \zeta_v\left(\tau_{vib}\right)\tau_{vib}}{3 + j + \zeta_v\left(\tau_{tot}\right)},$$

where

$$\zeta_v\left(\tau_{vib}\right) = \frac{2}{\tau_{vib}}\sum_{i=1}^{N}\frac{\theta_{v,i}}{\exp\left(\theta_{v,i}/\tau_{vib}\right) - 1} \quad \text{and} \quad \zeta_v\left(\tau_{tot}\right) = \frac{2}{\tau_{tot}}\sum_{i=1}^{N}\frac{\theta_{v,i}}{\exp\left(\theta_{v,i}/\tau_{tot}\right) - 1} \tag{5.23}$$

are the vibrational degrees of freedom in dimensionless temperatures τ_{vib} and τ_{rot} respectively. From Eq. (5.20) the energy conservation equation $\partial q_{tot}/\partial y = 0$ is readily reduced and it is implemented to benchmark the computations.

Next, the boundary conditions are defined. The typical purely diffuse boundary conditions are implemented where the distribution function of the particles departing by the two plates

109

takes the form [144]

$$\hat{f}_S^{(+)} = n_w \left(\frac{m}{2\pi k_B T_w} \right)^{3/2} \exp\left(-\frac{mv^2}{2k_B T_w} \right) \frac{\hat{I}^{j/2-1}}{(k_B T_w)^{j/2} \Gamma(j/2)} \exp\left(-\frac{\hat{I}}{k_B T_w} \right)$$

$$\times \prod_{i=1}^{N} \left[1 - \exp\left(-\frac{\hbar\varpi_i}{k_B T_w} \right) \right] \exp\left(-\frac{\sum_{i=1}^{N} \hbar\varpi_i S_i}{k_B T_w} \right). \quad (5.24)$$

The superscript $(+)$ denotes outgoing distributions, $T_w(\pm 1/2)$ is either the cold or the hot temperatures of the plates and $n_w(\pm 1/2)$ is a parameter specified by the condition of no penetration at the walls. Introducing in Eq. (5.24), the same normalization and projection as for the kinetic equations, lead to the outgoing distributions

$$F_{\pm 1/2}^{(+)} = \frac{\rho_{w,\pm 1/2}}{\sqrt{\pi\tau_w}} \exp\left(-\frac{c_y^2}{\tau_w} \right), \quad G_{\pm 1/2}^{(+)} = \frac{\rho_{w,\pm 1/2}\sqrt{\tau_w}}{\sqrt{\pi}} \exp\left(-\frac{c_y^2}{\tau_w} \right),$$

$$K_{\pm 1/2}^{(+)} = \frac{j\rho_{w,\pm 1/2}\sqrt{\tau_w}}{2\sqrt{\pi}} \exp\left(-\frac{c_y^2}{\tau_w} \right), \quad L_{\pm 1/2}^{(+)} = \frac{\zeta_v(\tau_w)\rho_{w,\pm 1/2}\sqrt{\tau_w}}{2\sqrt{\pi}} \exp\left(-\frac{c_y^2}{\tau_w} \right) \quad (5.25)$$

at $y = \pm 1/2$, where ρ_w is specified by applying the no penetration condition at the walls as

$$\rho_{w,\pm 1/2} = \frac{2\sqrt{\pi}}{\sqrt{\tau_w}} \int_0^\infty F_{\pm 1/2}^{(-)} c_y dc_y. \quad (5.26)$$

In Eqs. (5.25) and (5.26) the superscripts $(+)$ and $(-)$ denote outgoing and impinging distributions respectively. Also, $\tau_w = T_w/T_0$ in terms of the temperature ratio β is equal to $2\beta/(\beta+1)$ at $y = -1/2$ (hot wall) and $2/(\beta+1)$ at $y = 1/2$ (cold wall).

The governing equations (5.20) and (5.21) with the associated expressions (5.22) subject to boundary conditions (5.25)-(5.26) are solved numerically in an iterative manner. More specifically for prescribed values of β, δ_0 and $\theta_{v,i}$ the iteration map starts by assuming all needed macroscopic quantities. The kinetic equations (5.20)-(5.21) are solved numerically discretizing in the physical space by the control volume approach and in the molecular velocity space by the discrete velocity method to yield the reduced distributions F, G, K and L, which are introduced

110

into the moment equations (5.22) and (5.26). Integration is performed via the Gauss-Legendre quadrature to find the new estimates of all bulk quantities which are introduced in the next iteration. The iteration process is terminated when convergence criteria

$$\frac{1}{3K} \sum_{i=1}^{K} \left[\left| \rho_i^{(t+1)} - \rho_i^{(t)} \right| + \left| \tau_{tot,i}^{(t+1)} - \tau_{tot,i}^{(t)} \right| + \left| q_{tot,i}^{(t+1)} - q_{tot,i}^{(t)} \right| \right] < \varepsilon, \tag{5.27}$$

with t denoting the iteration index and K the number of nodes in the physical space, is fulfilled. The kinetic results presented here have been obtained with $\Delta y = 0.2 \times 10^{-3}$ and 96 molecular velocities being the roots of the corresponding Legendre polynomial.

5.4 Results and discussion

Results for the density, temperature and heat flux distributions are obtained by the Holway kinetic model for $\beta = [1.1, 4, 5, 11]$ covering small, moderate and large temperature differences, $\delta_0 \in [0, 100]$ representing heat transfer flow from the free molecular up to the slip regime and $\theta_v = [0.1, 1, 2, 5]$ corresponding to mean temperatures T_0 higher, equal and lower compared to the characteristic vibrational temperature. At $\theta_v = 0.1$ almost all vibrational degrees of freedom are fully excited, while at $\theta_v = 5$ almost no vibrational excitation occurs.

The results are organized as follows: Benchmarking is displayed in Subsection 5.4.1 by comparing the kinetic model with the DSMC results for N_2 and O_2, as well as simulations with experimental data for N_2, CO_2, CH_4 and SF_6. In Subsection 5.4.2, general results for all macroscopic quantities are presented for diatomic gases in terms of β, δ_0, θ_v including a sensitivity analysis of the dependency of the heat fluxes on Z_r, Z_v. Finally, in Subsection 5.4.3 results for the specific gases of N_2, O_2, CO_2, CH_4 and SF_6 are presented showing the effect of the vibrational degrees of freedom on the total heat fluxes and on the translational, rotational and vibrational parts. Also the concept of the effective thermal conductive in polyatomic gases is investigated.

5.4.1 Benchmarking

The comparison between the Holway kinetic model and the DSMC method is performed considering N_2 and O_2 as working gases ($j = 2$). To have a valid comparison it is ensured that the two approaches have the same relaxation rates and therefore the relaxation parameters of the Holway model are accordingly fixed. Following common practice the DSMC relaxation parameters are set as $Z_r^{(DSMC)} = 5$ and $Z_v^{(DSMC)} = 50$ [29] and then following Appendix A, the Holway relaxation parameters are $Z_r^{(H)} = 2.47$, $Z_v^{(H)} = 24.7$ for N_2 and $Z_r^{(H)} = 2.62$, $Z_v^{(H)} = 26.2$ for O_2. Furthermore, in both approaches the viscosity index takes the values $\omega = 0.74$ for N_2 and $\omega = 0.66$ for O_2 to reproduce the recommended data in [145]. Also, the Pr number in the kinetic model simulations is independent of temperature and equal to $Pr = 0.764$ and 0.751 for N_2 and O_2 respectively to ensure that the thermal conductivities obtained by the two methods are equal to each other.

In Tables 5.2 and 5.3, a comparison between the results obtained by the Holway model and the DSMC method is performed for N_2 and O_2 respectively. In both tables $\delta_0 \in [0, 100]$, $\beta = 5$ and $\theta_v = 1$ (the mean temperature T_0 is taken equal to the characteristic vibrational temperatures of 3371 K for N_2 and 2256 K for O_2). In all cases the agreement between the results, taking into account the different models implemented in the two approaches, is very good. The translational heat fluxes computed by the Holway model are smaller than the DSMC ones, while it is the other way around for the rotational and vibrational heat fluxes. The largest relative error occurs in the vibrational heat fluxes being always however less than 10%, while in the total heat fluxes is less than 1%. The results at $\delta_0 = 0$ are in excellent agreement with the analytical free molecular ones presented in Appendix C.

The comparison is extended to the number density as well as to the translational, rotational and vibrational temperature distributions plotted in Fig. 5.1 for various values of values of δ_0. Excellent agreement between the deterministic and stochastic approaches is shown. It is also observed that for large values of δ_0 the translational, rotational and vibrational are thermally equilibrated ($\tau_{tr} = \tau_{rot} = \tau_{vib}$), while as the rarefaction level of the gas is increased the three temperatures depart from each other with the vibrational temperature being higher than the other two.

Next, a comparison with the experimental data in [141] is performed in Fig. 5.2 based on the Holway kinetic model in terms of the thermal conductivity. More specifically the experimental data for the thermal conductivities of N_2, CO_2, CH_4 and SF_6 obtained from Tables 1, 5, 7 and 9 respectively in [141] are shown in terms of the corresponding temperatures $300 \leq T \leq 3273$ (K). Simulations have been also performed close to the hydrodynamic limit at $\delta_0 = 100$, with $T_C = 300$ K and $T_H = 3273$ K ($T_0 = 1786.5$ K, $\beta = 10.91$) and for all these gases (gas properties including characteristic vibrational temperatures are shown in Table 5.1). The rotational and vibrational collision numbers are $Z_r = 5$ and $Z_v = 50$. The Pr number is taken as a function of temperature according to the data in ([141]; see Tables 1, 5, 7 and 9). Once the problem is solved, an effective thermal conductivity $k_{eff}(y)$ is determined based on the Fourier law, which in the present dimensionless notation reads as

$$q_{tot} = \left(\frac{m}{2 k_B \delta_0 \mu_0} \right) k_{eff}(y) \frac{\partial \tau_{tot}}{\partial y}, \tag{5.28}$$

with the spatial derivative $\partial \tau_{tot}/\partial y$ being approximated by central differences. Previous studies (see [142] and references therein for monatomic gases and [143] for a diatomic gas), have shown that $k_{eff}(y)$ approximates extremely well the Chapman-Enskog value of the thermal conductivity in a central strip of the domain, provided its boundaries are sufficiently far from the walls where Knudsen layers cause deviations from hydrodynamic behavior. The computed $k_{eff}(y)$ is plotted in Fig. 5.2 and compared to the experimental one. As it is seen the computational results are in excellent agreement with the experimental data in the whole region between the plates except very close to the boundaries, i.e., inside the thin Knudsen layers which are present even at $\delta_0 = 100$ and where the Fourier constitutive law is not valid.

Based on all above the effectiveness of the Holway kinetic model to simulate this heat transfer configuration is demonstrated. Also, the efficiency of the implemented computational scheme and the accuracy of the deduced numerical results are verified.

5.4.2   Effect of vibrational degrees of freedom

The effect of θ_v on the heat fluxes and other macroscopic quantities is investigated. The analysis is kept as general as possible and therefore only diatomic gases ($j = 2$) with hard sphere (HS) molecules ($\omega = 0.5$) are considered.

However, before we proceed it is interesting to examine the effect of the prescribed collision numbers Z_r and Z_v on the results. A computational sensitivity analysis related to these two parameters is shown in Tables 5.4 and 5.5. The temperature ratio of the two plates is taken large and equal to $\beta = 5$, while the parameter $\theta_v = [0.1,\ 5]$. Also, the results are for $\delta_0 \times \mathrm{Pr} = 71.4$ without being necessary to specify exactly either of the two quantities. However, since for a diatomic gas $\mathrm{Pr} \simeq 0.7$ the analysis is performed, in purpose, at high values of $\delta_0 \simeq 10^2$, where the effect of the rotational and vibrational degrees of freedom is more dominant. Based on the above input data, in Table 5.4, all heat fluxes are tabulated by keeping the vibrational collision number constant, $Z_v = 50$, while the rotational one varies as $Z_r \in [3, 80]$. The corresponding results for constant rotational number $Z_r = 5$ and the vibrational number varying as $Z_v \in \left[5, 10^3\right]$ are tabulated in Table 5.5. As Z_r is increased, with Z_v being constant, q_{tr} is slightly increased not more than 2% and q_{rot} is slightly decreased not more than 3%. Also q_{vib} and q_{tot} are not affected at all for the significant figures shown. These observations are valid for both $\theta_v = 0.1$ and 5. As Z_v is increased, with Z_r being constant, the variation in q_{tr} and q_{rot} is very small not exceeding 5% for both θ_v. More interesting is the effect of Z_v on q_{vib}, which for $\theta_v = 0.1$ is decreased about only by 3%, while for $\theta_v = 5$ is decreased by 36%. However, in this latter case the vibrational heat flux is one order of magnitude smaller than the translational one and therefore, once again, there is no variation of the total heat flux q_{tot} with respect to the vibrational collision number. The fact that the total heat flux remains invariant in terms of Z_r and Z_v is of major importance and reduces the introduced modeling error, particularly when performing comparisons with experimental work. The effect of Z_r and Z_v on the density and temperatures distributions is negligible. Also, in general the effect of Z_r and Z_v is decreased as the temperature difference between the plates is decreased.

Next, in Table 5.6 the translational, rotational and vibrational heat fluxes as percentage of the total heat flux along with the total heat fluxes are provided for a diatomic HS gas

$(j = 2, \omega = 0.5)$ and for various values of θ_v and of the product $\delta_0 \times$ Pr with $\beta = 1.1$. The collision numbers are set to $Z_r = 5$ and $Z_v = 50$. The percentage results are at the hot plate $(y = -1/2)$, while q_{tot} remains constant between the plates. Depending upon θ_v the ratios of the translational, rotational and vibrational heat fluxes over the total one vary as $0.5 \leq q_{tr}/q_{tot} \leq 0.66$, $0.23 \leq q_{rot}/q_{tot} \leq 0.32$ and $0.05 \leq q_{vib}/q_{tot} \leq 0.25$ respectively. As expected, independently of θ_v, the rotational heat flux is about $43 - 50\%$ of the corresponding translational ones. Also, as θ_v is decreased the vibrational part becomes of the same order of the rotational one and corresponds to about 25% of the total heat flux. This is justified by the fact that as the parameter θ_v is decreased the mean temperature is increased causing activation of a larger number of vibrational degrees of freedom. It is noted that in the case of $\theta_v = 0.1$ the vibrational degrees of freedom are almost fully excited with $\zeta_v \cong 1.9$. The corresponding mean values of ζ_v for $\theta_v = 1$ and 5 is about 1.2 and 0.07 respectively. These results are valid in the whole range of the gas rarefaction examined. It is noted that the percentage of each part of heat flux to the total heat flux remains almost constant with regard to δ_0.

The dimensionless translational $e_{tr}(y)$, rotational $e_{rot}(y)$ and vibrational $e_{vib}(y)$ energies of a diatomic HS gas $(j = 2, \omega = 0.5, Z_r = 5, Z_v = 5)$ are shown in Fig. 5.3 for various values of $\delta_0 \times$ Pr with $\beta = 1.1$ and $\theta_v = [0.1, 5]$. The translational and vibrational energies are independent of θ_v, while the vibrational energy depends strongly on θ_v. Therefore the latter one is presented in two subfigures. The vibrational energy for $\theta_v = 0.1$ is approximately 28 times higher than the corresponding one for $\theta_v = 5$, with the exact number depending on the position between the plates and on the gas rarefaction. The difference in the vibrational distribution energies between $\theta_v = 0.1$ and $\theta_v = 5$ is increased moving from the hot plate towards the cold plate wall. Also, all energies are higher, as they should, near the hot wall than the corresponding ones at the cold wall.

In Fig. 5.4 the dimensionless vibrational temperature is plotted for the same input parameters as in Fig. 5.3. At large $\delta_0 \times$ Pr the vibrational temperatures for $\theta_v = [0.1, 5]$ almost coincide, while as $\delta_0 \times$ Pr (or δ_0) is decreased they depart from each other with $\tau_{vib}(y)$ for $\theta_v = 5$ being higher than the corresponding ones for $\theta_v = 0.1$. This latter observation is probably not expected but it may be explained by considering the reported vibrational energies for

115

$\theta_v = [0.1,\ 5]$ in Fig. 5.3 and the vibrational temperature in diatomic gases given by

$$\tau_{vib} = \frac{\theta_v}{\ln\left(1 + \frac{\theta_v}{e_{vib}}\right)}. \tag{5.29}$$

Based on the above this behavior is contributed to the relative decrease of e_{vib} with regard to the increase of θ_v. This behavior is also seen in the analytical expressions provided in the free molecular limit in Appendix C. Furthermore, the parameter θ_v has no effect on the number density distribution and the corresponding plots are omitted. Since θ_v has a very small effect on the translational and rotational temperatures they are not plotted here and they may be found in Chapter 3. In large values of δ_0 the vibrational temperature is thermally equilibrated with the translational and rotational temperatures ($\tau_{tr} \simeq \tau_{rot} \simeq \tau_{vib}$) independent of θ_v.

5.4.3 Heat fluxes for specific gases

At this subsection some results are provided for the nonpolar polyatomic gases of N_2, O_2, CO_2, CH_4 and SF_6 based on the Holway kinetic model. Results are provided for the typical values of $Z_r^{(H)} = 5$ and $Z_v^{(H)} = 50$ with temperature ratio $\beta = 1.1$ in a wide range of the rarefaction parameter δ_0. Two values of the reference mean temperature $T_0 = 500$ K and 2000 K are considered. The parameters of each gas are given in Table 1 and the Pr number is a function of temperature according to [141].

In Fig. 5.5 the rotational, vibrational and total heat fluxes at the hot wall ($y = -1/2$) are given in a wide range of the rarefaction parameter δ_0. It is seen that the rotational heat fluxes are in practice independent of the mean temperature T_0. The rotational heat fluxes q_{rot} of the linear gases (N_2, O_2, CO_2) are very close to each other (almost coincide) and the same happens for the nonlinear gases (CH_4, SF_6) with the latter ones being $30-60\%$ higher than the former ones for both T_0. The vibrational heat fluxes depend on T_0 and this dependency becomes stronger as depending upon the working gas, the characteristic vibrational temperatures are decreased and the number of vibrational degrees of freedom is increased. The vibrational heat fluxes of N_2 and O_2 are about the same with small dependency on T_0. However, for CO_2 there is a significant difference in q_{vib} as the mean temperature is increased from 500 K to 2000

K, which becomes even larger in the cases of CH_4 and SF_6. More specifically, since the SF_6 contains 15 vibrational modes and most of them are well excited at $T_0 = 500$ K is characterized compared to the other gases by the largest vibrational heat flux which is about $74 - 76\%$ of the total heat flux. Computations for SF_6 have been also performed with $T_0 = 300$ K. As it is seen in Fig. 5.6 the resulting to a vibrational heat flux corresponds up to 67% of the total heat flux. On the other hand, since the one vibrational mode of N_2 is fully activated at 3371 K, its vibrational heat flux is only about 2% and 19% of the total heat flux when the mean temperature is $T_0 = 500$ K and 2000 K respectively. With regard to δ_0, it is noted that the previous remark, related to diatomic gases, i.e. that the percentage of each part of heat flux to the total heat flux remains almost constant in the whole range of gas rarefaction (see Table 5.6), is also valid for linear and nonlinear polyatomic gases.

In monatomic gases it has been shown that when the flow is in the hydrodynamic regime with non-continuum effects (large local gradients) the effective thermal conductivity concept may be successfully applied to compute the corresponding heat fluxes [142]. A similar investigation is performed here for polyatomic gases. In Fig. 5.7, indicative results of the variation of the effective thermal conductivity $k_{eff}(y)$, computed according to Eq. (5.28), over the corresponding experimental values in [141] are plotted along the distance between the plates. The working gas is N_2 ($\omega = 0.69$, $j = 2$) with $\delta_0 = 50$, $\beta = 1.1$, 4 and $\theta_v = 3.371$ ($T_0 = 3371$ K). It is noted that the computed effective and experimental thermal conductivities (also seen in Fig. 5.2) are not constant within the domain but they are both decreasing moving from the hot towards the cold plate along with the temperature. It is seen that in the region approximately defined by $-0.45 \leq y \leq 0.45$ the ratio is constant and equal to one, clearly indicating that under both weakly ($\beta = 1.1$) or highly ($\beta = 4$) non-equilibrium conditions the Fourier law works satisfyingly far from the boundaries, i.e., outside the Knudsen layers. Also, the hot wall Knudsen layer is thicker than the corresponding one at the cold wall since the mean free path is an increasing function of temperature at constant pressure. Corresponding results are readily obtained for the other polyatomic gases. Thus, the effective thermal conductivity approximation may be also applied in polyatomic gases provided that the system Knudsen number is small.

5.5   Concluding remarks

The problem of heat transfer through rarefied polyatomic gases between parallel plates maintained at different temperatures has been considered by taking into consideration the gas rotational and vibrational degrees of freedom. The solution is obtained by the Holway kinetic model and the DSMC method. The very good agreement between the two approaches as well as with experimental data clearly demonstrates the capability of the Holway model to accurately simulate polyatomic gas heat transfer in the whole range of gas rarefaction for small, moderate and large temperature differences between the plates.

The translational, rotational, vibrational and total heat fluxes of N_2, O_2, CO_2, CH_4 and SF_6 are computed to examine the effect of the mean reference temperature and of the gas rarefaction with regard to the characteristic vibrational temperatures and the corresponding number of vibrational degrees of freedom of each gas. It has been shown that for gases with low and moderate characteristic excitation temperatures (e.g. CO_2, CH_4 and SF_6) the vibrational heat flux may be, even at ambient temperatures, a significant portion of the total heat flux independent of the gas rarefaction. For example in the case of SF_6 at reference temperatures of 300 K and 500 K the vibrational heat fluxes are 67% and 76% respectively of the corresponding total ones. The effective thermal conductivity approximation has been also studied finding out that it can be successfully applied in polyatomic gases to study non-equilibrium effects providing that the system Knudsen number is small.

Overall, the present work aims to provide some useful insight in the heat transfer design and optimization of technological applications operating in a temperature range where the vibrational modes of the involved gases are excited and must be taken into consideration. It is evident that in such heat transfer and flow configurations modeling must include the effect of the vibrational degrees of freedom.

Table 5.2: Dimensionless heat fluxes for N_2 ($j = 2$, Pr = 0.764) with IPL molecules ($\omega = 0.74$) at the hot plate ($y = -1/2$) for various values of δ_0, $\beta = 5$ ($T_H = 5618$ K, $T_C = 1124$ K, $T_0 = 3371$ K) and $\theta_v = 1$ ($Z_r^{(DSMC)} = 5$, $Z_v^{(DSMC)} = 50$, $Z_r^{(H)} = 2.47$, $Z_v^{(H)} = 24.7$).

δ_0	q_{tr}		q_{rot}		q_{vib}		q_{tot}	
	Holway	DSMC	Holway	DSMC	Holway	DSMC	Holway	DSMC
0	6.00(-1)		3.00(-1)		2.62(-1)		1.16	
0.1	5.76(-1)	5.76(-1)	2.86(-1)	2.83(-1)	2.49(-1)	2.47(-1)	1.11	1.11
1	4.35(-1)	4.41(-1)	2.07(-1)	2.01(-1)	1.81(-1)	1.72(-1)	8.23(-1)	8.14(-1)
5	2.32(-1)	2.43(-1)	1.05(-1)	1.02(-1)	9.24(-2)	8.45(-2)	4.29(-1)	4.30(-1)
10	1.49(-1)	1.58(-1)	6.65(-2)	6.53(-2)	5.95(-2)	5.42(-2)	2.75(-1)	2.77(-1)
50	3.82(-2)	4.05(-2)	1.68(-2)	1.65(-2)	1.57(-2)	1.43(-2)	7.07(-2)	7.13(-2)
100	1.97(-2)	2.08(-2)	8.68(-3)	8.35(-3)	8.15(-3)	7.48(-3)	3.66(-2)	3.66(-2)

Table 5.3: Dimensionless heat fluxes for O_2 ($j = 2$, Pr = 0.751) with IPL molecules ($\omega = 0.66$) at the hot plate ($y = -1/2$) for various values of δ_0, $\beta = 5$ ($T_H = 3760$ K, $T_C = 752$ K, $T_0 = 2256$ K) and $\theta_v = 1$ ($Z_r^{(DSMC)} = 5$, $Z_v^{(DSMC)} = 50$, $Z_r^{(H)} = 2.62$, $Z_v^{(H)} = 26.2$).

δ_0	q_{tr}		q_{rot}		q_{vib}		q_{tot}	
	Holway	DSMC	Holway	DSMC	Holway	DSMC	Holway	DSMC
0	6.00(-1)		3.00(-1)		2.62(-1)		1.16	
0.1	5.76(-1)	5.76(-1)	2.86(-1)	2.84(-1)	2.50(-1)	2.47(-1)	1.11	1.11
1	4.38(-1)	4.42(-1)	2.09(-1)	2.01(-1)	1.82(-1)	1.73(-1)	8.29(-1)	8.17(-1)
5	2.35(-1)	2.43(-1)	1.06(-1)	1.02(-1)	9.33(-2)	8.49(-2)	4.34(-1)	4.30(-1)
10	1.51(-1)	1.57(-1)	6.73(-2)	6.53(-2)	6.01(-2)	5.42(-2)	2.78(-1)	2.76(-1)
50	3.87(-2)	4.03(-2)	1.70(-2)	1.65(-2)	1.59(-2)	1.43(-2)	7.16(-2)	7.11(-2)
100	2.00(-2)	2.08(-2)	8.80(-3)	8.52(-3)	8.25(-3)	7.40(-3)	3.71(-2)	3.67(-2)

Table 5.4: Effect of Z_r on the translational, rotational, vibrational and total heat fluxes at the hot plate ($y = -1/2$) for a diatomic HS gas ($j = 2$, $\omega = 0.5$) with $\beta = 5$, $\delta_0 \times \mathrm{Pr} = 71.4$ and $Z_v = 50$.

Z_r	q_{tr}		q_{rot}		q_{vib}		q_{tot}	
	$\theta_v = 0.1$	$\theta_v = 5$	$\theta_v = 0.1$	$\theta_v = 5$	$\theta_v = 0.1$	$\theta_v = 5$	$\theta_v = 0.1$	$\theta_v = 5$
3	2.13(-2)	2.02(-2)	9.35(-3)	8.85(-3)	9.02(-3)	3.81(-3)	3.97(-2)	3.29(-2)
5	2.14(-2)	2.03(-2)	9.29(-3)	8.80(-3)	9.02(-3)	3.81(-3)	3.97(-2)	3.29(-2)
7.5	2.14(-2)	2.03(-2)	9.25(-3)	8.76(-3)	9.02(-3)	3.81(-3)	3.97(-2)	3.29(-2)
10	2.15(-2)	2.03(-2)	9.22(-3)	8.73(-3)	9.02(-3)	3.81(-3)	3.97(-2)	3.29(-2)
20	2.15(-2)	2.04(-2)	9.15(-3)	8.66(-3)	9.02(-3)	3.81(-3)	3.97(-2)	3.29(-2)
40	2.16(-2)	2.05(-2)	9.10(-3)	8.61(-3)	9.02(-3)	3.81(-3)	3.97(-2)	3.29(-2)
60	2.16(-2)	2.05(-2)	9.08(-3)	8.59(-3)	9.02(-3)	3.81(-3)	3.97(-2)	3.29(-2)
80	2.16(-2)	2.05(-2)	9.07(-3)	8.58(-3)	9.02(-3)	3.81(-3)	3.97(-2)	3.29(-2)

Table 5.5: Effect of Z_v on the translational, rotational, vibrational and total heat fluxes at the hot plate ($y = -1/2$) for a diatomic HS gas ($j = 2$, $\omega = 0.5$) with $\beta = 5$, $\delta_0 \times \mathrm{Pr} = 71.4$ and $Z_r = 5$.

Z_v	q_{tr}		q_{rot}		q_{vib}		q_{tot}	
	$\theta_v = 0.1$	$\theta_v = 5$	$\theta_v = 0.1$	$\theta_v = 5$	$\theta_v = 0.1$	$\theta_v = 5$	$\theta_v = 0.1$	$\theta_v = 5$
5	2.12(-2)	2.00(-2)	9.30(-3)	8.76(-3)	9.21(-3)	4.15(-3)	3.97(-2)	3.29(-2)
10	2.13(-2)	2.01(-2)	9.28(-3)	8.76(-3)	9.15(-3)	4.08(-3)	3.97(-2)	3.29(-2)
25	2.13(-2)	2.02(-2)	9.28(-3)	8.77(-3)	9.07(-3)	3.95(-3)	3.97(-2)	3.29(-2)
70	2.14(-2)	2.03(-2)	9.30(-3)	8.82(-3)	9.00(-3)	3.73(-3)	3.97(-2)	3.29(-2)
100	2.14(-2)	2.04(-2)	9.30(-3)	8.85(-3)	8.97(-3)	3.63(-3)	3.97(-2)	3.29(-2)
400	2.15(-2)	2.07(-2)	9.32(-3)	8.99(-3)	8.91(-3)	3.10(-3)	3.97(-2)	3.28(-2)
700	2.15(-2)	2.09(-2)	9.32(-3)	9.06(-3)	8.89(-3)	2.83(-3)	3.97(-2)	3.28(-2)
1000	2.15(-2)	2.10(-2)	9.32(-3)	9.10(-3)	8.88(-3)	2.66(-3)	3.97(-2)	3.27(-2)

Table 5.6: Dimensionless total heat fluxes with the corresponding percentages of the vibrational, rotational and translational heat fluxes for a diatomic HS gas ($j = 2$, $\omega = 0.5$) at the hot plate ($y = -1/2$) with various values of $\delta_0 \times$ Pr, $\beta = 1.1$ and $\theta_v = 1$ ($Z_r = 5$, $Z_v = 50$).

| $\delta_0 \times$ Pr | $\theta_v = 5$ | | | | $\theta_v = 2$ | | | | $\theta_v = 1$ | | | | $\theta_v = 0.1$ | | | |
| | | i | | | | i | | | | i | | | | i | | |
	tr	rot	vib	q_{tot}	tr	rot	vib	q_{tot}	tr	rot	vib	q_{tot}	tr	rot	vib	q_{tot}
0	63.1	31.5	5.39	8.51(-2)	53.7	26.8	19.4	1.00(-1)	51.0	25.5	23.5	1.05(-1)	50.0	25.0	25.0	1.07(-1)
7.14(-2)	63.2	31.4	5.36	8.08(-2)	53.9	26.8	19.4	9.48(-2)	51.2	25.4	23.3	9.98(-2)	50.2	24.9	24.8	1.02(-1)
7.14(-1)	64.2	30.5	5.22	5.91(-2)	54.9	26.1	18.8	6.90(-2)	52.2	24.8	22.9	7.26(-2)	51.2	24.3	24.3	7.40(-2)
3.57	65.8	29.2	5.01	2.93(-2)	56.7	25.2	18.2	3.40(-2)	54.0	24.0	22.0	3.57(-2)	53.0	23.6	23.4	3.64(-2)
7.14	66.1	28.9	4.99	1.83(-2)	57.2	24.9	17.9	2.12(-2)	54.5	23.8	21.6	2.22(-2)	53.6	23.4	23.0	2.26(-2)
35.7	66.1	28.6	5.26	4.58(-3)	57.4	24.8	17.8	5.28(-3)	54.8	23.9	21.3	5.53(-3)	54.0	23.5	22.7	5.63(-3)
71.4	65.9	28.6	5.37	2.37(-3)	57.2	24.8	17.9	2.73(-3)	54.7	23.8	21.4	2.85(-3)	54.1	23.4	22.7	2.90(-3)
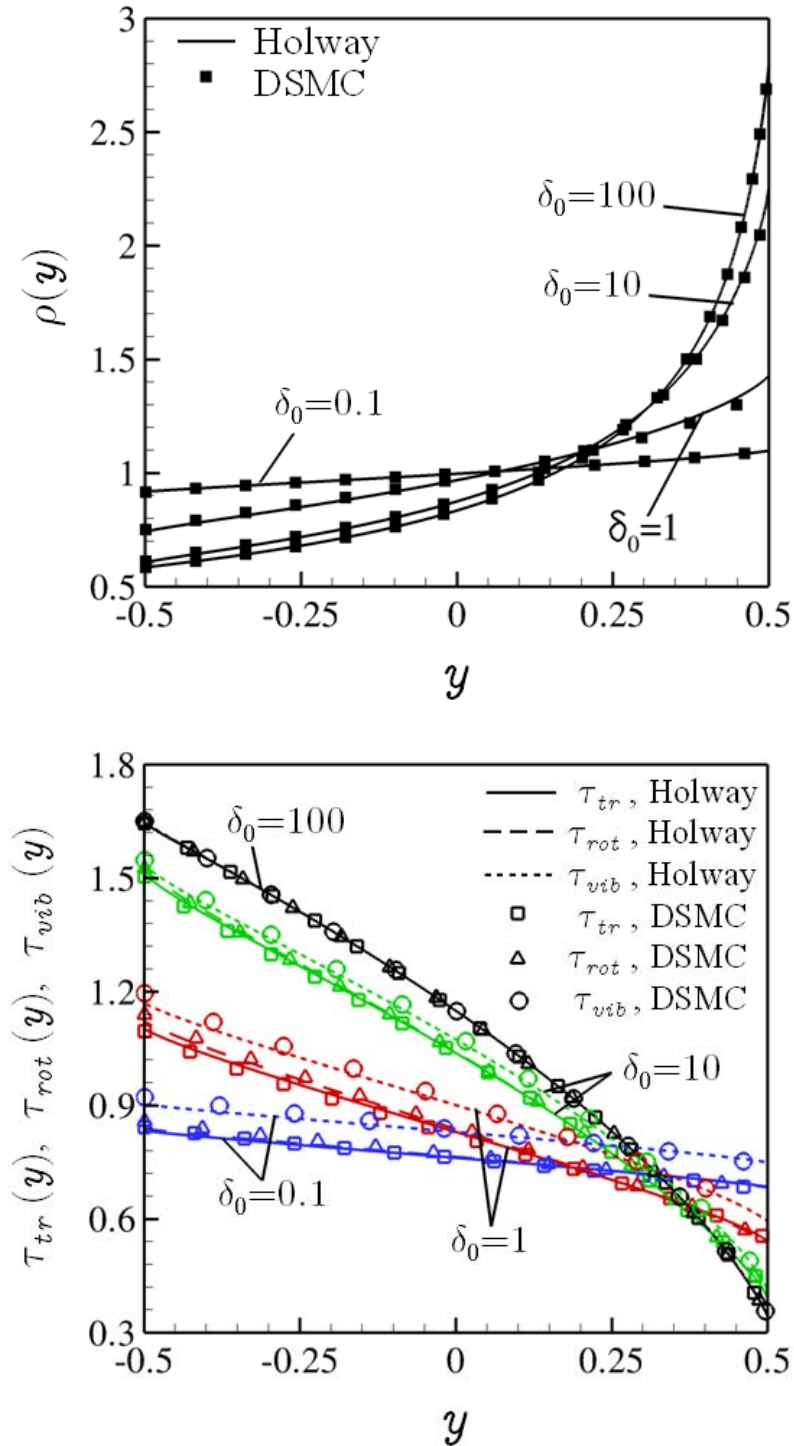
Figure 5.1: Comparison between the dimensionless density and temperature distributions of the Holway model and the DSMC method for N_2 ($j = 2$, $Pr = 0.764$) with VHS molecules ($\omega = 0.74$) or various values of δ_0, $\beta = 5$ ($T_H = 5618\,\text{K}$, $T_C = 1124\,\text{K}$, $T_0 = 3371\,\text{K}$) and $\theta_v = 1$ ($Z_r^{(DSMC)} = 5$, $Z_v^{(DSMC)} = 50$, $Z_r = 2.47$, $Z_v = 24.7$).
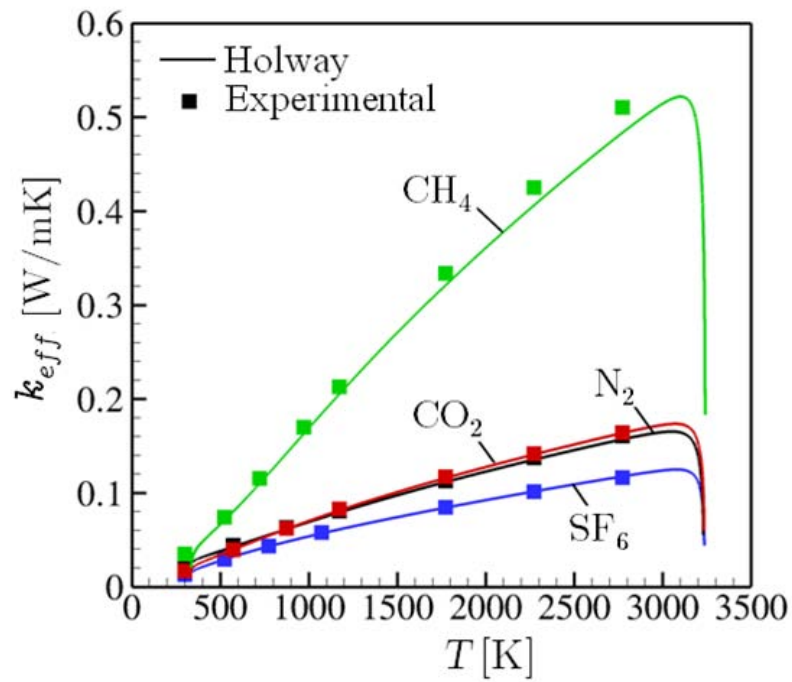
Figure 5.2: Comparison between the experimental thermal conductivities in [141] with $T_C = 300$ K, $T_H = 3273$ K and the corresponding computed ones obtained by the Holway model with $\delta_0 = 100$ and $\beta = 10.9$ ($Z_r = 5$, $Z_v = 50$) for various gases.
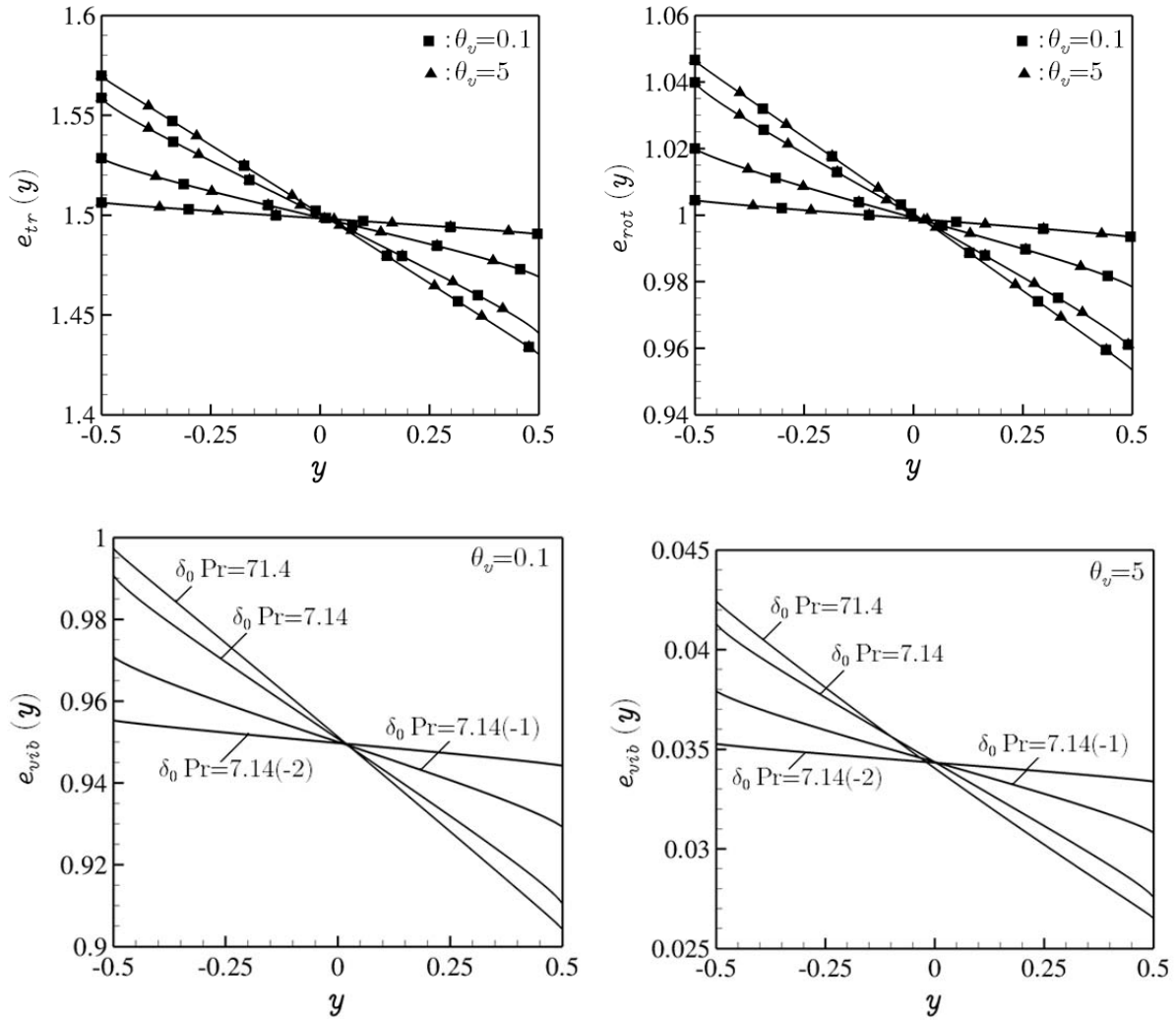
Figure 5.3: Dimensionless translational (left-up), rotational (right-up) and vibrational (down) energy distributions for a diatomic HS gas ($j = 2$, $\omega = 0.5$) with $\beta = 1.1$, various values of $\delta_0 \times \mathrm{Pr}$ and $\theta_v = [0.1, 5]$ ($Z_r = 5$, $Z_v = 50$).
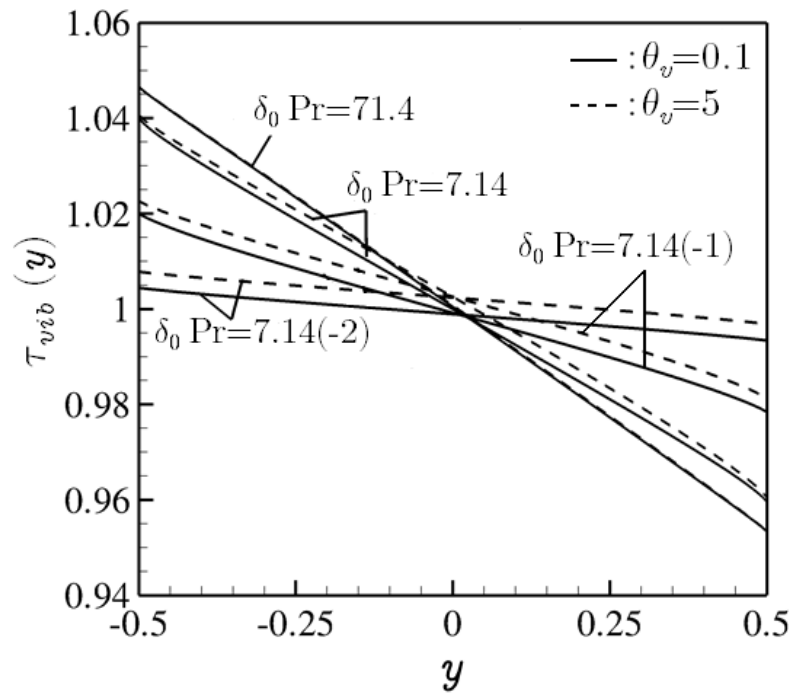
Figure 5.4: Dimensionless vibrational temperature distributions for a diatomic HS gas ($j = 2$, $\omega = 0.5$) with $\beta = 1.1$, various values of $\delta_0 \times \mathrm{Pr}$ and $\theta_v = [0.1, 5]$ ($Z_r = 5$, $Z_v = 50$).
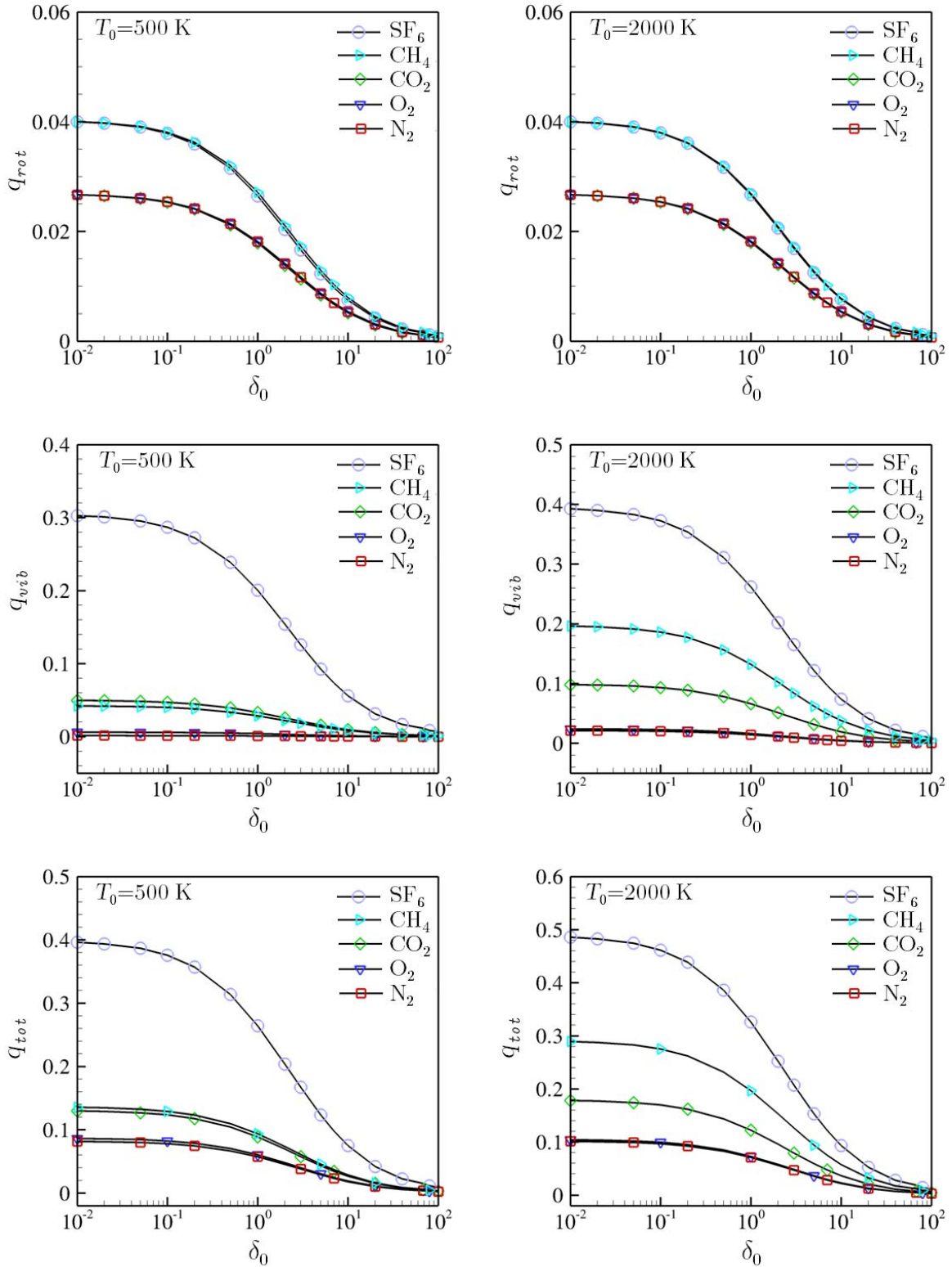
Figure 5.5: Dimensionless rotational (up), vibrational (middle) and total (down) heat fluxes at the hot plate ($y = -1/2$) in terms of δ_0 for various polyatomic gases, with $\beta = 1.1$ and $T_0 = 500$ K (left) and $T_0 = 2000$ K (right) ($Z_r = 5$, $Z_v = 50$).

126
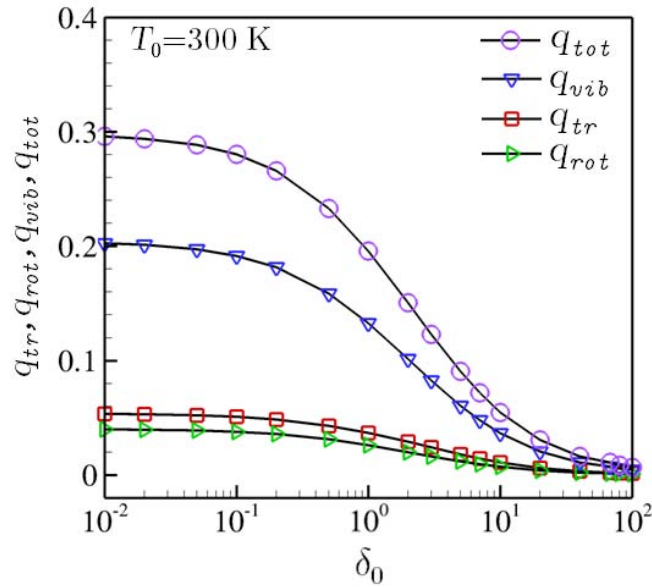
Figure 5.6: Dimensionless translational, rotational, vibrational and total heat fluxes at the hot plate ($y = -1/2$) in terms of δ_0 for SF_6, with $\beta = 1.1$ and $T_0 = 300$ K ($Z_r = 5$, $Z_v = 50$).
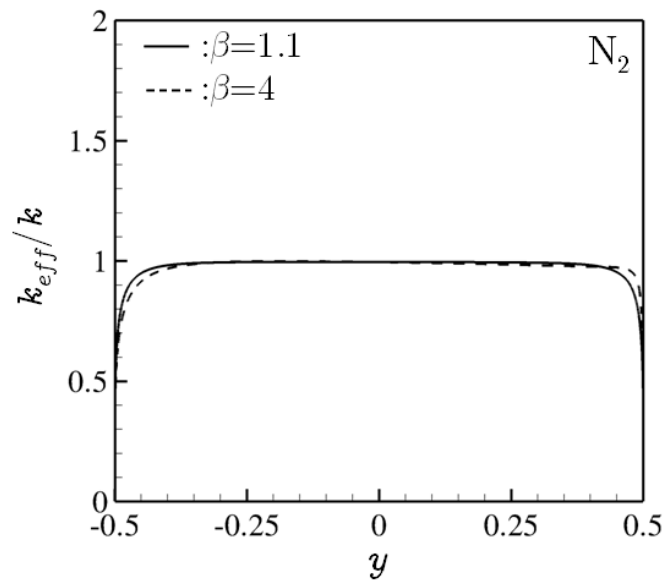
Figure 5.7: Ratio k_{eff}/k between the plates for N_2 ($\omega = 0.69$, $j = 2$) at $\theta_v = 3.371$ K ($Z_r = 5$, $Z_v = 50$).

127

Chapter 6

Polyatomic flows through circular capillaries

6.1 Introduction

Flows through long channels have been considered by many researchers and for various geometries [146–148] both numerically and experimentally. The wide availability of results comes from the simplifications occurring because of the fully developed flow conditions (the pressure is constant at each cross section). The problem admits, firstly, linearization (due to the smallness of the pressure and temperature differences) and, secondly, further simplification due to the fact that the tube is very long. However, in many practical situations [149, 150] the length of the tube is comparable with its radius and the whole problem is described by large pressure differences. For instance, micro-nozzles are often used as low-thrust propulsion systems in order to produce accurate orbital maneuvers in micro-satellites. Therefore, a systematic study of the gas flow in such devices is needed in order to determine the optimal geometry and design. It is well known that, at low Reynolds numbers, the viscous losses in micronozzles become large enough making the concept of a nozzle expansion useless and micronozzles can be replaced by short circular tubes. In such cases the problem is described by the non-linear theory of short tubes described in [151]. The majority of the studies in literature was made for monatomic gases [73, 100, 102], while corresponding work in the case of polyatomic gases is very limited.

Here, the rarefied gas flow of polyatomic gases through short and long circular tubes is modelled via the Holway and Rykov polyatomic kinetic models respectively. The study is focused on polyatomic gas expansion into very low pressures through short circular tubes in a wide range of the Knudsen number based on the Holway model. The kinetic modeling of flows through short tubes is described in Sections 6.2 - 6.4 while the corresponding results including the deduced flow rate, discharge coefficient, thrust the impulse factor in terms of flow and geometric parameters as well as the effects of the internal degrees of freedom on the aforementioned quantities are presented in Section 6.8.

The study is extended in the case of polyatomic gas flows through tubes of infinite length under a given small pressure gradient (Poiseuille flow) or a small temperature gradient (Thermal creep flow) based on the Rykov kinetic model. The simulation results are compared to available numerical results for nitrogen in [106]. Also, the thermomolecular pressure effect in polyatomic gases is considered and the simulation results are compared with corresponding experimental data in literature [152]. The formulation of the problem for long tubes is described in Sections 6.5 - 6.7 while the corresponding results are given in Section 6.9.

6.2 Pressure driven polyatomic flows through short tubes

In the case of short tubes the assumption of constant density at each cross-section is not valid and the flow becomes two- or three-dimensional. As a consequence, the complete geometry must be simulated, including a part of the reservoirs before and after the tube. Thus, the flow of polyatomic gas through a tube of radius R and finite length L is considered. The tube connects two large reservoirs A and B, which are maintained at constant pressures $\hat{P}_A$ and $\hat{P}_B$, with $\hat{P}_B/\hat{P}_A = 0.01$. The walls and the gas in the container areas far from the tube are maintained at the same temperature $T_A = T_B = T_0$. The computational domain consists of two large computational areas, which correspond to the upstream and downstream reservoirs including an intermediate area which contains the tube. The flow configuration and the computational domain are shown in Fig. 6.1.
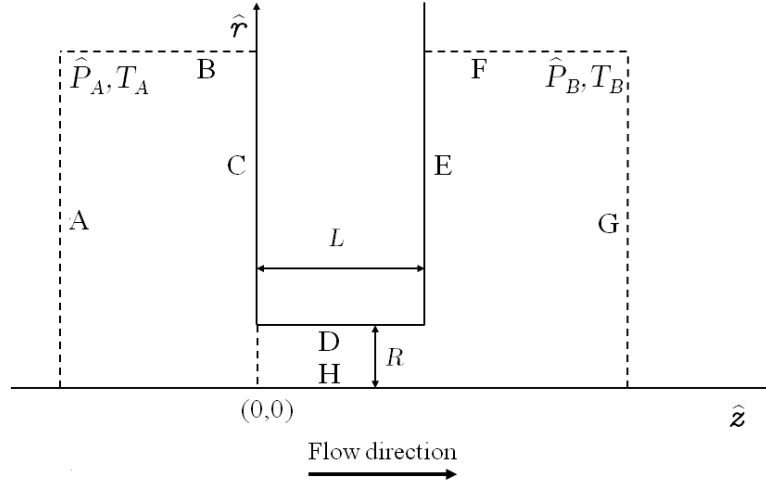
Figure 6.1: Flow configuration and computational domain.

6.3 Governing equations and macroscopic quantities

The investigation is based on the description of the state of a polyatomic gas using the distribution function $\hat{f}\left(\hat{r}, \hat{z}, \boldsymbol{v}, \hat{I}\right)$, which is a function of the spatial coordinates $\hat{r}$ and $\hat{z}$, the molecular velocity vector $\boldsymbol{v} = (\xi \cos\theta, \xi \sin\theta, \xi_z)$, where $\xi^2 = \xi_x^2 + \xi_y^2$ and $\theta = \tan^{-1}(\xi_y/\xi_x)$, and the rotational motion energy $\hat{I}$. Since the investigation is limited to the case of pressure driven flow the expected variation of temperature in the flow field is small and the nonlinear Holway kinetic model is implemented. For the specific problem under consideration the computational effort is reduced by eliminating, based on a projection procedure, the $\hat{I}$ component of energy by introducing the reduced distributions $\hat{g}$ and $\hat{h}$ as it was described in Chapter 2. Then, for the present flow problem the Holway model may be written in dimensional form as [123, 153]

$$
\xi \cos\theta \frac{\partial \hat{g}}{\partial \hat{r}} - \frac{\xi \sin\theta}{\hat{r}} \frac{\partial \hat{g}}{\partial \theta} + \xi_z \frac{\partial \hat{g}}{\partial \hat{z}} = \frac{\hat{P}_{tr}}{\mu_{tr}} \left[\frac{1}{Z} \left(\hat{g}_{rot} - \hat{g} \right) + \left(1 - \frac{1}{Z} \right) \left(\hat{g}_{tr} - \hat{g} \right) \right],
$$

$$
\xi \cos\theta \frac{\partial \hat{h}}{\partial \hat{r}} - \frac{\xi \sin\theta}{\hat{r}} \frac{\partial \hat{h}}{\partial \theta} + \xi_z \frac{\partial \hat{h}}{\partial \hat{z}} = \frac{\hat{P}_{tr}}{\mu_{tr}} \left[\frac{1}{Z} \left(\hat{h}_{rot} - \hat{h} \right) + \left(1 - \frac{1}{Z} \right) \left(\hat{h}_{tr} - \hat{h} \right) \right],
$$

$$
\hat{g}_{tr} = n \left(\frac{m}{2\pi k_B T_{tr}} \right)^{3/2} \exp\left[\frac{-m(\boldsymbol{v} - \hat{\boldsymbol{u}})^2}{2 k_B T_{tr}} \right], \quad \hat{h}_{tr} = \frac{j k_B T_{rot}}{2} \hat{g}_{tr},
$$

$$
\hat{g}_{rot} = n \left(\frac{m}{2\pi k_B T} \right)^{3/2} \exp\left(\frac{-m(\boldsymbol{v} - \hat{\boldsymbol{u}})^2}{2 k_B T} \right), \quad \hat{h}_{rot} = \frac{j k_B T}{2} \hat{g}_{rot},
$$

(6.1)

131

where $0 < Z^{-1} \leq 1$ is a parameter and j is the number of rotational degrees of freedom ($j = 0$ refers to monoatomic molecules, $j = 2$ for diatomic and linear polyatomic molecules and $j = 3$ for nonlinear polyatomic molecules). Also, n is the number density, $\hat{P}$ is the pressure, $\hat{\boldsymbol{u}}$ is the velocity vector and T is the total (thermodynamic) temperature. The subscripts tr and rot denote the translational and rotational parts.

The left reservoir conditions, i.e. the number density n_A and pressure $\hat{P}_A$, with $\hat{P}_A = n_A k_B T_0$ from the ideal gas law, are chosen as reference quantities. Then, all quantities of interest are non-dimensionalized according to

$$
z = \frac{\hat{z}}{R}, \quad r = \frac{\hat{r}}{R}, \quad \zeta = \frac{\xi}{v_0}, \quad c_z = \frac{\xi_z}{v_0}, \quad g = \frac{\hat{g} v_0^3}{n_A}, \quad h = \frac{\hat{h} v_0^3}{\hat{P}_A},
$$

$$
\rho = \frac{n}{n_A}, \quad \boldsymbol{u} = \frac{\hat{\boldsymbol{u}}}{v_0}, \quad p = \frac{\hat{P}}{\hat{P}_A}, \tau_{tr} = \frac{T_{tr}}{T_0}, \quad \tau_{rot} = \frac{T_{rot}}{T_0}, \quad \tau = \frac{3\tau_{tr} + j\tau_{rot}}{3 + j},
$$

(6.2)

where $v_0 = \sqrt{2k_B T_0/m}$, with m and k_B denoting the molecular mass and the Boltzmann constant respectively, being the most probable molecular speed.

It is seen that the distribution functions $g = g(z, r, \zeta, \theta, c_z)$ and $h = h(z, r, \zeta, \theta, c_z)$ are five dimensional for the current problem and no projection in the velocity space is possible. the final dimensionless form of the governing equations is

$$
\zeta \cos\theta \frac{\partial g}{\partial r} - \frac{\zeta \sin\theta}{r} \frac{\partial g}{\partial \theta} + c_z \frac{\partial g}{\partial z} = \delta_0 \rho \sqrt{\tau_{tr}} \left[\left(1 - \frac{1}{Z}\right)(g_{tr} - g) + \frac{1}{Z}(g_{rot} - g) \right],
$$

$$
\zeta \cos\theta \frac{\partial h}{\partial r} - \frac{\zeta \sin\theta}{r} \frac{\partial h}{\partial \theta} + c_z \frac{\partial h}{\partial z} = \delta_0 \rho \sqrt{\tau_{tr}} \left[\left(1 - \frac{1}{Z}\right)(h_{tr} - h) + \frac{1}{Z}(h_{rot} - h) \right],
$$

(6.3)

$$
g_{tr} = \frac{\rho}{(\pi \tau_{tr})^{3/2}} \exp\left[\frac{-(\boldsymbol{c} - \boldsymbol{u})^2}{\tau_{tr}}\right], \quad h_{tr} = \frac{j}{2}\tau_{rot} g_{tr},
$$

$$
g_{rot} = \frac{\rho}{(\pi \tau)^{3/2}} \exp\left[\frac{-(\boldsymbol{c} - \boldsymbol{u})^2}{\tau}\right], \quad h_{rot} = \frac{j}{2}\tau g_{rot},
$$

where $\boldsymbol{c} = (\zeta, \theta, c_z)$, with $\theta = [0, \pi]$ since the distribution function is axisymmetrical, is the

dimensionless velocity vector in cylindrical coordinates and δ_0 is the reference rarefaction parameter defined as

$$\delta_0 = \frac{\hat{P}_A R}{\mu_0 \upsilon_0},\tag{6.4}$$

with μ_0 being the reference viscosity at temperature T_0. The rarefaction parameter is proportional to the inverse Knudsen number, with the limiting values at $\delta_0 = 0$ and $\delta_0 \to \infty$ corresponding to the free molecular and hydrodynamic limits respectively. It is noted that in the derivations of the Eq. (6.3) the hard sphere model has been used and therefore the variation of the viscosity is proportional to the square root of the temperature ($\mu/\mu_0 = \sqrt{T/T_0}$).

The macroscopic quantities of practical interest are obtained by the moments of g and h for the problem examined here as [102]

$$\rho\left(z,r\right) = 2 \int\limits_{-\infty}^{\infty} \int\limits_{0}^{\pi} \int\limits_{0}^{\infty} \zeta g \, d\zeta d\theta dc_z,\tag{6.5}$$

$$u_r\left(z,r\right) = \frac{2}{\rho} \int\limits_{-\infty}^{\infty} \int\limits_{0}^{\pi} \int\limits_{0}^{\infty} \zeta^2 \cos\theta g \, d\zeta d\theta dc_z,\tag{6.6}$$

$$u_z\left(z,r\right) = \frac{2}{\rho} \int\limits_{-\infty}^{\infty} \int\limits_{0}^{\pi} \int\limits_{0}^{\infty} \zeta c_z g \, d\zeta d\theta dc_z,\tag{6.7}$$

$$\tau_{tr}\left(z,r\right) = \frac{4}{3\rho} \int\limits_{-\infty}^{\infty} \int\limits_{0}^{\pi} \int\limits_{0}^{\infty} \left[\left(\zeta\cos\theta - u_r\right)^2 + \left(\zeta\sin\theta\right)^2 + \left(c_z - u_z\right)^2\right] \zeta g \, d\zeta d\theta dc_z,\tag{6.8}$$

$$\tau_{rot}\left(z,r\right) = \frac{4}{j\rho} \int\limits_{-\infty}^{\infty} \int\limits_{0}^{\pi} \int\limits_{0}^{\infty} \zeta h \, d\zeta d\theta dc_z,\tag{6.9}$$

$$\tau\left(z,r\right) = \frac{3\tau_{tr}\left(z,r\right) + j\tau_{rot}\left(z,r\right)}{3+j}.\tag{6.10}$$

An other quantity with practical interest is the mass flow rate $\dot{M}$ [Kg/s] defined as the rate of movement of gas mass through a unit area. The dimensionless mass flow rate through the tube

is given as

$$W = \frac{\dot{M}\,v_0}{\sqrt{\pi}\,R^2\,\hat{P}_A} = 4\sqrt{\pi}\int\limits_0^1 \rho\,(L,r)\,u_z\,(L,r)\,r\,dr. \tag{6.11}$$

For a typical micronozzle, thrust $\hat{F}_t$ [N] and impulse factor $\hat{I}_{SP}$ [s] are essential parameters in order to describe its performance and efficiency. The specific impulse is a measure of the impulse per unit of gas flow that is expended, while thrust is a measure of the momentary force supplied by a particular propulsion system. A higher number of impulse factor means better performance, since the less gas flow is needed to gain a given amount of momentum. Both quantities, thrust and impulse factor, should be investigated while the efficiency of a propulsion system is examined. Dimensionless thrust F_t and thrust per unit mass flow rate I_{SP} are defined as [154]

$$F_t = \frac{\hat{F}_t}{\pi\,R^2\,\hat{P}_A} = 2\int\limits_0^1 \left[2\rho\,(L,r)\,u_z^2\,(L,r) + p\,(L,r)\right]\,r\,dr \tag{6.12}$$

and

$$I_{SP} = \frac{\hat{I}_{SP}\,g_r\,\sqrt{m}}{\sqrt{2\pi\,k_B\,T_0}} = \frac{F_t}{W}, \tag{6.13}$$

where $g_r = 9.81$ m/s^2 is the gravity acceleration and $p = \rho\tau$ is the dimensionless pressure. Furthermore, the discharge coefficient C_d is calculated, which is defined as [154]

$$C_d = \frac{\dot{M}\,v_0}{\sqrt{\pi}\,R^2\,\hat{P}_A\,\sqrt{2\,\pi\,\gamma}\left(\frac{2}{\gamma+1}\right)^{\frac{\gamma+1}{2(\gamma-1)}}} = \frac{W}{\sqrt{2\pi\gamma}\left(\frac{2}{\gamma+1}\right)^{\frac{\gamma+1}{2(\gamma-1)}}}, \tag{6.14}$$

where $\gamma = (5+j)/(3+j)$ is the ratio of the specific heats of the gas. The discharge coefficient is the ratio of the actual mass flow rate over the mass rate of flow of an ideal gas through an isentropic nozzle. Another interesting parameter in such flows is the Mach number given by

$$Ma = \frac{|\hat{u}|}{c_s} = \sqrt{\frac{2}{\gamma}}\,|u|, \tag{6.15}$$

where $c_s = \sqrt{\gamma k_B T_0/m}$ is the speed of sound and $|u| = \sqrt{u_r^2 + u_z^2}$ is the magnitude of $\boldsymbol{u}$. In Subsection 6.8.2 all the aforementioned quantities are calculated for a wide range of the parameters characterizing the flow: the reference rarefaction parameter δ_0, the channel aspect

ratio L/R, the parameter Z and the number of the rotational degrees of freedom j.

6.4   Boundary conditions

To close the kinetic description of the flows through short tubes the formulation of the boundary conditions is provided. For the open boundaries (A), (B), (F) and (G), a Maxwellian distribution is supposed based on the local values of the pressure and temperature assuming zero bulk velocity. The incoming distributions at the surfaces (A) and (B) in terms of the distribution functions g and h are

$$g^+ = \frac{1}{\pi^{3/2}} \exp\left(-c^2\right), \quad h^+ = \frac{j}{2}\frac{1}{\pi^{3/2}} \exp\left(-c^2\right) \tag{6.16}$$

and at the surfaces (F) and (G) are

$$g^+ = \frac{P_B}{P_A}\frac{1}{\pi^{3/2}} \exp\left(-c^2\right), \quad h^+ = \frac{P_B}{P_A}\frac{j}{2}\frac{1}{\pi^{3/2}} \exp\left(-c^2\right). \tag{6.17}$$

Furthermore, on the solid walls (C), (D) and (E) purely diffuse type boundary conditions are considered. Then, the outgoing distributions from the surfaces (C), (D) and (E) can be written as

$$g^+ = \frac{\rho_w}{\pi^{3/2}} \exp\left(-c^2\right), \quad h^+ = \frac{j}{2}\frac{\rho_w}{\pi^{3/2}} \exp\left(-c^2\right), \tag{6.18}$$

where the parameters ρ_w are given by the no-penetration condition at the walls ($u_{normal} = 0$). More specifically, the parameters ρ_w at each wall are

$$\text{C}: \quad \rho_w = 4\sqrt{\pi} \int\limits_0^\infty \int\limits_0^\pi \int\limits_0^\infty \zeta c_z g^- d\zeta d\theta dc_z,$$

$$\text{D}: \quad \rho_w = 4\sqrt{\pi} \int\limits_{-\infty}^\infty \int\limits_0^{\pi/2} \int\limits_0^\infty \zeta^2 \cos\theta g^- d\zeta d\theta dc_z, \tag{6.19}$$

$$\text{E}: \quad \rho_w = -4\sqrt{\pi} \int\limits_{-\infty}^0 \int\limits_0^\pi \int\limits_0^\infty \zeta c_z g^- d\zeta d\theta dc_z,$$

135

where the superscript (-) denotes the incoming distributions at the surfaces. Finally, specular reflection is imposed at $r = 0$ due to the axial symmetry

$$g^+ \left(0, z, \zeta, \theta, c_z\right) = g^- \left(0, z, \zeta, \pi - \theta, c_z\right), \tag{6.20}$$

for angles in $\theta \in [0, \pi/2]$.

Summarizing, the formulation of the flow through short tubes is described by the kinetic equations (6.3) coupled by the macroscopic quantities (6.5)-(6.10) and subject to the boundary conditions (6.16)-(6.20). The set of integro-differential Eq. (6.3) with the boundary conditions Eq. (6.16)-(6.20) are solved numerically discretizing in the physical space by the control volume approach and in the molecular velocity space by the discrete velocity method. The macroscopic quantities are computed by Gauss-Legendre quadrature in the velocity magnitudes and trapezoidal rule in the polar angles. It is noted that due to the very large computational effort the physical grid refinement technique is applied, which is described as follows: Initially, the physical mesh is uniformly distributed with only 10 intervals per unit length in each direction. The simulation is performed with this grid and, after convergence has been reached, it is repeated in a refined mesh, where the number of intervals at each physical direction has been doubled, using the previous solution as an initial condition. This procedure is repeated until the final number of nodes has been reached in order to avoid a large number of iterations for the dense grid. The implemented algorithm has been extensively applied in previous works to solve with considerable success non-linear flows of monatomic gases through short tubes due to pressure and temperature gradients [102, 155]. Therefore, a detailed description of the numerical algorithm is omitted, since it can be found in [102, 156]. Finally, the iteration process is terminated when the convergence criteria

$$\frac{1}{4K} \sum_{i=1}^{K} \left[\left| \rho_i^{(t+1)} - \rho_i^{(t)} \right| + \left| \tau_i^{(t+1)} - \tau_i^{(t)} \right| + \left| u_{z,i}^{(t+1)} - u_{z,i}^{(t)} \right| + \left| u_{r,i}^{(t+1)} - u_{r,i}^{(t)} \right| \right] < \varepsilon, \tag{6.21}$$

with t denoting the iteration index and K the number of nodes in the physical space, is fulfilled, while the termination parameter is set to $\varepsilon = 10^{-9}$.

136

6.5 Pressure and temperature driven polyatomic flows through long tubes

A polyatomic gas flow through a long circular tube with radius R connecting two large reservoirs A and B is considered. The reservoir A is maintained at constant pressure and temperature $\hat{P}_A$ and T_A respectively, while the reservoir B is maintained at constant pressure and temperature $\hat{P}_B$ and T_B respectively, with $\hat{P}_A > \hat{P}_B$ and $T_A < T_B$. Moreover, the pressure and temperature differences are assumed to be small compared to their arithmetic means

$$\hat{P}_A - \hat{P}_B \ll \frac{\hat{P}_A + \hat{P}_B}{2}, \quad T_A - T_B \ll \frac{T_A + T_B}{2}. \tag{6.22}$$

The flow configuration is shown in Fig. 6.1. When the reservoirs are maintained at different temperatures in order to mantain the temperature difference the gas begins to move from the cold vessel to the hot one even when there is no pressure drop. This phenomenon is called the thermal creep. If the system is closed, a pressure drop is established between the vessels. The pressure drop causes a gas flow which is opposite to the thermal creep so that the whole mass flow through the capillary vanishes in the stationary state. This is the so-called thermomolecular pressure effect. The thermomolecular pressure effect has been investigated for monatomic gases in [157], while the corresponding work in polyatomic gases is not available. Here the aim is to investigate the thermomolecular pressure effect in polyatomic gases based on the assumptions of the long tube ($R \ll L$) and of the small pressure and temperature differences. The study is based on the Rykov kinetic model, since this model can describe correctly the isothermal and nonisothermal polyatomic gas flow simultaneously for any rarefaction level of the gas.

6.6 Linearization for long tubes

By taking ($R \ll L$) the flow is considered as fully developed, and then, end effects at the inlet and the outlet of the channel are ignored. In addition, due to the small pressure and temperature differences assumed here in the flow direction the problem can be linearized as

[17, 106]

$$\hat{g} = \hat{f}_w^{(M)}\left(1 + L\right), \quad \hat{h} = \frac{j}{2}k_B T_w \hat{f}_w^{(M)}\left(1 + H\right), \tag{6.23}$$

with

$$\hat{f}_w^{(M)} = n_w\left(\frac{m}{2\pi k_B T_w}\right)^{3/2}\exp\left(\frac{-m\upsilon^2}{2k_B T_w}\right), \tag{6.24}$$

where $L\left(\hat{r}, \boldsymbol{\upsilon}\right)$ and $H\left(\hat{r}, \boldsymbol{\upsilon}\right)$ are the unknown linearized distribution functions, $0 \leq \hat{r} \leq R$ is the radial spatial coordinate and $\upsilon = (\xi\cos\theta, \xi\sin\theta, \xi_z)$, with $\theta = \tan^{-1}\left(\xi_y/\xi_x\right)$, is the molecular velocity vector in cylindrical coordinates. It is noted that the unknown linearized distribution functions L and H are independent of the longitudinal coordinate $\hat{z}$. The $\hat{z}-$ dependence enters implicitly in the local-Maxwellian function $\hat{f}_w^{(M)}$, since the number density n_w, the temperature T_w and the pressure $\hat{P}_w = n_w k_B T_w$ depend on the longitudinal coordinate $\hat{z}-$ direction and are constant at each cross section. In addition, at each cross section the translational, rotational and total temperatures are equal to each other and equal to T_w $(T_{tr} = T_{rot} = T = T_w)$.

The equations for the perturbation functions L and H can be written as [17, 46, 106]

$$\xi\cos\theta\frac{\partial L}{\partial\hat{r}} - \frac{\xi\sin\theta}{\hat{r}}\frac{\partial L}{\partial\theta} = \upsilon\left(L_0 - L\right) - \xi_z\frac{d\ln\hat{P}_w}{d\hat{z}} - \xi_z\left(\frac{m\upsilon^2}{2k_B T_w} - \frac{5}{2}\right)\frac{d\ln T_w}{d\hat{z}},$$

$$\xi\cos\theta\frac{\partial H}{\partial\hat{r}} - \frac{\xi\sin\theta}{\hat{r}}\frac{\partial H}{\partial\theta} = \upsilon\left(H_0 - H\right) - \xi_z\frac{d\ln\hat{P}_w}{d\hat{z}} - \xi_z\left(\frac{m\upsilon^2}{2k_B T_w} - \frac{3}{2}\right)\frac{d\ln T_w}{d\hat{z}},$$

$$L_0 = 2\frac{m\xi_z\hat{u}_z}{2k_B T_w} + \left(\frac{\varpi_0 - 1}{Z} + 1\right)\frac{2}{15}Q_{tr}\frac{m\xi_z}{\hat{P}_w k_B T_w}\left(\frac{m\upsilon^2}{2k_B T_w} - \frac{5}{2}\right), \tag{6.25}$$

$$H_0 = 2\frac{m\xi_z\hat{u}_z}{2k_B T_w} + \left(\frac{\varpi_0 - 1}{Z} + 1\right)\frac{2}{15}Q_{tr}\frac{m\xi_z}{\hat{P}_w k_B T_w}\left(\frac{m\upsilon^2}{2k_B T_w} - \frac{5}{2}\right)$$
$$+ \left(\frac{\varpi_1 - 1}{Z} + 1\right)\left(1 - \kappa\right)Q_{rot}\frac{2m\xi_z}{j\hat{P}_w k_B T_w},$$

where $\upsilon = \hat{P}_w/\mu(T_w)$ is the collision frequency, $\mu(T_w)$ is the viscosity at temperature T_w, Z^{-1} is a parameter which indicates the fraction of the rotational collisions of their total number, j is the number of the rotational degrees of freedom taking the values 2 and 3 for linear and nonlinear polyatomic molecules. Also, the parameters ϖ_0 and ϖ_1 are determined in order to obtain the correct translational and rotational thermal conductivity coefficients from the

Eqs. (3.15) and (3.16), while κ is a constant which for a power intermolecular potential varies between the values of $1/1.2$ for hard spheres and $1/1.543$ for Maxwell molecules. Furthermore, following similar manipulations as for the Eqs. (6.25), the velocity $\hat{u}_z$, the translational heat flux Q_{tr} and the rotational heat flux Q_{rot} in terms of the perturbation functions L and H are obtained as

$$\hat{u}_z\left(\hat{r}\right) = \frac{1}{n_w} \int\limits_{-\infty}^{\infty} \int\limits_{0}^{2\pi} \int\limits_{0}^{\infty} \xi\xi_z \hat{f}_w^{(M)} L d\xi d\theta d\xi_z, \tag{6.26}$$

$$Q_{tr}\left(\hat{r}\right) = \frac{m}{2} \int\limits_{-\infty}^{\infty} \int\limits_{0}^{2\pi} \int\limits_{0}^{\infty} \xi\xi_z \left(\upsilon^2 - \frac{5k_B}{m} T_w\right) \hat{f}_w^{(M)} L d\xi d\theta d\xi_z, \tag{6.27}$$

$$Q_{rot}\left(\hat{r}\right) = \frac{jk_B T_w}{2} \int\limits_{-\infty}^{\infty} \int\limits_{0}^{2\pi} \int\limits_{0}^{\infty} \xi\xi_z \hat{f}_w^{(M)} \left(H - L\right) d\xi d\theta d\xi_z, \tag{6.28}$$

where m is the molecular mass and k_B is the Boltzmann constant. The Eqs. (6.25)-(6.28) hold true in any cross section of the tube. Taking the values of the macroscopic parameters in a certain cross section $\hat{z} = \hat{z}_0$ as reference quantities the following non-dimensional quantities are introduced

$$r = \frac{\hat{r}}{R}, \ \zeta = \frac{\xi}{\upsilon_0}, \ c_z = \frac{\xi_z}{\upsilon_0}, \ f_w^{(M)} = \frac{\hat{f}_w^{(M)} \upsilon_0^3}{n_0}, \ u_z = \frac{\hat{u}_z}{\upsilon_0}, \ q_{tr} = \frac{Q_{tr}}{\hat{P}_0 \upsilon_0}, \ q_{rot} = \frac{Q_{rot}}{\hat{P}_0 \upsilon_0}, \tag{6.29}$$

with $\upsilon_0 = \sqrt{2k_B T_0/m}$ and $\hat{P}_0 = n_0 k_B T_0$ being the most probable molecular speed and the reference pressure respectively. It is obvious that $n_0 = n_w$, $T_0 = T_w$ and $\hat{P}_0 = \hat{P}_w$. The problem can be further simplified eliminating the variable c_z introducing the following integrals

$$F = \frac{1}{\sqrt{\pi}} \int\limits_{-\infty}^{\infty} L c_z \exp\left(-c_z^2\right) dc_z, \tag{6.30}$$

$$G = \frac{1}{\sqrt{\pi}} \int\limits_{-\infty}^{\infty} L c_z^3 \exp\left(-c_z^2\right) dc_z, \tag{6.31}$$

139

$$S = \frac{1}{\sqrt{\pi}} \int\limits_{-\infty}^{\infty} H c_z \exp\left(-c_z^2\right) dc_z. \tag{6.32}$$

Then the system of equations (6.25) is rewritten as

$$\zeta \cos\theta \frac{\partial F}{\partial r} - \frac{\zeta \sin\theta}{r} \frac{\partial F}{\partial \theta} = \delta_0 \left(F_0 - F\right) - \frac{1}{2}\left[\mathrm{X}_P + \left(\zeta^2 - 1\right)\mathrm{X}_T\right],$$

$$\zeta \cos\theta \frac{\partial G}{\partial r} - \frac{\zeta \sin\theta}{r} \frac{\partial G}{\partial \theta} = \delta_0 \left(G_0 - G\right) - \frac{3}{4}\left(\mathrm{X}_P + \zeta^2\mathrm{X}_T\right),$$

$$\zeta \cos\theta \frac{\partial S}{\partial r} - \frac{\zeta \sin\theta}{r} \frac{\partial S}{\partial \theta} = \delta_0 \left(S_0 - S\right) - \frac{1}{2}\left(\mathrm{X}_P + \zeta^2\mathrm{X}_T\right),$$

$$F_0 = u_z + \left(\frac{\varpi_0 - 1}{Z} + 1\right)\frac{2}{15}q_{tr}\left(\zeta^2 - 1\right), \tag{6.33}$$

$$G_0 = \frac{3u_z}{2} + \left(\frac{\varpi_0 - 1}{Z} + 1\right)\frac{1}{5}q_{tr}\zeta^2,$$

$$S_0 = u_z + \left(\frac{\varpi_0 - 1}{Z} + 1\right)\frac{2}{15}q_{tr}\left(\zeta^2 - 1\right) + \left(\frac{\varpi_1 - 1}{Z} + 1\right)\left(1 - \kappa\right)\frac{2q_{rot}}{j},$$

while the macroscopic quantities u_z, q_{tr} and q_{rot} are given by

$$u_z = \frac{1}{\pi} \int\limits_{0}^{2\pi} \int\limits_{0}^{\infty} \zeta F \exp\left(-\zeta^2\right) d\zeta d\theta, \tag{6.34}$$

$$q_{tr} = \frac{1}{\pi} \int\limits_{0}^{2\pi} \int\limits_{0}^{\infty} \zeta\left[F\left(\zeta^2 - \frac{5}{2}\right) + G\right]\exp\left(-\zeta^2\right) d\zeta d\theta, \tag{6.35}$$

$$q_{rot} = \frac{j}{2\pi} \int\limits_{0}^{2\pi} \int\limits_{0}^{\infty} \zeta(S - F)\exp\left(-\zeta^2\right) d\zeta d\theta, \tag{6.36}$$

while the total heat flux is defined as $q = q_{rot} + q_{tr}$. In Eq. (6.33) the parameter δ_0 is the rarefaction parameter defined as

$$\delta_0 = \frac{\hat{P}_0 R}{\mu_0 \upsilon_0} \tag{6.37}$$

140

and the parameters X_P and X_T are the dimensionless pressure and temperature gradients which are determined by the following formulas

$$\mathrm{X}_P = \frac{R}{\hat{P}_w} \frac{\partial \hat{P}_w}{\partial \hat{z}}, \quad \mathrm{X}_T = \frac{R}{T_w} \frac{\partial T_w}{\partial \hat{z}}. \tag{6.38}$$

The gas-wall interaction is modeled by the Maxwell diffuse-specular reflection condition [17]. At the boundaries we have

$$\hat{g}^+ = \alpha_M \hat{f}_w^{(M)} + (1 - \alpha_M)\, \hat{g}^-, \quad \hat{h}^+ = \alpha_M \frac{j}{2} k_B T_w \hat{f}_w^{(M)} + (1 - \alpha_M)\, \hat{h}^-, \tag{6.39}$$

where $\hat{g}^+$, $\hat{h}^+$ and $\hat{g}^-$, $\hat{h}^-$ are the distributions representing particles departing and arriving at the wall, respectively, while $\hat{f}_w^{(M)}$ is the Maxwellian defined by the wall temperature. The parameter α_M is the so-called tangential momentum accommodation coefficient and denotes the portion of the particles reflecting diffusively from the wall. Applying the above described procedure (nondimensionalization, linearization, projection) the boundary conditions for the reduced distribution functions F, G and S at $r = 1$ become [17]

$$F^+ (1, \zeta, \theta) = (1 - \alpha_M)\, F^- (1, \zeta, \pi - \theta) ,$$

$$G^+ (1, \zeta, \theta) = (1 - \alpha_M)\, G^- (1, \zeta, \pi - \theta) , \tag{6.40}$$

$$S^+ (1, \zeta, \theta) = (1 - \alpha_M)\, S^- (1, \zeta, \pi - \theta) ,$$

while at $r = 0$ using the symmetry condition become

$$F^+ (0, \zeta, \theta) = F^- (0, \zeta, \pi - \theta) ,$$

$$G^+ (0, \zeta, \theta) = G^- (0, \zeta, \pi - \theta) , \tag{6.41}$$

$$S^+ (0, \zeta, \theta) = S^- (0, \zeta, \pi - \theta) .$$

Boundary conditions (6.40) and (6.41) are valid for $\theta \in [\pi/2, 3\pi/2]$ and $\theta \in [-\pi/2, \pi/2]$ respectively.

The linear integrodifferential equation (6.33), supplemented by the corresponding macroscopic quantities (6.34)-(6.36) and subject to the boundary conditions (6.40) and (6.41), are solved numerically. The implemented numerical scheme has been described, in detail, for channels with circular, rectangular, and triangular cross sections in the case of monatomic gases in a series of previous works [146–148]. In all cases, the kinetic equation is discretized in the molecular velocity space by the discrete velocity method and in the physical space by typical finite difference scheme. Then, the discretized equations are solved in an iterative manner.

The kinetic solution depends on three dimensionless parameters, namely, the reference rarefaction parameter δ_0, the accommodation coefficient α_M and the parameter Z. Moreover, in the Rykov model the parameters ϖ_0, ϖ_1 and κ ,depending on the working gas, must be specified as it has already been described previously. Based on the kinetic solution, several overall macroscopic quantities of practical interest may be deduced. The main calculated quantities are the dimensionless mass (W) and heat (E) flow rates, which are defined as

$$W = \frac{\dot{M}\upsilon_0}{\pi R^2 \hat{P}_0} = 4 \int_0^1 u_z r dr \qquad (6.42)$$

and

$$E = \frac{2\dot{E}}{\pi R^2 \hat{P}_0 \upsilon_0} = 4 \int_0^1 q r dr, \qquad (6.43)$$

where $\dot{M}$ [Kg/s] and $\dot{E}$ [J/s] are the dimensional mass and heat flow rates respectively. In polyatomic gases the dimensionless heat flow rate (E) can be written as a sum of the two heat flow rates, one related to the translational degrees of freedom and the other related to the rotational degrees of freedom

$$E = E_{tr} + E_{rot}, \quad E_{tr} = 4 \int_0^1 q_{tr} r dr, \quad E_{rot} = 4 \int_0^1 q_{rot} r dr. \qquad (6.44)$$

Based on the assumption of the small pressure and temperature differences the flow rates (W) and (E) can be split in two parts [17]

$$W = -W_P \mathrm{X}_P + W_T \mathrm{X}_T, \quad E = E_P \mathrm{X}_P - E_T \mathrm{X}_T, \quad E_i = E_{tr,i} + E_{rot,i}, \quad i = P, T. \quad (6.45)$$

Here the coefficients W_P, $E_{tr,P}$ and $E_{rot,P}$ are obtained by solving the Poiseuille problem $(\mathrm{X}_P = 1, \mathrm{X}_T = 0)$, while for the coefficients W_T, $E_{tr,T}$ and $E_{rot,T}$ the thermal creep flow $(\mathrm{X}_P = 0, \mathrm{X}_T = 1)$ is solved. It is noted that the dimensionless mass flow rate (W_T) due to temperature difference can be obtained from the solution of the Poiseuille problem using the Onsager relation [17]

$$W_T = E_P. \quad (6.46)$$

Eq. (6.46) is used for benchmarking purposes in order to estimate the accuracy of the calculations.

6.7   Thermomolecular pressure effect

The thermomolecular pressure effect pointed out by Reynolds [159] and named by him as thermal transpiration. Knudsen [158] continued the experimental investigations of the effect, while Maxwell [122] gave some theoretical explanations of this phenomenon. The thermomolecular pressure effect is very important due to its scientific importance including calculations of the Eucken factor, rotational collision number and other thermal properties of polyatomic gases. Furthermore, the thermomolecular pressure effect is useful in practice because in many studies it is necessary to calculate the pressure $\hat{P}_A$ in a reservoir maintained at temperature T_A, from a measured pressure $\hat{P}_B$ in an other reservoir which is maintained at different temperature T_B. The pressures $\hat{P}_A$, $\hat{P}_B$ and the temperatures T_A, T_B are related by the law [17, 157]

$$\frac{\hat{P}_B}{\hat{P}_A} = \left(\frac{T_B}{T_A} \right)^\gamma, \quad (6.47)$$

where the coefficient γ depends on many parameters: length-to-radius ratio of the tube, type of the gas, nature of the gas-surface interaction, etc. It is noted that the coefficient γ depends

143

strongly on the rarefaction parameter δ_0 given by Eq. (6.37). If the pressure and temperature drops are small according to Eq. (6.23) the coefficients W_P and W_T do not vary along the tube. Then, the coefficient γ is calculated setting $W = 0$ in Eq. (6.45)

$$\gamma = \frac{W_T}{W_P}. \tag{6.48}$$

Under small temperature and pressure differences, the coefficients W_P and W_T are taken for any value of the rarefaction parameter between its values at the inlet ($\hat{z} = 0$) and at the outlet ($\hat{z} = L$) of tube.

6.8 Results and discussion of flows through short tubes

Calculations have been carried out in the range of the rarefaction parameter δ_0 from 0 to 10, i.e. in the free molecular and transition regimes and for $L/R = 1$ and 5. The limits of the variation of the parameter Z in a shock wave are 1 and 5, so the choice of $Z = 3$ for the problem under question is reasonable. Some indicative simulations have been performed for $Z = 6$ showing very small effect on the calculated quantities. The presented results have been obtained for purely diffuse boundary conditions and the HS model. All the discretization parameters used are displayed in Table 6.1. It is noted that the supercomputing facility of Helios in Japan provided the computational resources for the simulations. Tabulated results for macroscopic quantities as well as plotted results for the distribution of various macroscopic quantities are presented in Subsection 6.8.1. In Subsection 6.8.2 the quantities appearing in the parametric study on propulsion performance of micro tubes are shown. Also, the influence of the rotational degrees of freedom is investigated and the differences-similarities compared to the corresponding monatomic modelling are pointed out.

144

Table 6.1: Discrete velocity algorithm numerical parameters

Initial number of nodes per unit length in each direction	10
Number of grid levels	4
Final nodes per unit length $N_x = N_r$	80
Discrete angles in $(0, \pi)$	160
Discrete magnitudes	16×16
Convergence criterion	$< 10^{-9}$
Container sizes	15×15

6.8.1 Flow rates and field distributions

In Table 6.2 the dimensionless flow rate W for $j = 0, 2, 3$ ($j = 0$ refers to monatomic gases) is given. It is noted that the simulation for $j = 0$ has been performed based on the BGK model for monatomic gases. Clearly, the effect of the internal degrees of freedom on the gas flow rate is very small for all values of the rarefaction parameter and for both $L/R = 1$ and 5. It is noted however that for $\delta_0 = 1$ and 10, W is decreased as j is increased. Also, W is increased as the length of the channel is decreased and the rarefaction parameter is increased. More specifically, the flow rate for $\delta_0 \in [0.1, 1]$ increases very slowly and then more rapidly for $\delta_0 \in [1, 10]$. Additional simulations have been performed with $Z = 6$ for $\delta_0 = 1$ and $L/R = 1$ and 5 showing that the mass flow rate does not change more than 0.1%.

In Fig. 6.2 the distributions of the Mach number along the symmetry axis $r = 0$ for $L/R = 1$ and 5 at $\delta_0 = 10$ are shown. The Mach number far upstream is almost zero and is increased in the region just before the tube, while after the tube it is rapidly decreased. It is seen that as the number of the internal degrees of freedom is increased the Mach number is increased due to the decrease of the ratio of the specific heat while the magnitude of the velocity vector in the two types of gas is almost the same.

In Fig. 6.3 the distributions of the dimensionless axial velocity, pressure, and temperature along the symmetry axis $r = 0$ for $\delta_0 = 0.1$ and 10 with $L/R = 1$ are shown. In Fig. 6.4 the corresponding results for $L/R = 5$ are presented. Starting with the pressure variation, it is seen that far upstream is equal to one, then it is rapidly decreased through the tube and finally after the tube it gradually approaches the far downstream conditions. As expected the axial velocity

has the same behavior with the Mach number. The maximum value of the velocity is increased as δ_0 is increased. The axial velocity and the pressure profiles in polyatomic gases ($j = 2, 3$) are quantitatively very close to corresponding profiles for monatomic gases. The temperature equals unity in most of the domain, while inside the tube is decreased. The minimum value of the temperature distribution is decreased as the rarefaction of the gas is increased and the ratio L/R is increased. In the case of polyatomic gases the translational τ_{tr} and total τ_{rot} temperatures have the same qualitative behavior with the temperature of the monatomic gas. The rotational temperature τ_{rot} is maintained almost constant in the whole domain for small δ_0, but as the rarefaction level of the gas is decreased it is also decreased in the same way as the translational and total temperatures.

Distributions of the dimensionless axial velocity and temperatures in the radial direction at the middle ($z = L/2R$) of the tube are shown in Fig. 6.5 for $\delta_0 = 1$ and $\delta_0 = 10$ with $L/R = 1$. As expected, the velocities follow a parabolic type shape having minimum and maximum values at the wall and at the center of the tube, respectively. The velocity profiles of diatomic gases ($j = 2$) are almost identical with the corresponding monatomic profiles. The corresponding temperature profiles are also shown. In all cases a temperature drop across the tube (radial direction) is observed. For $\delta_0 = 1$, the translational temperature of a diatomic gas is close to the corresponding temperature of a monatomic gas, while the rotational temperature is kept almost constant. For $\delta_0 = 10$, the translational temperature of a diatomic gas is higher than the temperature of a monatomic gas, while the rotational temperature is not constant anymore and it is reduced moving from the wall towards the center of the tube.

For completeness purposes in Fig. 6.6, a more complete picture of the flow field is provided for $L/R = 1$. Isolines of the number density, axial velocity and temperatures (translational, rotational and total) along with the streamlines are plotted for $\delta_0 = 0.1$ and $\delta_0 = 10$. It is seen that the structure of the flow field between rarefied and dense atmospheres is different. At $\delta_0 = 0.1$ the density is almost symmetric with regard to the y axis, while at $\delta_0 = 10$ there is no symmetry. Also, as the atmosphere becomes more dense, the flow accelerates faster and the maximum axial velocity is increased. Furthermore, the ray effect are quite strong in the low rarefaction fields due to the discontinuities of the distribution function. For both values of δ_0 the

146

translational and total temperatures are decreased slightly inside the channel and more intense at the outlet of the tube. However, the rotational temperature remains constant at $\delta_0 = 0.1$, while at $\delta_0 = 10$ is decreased in the same way as the translational and total temperatures as it has been already observed in Fig. 6.3.

6.8.2 Propulsion characteristics of micro-tubes

In Table 6.2 the variation of the dimensionless thrust F_t, the impulse factor I_{SP} and the discharge coefficient C_d in terms of the rarefaction parameter δ_0 and the ratio L/R is presented. The thrust is increased as the rarefaction parameter δ_0 is increased and the ratio L/R is decreased. It is clear that the propulsion efficient is increased as the tube length is decreased. Similarly to the flow rates, the rotational degrees of freedom and the parameter Z have a small effect on the values of F_t. It is seen however, that as j is increased F_t is slightly increased. As the flow becomes more rarefied, I_{SP} is decreased. The increment of the rotational degrees of freedom leads to an increment of the impulse factor. This is well expected since the impulse factor is defined as the ratio of the thrust over the flow rate, with the former one increasing and the latter one decreasing as j is increased. The discharge coefficient C_d decreases by increasing the tube ratio L/R, while for fixed L/R, C_d is increased as δ_0 is increased. In addition, as the rotational degrees of freedom are increased from zero to two and then to three the coefficient C_d is increased. This is due to the fact that the ratio of the specific heats of the gas is decreased as j is increased, taking also into account that the flow rates of the two types of gases are about the same. Overall it may be concluded that the propulsion characteristics of polyatomic gas expansion through micro-tubes are slightly improved compared to the corresponding ones in the case of monatomic gases.

In order to facilitate comparisons with experiments, in Fig. 6.7 the dimensional mass flow rate $\dot{M}$ [Kg/s], thrust $\hat{F}_t$ [N] and impulse factor $\hat{I}_{SP}$ [s] are presented in terms of the reference pressure $\hat{P}_A$ [Pa] for two monatomic gases (He, Ne), one diatomic gas (N$_2$) and for one polyatomic gas (CH$_4$). The length and the radius of the tube is $L = R = 0.05$ cm. The reference temperature is $T_0 = 295$ K. As it is seen as the molecular weight of the gas is decreased the mass flow rate is also decreased. This behaviour is well expected because from Eq. (6.11) the

mass flow rate is proportional to the square root of the molecular mass for the same pressure, temperature and dimensionless mass flow rate W. The thrust $\hat{F}_t$ is almost independent of the gas and depends only on the pressure. Both quantities, mass flow rate and thrust, are increased as the reference pressure is increased and the atmosphere becomes more dense. Finally, the impulse factor changes slightly with the pressure and depends strongly on the working gas. This is justified by the fact that the dimensional impulse factor is inversely proportional to the square root of the molecular mass and depends slightly on the molecular structure as it is seen on Table 6.2. Similar qualitatively behaviour is observed for $L = 5R = 0.25$ cm, therefore the corresponding figures are omitted.

6.9 Flow rates and thermomolecular pressure effect in long tubes

The problem of the fully developed flows of polyatomic gases through long tubes depends on the parameter Z, the rarefaction parameter δ_0, the number of the rotational degrees of freedom j, the parameter κ and on the tangential momentum accommodation coefficient α_M. The main calculations were carried out for $Z = 1$ and 5 and for $\delta_0 \in [0, 100]$. Values for the parameter κ for various polyatomic gases are given in [120], while for a given κ and Z the quantities ϖ_0 and ϖ_1 are chosen according to Eqs. (3.15) and (3.16). Three typical values of the accommodation coefficient α_M have been examined namely 0.5, 0.8 and 1. Depending on the value of rarefaction parameter δ_0, the discretization has been progressively refined to ensure grid independent results up to several significant figures. The presented results are for 400 angles in $[0, \pi]$, 800 nodes in radial direction and for 80 discrete magnitudes.

A comparison with the numerical results in [106] is performed in Tables 6.3 and 6.4 for N_2 ($j = 2$, $\varpi_0 = 0.2354$, $\varpi_1 = 0.3049$, $\kappa = 0.645$) and various values of δ_0, with $\alpha_M = 1$. The dimensionless mass and heat flow rates under pressure ($X_P = 1$, $X_T = 0$) and temperature ($X_P = 0$, $X_T = 1$) gradients, based on the Rykov kinetic model, for $Z = 1$ and 5 are provided. In this case of the pressure driven flow, the heat flow due to the rotational degrees of freedom is always 0 ($E_{rot,P} = 0$) [106]. As it is seen the comparison between the present results and the

corresponding results in [106] is very good with the relative error being less than 1%. Also the Eq. (6.46) is clearly fulfilled in the whole range of δ_0. Overall, the accuracy of the numerical results is clearly demonstrated.

In order to examine the effect of the rotational degrees of freedom in Tables 6.5 and 6.6 the corresponding mass flow and heat flow rates are shown for the linear polyatomic CO_2 ($j = 2$) and for the nonlinear polyatomic gas CH_4 ($j = 3$). For completeness and comparison purposes, the corresponding results obtained by the Shakhov model for monatomic gases are also given. The parameter κ for CO_2 and CH_4 is taken equal to 0.633 and 0.690 respectively [120]. Values of ϖ_0 and ϖ_1 for CO_2 ($Z = 1 : \varpi_0 = 0.549$, $\varpi_1 = 1.373$; $Z = 5 : \varpi_0 = 0.618$, $\varpi_1 = 1.451$) and for CH_4 ($Z = 1 : \varpi_0 = 0.288$, $\varpi_1 = 1.462$; $Z = 5 : \varpi_0 = 0.446$, $\varpi_1 = 1.554$) are chosen according to Eqs. (3.15) and (3.16). It is seen that the mass flow rates W_P are very close to those obtained by the Shakhov model for all values of the rarefaction parameter δ_0. However, the effect of the rotational degrees of freedom on the heat flow E_P is greater and amounts to $20 - 30\%$ at $Z = 1$ and moderate values of the rarefaction parameter. Independently of the parameter δ_0, with increase in Z the mass W_P and heat E_P flow rates approach the corresponding values obtained by the Shakhov model. The results for W_T are omitted since heat flow rates in Poiseuille flow are identical to the mass flow rates in thermal creep flows. As with Poiseuille flow, $E_{tr,T}$ increases as Z is increased. However, $E_{rot,T}$ increases as Z decreases because the rotational thermal conductivity increases with decreasing Z [46]. The heat flow $E_T = E_{tr,T} + E_{rot,T}$ of the linear polyatomic gases (N_2, CO_2) can be higher about $30 - 40\%$ than the corresponding monatomic heat flow, while this difference in the case of nonlinear polyatomic gas (CH_4) can reach $50 - 65\%$. Furthermore, the rotational heat flow rate of nonlinear polyatomic gases is higher about $40 - 50\%$ than the heat flow of the linear polyatomic gases. It is noted that the rotational heat flow rates of nonlinear polyatomic gases are one-and-a-half times larger than those of diatomic gases, provided the values of Z, ϖ_0, ϖ_1, κ for diatomic and nonlinear polyatomic gases are the same.

The effect of the tangential momentum accommodation coefficient α_M on the flow rates is shown on Tables 6.7 and 6.8. Two values of the tangential momentum accommodation coefficient namely $\alpha_M = 0.5$ and $\alpha_M = 0.8$ are considered. It is noted that the values of the

parameters $\varpi_0 = 0.2354$, $\varpi_1 = 0.3049$ and $\kappa = 0.645$ are the same with those used in the simulations of N_2 for $\alpha_M = 1$ (Tables 6.3 and 6.4). It is seen that as α_M is decreased the mass flow rates in the Poiseuille flow and the heat flow rates in the thermal creep flow are increased for all values of the rarefaction parameter δ_0. However, the heat flow rate E_P in Poiseuille flow for large values of the rarefaction parameter ($\delta_0 > 1$) is decreased as α_M decreases. All these observations have been already mentioned for monatomic gases in literature [17, 157]. It is noted that the results for $\alpha_M \neq 1$ are qualitatively similar with those obtained for $\alpha_M = 1$ regarding the effect of internal degrees of freedom on the mass and heat flow rates for both types of flow.

Next, the thermomolecular pressure effect in the case of polyatomic gases with rotational degrees of freedom is investigated in a wide range of rarefaction parameter δ_0 from 0 to 30. In Fig. 6.8 the numerical results for the coefficient γ are given in terms of the rarefaction parameter δ_0. Two gases are examined namely N_2 and CH_4 with 2 and 3 rotational degrees of freedom respectively. The results are provided for two indicative values $Z = 1$ and 5, while the parameters ϖ_0, ϖ_1 and κ are chosen to be the same with those given in Tables 6.3 - 6.6 for N_2 and CH_4. Also in Fig. 6.8, for comparison purposes the results obtained from the Shakhov model for monatomic gases are shown. As it seen the coefficient γ of N_2 is almost the same with those obtained for CH_4 independently of the parameter Z. Also, it is deduced that for moderate values of the rarefaction parameter δ_0 the coefficient $\gamma = E_P/W_P$ of monatomic gases is higher than the corresponding one of polyatomic gases. The highest differences can reach $30 - 40\%$ at $Z = 1$. It is noted that at $\delta_0 = 0$ the results obtained by the monatomic modeling and the corresponding polyatomic ones coincide. Furthermore, as the parameter Z is increased the differences between monatomic and polyatomic calculations on γ are decreased.

A comparison with experimental data in [152] is performed in Fig. 6.9. The working gas is N_2, while the temperature is $T = 544$ K. The parameters Z and κ for N_2 at $T = 544$ K are taken equal to 3.513 and 0.752 respectively. Then based on the Eqs. (3.15) and (3.16) we obtain $\varpi_0 = 0.499$ and $\varpi_1 = 1.967$. As it is seen very good agreement is observed between the simulations and experiments in the whole range of the rarefaction parameter.

6.10   Concluding remarks

The nonlinear polyatomic flows through short and long tubes have been investigated. The nonlinear flows through short tube due to small pressure differences ($\hat{P}_B/\hat{P}_A = 0.01$) have been studied based on the Holway kinetic model subject to Maxwell boundary conditions. The quantitative behaviour of all macroscopic quantities in terms of the rarefaction parameter δ_0, L/R and j are examined in detail. Also, the characteristic parameters of short tubes operating as propulsion systems in the case of polyatomic gases have been computed. It is found that the effect of the rotational degrees of freedom on the macroscopic quantities is small except in the case of temperature distributions. It may be concluded that the overall propulsion efficiency in the case of polyatomic gases compared to the one in monatomic gases is slightly improved. The analysis has been extended to include pressure and temperature driven flows through long tubes using the Rykov kinetic model. The very good agreement with available numerical results in literature along with the successful comparison between simulations and experiments demonstrate the validity of the modelling. It is shown that the main effect of the rotational degrees of freedom exhibits itself in a flow under small temperature difference, while the effect of the rotational degrees of freedom on the mass flow rates through long tubes in the case of the small pressure differences is almost negligible. More specifically the heat flow of the linear polyatomic gases (N_2, CO_2) can be higher about $30 - 40\%$ than the corresponding monatomic heat flow, while this difference in the case of nonlinear polyatomic gas (CH_4) can reach $50 - 65\%$. Finally, the thermomolecular pressure effect in the case of polyatomic gases has been considered, showing that the coefficient $\gamma = E_P/W_P$ of monatomic gases is higher than the corresponding one of polyatomic gases. The highest differences can reach $30 - 40\%$ at $Z = 1$.

Table 6.2: Dimensionless flow rate W, thrust F_t, impulse factor I_{SP} and discharge coefficient C_d in terms of the rarefaction parameter and tube length to radius ratio.

	j	δ_0							
		0		0.1		1		10	
		$L/R = 1$	$L/R = 5$	$L/R = 1$	$L/R = 5$	$L/R = 1$	$L/R = 5$	$L/R = 1$	$L/R = 5$
W	0	0.6658	0.3071	0.6781	0.3099	0.7612	0.3344	1.070	0.5487
	2	0.6658	0.3071	0.6779	0.3099	0.7598	0.3341	1.053	0.5435
	3	0.6658	0.3071	0.6779	0.3099	0.7594	0.3341	1.049	0.5421
F_t	0	0.4500	0.2079	0.4591	0.2103	0.5215	0.2293	0.7623	0.3867
	2	0.4834	0.2232	0.4925	0.2255	0.5546	0.2442	0.7859	0.4027
	3	0.4918	0.2270	0.5009	0.2293	0.5629	0.2480	0.7922	0.4069
I_{SP}	0	0.6759	0.6771	0.6771	0.6786	0.6852	0.6857	0.7123	0.7049
	2	0.7261	0.7268	0.7265	0.7275	0.7300	0.7309	0.7463	0.7409
	3	0.7386	0.7392	0.7388	0.7398	0.7413	0.7423	0.7556	0.7506
C_d	0	0.3658	0.1687	0.3725	0.1703	0.4182	0.1837	0.5879	0.3014
	2	0.3879	0.1789	0.3950	0.1806	0.4427	0.1947	0.6136	0.3167
	3	0.3945	0.1819	0.4017	0.1836	0.4500	0.1980	0.6213	0.3212

Table 6.3: Dimensionless flow rates W_P, E_P and W_T of N_2 ($\varpi_0 = 0.2354$, $\varpi_1 = 0.3049$, $\kappa = 0.645$) in the Poiseuille ($X_P = 1$, $X_T = 0$) and thermal creep ($X_P = 0$, $X_T = 1$) flows.

	δ_0	$Z = 1$		$Z = 5$	
		Present work	[106]	Present work	[106]
W_P	0	1.5045	1.4962	1.5045	1.4962
	0.1	1.4051	1.4043	1.4082	1.4075
	0.5	1.3896	1.3889	1.3982	1.3975
	1	1.4619	1.4612	1.4731	1.4724
	10	3.5662	3.5647	3.5737	3.5724
	100	26.02	26.00	26.02	26.01
E_P	0	0.7522	0.7424	0.7522	0.7424
	0.1	0.6028	0.6008	0.6172	0.6156
	0.5	0.4300	0.4288	0.4678	0.4666
	1	0.3368	0.3356	0.3830	0.3820
	10	0.0744	0.0742	0.0950	0.0948
	100	0.0083	0.0082	0.0107	0.0108
W_T	0	0.7523	0.7461	0.7523	0.7461
	0.1	0.6029	0.6023	0.6171	0.6166
	1	0.3367	0.3364	0.3831	0.3826
	10	0.0743	0.0742	0.0950	0.0948
	100	0.0083	0.0084	0.0107	0.0106

Table 6.4: Dimensionless heat flow rates ($E_{tr,T}$, $E_{rot,T}$) of N_2 ($\varpi_0 = 0.2354$, $\varpi_1 = 0.3049$, $\kappa = 0.645$) in the thermal creep flow ($X_P = 0$, $X_T = 1$).

δ_0	$Z = 1$				$Z = 5$			
	Present work		[106]		Present work		[106]	
	$E_{tr,T}$	$E_{rot,T}$	$E_{tr,T}$	$E_{rot,T}$	$E_{tr,T}$	$E_{rot,T}$	$E_{tr,T}$	$E_{rot,T}$
0	3.3852	1.5046	3.3608	1.4944	3.3852	1.5046	3.3608	1.4944
0.1	2.7964	1.2454	2.7878	1.2414	2.863	1.2772	2.8556	1.274
1	1.4246	0.622	1.4204	0.6202	1.6176	0.7116	1.6134	0.7098
10	0.2522	0.1052	0.2522	0.1052	0.3186	0.1322	0.3184	0.1332
100	0.027	0.0111	0.027	0.0112	0.0345	0.0143	0.0346	0.0142

153

Table 6.5: Dimensionless flow rates W_P and E_P in the Poiseuille flow ($X_P = 1$, $X_T = 0$).

	δ_0	Rykov				Shakhov
		CO_2		CH_4		
		$Z = 1$	$Z = 5$	$Z = 1$	$Z = 5$	
W_P	0	1.5045	1.5045	1.5045	1.5045	1.5045
	0.1	1.4067	1.4086	1.4054	1.4084	1.4090
	1	1.4673	1.4748	1.4628	1.4740	1.4764
	10	3.5696	3.5749	3.5667	3.5744	3.5761
	100	26.02	26.02	26.02	26.02	26.02
$W_T{=}E_P$	0	0.7522	0.7522	0.7522	0.7522	0.7522
	0.1	0.6101	0.6190	0.6040	0.6182	0.6208
	1	0.3590	0.3898	0.3403	0.3868	0.3968
	10	0.0837	0.0984	0.0758	0.0968	0.1020
	100	0.0094	0.0111	0.0084	0.0110	0.0116

Table 6.6: Dimensionless heat flow rates ($E_{tr,T}$, $E_{rot,T}$) in the thermal creep flow ($X_P = 0$, $X_T = 1$).

δ_0	$E_{tr,T}$				$E_{rot,T}$				Shakhov
	CO_2		CH_4		CO_2		CH_4		
	$Z = 1$	$Z = 5$	$Z = 1$	$Z = 5$	$Z = 1$	$Z = 5$	$Z = 1$	$Z = 5$	
0	3.385	3.385	3.385	3.385	1.505	1.505	2.257	2.257	3.385
0.1	2.830	2.871	2.802	2.868	1.311	1.293	1.953	1.926	2.880
1	1.517	1.646	1.439	1.633	0.8329	0.7647	1.198	1.099	1.675
10	0.282	0.329	0.257	0.324	0.1822	0.1528	0.250	0.211	0.341
100	0.0304	0.0358	0.0275	0.0352	0.0200	0.0165	0.0272	0.0227	0.0372

Table 6.7: Dimensionless flow rates W_P and E_P of N$_2$ ($\varpi_0 = 0.2354$, $\varpi_1 = 0.3049$, $\kappa = 0.645$) in the Poiseuille flow ($X_P = 1$, $X_T = 0$) for $\alpha_M = 0.5$ and $\alpha_M = 0.8$.

	δ_0	$Z = 1$		$Z = 5$	
		$\alpha_M = 0.5$	$\alpha_M = 0.8$	$\alpha_M = 0.5$	$\alpha_M = 0.8$
	0	4.514	2.257	4.514	2.257
	0.1	3.695	2.000	3.708	2.005
W_P	0.5	3.340	1.889	3.359	1.901
	1	3.328	1.936	3.345	1.949
	10	5.394	4.031	5.401	4.038
	0	2.257	1.128	2.257	1.128
	0.1	1.266	0.798	1.334	0.824
$W_T = E_P$	0.5	0.631	0.498	0.722	0.551
	1	0.414	0.364	0.493	0.421
	10	0.0648	0.0706	0.0833	0.0905

Table 6.8: Dimensionless heat flow rates ($E_{tr,T}$, $E_{rot,T}$) of N$_2$ ($\varpi_0 = 0.2354$, $\varpi_1 = 0.3049$, $\kappa = 0.645$) in the thermal creep flow ($X_P = 0$, $X_T = 1$) for $\alpha_M = 0.5$ and $\alpha_M = 0.8$.

δ_0	$Z = 1$				$Z = 5$			
	$\alpha_M = 0.5$		$\alpha_M = 0.8$		$\alpha_M = 0.5$		$\alpha_M = 0.8$	
	$E_{tr,T}$	$E_{rot,T}$	$E_{tr,T}$	$E_{rot,T}$	$E_{tr,T}$	$E_{rot,T}$	$E_{tr,T}$	$E_{rot,T}$
0	10.155	4.514	5.078	2.257	10.155	4.514	5.078	2.257
0.1	6.240	2.769	3.801	1.692	6.578	2.931	3.924	1.751
0.5	3.075	1.334	2.314	1.016	3.519	1.538	2.560	1.131
1	1.947	0.833	1.615	0.700	2.317	0.998	1.864	0.814
10	0.262	0.109	0.256	0.107	0.333	0.138	0.324	0.135

155
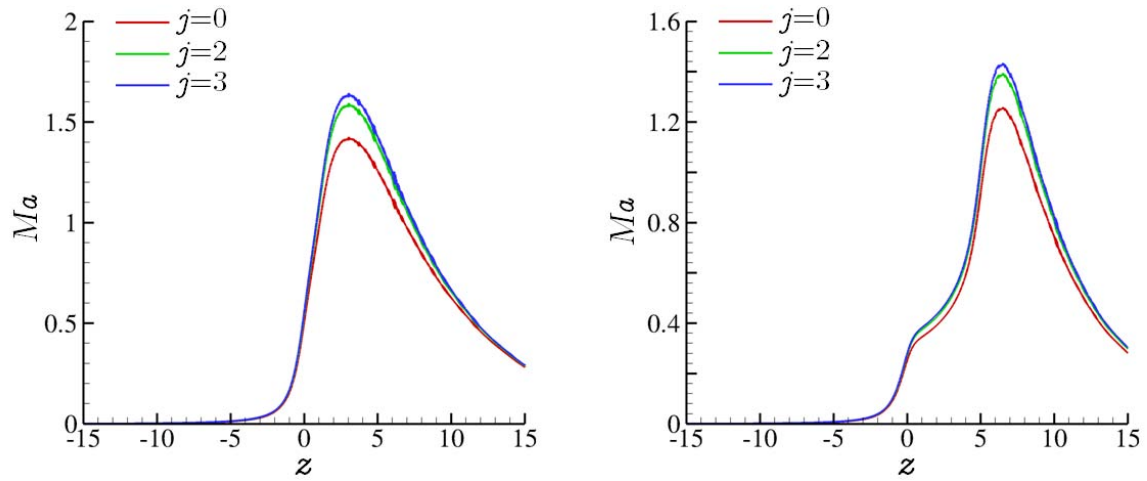
Figure 6.2: Distributions of the Mach number for $L/R = 1$ (left) and $L/R = 5$ (right) with $\delta_0 = 10$ along the symmetry axis.
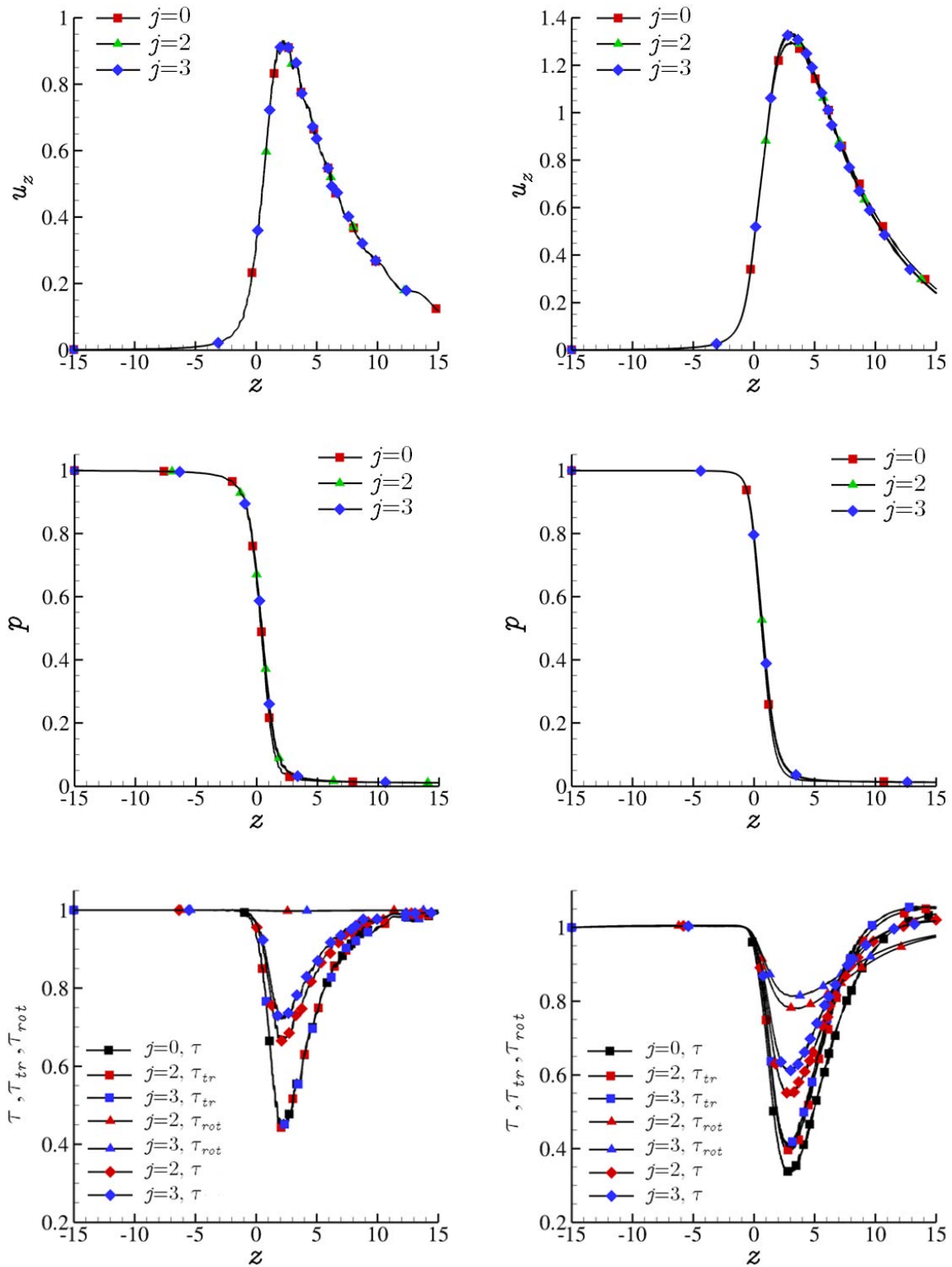
Figure 6.3: Dimensionless distributions of axial velocity (up), pressure (middle) and temperatures (down) for $\delta_0 = 0.1$ (left) and $\delta_0 = 10$ (right) with $L/R = 1$ along the symmetry axis.

157
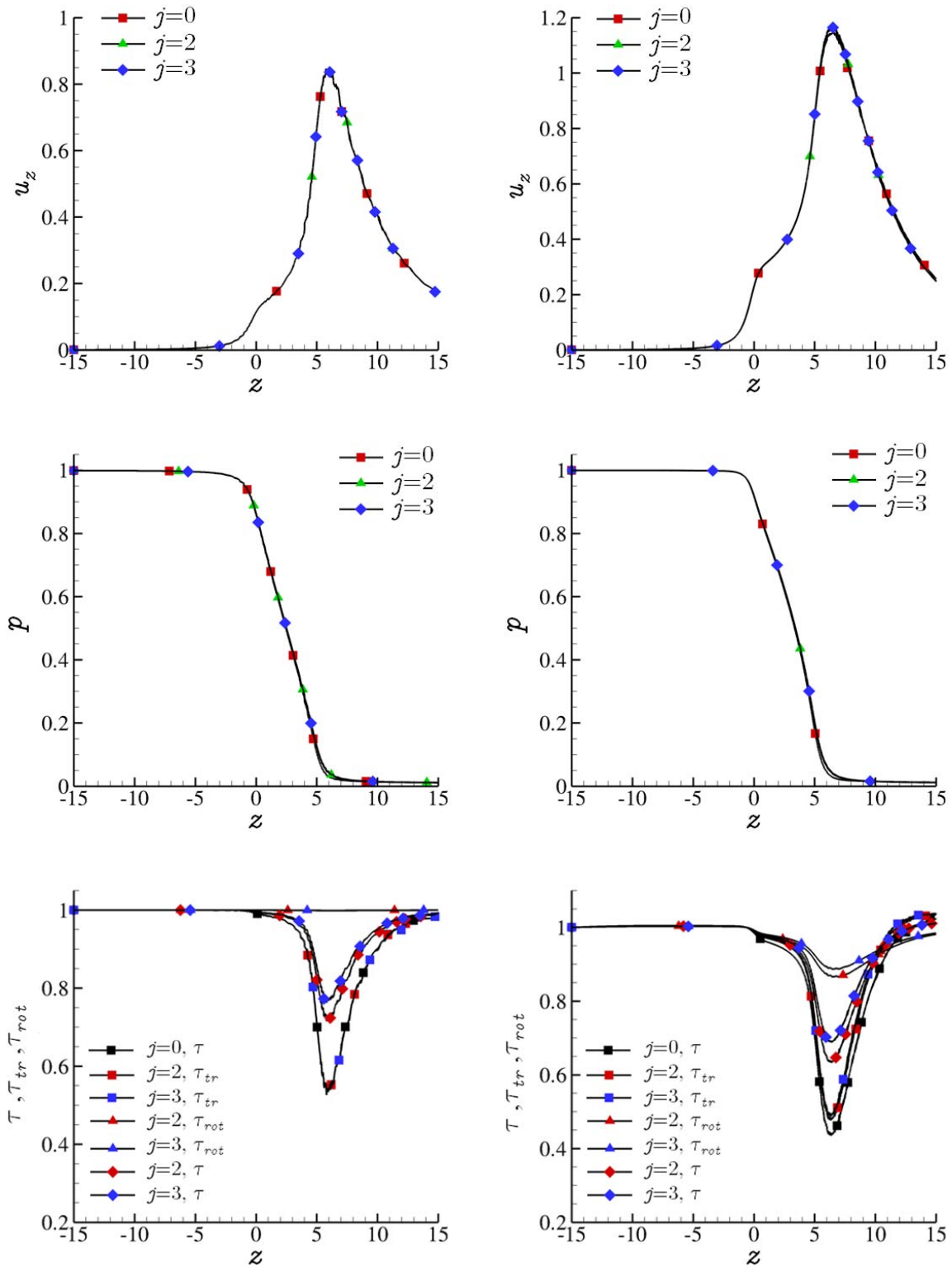
Figure 6.4: Dimensionless distributions of axial velocity (up), pressure (middle) and temperatures (down) for $\delta_0 = 0.1$ (left) and $\delta_0 = 10$ (right) with $L/R = 5$ along the symmetry axis.

158
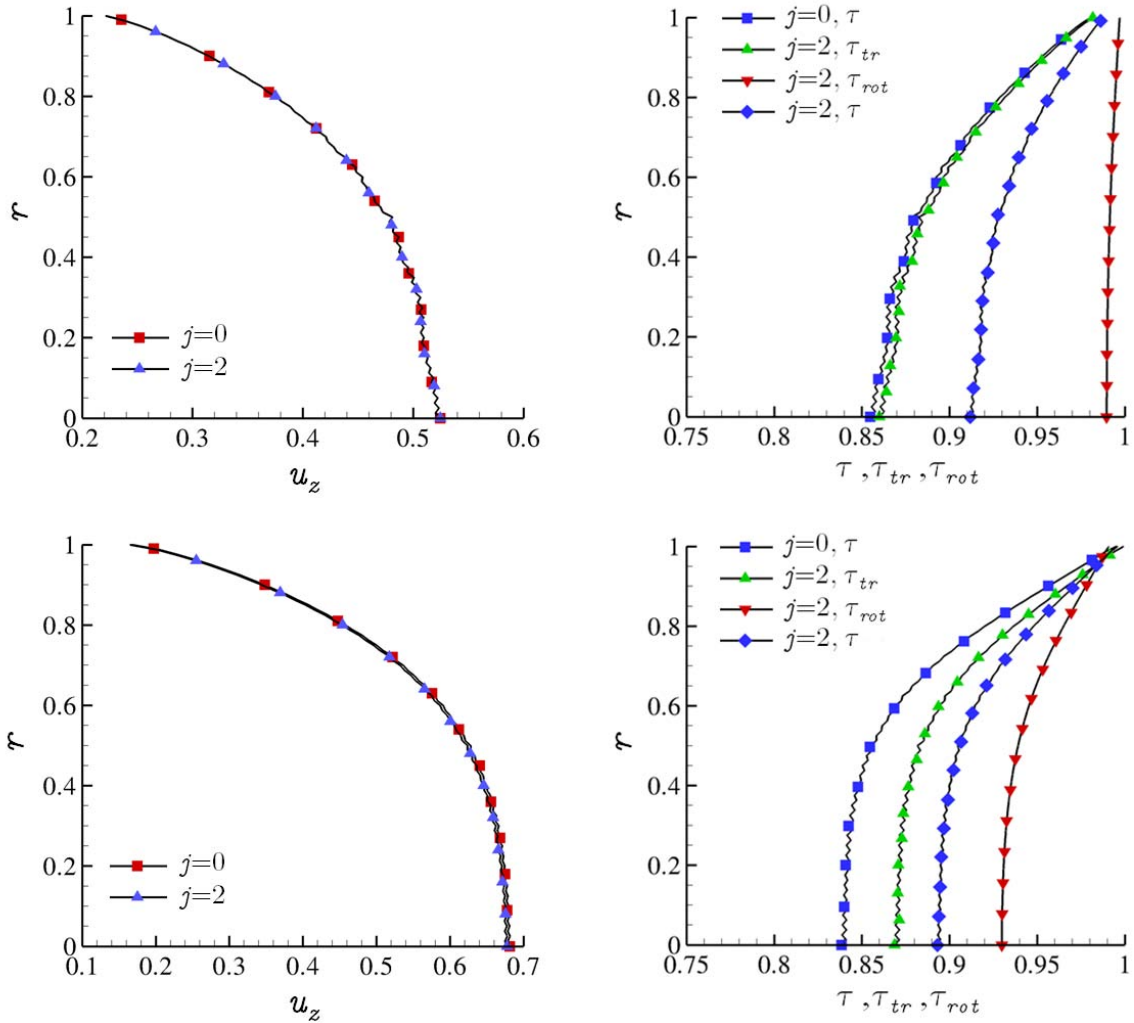
Figure 6.5: Distributions of axial velocity (left) and temperatures (right) for $\delta_0 = 1$ (up) and $\delta_0 = 10$ (down) with $L/R = 1$ at $z = L/(2R)$.

159
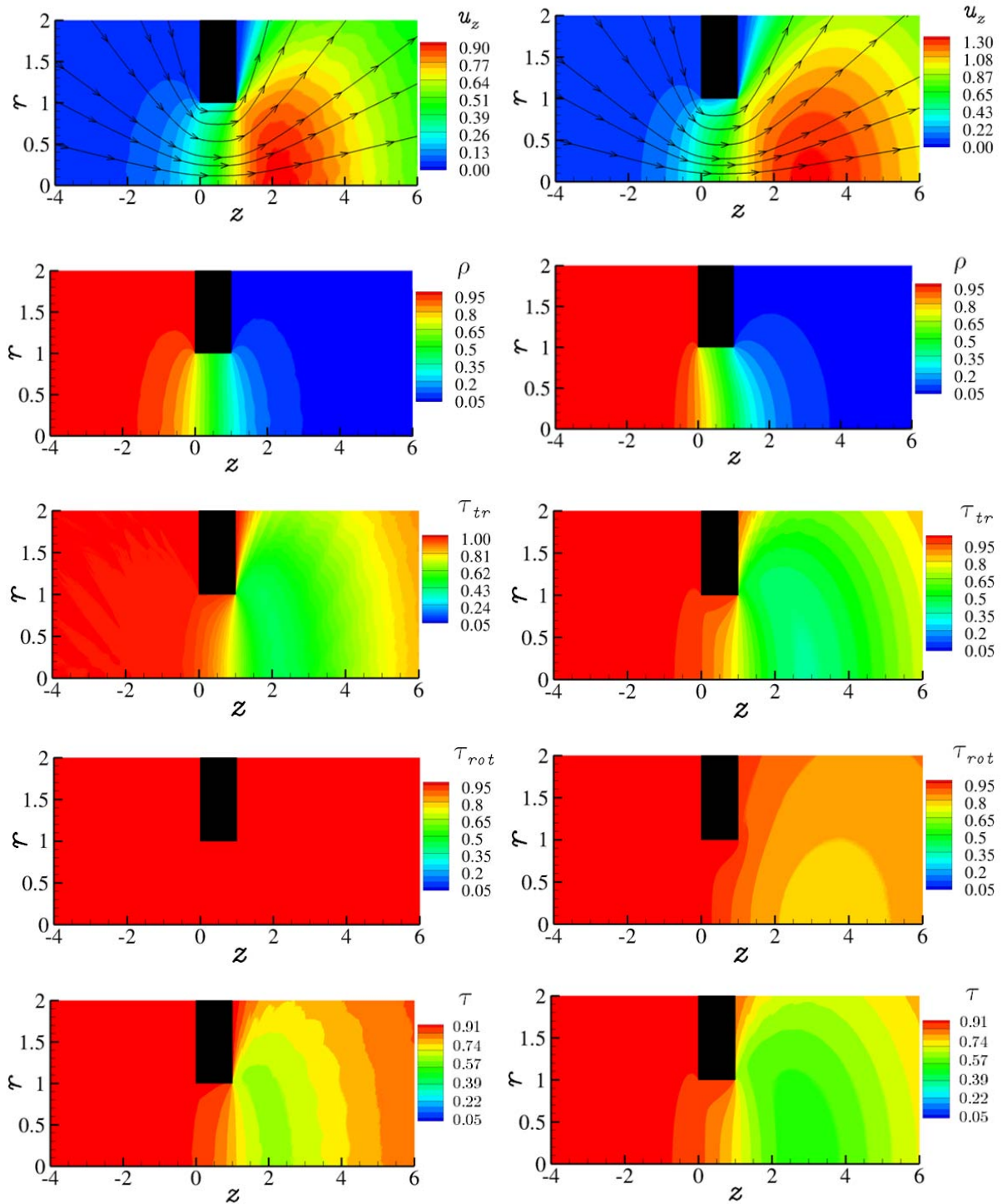
Figure 6.6: Diatomic gas flow ($j = 2$) through a tube for $L/R = 1$ and $\delta_0 = 0.1$ (left) and $\delta_0 = 10$ (right): isolines of axial velocity, number density and temperatures (translational, rotational and total).

160
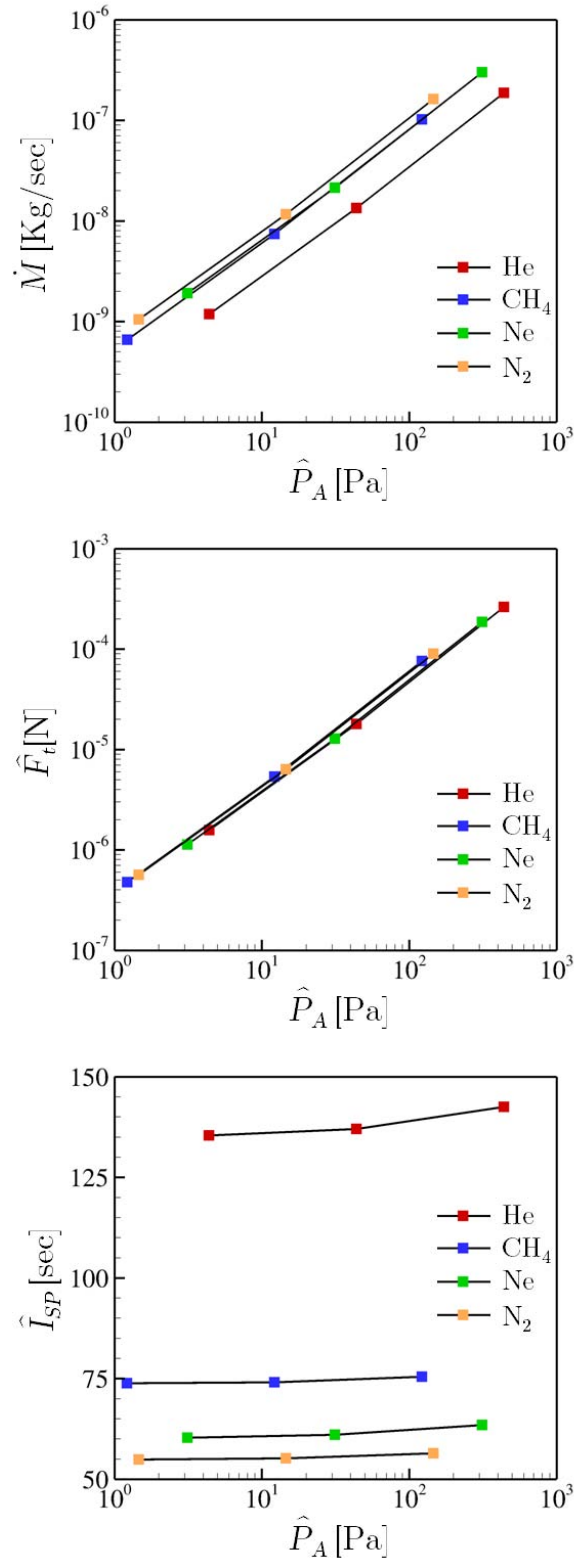
Figure 6.7: Dimensional mass flow rate $\dot{M}$, Thrust $\hat{F}_t$ and impulse factor $\hat{I}_{SP}$ of various gases with reference temperature $T_0 = 295$ K through tube with $L = R = 0.05$ cm.

161
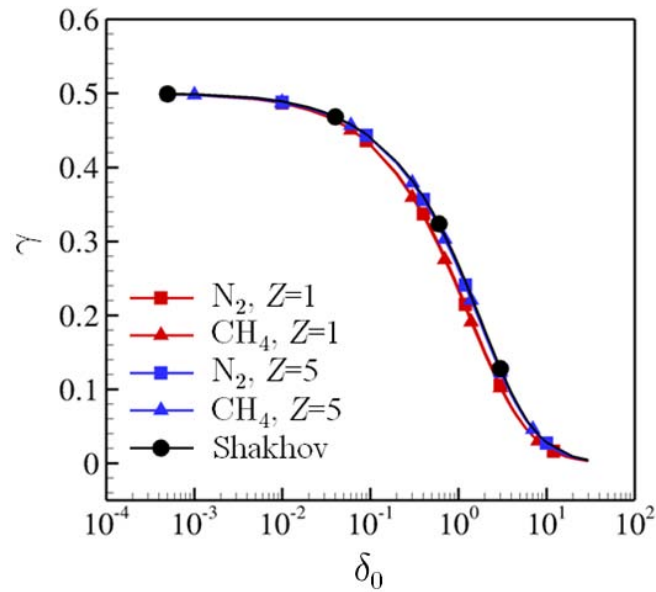
Figure 6.8: Thermomolecular pressure effect γ as function of the rarefaction parameter δ_0 for N_2, CH_4 with $Z = 1$ and 5 and for monatomic gases.
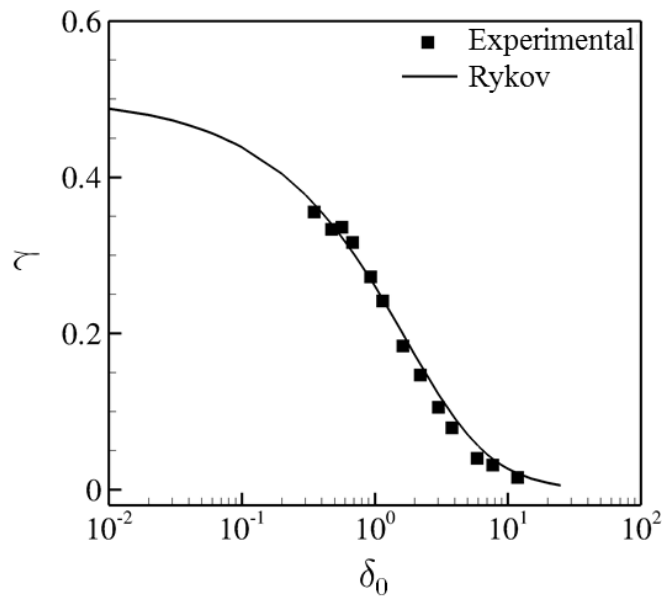
Figure 6.9: Comparison between computational and experimental [152] measurements of the thermomolecular pressure effect for N_2 at $T = 544$ K.

162

Chapter 7

Rarefied polyatomic gas flows driven by adsorption

7.1 The sticking coefficient and the thermal accommodation coefficient

Gas adsorption processes are present in many practical applications, as seen in literature review. Due to mass transfer a gas adsorption flow is induced. Since in most cases the surface temperature is lower (or much lower) than the gas temperature in the bulk flow, heat transfer is also present. Thus, gas adsorption flow combines both mass and heat transfer. Actually, at the boundary between the gaseous and condensed phase the difference between the distribution function of impinging and re-emitted molecules creates a Knudsen layer [1] to be described by kinetic equations. The modeling of such flows is commonly based on kinetic theory by applying the Boltzmann equation or kinetic model equations [1] or alternatively the Direct Simulation Monte Carlo Method (DSMC) [19].

In gas adsorption a fraction of molecules impinging to the surface is adsorbed (stick to the surface), while the remaining fraction is re-emitted (reflected) into the gas. This fraction is expressed in terms of the sticking coefficient $\alpha_{SC} \in [0,1]$ which is a measure of the probability that a molecule landing on the surface will permanently stick on it and provides an indication

163

of the effectiveness of gas removal from the system. The sticking coefficient is defined as [11]

$$\alpha_{SC} = \frac{\hat{N}^- - \hat{N}^+}{\hat{N}^-}, \tag{7.1}$$

where $\hat{N}^-$ and $\hat{N}^+$ are the particle fluxes impinging to and reflected from the surface respectively. It may be estimated as a free parameter by matching experimental with corresponding computational results characterizing a specific gas-surface set up (surface porosity, gas type, gas and surface temperatures). Then, these estimates may be applied in deriving boundary conditions for the simulation of adsorption processes in similar set-ups. Following this procedure the sticking coefficients of several gases for cryopanels coated with activated carbon at very low temperatures have been estimated [160, 161] and then, they have been applied in the numerical modeling of cryopumps used in the main pumping systems of magnetic confinement fusion reactors [116, 117].

It is noted that all available work is based on the assumption that the emitted particles are in thermal equilibrium with the surface, i.e., the reflected particles have the same temperature with that of the adsorption surface. In cases however, where the temperatures of the surface and of the gas far from the surface differ significantly it is reasonable to argue that the reflected particles are not fully thermally accommodated at the surface. This type of gas-surface thermal interaction is modeled by the so-called thermal accommodation coefficient α_{TAC} [85]. Combining computational and experimental results it has been shown that it varies as $\alpha_{TAC} \in [0, 1]$ [84–86], while in light gases may be significantly less than one. For instance in [84] the measured values of the thermal accommodation coefficient for He and D_2 on polished surfaces is about 0.4 and 0.5 respectively. Furthermore, in [162] it is observed that for light gases the surface roughness effect on the thermal accommodation coefficient is in vicinity only of $10 - 20\%$. Thus, it is reasonable to argue that even in rough surfaces imperfect thermal accommodation may occur.

Here, the thermal accommodation coefficient for that fraction of the incident molecular stream which is reflected from the surface can be written as [144]

$$\alpha_{TAC} = \frac{(1 - \alpha_{SC})\,\hat{E}^- - \hat{E}^+}{(1 - \alpha_{SC})\,\hat{E}^- - \hat{E}^w}. \tag{7.2}$$

In Eq. (7.2), $\hat{E}^-$ is the incident energy flux, $\hat{E}^+$ is the reflected energy flux and $\hat{E}^w$ is the energy flux that would have been achieved if the reflected molecules were in thermal equilibrium with the surface. For $\alpha_{SC} = 0$, the thermal accommodation coefficient is reduced to the typical one introduced in purely heat transfer problems presented in Chapter 3 ($\alpha_{TAC} = \alpha$). The first step of the modeling of adsorption process is to consider an ideal one-dimensional steady flow of a rarefied gas that is absorbed with given sticking and thermal accommodation coefficients onto a planar wall. The corresponding analysis including the numerical results are presented in Sections 7.2 - 7.5. Next, the modeling is extented to a 2D geometry which represents the TIMO (Test facility for ITER Model pump) open panel experiment, conducted in the TIMO-2 (Upgrade of the Test facility for ITER Model pump) test facility at KIT (Karlsruhe Institute of Technology, Germany), aiming at gaining a deeper understanding of cryoadsorption phenomena. Combining computational results with experimental data, the values of the sticking coefficients of different gases are estimated, supporting decision making related to the design of the cryogenic pumping system. The corresponding analysis, including representative results, is presented in Sections 7.6. Finally, the concluding remarks of the present work are given in Section 7.7.

7.2   Half space adsorption flow

Consider an ideal polyatomic gas occupying the half space $\hat{x} > 0$ bounded by a planar infinite plate located at $\hat{x} = 0$, with $\hat{x}$ being the coordinate which spans the direction normal to the plate. The flow setup is shown in Fig. 7.1. The gas motion is generated by the adsorbing plate maintained at uniform temperature T_w, while the mass and heat transfer between the gas and the plate are characterized by the sticking coefficient $\alpha_{SC} \in [0, 1]$ and thermal accommodation coefficient $\alpha_{TAC} \in [0, 1]$. Far upstream the gas is at local equilibrium at some temperature

$T_\infty \geq T_w$ flowing with some velocity $\hat{u}_\infty$ in the negative $\hat{x}$ direction. As shown in Fig. 7.1, the flow is one-dimensional normal to the plate. The molecular velocity vectors $\boldsymbol{v} = (\xi_x, \xi_y, \xi_z)$, with $\xi_x < 0$ and $\xi_x > 0$ refer to incoming and outgoing particles. In spite of the simplicity of the flow configuration the relationship among the flow parameters and their effect on the flow bulk quantities have not been fully investigated yet.

In Section 7.3 the kinetic formulation of the gas 1D adsorption flow is presented while in Section 7.4 a detailed description of the modeling of the gas-surface interaction is given. Then, in the Section 7.5 the numerical results are presented.
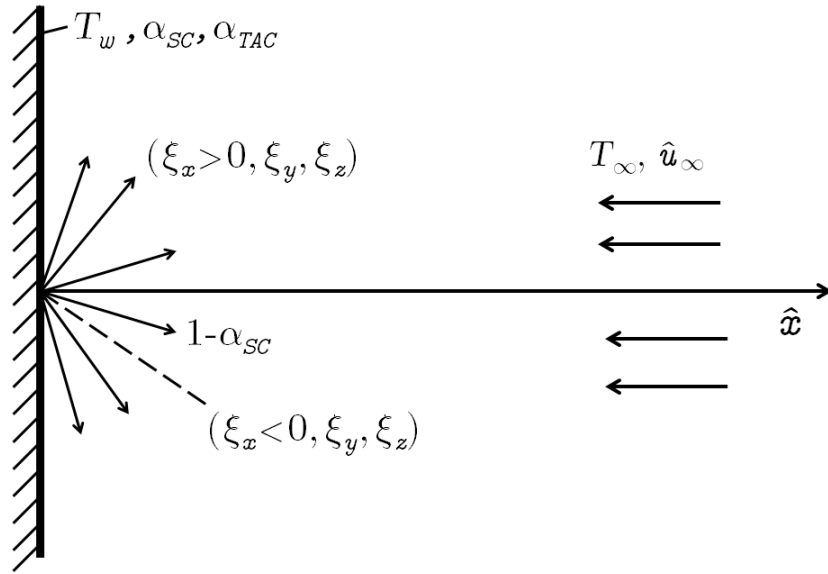
Figure 7.1: Half-space flow configuration.

7.3   Basic equations

Applying the projection procedure in energy space, as described in Chapter 2, the adsorption polyatomic flow is governed by the steady-state one-dimensional Holway kinetic equation given by

$$\xi_x \frac{\partial \hat{\boldsymbol{L}}}{\partial \hat{x}} = \nu \left[\left(1 - \frac{1}{Z} \right) \left(\hat{\boldsymbol{L}}_{tr} - \hat{\boldsymbol{L}} \right) + \frac{1}{Z} \left(\hat{\boldsymbol{L}}_{rot} - \hat{\boldsymbol{L}} \right) \right]. \tag{7.3}$$

Here, the main unknown is the distribution functions $\hat{\boldsymbol{L}}(\hat{x}, \boldsymbol{v}) = \left[\hat{g}(\hat{x}, \boldsymbol{v}), \hat{h}(\hat{x}, \boldsymbol{v})\right]^T$, with $\boldsymbol{v} = (\xi_x, \xi_y, \xi_z)$ being the molecular velocity vector, $\nu = \hat{P}_{tr}\big/\mu_{tr}$, where $\hat{P}_{tr}$ is the local translational pressure defined by the translational temperature and μ_{tr} is the viscosity at local translational temperature T_{tr}, is the total collision frequency and $Z \in [1, \infty)$ is a collision parameter. The reference translational and rotational distribution functions in Eq. (7.3) are given by $\hat{L}_{tr} = \left[\hat{g}_{tr}, \hat{h}_{tr}\right]^T$ and $\hat{L}_{rot} = \left[\hat{g}_{rot}, \hat{h}_{rot}\right]^T$, where the components of these vectors are as follows

$$
\begin{aligned}
\hat{g}_{tr} &= \frac{n}{(2\pi R T_{tr})^{3/2}} \exp\left[\frac{-(\xi_x - \hat{u}_x)^2 - \xi_y^2 - \xi_z^2}{2R T_{tr}}\right], \quad \hat{h}_{tr} = \frac{j k_B T_{rot}}{2}\hat{g}_{tr}, \\
\hat{g}_{rot} &= \frac{n}{(2\pi R T)^{3/2}} \exp\left[\frac{-(\xi_x - \hat{u}_x)^2 - \xi_y^2 - \xi_z^2}{2R T}\right], \quad \hat{h}_{rot} = \frac{j k_B T}{2}\hat{g}_{rot},
\end{aligned}
\tag{7.4}
$$

where j is the number of rotational degrees of freedom and $R = k_B/m$ is the gas constant with m and k_B being the molecular mass and the Boltzmann constant respectively. Also, the number density n, the $\hat{x}$-component of the bulk velocity $\hat{u}_x$ (the other two components are zero), the translational temperature T_{tr}, the rotational temperature T_{rot} and the total temperature T are defined by the moments of $\hat{g}$ and $\hat{h}$ as follows:

$$
n(\hat{x}) = \int\limits_{-\infty}^{\infty}\int\limits_{-\infty}^{\infty}\int\limits_{-\infty}^{\infty} \hat{g}\, d\xi_x d\xi_y d\xi_z
\tag{7.5}
$$

$$
\hat{u}_x(\hat{x}) = \frac{1}{n}\int\limits_{-\infty}^{\infty}\int\limits_{-\infty}^{\infty}\int\limits_{-\infty}^{\infty} \xi_x \hat{g}\, d\xi_x d\xi_y d\xi_z
\tag{7.6}
$$

$$
T_{tr}(\hat{x}) = \frac{m}{3n k_B}\int\limits_{-\infty}^{\infty}\int\limits_{-\infty}^{\infty}\int\limits_{-\infty}^{\infty} \left[(\xi_x - \hat{u}_x)^2 + \xi_y^2 + \xi_z^2\right]\hat{g}\, d\xi_x d\xi_y d\xi_z
\tag{7.7}
$$

$$
T_{rot}(\hat{x}) = \frac{2}{jn k_B}\int\limits_{-\infty}^{\infty}\int\limits_{-\infty}^{\infty}\int\limits_{-\infty}^{\infty} \hat{h}\, d\xi_x d\xi_y d\xi_z
\tag{7.8}
$$

$$
T(\hat{x}) = \frac{3T_{tr}(\hat{x}) + jT_{rot}(\hat{x})}{3 + j}
\tag{7.9}
$$

Other macroscopic quantities of some practical interest in the present work are the translational pressure defined by the equation of state $\hat{P}_{tr} = nk_B T_t r$, where k_B is the Boltzmann constant, the normal pressure

$$\hat{P}_{xx}(\hat{x}) = m \int\limits_{-\infty}^{\infty} \int\limits_{-\infty}^{\infty} \int\limits_{-\infty}^{\infty} (\xi_x - \hat{u}_x)^2 \hat{g} d\xi_x d\xi_y d\xi_z \tag{7.10}$$

and the energy and heat fluxes due to translational and rotational degrees of freedom in the x direction given by

$$\hat{E}_{tr}(\hat{x}) = \frac{m}{2} \int\limits_{-\infty}^{\infty} \int\limits_{-\infty}^{\infty} \int\limits_{-\infty}^{\infty} \upsilon^2 \xi_x \hat{g} d\xi_x d\xi_y d\xi_z, \quad \hat{E}_{rot}(\hat{x}) = \int\limits_{-\infty}^{\infty} \int\limits_{-\infty}^{\infty} \int\limits_{-\infty}^{\infty} \xi_x \hat{h} d\xi_x d\xi_y d\xi_z \tag{7.11}$$

and

$$Q_{tr}(\hat{x}) = \frac{m}{2} \int\limits_{-\infty}^{\infty} \int\limits_{-\infty}^{\infty} \int\limits_{-\infty}^{\infty} \left[(\xi_x - \hat{u}_x)^2 + \xi_y^2 + \xi_z^2 \right] (\xi_x - \hat{u}_x) \hat{g} d\xi_x d\xi_y d\xi_z,$$

$$\tag{7.12}$$

$$Q_{rot}(\hat{x}) = \int\limits_{-\infty}^{\infty} \int\limits_{-\infty}^{\infty} \int\limits_{-\infty}^{\infty} (\xi_x - \hat{u}_x) \hat{h} d\xi_x d\xi_y d\xi_z,$$

respectively, where the subscripts tr and rot refer to translational and rotational parts. As it is well known correct expressions for both viscosity and thermal conductivity cannot be proved simultaneously based on the Holway approximation. In spite of this pitfall and its simplicity it has been numerically demonstrated that it is a very reliable model for solving nonisothermal flows deducing results which are very close to the corresponding ones obtained by solving other kinetic models and the DSMC method [163, 164]. It is noted that for $j = 0$ and as $Z \to \infty$ the Holway model is transformed into BGK model for monatomic gases.

It is convenient to rewrite the governing equations in dimensionless form using the far upstream ($\hat{x} \to \infty$) macroscopic distributions as reference quantities. Thus, the dimensionless number density, velocity, temperatures (rotational, translational and total), normal stress in

168

$x-$ direction, translational pressure, energy fluxes and heat fluxes are defined as

$$\rho = \frac{n}{n_\infty}, \quad u_x = \frac{\hat{u}_x}{v_\infty}, \quad \tau_{tr} = \frac{T_{tr}}{T_\infty}, \quad \tau_{rot} = \frac{T_{rot}}{T_\infty}, \quad \tau = \frac{3\tau_{tr} + j\tau_{rot}}{3 + j}, \quad p_{xx} = \frac{\hat{P}_{xx}}{2\hat{P}_\infty},$$

$$p_{tr} = \frac{\hat{P}_{tr}}{\hat{P}_\infty}, \quad e_{tr} = \frac{\hat{E}_{tr}}{\hat{P}_\infty v_\infty}, \quad e_{rot} = \frac{\hat{E}_{rot}}{\hat{P}_\infty v_\infty}, \quad q_{tr} = \frac{Q_{tr}}{\hat{P}_\infty v_\infty}, \quad q_{rot} = \frac{Q_{rot}}{\hat{P}_\infty v_\infty}$$

(7.13)

respectively. All quantities with the subscript ∞ are the reference quantities, with $v_\infty = \sqrt{2RT_\infty}$ and $\hat{P}_\infty = n_\infty k_B T_\infty$ being the most probable molecular speed and the pressure far upstream respectively. In equilibrium state $T_{tr} = T_{rot} = T_\infty$. The equivalent mean free path far upstream, defined as [17, 165]

$$\lambda_\infty = \frac{2}{\sqrt{\pi}} \frac{\mu(T_\infty) v_\infty}{\hat{P}_\infty}, \tag{7.14}$$

is taken as the characteristic length. The dimensionless distribution functions are given by $g = \hat{g} v_\infty^3 / n_\infty$ and $h = \hat{h} v_\infty^3 / \hat{P}_\infty$, while the dimensionless length and molecular velocity vector are defined as $x = \hat{x}/\lambda_\infty$ and $\boldsymbol{c} = \boldsymbol{v}/v_\infty$ respectively.

Furthermore, the computational effort is significantly reduced by eliminating, based on the well-known projection procedure, the $y-$ and $z-$ components of the molecular velocity vector $\boldsymbol{c} = [c_x, c_y, c_z]$. This is achieved by introducing the reduced distributions:

$$F(x, c_x) = \int\limits_{-\infty}^{\infty} \int\limits_{-\infty}^{\infty} g \, dc_y dc_z,$$

$$G(x, c_x) = \int\limits_{-\infty}^{\infty} \int\limits_{-\infty}^{\infty} g\left(c_y^2 + c_z^2\right) dc_y dc_z, \tag{7.15}$$

$$S(x, c_x) = \int\limits_{-\infty}^{\infty} \int\limits_{-\infty}^{\infty} h \, dc_y dc_z.$$

Next, operating successively on the dimensionless form of Eqs. (7.3)-(7.12) with the integral operators $\int_{-\infty}^{\infty} \int_{-\infty}^{\infty} (.) \, dc_y dc_z$ and $\int_{-\infty}^{\infty} \int_{-\infty}^{\infty} (.) \left(c_y^2 + c_z^2\right) dc_y dc_z$, yields the following system of

three integro-differential equations for the reduced distributions functions

$$c_x \frac{\partial \mathbf{\Psi}}{\partial x} = \frac{2}{\sqrt{\pi}} \rho \sqrt{\tau_{tr}} \left[\left(1 - \frac{1}{Z} \right) (\mathbf{\Psi}_{tr} - \mathbf{\Psi}) + \frac{1}{Z} (\mathbf{\Psi}_{rot} - \mathbf{\Psi}) \right], \qquad (7.16)$$

where $\mathbf{\Psi} = [F, G, S]^T$ is the vector with unknown distributions. The translational and rotational relaxing distributions in Eq. (7.16) are given by $\mathbf{\Psi}_{tr} = [F_{tr}, G_{tr}, S_{tr}]^T$ and $\mathbf{\Psi}_{rot} = [F_{rot}, G_{rot}, S_{rot}]^T$ respectively, where the components of these vectors are read as

$$
\begin{aligned}
F_{tr} &= \frac{\rho}{\sqrt{\pi \tau_{tr}}} \exp\left[\frac{-(c_x - u_x)^2}{\tau_{tr}} \right], \quad G_{tr} = \tau_{tr} F_{tr}, \quad S_{tr} = \frac{j}{2} \tau_{rot} F_{tr}, \\
F_{rot} &= \frac{\rho}{\sqrt{\pi \tau}} \exp\left[\frac{-(c_x - u_x)^2}{\tau} \right], \quad G_{rot} = \tau F_{rot}, \quad S_{rot} = \frac{j}{2} \tau F_{rot},
\end{aligned}
\qquad (7.17)
$$

while the moments in terms of F, G and S are given as

$$\rho = \int\limits_{-\infty}^{\infty} F dc_x, \quad u_x = \frac{1}{\rho} \int\limits_{-\infty}^{\infty} c_x F dc_x, \qquad (7.18)$$

$$\tau_{tr} = \frac{2}{3\rho} \int\limits_{-\infty}^{\infty} \left[(c_x - u_x)^2 F + G \right] dc_x, \quad \tau_{rot} = \frac{2}{j\rho} \int\limits_{-\infty}^{\infty} S dc_x, \quad p_{xx} = \int\limits_{-\infty}^{\infty} (c_x - u_x)^2 F dc_x, \quad (7.19)$$

$$q_{tr} = \int\limits_{-\infty}^{\infty} (c_x - u_x) \left[(c_x - u_x)^2 F + G \right] dc_x, \quad q_{rot} = \int\limits_{-\infty}^{\infty} (c_x - u_x) S dc_x, \qquad (7.20)$$

$$e_{tr} = \int\limits_{-\infty}^{\infty} c_x \left(c_x^2 F + G \right) dc_x, \quad e_{rot} = \int\limits_{-\infty}^{\infty} c_x S dc_x. \qquad (7.21)$$

In the formulation of the basic equations Eqs. (7.16) the hard-sphere (HS) intermolecular interaction model has been applied. It is noted that all conservation principles are easily deduced by taking appropriate moments of the governing equations. Eqs. (7.16) are multiplied successively by 1, c_x and c_x^2 and the resulting equations are integrated over the molecular velocity space to yield, after some typical manipulations, the following conservation equations:

- Mass:

$$\frac{\partial}{\partial x}\left(\rho u_x\right) = 0 \tag{7.22}$$

- $x-$ momentum:

$$\frac{\partial}{\partial x}\left(p_{xx} + \rho u_x^2\right) = 0 \tag{7.23}$$

- Energy:

$$\frac{\partial}{\partial x}\left(e_{tr} + e_{rot}\right) = 0 \tag{7.24}$$

The above conservation equations are applied to benchmark the accuracy of the numerical scheme.

7.4   Gas-surface interaction

The adsorption process on the planar surface at $\hat{x} = 0$ is modeled by prescribing the distribution of reflected molecules according to

$$\hat{f}\left(0, \boldsymbol{v}\right) = \frac{n_w}{(2\pi RT^\alpha)^{3/2}} \exp\left(\frac{-\xi_x^2 - \xi_y^2 - \xi_z^2}{2RT^\alpha}\right) \frac{\hat{I}^{j/2-1}}{(k_B T^\alpha)^{j/2}\Gamma\left(j/2\right)} \exp\left(-\frac{\hat{I}}{k_B T^\alpha}\right), \ \xi_x > 0. \tag{7.25}$$

It should be noted that rotational degrees of freedom are described by the rotational energy $\hat{I}$, since no preferential alignment of molecular spinning motion is possible in the present problem. In Eq. (7.25) the parameters n_w and T^α may be defined as follows.

The parameter n_w is specified by substituting Eq. (7.25) into the expression of the reflected particle flux $\hat{N}^+ = \int_{\xi_x > 0} \int_0^\infty \xi_x \hat{f}\left(0, \boldsymbol{v}\right) d\hat{I} d\boldsymbol{v}$ to deduce $\hat{N}^+ = n_w \sqrt{RT^\alpha}/\sqrt{2\pi}$. In this expression the definition of the sticking coefficient given by Eq. (7.1) is introduced, to find

$$n_w = \left(1 - \alpha_{SC}\right)\sqrt{\frac{2\pi}{RT^\alpha}}\hat{N}^-, \tag{7.26}$$

where $\hat{N}^- = -\int_{\xi_x < 0} \int_0^\infty \xi_x \hat{f}\left(0, \boldsymbol{v}\right) d\hat{I} d\boldsymbol{v}$ is the incident particle flux.

The parameter T^α, which has been introduced in the boundary condition in order to take into account partial thermal accommodation, is defined by substituting Eq. (7.25) into

the expression for the reflected energy flux $\hat{E}^+ = \int_{\xi_x > 0} \int_0^\infty \left(\frac{m}{2} v^2 + \hat{I} \right) \xi_x \hat{f}(0, \boldsymbol{v}) d\hat{I} d\boldsymbol{v}$. In the resulting expression, Eq. (7.26) is introduced to yield $\hat{E}^+ = (2 + j/2)(1 - \alpha_{SC}) \hat{N}^- k_B T^\alpha$. Operating similarly in the case of full thermal accommodation (now T^α is replaced by T_w) is readily deduced that $\hat{E}^w = (2 + j/2)(1 - \alpha_{SC}) \hat{N}^- k_B T_w$. These two expressions for $\hat{E}^+$ and $\hat{E}^w$ are substituted into Eq. (7.2) for the thermal accommodation coefficient to find

$$T^\alpha = \alpha_{TAC} T_w + (1 - \alpha_{TAC}) \frac{2\hat{E}^-}{(4 + j) k_B \hat{N}^-}, \qquad (7.27)$$

where $\hat{E}^- = -\int_{\xi_x < 0} \int_0^\infty \left(\frac{m}{2} v^2 + \hat{I} \right) \xi_x \hat{f}(0, \boldsymbol{v}) d\hat{I} d\boldsymbol{v}$ is the total incident energy flux. Thus, boundary condition (7.25) for the reflected molecules is fully defined in terms of the impinging distribution, which is part of the solution.

Far upstream ($\hat{x} \to \infty$) the gas flow is described by a Maxwellian written as

$$\hat{f}_\infty(\boldsymbol{v}) = \frac{n_\infty}{(2\pi R T_\infty)^{3/2}} \exp\left[\frac{-(\xi_x - \hat{u}_\infty)^2 - \xi_y^2 - \xi_z^2}{2 R T_\infty} \right] \frac{\hat{I}^{j/2-1}}{(k_B T_\infty)^{j/2} \Gamma(j/2)} \exp\left(-\frac{\hat{I}}{k_B T_\infty} \right). \qquad (7.28)$$

At that end the distribution function and the resulting macroscopic quantities should not depend on the spatial variable $\hat{x}$.

Next, the projection procedure in energy space is applied according to $\hat{g} = \int_0^\infty \hat{f} d\hat{I}$ and $\hat{h} = \int_0^\infty \hat{f} \hat{I} d\hat{I}$. Then, the boundary conditions are non-dimensionalized and the projection procedure in the velocity space is introduced in the same manner as in the basic equations. Following this routine manipulation at $x = 0$ the emitted reduced distributions for $c_x > 0$ are

$$F(0, c_x) = \frac{\rho_w}{\sqrt{\pi \tau^\alpha}} \exp\left(-\frac{c_x^2}{\tau^\alpha} \right), \quad G(0, c_x) = \tau^\alpha F(0, c_x), \quad S(0, c_x) = \frac{j}{2} \tau^\alpha F(0, c_x), \quad (7.29)$$

where the parameters ρ_w and τ^α are given by

$$\rho_w = (1 - \alpha_{SC}) \frac{2\sqrt{\pi}}{\sqrt{\tau^\alpha}} N^-, \quad \tau^\alpha = \alpha_{TAC} \tau_w + (1 - \alpha_{TAC}) \frac{2e^-}{(4 + j) N^-}, \qquad (7.30)$$

with the incident particle and energy fluxes computed as

$$N^- = - \int_{c_x < 0} c_x F(0, c_x) \, dc_x, \quad e^- = - \int_{c_x < 0} c_x \left[c_x^2 F(0, c_x) + G(0, c_x) + S(0, c_x) \right] dc_x, \quad (7.31)$$

while at $\hat{x} \to \infty$ the Maxwellian takes the form

$$F_\infty = G_\infty = \frac{2}{j} S_\infty = \frac{1}{\sqrt{\pi}} \exp \left[-(c_x - u_\infty)^2 \right]. \qquad (7.32)$$

In Eqs. (7.29)-(7.32), the dimensionless quantities are $\rho_w = n_w / n_\infty$, $u_\infty = \hat{u}_\infty / v_\infty$, $\tau^\alpha = T^\alpha / T_\infty$, $\tau_w = T_w / T_\infty$, $N^- = \hat{N}^- / (v_\infty n_\infty)$ and $e^- = \hat{E}^- / \left(\hat{P}_\infty v_\infty \right)$.

Based on the above dimensionless formulation the flow parameters involved in the present one-dimensional adsorption flow problem are four, namely the coefficients α_{SC} and α_{TAC}, the temperature ratio τ_w and the velocity u_∞. Commonly, the dimensionless velocity at infinity u_∞ is presented via the Mach number far upstream, defined as $Ma_\infty = |\hat{u}_\infty| / c_\infty$, where $c_\infty = \sqrt{\gamma R T_\infty}$ is the corresponding sound speed [153]. Since for a polyatomic gas the ratio of the specific heats is $\gamma = (5 + j)/(3 + j)$ it is seen that $Ma_\infty = |u_\infty| \sqrt{(6 + 2j)/(5 + j)}$.

7.5 Results and discussion of the half space adsorption

The governing equations (7.16) with the associated expressions (7.17)-(7.21) subject to boundary conditions (7.29)-(7.32) are solved numerically in an iterative manner. More specifically for prescribed values of α_{SC}, α_{TAC} and τ_w the iteration map starts by assuming all needed macroscopic quantities including the far upstream velocity u_∞ as well as the parameters n_w and τ^α. The kinetic equations (7.16) are solved to yield the reduced distributions F, G and S, which are introduced into the moment equations (7.18)-(7.21) as well as in the flux equations (7.31) to find the new estimates of all bulk quantities which are now introduced in the next iteration. The iteration process is terminated when the imposed convergence criteria is fulfilled. Upon convergence the correct value of u_∞ is recovered. Thus, the present problem is properly defined only when three out of the four involved parameters are given. If all parameters both at the plane surface and far upstream are defined no steady-state flow conditions may be reached.

Here, we have chosen to compute u_∞ (or the associated Mach number Ma_∞) as a function of the remaining three parameters, i.e.,

$$u_\infty = u_\infty \left(\alpha_{SC}, \alpha_{TAC}, \tau_w \right). \tag{7.33}$$

The discretization of the kinetic equations in the molecular velocity space is based on the discrete velocity method. In the physical space a second order control volume approach is applied using non-uniform grid spacing which follows the geometric sequence $\Delta x_i = \Delta x_1 \times r^{i-1}$, with $\Delta x_1 = 4 \times 10^{-7}$ and $r = 1.0009$ (the subscript $i = 1, ..., K$ refers to the nodes in the physical space). The macroscopic quantities are computed by Gauss quadrature. The results presented in the next section have been obtained with about 15000 nodes in the physical space and 16 molecular speeds, while the convergence criteria to be fulfilled is

$$\frac{1}{3K} \sum_{i=1}^{K} \left[\left| \rho_i^{(t+1)} - \rho_i^{(t)} \right| + \left| \tau_i^{(t+1)} - \tau_i^{(t)} \right| + \left| u_i^{(t+1)} - u_i^{(t)} \right| \right] < \varepsilon. \tag{7.34}$$

In (7.34) the superscript t denotes the iteration index and $\varepsilon = 10^{-5}$ is the tolerance parameter. For $\alpha_{SC} = 0$ the solution of the corresponding half-space purely heat transfer solution is recovered.

A validation of the modeling approach and of the accuracy of the results is displayed in Subsection 7.5.1. In Subsection 7.5.2, the effect of the rotational degrees of freedom on the computed quantities is presented. Next, in Subsection 7.5.3 results are presented and discussed for the macroscopic velocity and the Mach number far upstream, as well as for the half space distributions of density, velocity, temperature and pressure in terms of the sticking and thermal accommodation coefficients varying between zero and one and for typical values of the temperature ratio $\tau_w = T_w / T_\infty$. The dependency of the thickness of the Knudsen layer on the flow parameters and the inclusion of an effective wall temperature to approximately compensate the thermal accommodation effect are also discussed. Finally, in Subsection 7.5.4 some dimensional results for specific gases are presented.

At this point it is useful to note that since the upstream quantities are taken as the reference quantities, $\rho_\infty = 1$ and thus $|u_\infty| = |N_\infty| = |\alpha_{SC} N^-|$, i.e. is equal to the upstream

net particle flux and to the adsorbed particle flux (all in dimensionless form) and therefore characterizes the intensity of the adsorption process.

7.5.1 Benchmarking

The accuracy of the results has been confirmed in several ways. In all cases the length L of the computational domain, i.e., the distance between the plate and the position on the x-axis, where the far upstream boundary condition is imposed, has been computationally checked to be long enough to properly recover space independent quantities at that end. Several runs have been performed for the same set of parameters by increasing L until no variation in the numerical results is observed. Grid independency of the results is also confirmed. Furthermore, in all tested cases, the computed macroscopic distributions fulfill the conservation laws derived in the Section 7.3. Based on the prescribed numerical parameters, convergence of the results up to at least three significant figures is confirmed.

To further validate the accuracy of the results a comparison with available corresponding results in the literature for monatomic gases ($j = 0$) is performed. In [113] the same flow configuration has been studied for $\alpha_{TAC} = 1$ based on the DSMC method. In Fig. 7.3, which reports the upstream Mach number Ma_{∞} versus α_{SC}, a comparison is performed between the results of the present work and the corresponding ones in [113] for $\tau_w = T_w/T_{\infty} = 1$ and 0.25. It is clearly seen that although the two computational approaches are completely different (the present one is deterministic, while the one in [113] is stochastic) the agreement between the results in the whole range of the sticking coefficient and for both temperature ratios is excellent with the relative error being less than 1%. Also, as shown in Fig. 7.3, increasing the Ma_{∞} leads to higher values of α_{SC}. In addition, as τ_w is reduced, i.e., the temperature difference between the upstream gas and surface temperatures $\Delta T = T_{\infty} - T_w$ is increased, for the same α_{SC}, the Ma_{∞} is increased, which means that the adsorption process becomes more intense. This remark may be alternatively stated by saying that as τ_w is reduced, for the same Ma_{∞}, a lower α_{SC} is needed in the specific adsorption processes. As expected the effect of ΔT is important.

7.5.2 Effect of the internal degrees of freedom

In this subsection the study is focused on the dependency of the macroscopic quantities on the rotational degrees of freedom. Results are presented for linear ($j = 2$) and nonlinear molecules ($j = 3$) and for $Z = 1$, 3 and 5, which are indicative for this type of simulations. All the results in this subsection are for $\alpha_{TAC} = 1$. In Fig. 7.4 the upstream Mach number Ma_∞ is plotted as a function of the α_{SC} for $j = 2$ and $T_w/T_\infty = 0.05$. The results obtained for $Z = 1$ are compared with the corresponding ones for $Z = 5$. It is clearly seen that the effect of the parameter Z on the upstream Mach number Ma_∞ is negligible. Also, it is noted that the distributions of the macroscopic quantities are not affected by the variation of the parameter Z.

In Fig. 7.5 a comparison between the upstream Mach number Ma_∞ curves for $j = 0$ with the corresponding curves for $j = 2$ and 3 is provided. Two temperature ratios are considered namely $T_w/T_\infty = 0.05$ and 1. Furthermore, the parameter Z is assumed to be temperature independent and set equal to 3. The chosen value is not specific for a particular substance and it simply appears to be reasonable for low temperature flows of polyatomic gases [166]. As it is shown the upstream Mach number Ma_∞ suffers a small drop when j changes from 2 to 0. The difference between a linear molecule and a nonlinear one with 3 rotational degrees of freedom is considerably smaller ($< 3\%$). For instance, at $\alpha_{SC} = 0.9$ and $j = 2$ the Mach number is increased about 6% for $T_w/T_\infty = 0.05$, while is about 9% for $T_w/T_\infty = 1$.

In Fig. 7.6 the dimensionless distributions of the number density $\rho(x)$, the normalized velocity $|u(x)/u_\infty|$ and dimensionless translational $\tau_{tr}(x)$, rotational $\tau_{rot}(x)$ and total temperatures $\tau(x)$ are plotted for temperature ratio $T_w/T_\infty = 0.05$ with the sticking coefficients $\alpha_{SC} = [0.1, 0.7]$ and $j = [0, 2, 3]$. As it is seen the number density and velocity profiles of diatomic ($j = 2$) and polyatomic ($j = 3$) gases are almost identical with the corresponding monatomic ($j = 0$) profiles for both values of the sticking coefficient. The gas rotational, translational and total temperatures far from the adsorption plate are equal to each other and are decreased close to the adsorption surface. For $\alpha_{SC} = 0.1$ the three temperatures translational, rotational and total are equal to each other and are almost identical with the corresponding monatomic profile of temperature. However, at $\alpha_{SC} = 0.7$ there exists a narrow strip, about

one mean free path wide, in which temperatures take different values. Temperature differences are not large with the monatomic profile being very close to the corresponding profile of the polyatomic translational temperature, while the rotational temperature takes lower values. It is noted that the differences between linear and nonlinear polyatomic profiles are almost negligible.

Overall the effect of the rotational degrees of freedom on the computed quantities is very small (about 10%) in the present problem. Therefore, for the rest of the chapter the analysis is performed for monatomic gases with the results being applicable even for polyatomic gases.

7.5.3   Effect of partial thermal accommodation

Next, we focus on the main objective of the present work which is the investigation of the effect of α_{TAC} on the adsorption process. In Fig. 7.7, the magnitude of the computed far upstream velocity u_∞ is plotted as a function of α_{SC} for $\alpha_{TAC} = [1, 0.8, 0.2]$ and $\tau_w = T_w/T_\infty = [1, 0.27, 0.05]$. For $\tau_w = 1$, the effect of α_{TAC} is negligible. This is well expected since when the surface and upstream temperatures are equal there is no heat transfer mechanism. However, as τ_w is reduced (the temperature difference is increased) heat transfer is enhanced and as a result the effect of α_{TAC} is also increased. In general, $|u_\infty|$ is reduced as α_{TAC} is reduced, i.e., as the gas thermal accommodation at the plate becomes less complete. This is physically justified since, in practice, a lower thermal accommodation at the surface corresponds (at some sense) to some smaller temperature difference ΔT than the imposed one. Indicatively, at fixed values of $\alpha_{SC} = 0.7$ and $\tau_w = 0.27$, when $\alpha_{TAC} = 0.8$ and 0.2, the reductions in $|u_\infty|$, compared to the ones for $\alpha_{TAC} = 1$, are 9% and 27% respectively. The corresponding reductions at $\tau_w = 0.05$ are 20% and 42%. Also, for prescribed adsorbing flux and temperature difference, as α_{TAC} is reduced, the sticking coefficient must be increased to sustain the prescribed flux. For instance in the case of $\tau_w = 0.05$, when α_{TAC} is reduced from 1 to 0.2, in order to preserve $|u_\infty| \simeq 0.6$ the sticking coefficient is increased about 25%. The effect of α_{TAC} becomes more important at low and intermediate values of α_{SC} between 0.1 and 0.8. Overall, the effect of α_{TAC} is of similar importance with τ_w.

It is noted that the specific temperature ratios of 0.27 and 0.05 have been selected because, for $T_\infty = 300$ K, they correspond to $T_w = 80$ K and 15 K respectively, which are two typical

temperatures in the design of multistage cryopumps [167] including the design of a three-stage cryopump that is recently under consideration within the EUROfusion programme [168]. Of course, they are also indicative for other temperature ratios covering a wide range of temperature differences.

Based on the results of Fig. 7.7 it may be useful to attempt to compensate the effect of $\alpha_{TAC} < 1$ by introducing an effective wall temperature $T_w^{eff} > T_w$ associated always with perfect thermal accommodation ($\alpha_{TAC} = 1$). It should be like a weighted average temperature and therefore it is defined as

$$T_w^{eff} = \alpha_{TAC} T_w + (1 - \alpha_{TAC}) T_\infty. \tag{7.35}$$

In Fig. 7.8, the magnitude of the computed far upstream velocity $|u_\infty|$ is plotted as a function of α_{SC} for $T_w^{eff}/T_\infty = 0.81$ and 0.24 with $\alpha_{TAC} = 1$. In the same figure the corresponding results for $T_w/T_\infty = 0.05$ with $\alpha_{TAC} = 0.2$ and 0.8, which are the parameters used to obtain the two specific values of T_w^{eff}/T_∞, are also plotted for comparison purposes. In general the agreement is good at high and moderate values of α_{SC} and it deteriorates as α_{SC} is further decreased. At $\alpha_{SC} = 0.1$ the disagreement is about 30%. In general the effective temperature approach may be useful for practical applications when computational resources are limited.

A more detailed insight in the adsorption flow characteristics is displayed in Figs 7.9, 7.10, 7.11 and 7.12, where the dimensionless distributions of number density, velocity magnitude, temperature and pressure are displayed for two temperature ratios $\tau_w = [0.05, 0.27]$ with the sticking and thermal accommodation coefficients taking the typical values of $\alpha_{SC} = [0.1, 0.5, 0.9]$ and $\alpha_{TAC} = [0.2, 0.8, 1]$ respectively. In all cases the distance along the horizontal axis from the plate is in mean free paths and the total indicated length corresponds to the length L of the computational domain. This length also corresponds to the thickness of the adsorption Knudsen layer where non-equilibrium transport phenomena occur. As shown in Figs 7.9, 7.10, 7.11 and 7.12, it is influenced from both α_{SC} and τ_w. It is evident that increasing the sticking coefficient α_{SC} leads to lower values of L, which means that the far upstream conditions are recovered faster in a smaller number of mean free paths $\hat{x}/\lambda_\infty$ from the adsorption surface. The

effect of the temperature difference is not that clear but it has been observed that decreasing τ_w reduces the thickness L.

In Fig. 7.9, the number density profile $\rho(x)$ is plotted. The shape of $\rho(x)$ is qualitatively similar for both $\tau_w = 0.05$ and 0.27. However, in the former case (i.e. as the plate temperature is decreased), it is changing more rapidly reaching to higher number densities at the plate. The far upstream number density is (as it should) always equal to one. For $\alpha_{TAC} = 1$ and 0.8, as x is reduced, for all values of α_{SC}, the number densities are monotonically increased reaching their highest values on the surface ($x = 0$). In particular, for $\alpha_{SC} = 0.1$ the two profiles are very close and then for $\alpha_{SC} = 0.5$ and 0.9 there is a departure between the profiles with the number density taking lower values as the sticking coefficient is increased. This behavior remains the same for $\alpha_{TAC} = 0.2$ and $\alpha_{SC} = 0.1$. On the contrary for $\alpha_{TAC} = 0.2$ and $\alpha_{SC} = 0.5$ and 0.9, as x is reduced, the number densities are monotonically reduced reaching their lowest values at $x = 0$. Overall, increasing the sticking coefficient leads to lower values of density. For values of α_{TAC} low enough, the number density is even lower than the far upstream value. This behavior in terms of the thermal accommodation is physically explained since, as pointed out above, as α_{TAC} is decreased the gas is reflected from the surface with a temperature larger than the surface temperature and as a result the gas density is decreased.

In Fig. 7.10, the normalized velocity magnitude $|u(x)/u_\infty|$ is plotted. As expected in most cases the magnitude of the gas velocity is reduced as it approaches the adsorption surface. This speed decrease is reduced as α_{TAC} is decreased and finally for $\alpha_{TAC} = 0.2$ and $\alpha_{SC} = 0.9$ the gas moves faster as it approaches the plate. This behavior is the inverse of the one observed for the number density and it is fully justified since as shown in the Section 7.3 the particle flux conservation law $\rho(x) u(x) = u_\infty$ applies.

The corresponding dimensionless temperature profiles $\tau(x)$ are displayed in Fig. 7.11. The gas temperature far upstream is equal to one and then in most cases, as expected, the temperature is monotonically decreased approaching to the adsorption surface. This situation is reversed only at $\alpha_{SC} = 0.9$ and 0.5 combined with $\alpha_{TAC} = 0.2$, resulting to gas temperatures close to the plate higher than the far upstream ones. It may be justified by considering that the thermal energy transferred by the reflected particles at the wall may be larger than the

corresponding amount of particles at some location far from the wall and therefore, it appears only for $\alpha_{SC} < 1$ and it is enhanced as both $\Delta T = T_\infty - T_w$ and α_{TAC} are decreased.

The pressure profiles are shown in Fig. 7.12. In all cases the variation of pressure obeys the equation of state $p(x) = \rho(x)\,\tau(x)$. As α_{SC} is decreasing, independent of α_{TAC}, the half-space pressure distribution becomes more uniform, which is well expected since the purely half-space heat transfer problem is recovered. It is also noted that the behavior of the normal pressure $p_{xx}(x)$ is similar to p and therefore is not displayed.

The dimensionless density and temperature in the limiting case where $\alpha_{SC} = 1$ are shown in Fig. 7.13 for $\tau_w = 0.05$ with $\alpha_{TAC} = 1$ and 0.2. As it is seen the solution does not depend on the thermal accommodation coefficient. This is expected, since all particles are adsorbed and there are no reflected particles. Also, both the number density and temperature are monotonically reduced as x is reduced. Comparing these profiles with the corresponding ones for $\alpha_{SC} = 0.9$ and $\alpha_{TAC} = 1$ it is seen that there is a resemblance in temperatures, while the densities behave in an opposite manner (the one for $\alpha_{SC} = 0.9$ is increased as x is reduced).

All simulations reported above are based on the HS model. Corresponding simulations have been performed for the Maxwell intermolecular potential deducing results which are very close to the ones by the HS model. Therefore it is stated that the choice of the intermolecular potential model has negligible effect on the present adsorption flow problem.

7.5.4 Sticking coefficients of specific gases

Closing this section is useful to provide some results in dimensional form. The dimensionless results presented in Fig. 7.7 are applied to plot in Fig. 7.14 the net molar flux in terms of the sticking coefficient for specific monatomic gases namely protium (^{1}H), helium (He), neon (Ne) and xenon (Xe) for reference upstream pressure $\hat{P}_\infty = 0.1$ Pa, temperature $T_\infty = 300$ K and temperature ratio $\tau_w = T_w/T_\infty = 0.05$. This is easily performed as follows: For the prescribed $\hat{P}_\infty$ and T_∞ the far upstream number density is obtained from the equation of state ($\hat{P}_\infty = n_\infty k_B T_\infty$). Then, the far upstream velocity is computed as $\hat{u}_\infty = v_\infty |u_\infty|$, where $v_\infty = \sqrt{2k_B T_\infty / m}$ is known for the specific gas and $|u_\infty|$ is obtained from Fig. 7.7. Finally, the net particle flux is computed as $\hat{N}_\infty = n_\infty \hat{u}_\infty$ which is divided by the Avogadro number to be

180

converted into the net molar flux $\hat{N}_\infty^{(molar)}$ [mol/(m^2s)] shown, versus α_{SC} for $\alpha_{TAC} = [0.2, 0.8, 1]$, in Fig. 7.14.

It is clearly seen that as the thermal accommodation coefficient is reduced the net molar flux $\hat{N}_\infty^{(molar)}$, which is equal to the adsorbed molar flux at the surface, is reduced. It is readily deduced, from the above dimensionalization, that the ratio of the net molar fluxes of two gases, for prescribed α_{SC}, α_{TAC} and τ_w, is inversely proportional to the square route of their molar masses. Thus, it is stated that under the same prescribed reference conditions and coefficients, higher adsorption molar flow rate is sustained as the gas becomes lighter. Also, the net molar flux is directly proportional to the reference pressure $\hat{P}_\infty$. In that sense following the demonstration procedure shown here the dimensionless results of the previous subsection can be readily applied in a wide range of reference conditions and various gases for comparison with experiments and other practical purposes.

7.6 Modelling of a prototype cryopump

In the framework the EUROfusion TFV (tritium-matter injection-vacuum) project, the Karlsruhe Institute of Technology (KIT) has taken the lead to develop for DEMO (DEMOnstration Power Plant) a new concept for the reactor exhaust vacuum systems, consisting of continuously working and non-cryogenic pumps, i.e. metal foil pump, mercury diffusion pump, and mercury liquid ring pump. Due to the risk inherent to this new concept, cryogenic pumps, which reliability and efficiency for fusion reactors have been already proven, are developed in parallel as a fall-back solution. The aim of the project is the development of an integrated design of a multi-stage cryopump fulfilling all DEMO requirements.

Cryogenic pumping systems are well known and used in various applications including the vacuum systems of ITER (The way, an experimental fusion reactor) [169]. The key mechanism is the sorption of gas on a surface. In order for the whole process to be efficient, the surface has to be cooled down to a proper level. Thus, high cryogenic loads are required. The surface temperature is of the order of a few degrees Kelvin and this is one of the shortcomings of cryopumps. In addition, due to the needed periodic regeneration process, the continuous operation of such systems is not possible unless multiple pumping units are used. On the other hand,

cryopumps have no moving parts and their operation has been proved reliable and quite stable. Furthermore, multistage configurations are capable of gas separation, a requirement that is critical for DEMO. Finally, multistage design can reduce the cryogenic loads since each stage can be at different temperature, suitable for the gases that each stage is assumed to adsorb, while in the single stage design the temperature has to be cooled to the lowest gas adsorption temperature.

The operation is based on the sorption phenomenon where an activated charcoal surface is cooled down to the point where a sufficient portion of the gas to be pumped, is removed. The key feature that characterizes the efficiency of the process is the sticking coefficient. The estimation of the sticking coefficient is not a straightforward procedure and requires both experimental tests and gas flow simulations. The experiments are performed in the TIMO-2 (Upgrade of the Test facility for ITER Model pump) test facility at KIT in order to measure pumping speeds on an activated carbon surface. A CAD view of the experimental set up is shown in Fig. 7.15 with the basic parts of the configuration. The experimental work, including the description of the experimental configuration, is presented in [170] and is not repeated here.

Due to the fact that pressure level is quite small and gas flow is in the transition or even in the free molecular regimes conventional fluid dynamics, based on the well-known Navier-Stokes equations, is improper to simulate such flows since the continuum medium hypothesis is not valid. Consequently, a deterministic or stochastic kinetic approach must be used. Since, the effect of the internal degrees of freedom on the macroscopic quantities, as it is shown in Subsection 7.5.2, is very small the simulation of the TIMO open panel test configuration is based on the Bhatankar-Gross-Krook model for monatomic gases. In the Subsection 7.6.1 the kinetic formulation of the problem, including the governing equations, the boundary conditions and the macroscopic quantities, is described in detail. Next, the description of the choice of the input parameters in the modeling is presented Subsection 7.6.2. Finally, in Subsection 7.6.3 the numerical results focusing on the comparison with experimental data and on the computation of the sticking coefficients are discussed.

7.6.1   Kinetic modeling of the TIMO open panel test setup

The detailed geometry of the experimental configuration shown in Fig. 7.15 is complex. The external vessel and the radiation shield are both cylindrical, while the pumping inlet and the adsorbing plate are orthogonal. Consequently neither cylindrical nor Cartesian computational grids are fully suitable for the simulation of the whole flow field while coupling of two grids requires a fully three-dimensional computational domain. The corresponding computational cost is very high (actually not manageable) because it requires the solution of the kinetic equations in a six-dimensional space (3D in the physical space plus 3D in the velocity space). Therefore, certain simplifications in the flow setup are introduced. Following previous work performed by the DSMC method [116] the flow field is simulated in a two-dimensional $\hat{x} - \hat{y}$ geometry. This approach has been proved efficient in computational terms and accurate enough for engineering purposes.

The flow is modeled by the nonlinear BGK model equation subject to purely diffuse boundary conditions. The main unknown is the distribution function $\hat{f} = (\hat{x}, \hat{y}, \boldsymbol{v})$, with $\boldsymbol{v} = (\xi_x, \xi_y, \xi_z)$ being the molecular velocity vector. It is convenient to introduce the following non-dimensional quantities:

$$x = \frac{\hat{x}}{R}, \; y = \frac{\hat{y}}{R}, \; \boldsymbol{c} = \frac{\boldsymbol{\xi}}{v_0}, \; f = \frac{\hat{f}v_0^3}{n_0}, \; \rho = \frac{n}{n_0}, \; \boldsymbol{u} = \frac{\hat{\boldsymbol{u}}}{v_0}, \; \tau = \frac{T}{T_0}, \; p = \frac{\hat{P}}{\hat{P}_0}, \; \boldsymbol{N} = \frac{\hat{\boldsymbol{N}}}{n_0 v_0}, \quad (7.36)$$

where R is the radius of the pump, $v_0 = \sqrt{2RT_0}$, with R denoting the individual gas constant, is the reference velocity at reference temperature T_0, n_0 is the reference number density and $\hat{P}_0 = n_0 k_B T_0$ is the reference pressure with k_B denoting the Boltzmann constant. In Eqs. (7.36) the quantities ρ, $\boldsymbol{u} = (\boldsymbol{u}_x, \boldsymbol{u}_y)$, τ, $p = \rho\tau$ and $\boldsymbol{N} = (\boldsymbol{N}_x, \boldsymbol{N}_y)$ are the dimensionless number density, velocity vector, temperature, pressure and particle flux vector respectively. The inlet conditions of the pump are chosen as reference quantities. In Fig. 7.2, the geometry imported in the numerical algorithm is presented in non-dimensional with the radius of pump being $R = 890$ mm. The injection pipe is also included while the gas enters the pump through the pump inlet. The geometry is based on the device drawings provided by KIT.
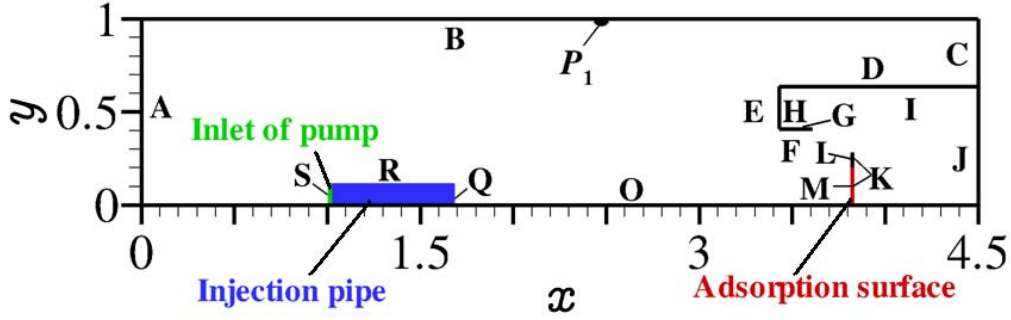
Figure 7.2: 2D geometry used for the simulation in non-dimensional form.

The non-dimensional quantities are introduced into the governing equation of the BGK model to yield [101, 102]

$$\zeta \cos\theta \frac{\partial f}{\partial x} + \zeta \sin\theta \frac{\partial f}{\partial y} = \delta_0 \rho \tau^{1-\omega} \left\{ \frac{\rho}{(\pi\tau)^{3/2}} \exp\left[\frac{-(\boldsymbol{c} - \boldsymbol{u})^2}{\tau}\right] - f \right\}, \qquad (7.37)$$

where $\omega = [1/2, 1]$ is the viscosity index and δ_0 is the rarefaction parameter defined as

$$\delta_0 = \frac{\hat{P}_0 R}{\mu(T_0)\, \upsilon_0}, \qquad (7.38)$$

with $\mu(T_0)$ being the reference viscosity at reference temperature T_0. Moreover, for computational purposes it is convenient to express the components (c_x, c_y, c_z) of the particle velocity in terms of cylindrical coordinates $(\zeta \cos\theta, \zeta \sin\theta, c_z)$. For the specific problem the computational effort is decreased by eliminating the c_z component introducing the following reduced distributions functions

$$F(x, y, c_x, c_y) = \int\limits_{-\infty}^{\infty} f(x, y, c_x, c_y, c_z) dc_z, \quad G(x, y, c_x, c_y) = \int\limits_{-\infty}^{\infty} c_z^2 f(x, y, c_x, c_y, c_z) dc_z, \quad (7.39)$$

184

into Eq. (7.37). After some typical manipulation the following coupled set of non-linear integro-differential equations is reduced:

$$
\zeta \cos \theta \frac{\partial F}{\partial x} + \zeta \sin \theta \frac{\partial F}{\partial y} = \delta_0 \rho \tau^{1-\omega} \left\{ \frac{\rho}{\pi \tau} \exp \left[\frac{-(\zeta \cos \theta - u_x)^2 - (\zeta \sin \theta - u_y)^2}{\tau} \right] - F \right\},
$$

$$
\zeta \cos \theta \frac{\partial G}{\partial x} + \zeta \sin \theta \frac{\partial G}{\partial y} = \delta_0 \rho \tau^{1-\omega} \left\{ \frac{\rho}{2\pi} \exp \left[\frac{-(\zeta \cos \theta - u_x)^2 - (\zeta \sin \theta - u_y)^2}{\tau} \right] - G \right\}.
$$

(7.40)

The macroscopic quantities ρ, u_x, u_y and τ are expressed in terms of F and G as

$$
\rho(x, y) = \int_0^{2\pi} \int_0^{\infty} F \zeta d\zeta d\theta,
\tag{7.41}
$$

$$
u_x(x, y) = \frac{1}{n} \int_0^{2\pi} \int_0^{\infty} \zeta \cos \theta F \zeta d\zeta d\theta,
\tag{7.42}
$$

$$
u_y(x, y) = \frac{1}{n} \int_0^{2\pi} \int_0^{\infty} \zeta \sin \theta F \zeta d\zeta d\theta,
\tag{7.43}
$$

$$
\tau(x, y) = \frac{2}{3n} \int_0^{2\pi} \int_0^{\infty} \left(\zeta^2 F + G \right) \zeta d\zeta d\theta - \frac{2}{3} \left(u_x^2 + u_y^2 \right).
\tag{7.44}
$$

Also, the particle fluxes in $x-$ and $y-$ are given as $N_x(x, y) = u_x(x, y) \rho(x, y)$ and $N_y(x, y) = u_y(x, y) \rho(x, y)$ respectively. An other interesting quantity is the Mach number defined as $Ma = \sqrt{(6/5) \left(u_x^2 + u_y^2 \right)}$. Applying the projection procedure, the simulation of the TIMO open panel test setup has been reduced to a 4D problem without losing any of the physical findings of the flow.

Next, the formulation of the boundary conditions is presented. The outgoing distributions from the surfaces (A), (B), (C), (D), (E), (F), (G), (H), (I), (J), (K), (L), (M), (Q), (R), (S) have a Maxwellian form with the number density obtained by the inlet conditions at the inlet of the pump (S) or by the condition of the no-penetration at the walls (A), (B), (C), (D), (E), (F), (G), (H), (I), (J), (K), (L), (M), (Q), (R). The surfaces with their notation are shown in Fig. 7.2.

185

The distributions of the outgoing molecules from all surfaces denoted by the superscript $(+)$ in terms of the reduced distributions F and G are defined as [101, 102]

$$F^+ = \frac{\rho_i}{\pi \tau_i} \exp\left(\frac{-\zeta^2}{\tau_i}\right), \quad G^+ = \frac{\rho_i}{2\pi} \exp\left(\frac{-\zeta^2}{\tau_i}\right), \tag{7.45}$$

where the subscript $i =$(A), (B), (C), (D), (E), (F), (G), (H), (I), (J), (K), (L), (M), (Q), (R), (S) is used to discern between the different surfaces. It is noted that the surfaces (A), (B), (C), (Q), (R), (S) are maintained at the same temperature T_0, the surfaces (D), (E), (F), (G), (H), (I), (J) are maintained at a lower temperature $T_{w,1}$ while the surfaces at the adsorption panel (K), (L), (M) are maintained at an even lower temperature $T_{w,2}$ $(T_0 > T_{w,1} > T_{w,2})$. Due to the reference values selection, the values $\rho_S = 1$ and $\tau_S = 1$ are obtained at the inlet of the pump (surface (S)) while for the other surfaces the parameter ρ_i is determined by

$$\rho_i = \frac{2\sqrt{\pi}}{\tau_i} \int\limits_{\theta_{1,i}}^{\theta_{2,i}} \int\limits_0^\infty \zeta^2 \varphi_i(\theta) F^- d\zeta d\theta. \tag{7.46}$$

The possible values of the quantities $\varphi_i(\theta)$, $\theta_{1,i}$, $\theta_{2,i}$ and τ_i are

$$\text{A}: \quad \varphi_A(\theta) = -\cos\theta, \quad \theta_{1,A} = \pi/2, \quad \theta_{2,A} = 3\pi/2, \quad \tau_A = 1, \tag{7.47}$$

$$\text{B}: \quad \varphi_B(\theta) = \sin\theta, \quad \theta_{1,B} = 0, \quad \theta_{2,B} = \pi, \quad \tau_B = 1, \tag{7.48}$$

$$\text{C}: \quad \varphi_C(\theta) = \cos\theta, \quad \theta_{1,C} = -\pi/2, \quad \theta_{2,C} = \pi/2, \quad \tau_C = 1, \tag{7.49}$$

$$\text{D}: \quad \varphi_D(\theta) = -\sin\theta, \quad \theta_{1,D} = \pi, \quad \theta_{2,D} = 2\pi, \quad \tau_D = T_{w,1}/T_0, \tag{7.50}$$

$$\text{E}: \quad \varphi_E(\theta) = \cos\theta, \quad \theta_{1,E} = -\pi/2, \quad \theta_{2,E} = \pi/2, \quad \tau_E = T_{w,1}/T_0, \tag{7.51}$$

$$\text{F}: \quad \varphi_F(\theta) = \sin\theta, \quad \theta_{1,F} = 0, \quad \theta_{2,F} = \pi, \quad \tau_F = T_{w,1}/T_0, \tag{7.52}$$

$$\text{G}: \quad \varphi_G(\theta) = -\sin\theta, \quad \theta_{1,G} = \pi, \quad \theta_{2,G} = 2\pi, \quad \tau_G = T_{w,1}/T_0, \tag{7.53}$$

$$\text{H}: \quad \varphi_H(\theta) = -\cos\theta, \quad \theta_{1,H} = \pi/2, \quad \theta_{2,H} = 3\pi/2, \quad \tau_H = T_{w,1}/T_0, \tag{7.54}$$

$$\text{I}: \quad \varphi_I(\theta) = \sin\theta, \quad \theta_{1,I} = 0, \quad \theta_{2,I} = \pi, \quad \tau_I = T_{w,1}/T_0, \tag{7.55}$$

$$\text{J}: \quad \varphi_J(\theta) = \cos\theta, \quad \theta_{1,J} = -\pi/2, \quad \theta_{2,J} = \pi/2, \quad \tau_J = T_{w,1}/T_0, \tag{7.56}$$

$$\text{K}: \quad \varphi_K(\theta) = -\cos\theta, \quad \theta_{1,K} = \pi/2, \quad \theta_{2,K} = 3\pi/2, \quad \tau_K = T_{w,2}/T_0, \tag{7.57}$$

$$\text{L}: \quad \varphi_L(\theta) = \cos\theta, \quad \theta_{1,L} = -\pi/2, \quad \theta_{2,L} = \pi/2, \quad \tau_L = T_{w,2}/T_0, \tag{7.58}$$

$$\text{Q}: \quad \varphi_Q(\theta) = -\cos\theta, \quad \theta_{1,Q} = \pi/2, \quad \theta_{2,Q} = 3\pi/2, \quad \tau_Q = 1, \tag{7.59}$$

$$\text{R}: \quad \varphi_R(\theta) = -\sin\theta, \quad \theta_{1,R} = \pi, \quad \theta_{2,R} = 2\pi, \quad \tau_R = 1, \tag{7.60}$$

where $T_{w,1}$ and $T_{w,2}$ are the temperature of the thermal shield walls and the adsorbing plate respectively. In all cases with superscripts (-) denoting the incoming distributions at the wall. The modeling of the adsorption process on surface (M) is based on the definition of the sticking coefficient α_{SC} presented in detail in Subsection 7.4. The outgoing distributions from the adsorption surface are given in Eq. (7.45), while the parameters τ_M and ρ_M are calculated as

$$\text{M}: \quad \tau_M = \frac{T_{w,2}}{T_0}, \quad \rho_M = (1 - \alpha_{SC})\frac{2\sqrt{\pi}}{\sqrt{\tau_M}}\int\limits_{-\pi/2}^{\pi/2}\int\limits_0^\infty \zeta^2 \cos\theta F^- d\zeta d\theta. \tag{7.61}$$

At the surface (O) ($y = 0$) specular refection is imposed due to the axial symmetry according to

$$F^+(x, 0, \zeta, \theta) = F^+(x, 0, \zeta, -\theta), \quad G^+(x, 0, \zeta, \theta) = G^+(x, 0, \zeta, -\theta). \tag{7.62}$$

Summarizing the formulation, it is noted that the kinetic modeling of the TIMO open panel test setup is described by the kinetic equations (7.40) coupled by the moments (7.41)-(7.44) and subject to boundary conditions (7.45)-(7.62). The discretization of the kinetic equations in the molecular velocity space is based on the discrete velocity method, while a second order control volume is applied in the physical space. The macroscopic quantities are calculated by Gauss-Legendre quadrature. The convergence criterion of the iteration process is

$$\frac{1}{3K}\sum_{i=1}^{K}\left[\left|\rho_i^{(t+1)} - n_i^{(t)}\right| + \left|\tau_i^{(t+1)} - \tau_i^{(t)}\right| + \left|u_i^{(t+1)} - u_i^{(t)}\right|\right] < \varepsilon, \tag{7.63}$$

187

where the superscript t denotes the iteration index, K is the total number of nodes in physical space and ε is the tolerance parameter. In Table 7.1 the discretization parameters used are given. It is noted that the numerical code is parallel based on message passing interface (MPICH2). The parallelization of the kinetic algorithm is implemented in the molecular velocity space. This is a simple and natural way of parallelization inherent in the structure of the algorithm reducing significantly the required computational effort. The estimates of the distribution functions at each processor are summed to estimate the updated macroscopic quantities. Before starting a new iteration, the macroscopic quantities and the impermeability constants are synchronized and re-transmitted to each processor. The scaling characteristics of the implemented parallelization are quite good and details can be found in [101, 102].

The solution of the problem depends on five dimensionless parameters, namely the rarefaction parameter δ_0, the temperature ratios $T_{w,1}/T_0$ and $T_{w,2}/T_0$, the sticking coefficient α_{SC} and the viscosity index ω.

Table 7.1: Numerical parameters used in simulations.

Number of nodes in $x-$ direction	3451
Number of nodes in $y-$ direction	765
Discrete angles in $(0, \pi)$	100
Discrete magnitudes	24
Convergence criterion	$< 10^{-4}$

7.6.2 Specification of the input parameters

As it is seen in Fig. 7.2 the whole geometry of the pump assuming $x - y$ geometry is imported, i.e. both vacuum vessel and the internal radiation shield, in the simulations except the baffle fins in order to avoid coupling different types of computational grids.

Following the experimental campaign that took place at KIT, two out of the four gases (H_2, D_2, Ne and He) that have been tested during the experimental campaign, namely H_2 and D_2, have been simulated. The walls of the external vessel are at temperature $T_0 = 300$ K, which is also the temperature of the injected gas. Following the experimental parameters, the thermal shield walls are at $T_{w,1} = 80$ K D_2 ($T_{w,1} = 85$ K for H_2) and the adsorbing plate are

at $T_{w,2} = 18$ K according to the basic scenario discussed in [171]. The reference viscosity at temperature $T_0 = 300$ K is 8.95×10^{-6} Pa s for H_2 and 1.26×10^{-5} Pa s for D_2, while their molecular masses are 2.016 gr/mole and 4.023 gr/mole respectively. The viscosity index for both gases is $\omega = 0.67$. It is noted that the developed software is suitable in simulating a much wider spectrum of gases.

It is important to note that the number of required simulations is significantly increased due to the proper implementation of the boundary condition at the inlet of the pump where the only known parameter is the throughput of the gas. Simulation tools require specific flow parameters at open boundaries, like local pressure and velocity. When these quantities are unknown, the typical treatment is to assume a Maxwellian distribution for the incoming to the vacuum vessel particles through the inlet of the pump, and setting the flow rate due to this incoming flow equal to the experimental value. This approach assumes that the portion of the particles crossing the inlet of the pump in the opposite direction is negligible. Nevertheless, following some extensive numerical experimentation, it has been clearly demonstrated that a significant amount of particles will exit from the vessel through the injection pipe. Thus, in order to achieve the net throughput to be equal to the experimental one (200 sccm), a much higher throughput for the incoming particles has to be assumed and this requires a number of simulations before the proper value is adjusted.

In order to achieve the required value for the throughput at the injection pipe outlet, the only solution is the try and error method. A first guess is used initially and depending on the recovered results, a new estimation is used resulting to multiple simulations for the recovery of the correct flow field for each set of parameters. Consequently, the required resources for each simulation are significantly increased.

It is noted that the desired experiment value of the gas net throughput of 200 sccm (0.338 Pa m^3/s) can be obtained for different combined values of the sticking coefficient α_{SC} and the rarefaction parameter δ_0. Next, for each set of values α_{SC} and δ_0 the pumping speed S_R [m^3/s] is estimated based on the numerical results using the following expression

$$S_R = \frac{\hat{N}}{P_1},\tag{7.64}$$

189

where $\hat{N}$ [Pa m^3/s] is the net gas throughput through the inlet of the pump and P_1 [Pa] is the pressure displayed in Fig. 7.2. Then, the sticking coefficient is estimated through the calculated values of the pumping speed that match the ones obtained from the experiments for the same gas net throughput.

7.6.3 Comparison with experiment and computation of the sticking coefficient

Tabulated numerical results obtained for H$_2$ for various values of the sticking coefficient α_{SC} are presented in Table 7.2. In all cases the net gas flow is about 200 sccm close to the experimental one. It is seen that as the sticking coefficient is decreased and the adsorbing plate is not removing gas from the flow domain, the injected gas flow is increased to maintain the net gas flow close to the experimental one and as expected the pressure P_1 is also increased. More specifically, the throughput for the incoming particles has drastically increased reaching values much higher than 2000 sccm (for $\alpha_{SC} = 0.1$) in order to achieve net flux of 200 sccm. Taking into account the fact that as the pressure is increased, the convergence rate for the algorithm is decreased and more time is required for the convergence of the numerical code. It is observed that the kinetic simulation results are close to the ones obtained by the Test Particle Monte Carlo method (TPMC). Taking into account that TPMC is valid only in the free molecular regime and that for most of the cases the flow is in the transition regime, in addition to the different modeling approach and geometry (TMPC is solving the detailed 3D flow configuration) the discrepancy of 10% in the lower limit of the transition regime (large α_{SC}) is reasonable. On the other end, for small values of α_{SC}, where the flow is in the typical transition regime, the discrepancy of 30% or more can be easily justified since TPMC does not take into account particle collisions. Furthermore, comparing the experimental result of a pumping speed of 2.61 m^3/s with the computational pumping speeds obtained for various values of the sticking coefficient it is concluded that a value of the sticking coefficient $\alpha_{SC} = 0.03$ is the one that matches best the experimental result.

In Table 7.3, the obtained results for D$_2$ are presented. The experimental pumping speed for D$_2$ is in the same order of magnitude to that of H$_2$ and because of that the sticking coefficient

should also be in the same order to the one for H_2. Therefore, simulations have been performed for small values of the sticking coefficient and more specifically for $\alpha_{SC} < 0.1$. In general similar remarks, as before, can be made. The throughput of the incoming particles is significantly enlarged as α_{SC} is reduced, to achieve the net particles flux of 200 sccm at the injection pipe outlet. The estimated value of the sticking coefficient in the case of D_2 is about $\alpha_{SC} = 0.064$.

Next, the axial velocity, density, temperature, pressure as well as Mach number isolines of H_2 are presented in Fig. 7.16 and 7.17 for two indicative values of the sticking coefficient $\alpha_{SC} = 0.07$ and 0.7. Small vortices are created close to the thermal shield, both inside and outside of it. All of them are of small magnitude, especially the ones in the gap between the vacuum vessel and the thermal shield. As the sticking coefficient α_{SC} is decreased and the pressure is increased the vortices are gradually increased. The density and the pressure variances in the vacuum vessel are quite small in both cases and significant changes are limited only in the space enclosed by the thermal shield. In addition, as expected the temperature of the gas at the inlet of the pump is equal to one and then is monotonically decreased approaching the adsorption surface, where its minimum value is observed. As it is seen, increasing the sticking coefficient leads to lower values of the density in the flow field. Finally, the contours of the Mach number give an idea for the magnitude of the velocity. As the sticking coefficient is decreased the Mach number is also decreased since the intensity of the adsorption is decreased. Moreover, the Mach number behind the adsorption panel is almost zero for both cases of α_{SC}.

7.7 Concluding remarks

To sum up, the adsorption process has been investigated based on the BGK and Holway model kinetic equations for monatomic and polyatomic gases respectively. First, the steady one-dimensional half-space flow of a polyatomic gas in the presence of an absorbing planar wall is investigated. The involved flow parameters include the sticking α_{SC} and thermal accommodation α_{TAC} coefficients, the ratio of the surface temperature over the far upstream temperature T_w/T_∞ and the upstream normalized velocity u_∞. Overall the effect of the rotational degrees of freedom on the computed quantities is very small (about 10%). Therefore, the dimensionless

results of monatomic gases may be also used in the case of polyatomic gases. Particular attention is given on the effect of the value of α_{TAC} on u_∞, as well as on the half space macroscopic distribution of density, velocity, temperature and pressure, for various prescribed values of α_{SC} and T_w/T_∞. It has been found that as the thermal accommodation of the gas on the surface is reduced the adsorbing flux is also reduced or otherwise for a prescribed adsorbing flux the sticking coefficient must be increased. Furthermore, the effect of partial thermal accommodation is enlarged as the difference, between the surface temperature and the far upstream temperature, is increased. Overall, the effect of α_{TAC} is significant in all flow quantities and the type of thermal gas-surface interaction must be accordingly taken into consideration.

Next, the modelling of a three stage prototype cryopump where the adsorption is the main process has been performed. For this reason a 2D kinetic adsorption code has been developed to simulate the experimental device configuration (TIMO open panel setup). Massive simulations have been performed for different sets of parameters following the experimental setup used at KIT. More specifically, numerical data have been recovered for H_2 and D_2 and different values of the sticking coefficient. Simulation results have been compared with experimental data, providing the values of the sticking coefficient for both gases ($\alpha_{SC} = 0.03$ for H_2 and $\alpha_{SC} = 0.064$ for D_2). These results have been also compared with the corresponding ones by the TPMC and will be also compared soon with corresponding DSMC (Direct Simulation Monte Carlo) results.
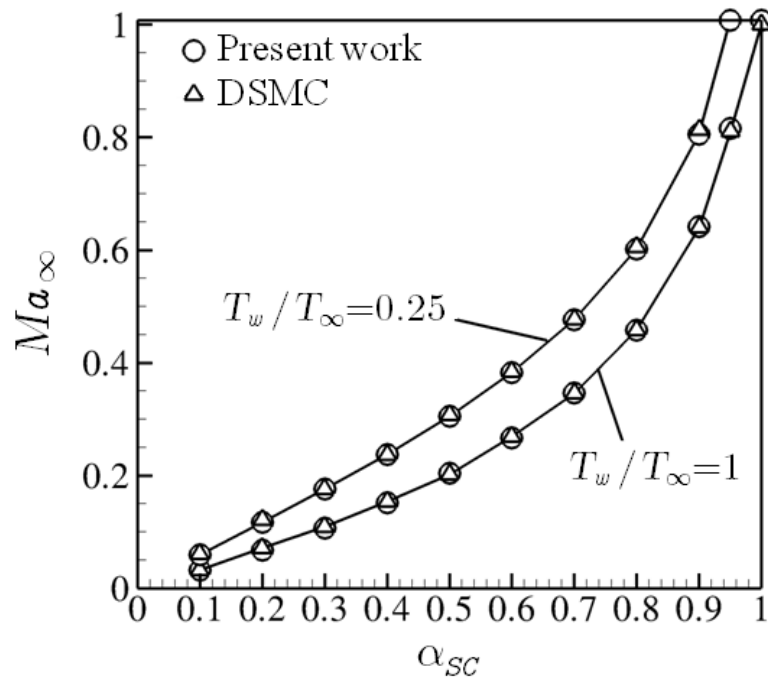
Figure 7.3: Upstream Mach number Ma_∞ as a function of the sticking coefficient α_{SC} for thermal accommodation coefficient $\alpha_{TAC} = 1$ and temperature ratio $\tau_w = [1, 0.25]$ based on the present kinetic model and the DSMC method [113].
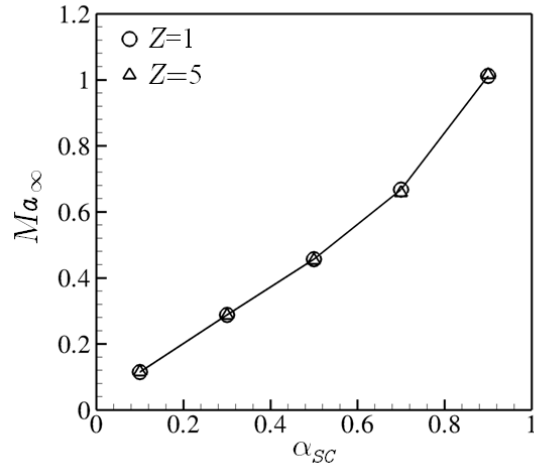
Figure 7.4: Upstream Mach number Ma_∞ as function of the sticking coefficient α_{SC} for $j = 2$ and $\tau_w = 0.05$ with $Z = 1$ and 5.
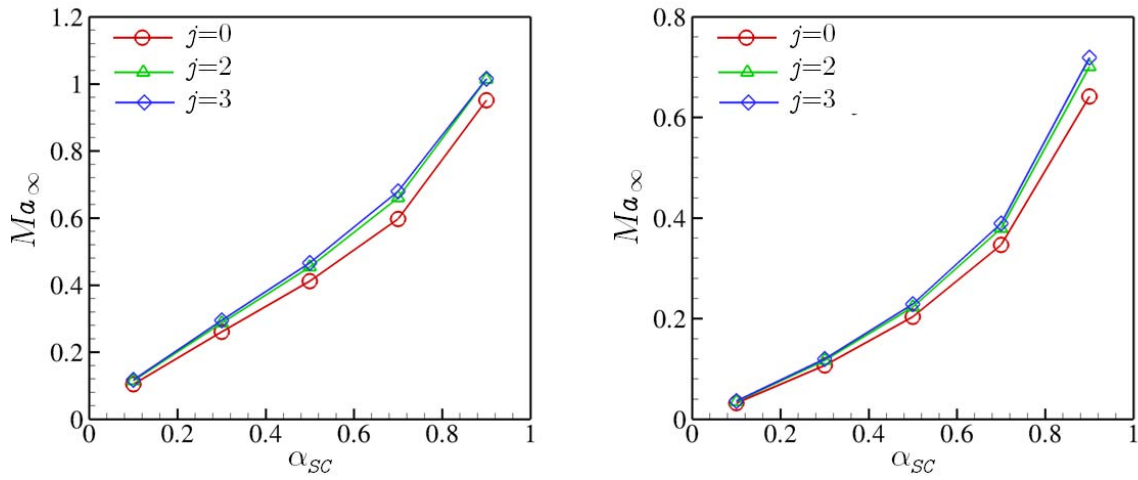
Figure 7.5: Upstream Mach number $\alpha_{TAC} = [1, 0.2]$ as function of the sticking coefficient α_{SC} for $j = [0, 2, 3]$ with $Z = 3$ and temperature ratios $\tau_w = 0.05$ (left) and $\tau_w = 1$ (right).

194
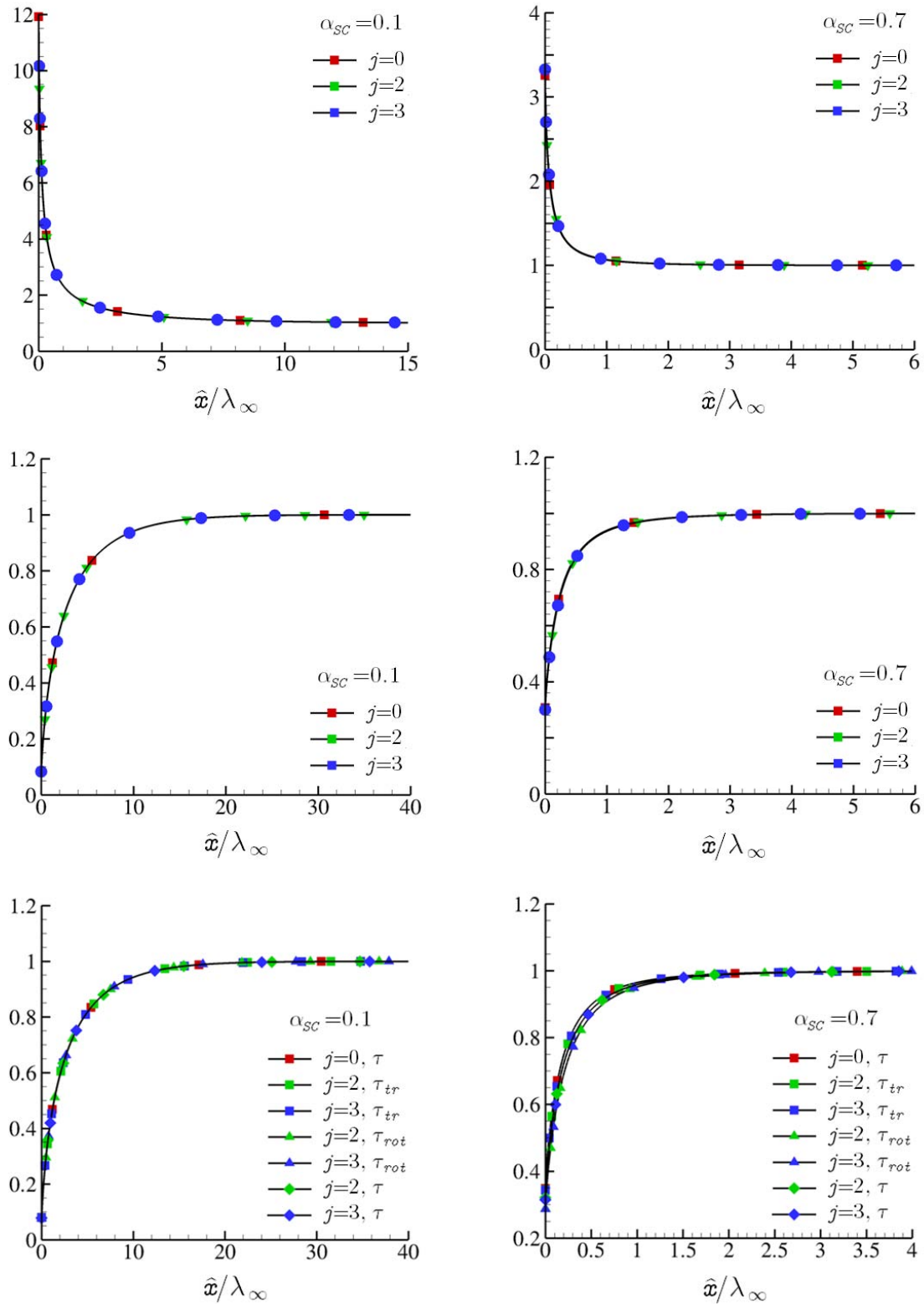
Figure 7.6: Dimensionless density (up), normalized velocity magnitude (middle) and dimensionless translational, rotational and total temperatures (down) for $j = [0, 2, 3]$ with $Z = 3$, temperature ratio $\tau_w = 0.05$ and sticking coefficients $\alpha_{SC} = [0.1, 0.7]$.

195
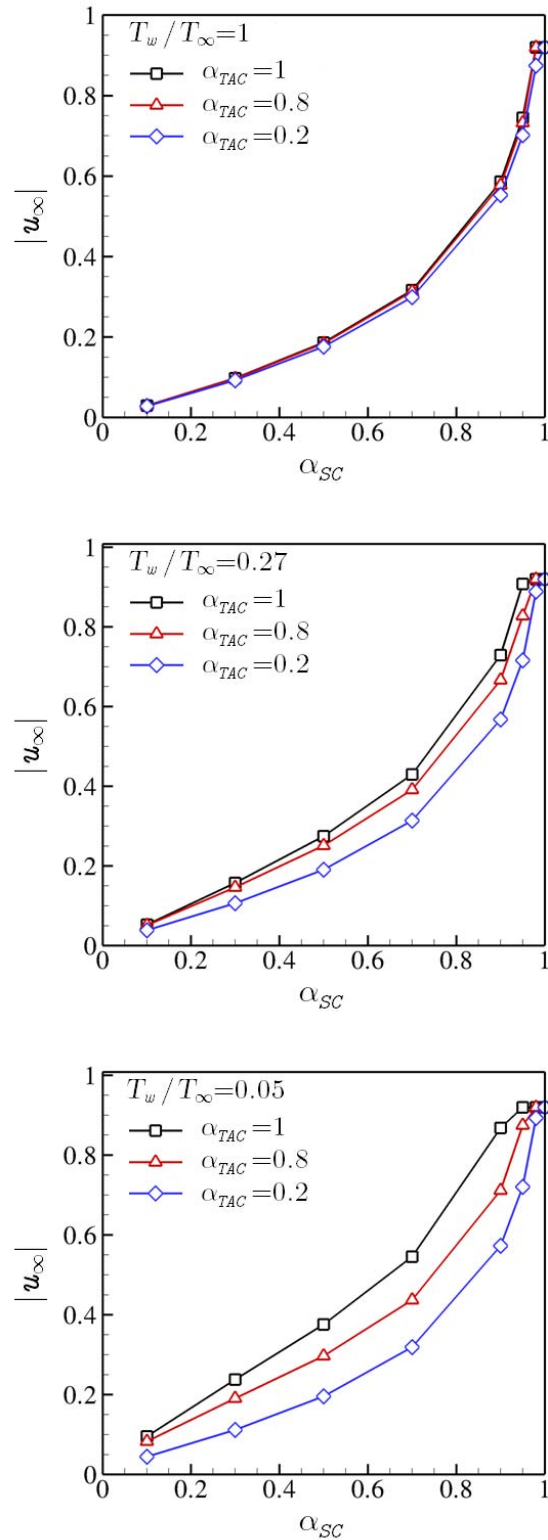
Figure 7.7: Upstream velocity $|u_\infty|$ as a function of the sticking coefficient α_{SC} for thermal accommodation coefficient $\alpha_{TAC} = [1, 0.8, 0.2]$ and temperature ratio $\tau_w = [1, 0.27, 0.05]$.
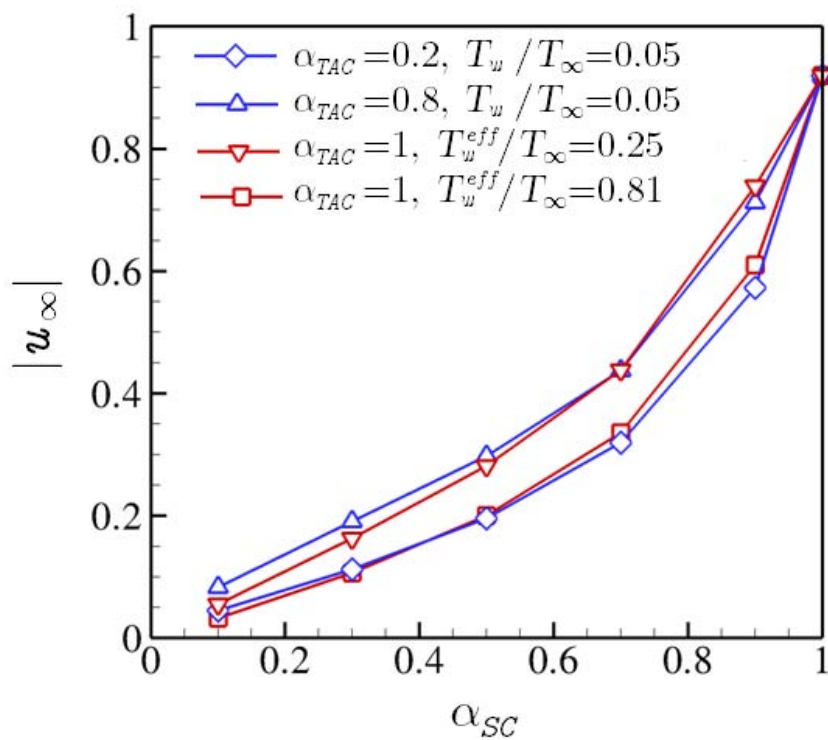
Figure 7.8: Comparison between the results obtained by using the ratio $T_w^{eff}/T_\infty = [0.24, 0.81]$ and $\alpha_{TAC} = 1$ with the corresponding "exact" ones.
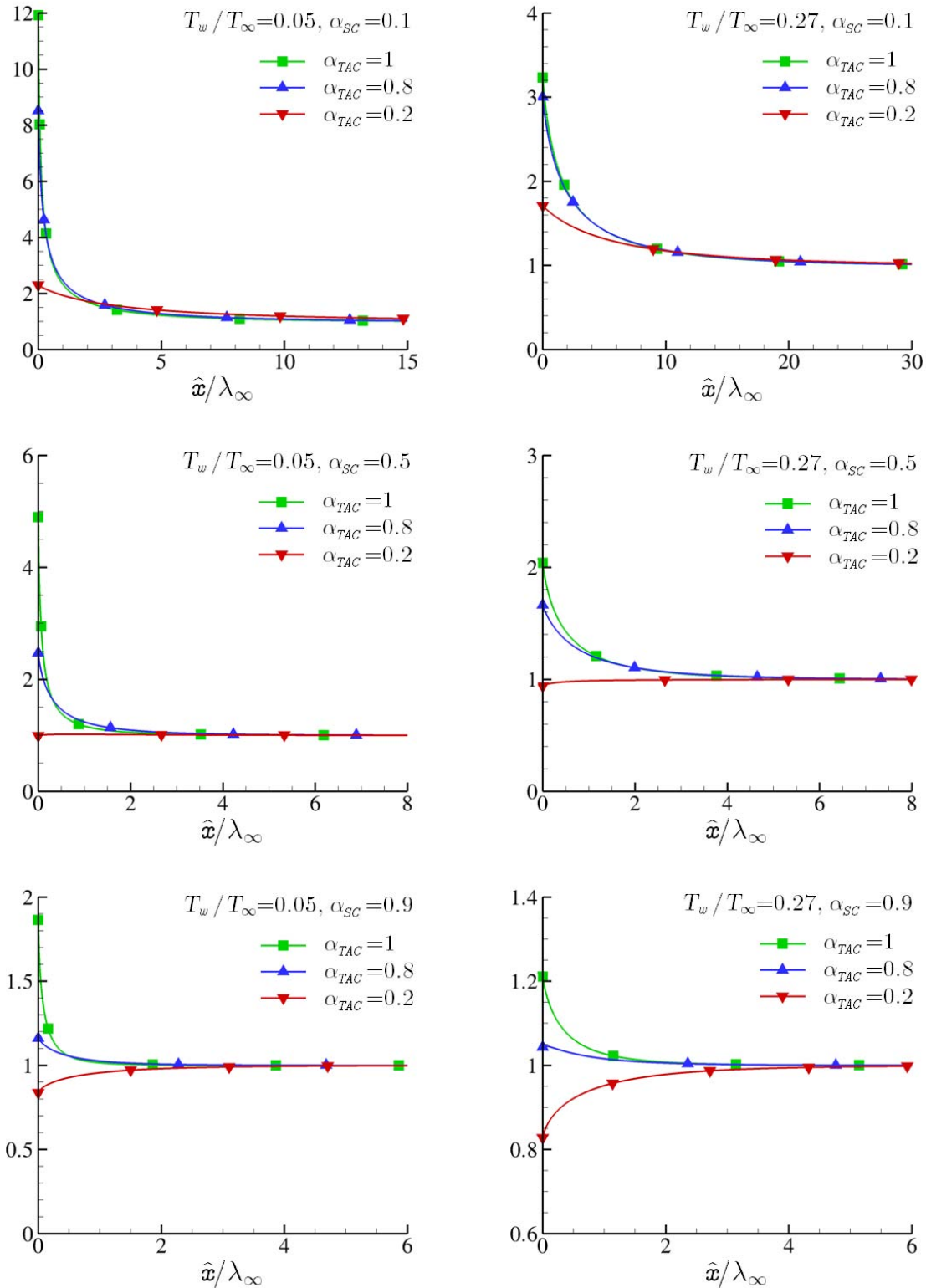
Figure 7.9: Dimensionless number density $\rho(x)$ for temperature ratios $\tau_w = [0.05, 0.27]$ with sticking coefficient $\alpha_{SC} = [0.1, 0.5, 0.9]$ and thermal accommodation coefficient $\alpha_{TAC} = [1, 0.8, 0.2]$.

198
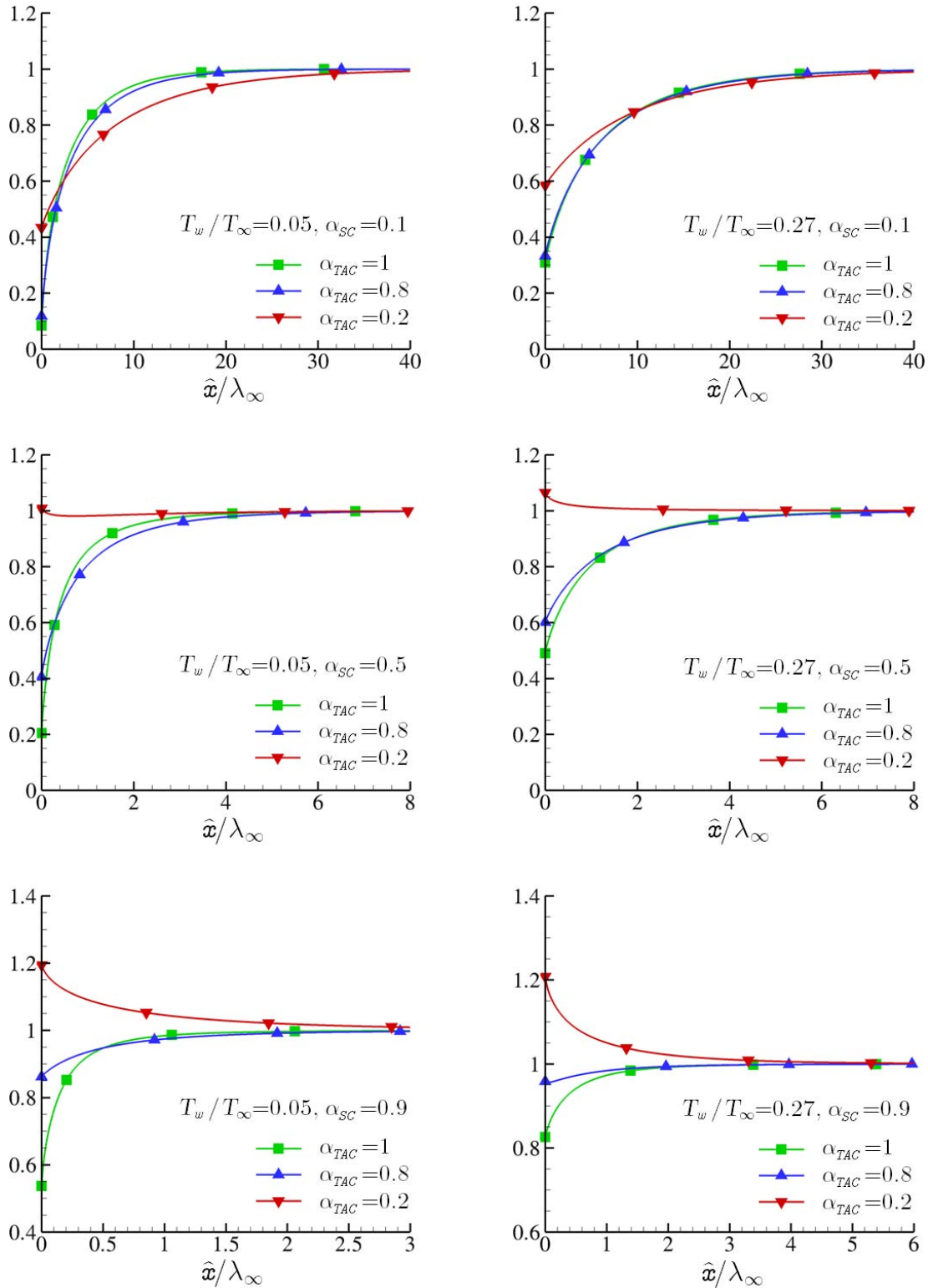
Figure 7.10: Dimensionless velocity magnitude $|u\left(x\right)/u_\infty|$ for temperature ratios $\tau_w = [0.05, 0.27]$ with sticking coefficient $\alpha_{SC} = [0.1, 0.5, 0.9]$ and thermal accommodation coefficient $\alpha_{TAC} = [1, 0.8, 0.2]$.
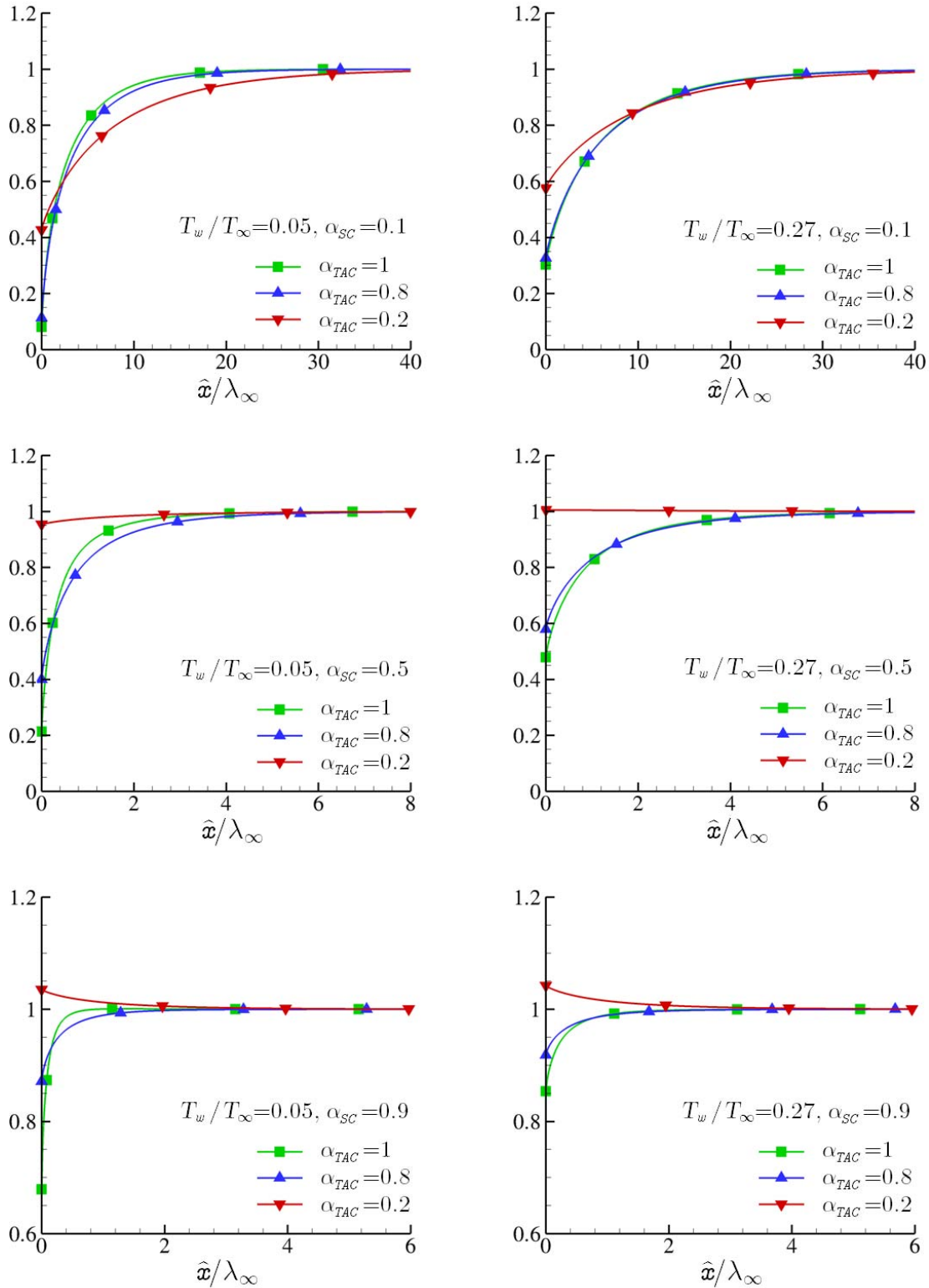
Figure 7.11: Dimensionless temperature $\tau(x)$ for temperature ratios $\tau_w = [0.05, 0.27]$ with sticking coefficient $\alpha_{SC} = [0.1, 0.5, 0.9]$ and thermal accommodation coefficient $\alpha_{TAC} = [1, 0.8, 0.2]$.

200
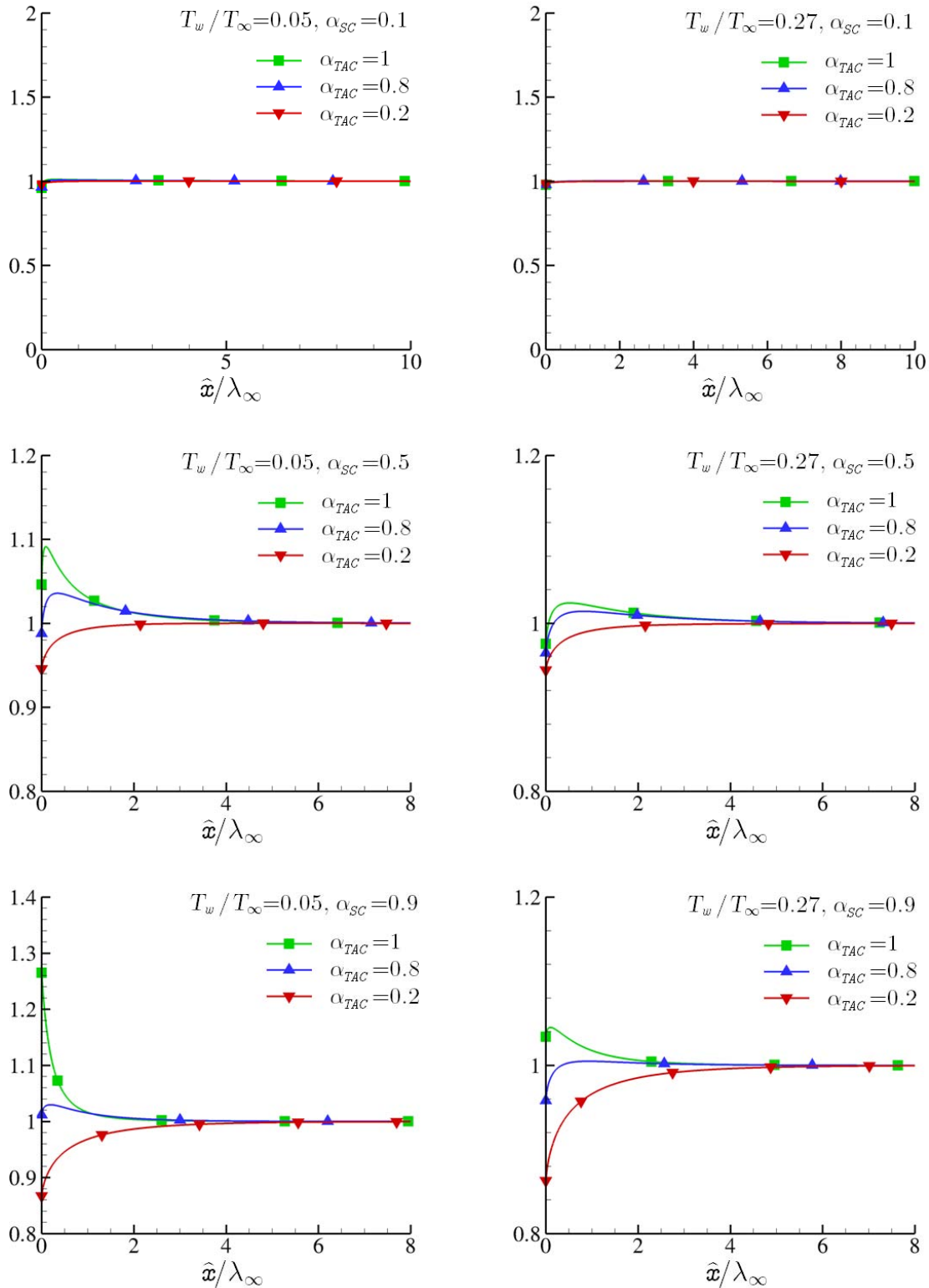
Figure 7.12: Dimensionless pressure $p(x)$ for temperature ratios $\tau_w = [0.05, 0.27]$ with sticking coefficient $\alpha_{SC} = [0.1, 0.5, 0.9]$ and thermal accommodation coefficient $\alpha_{TAC} = [1, 0.8, 0.2]$.
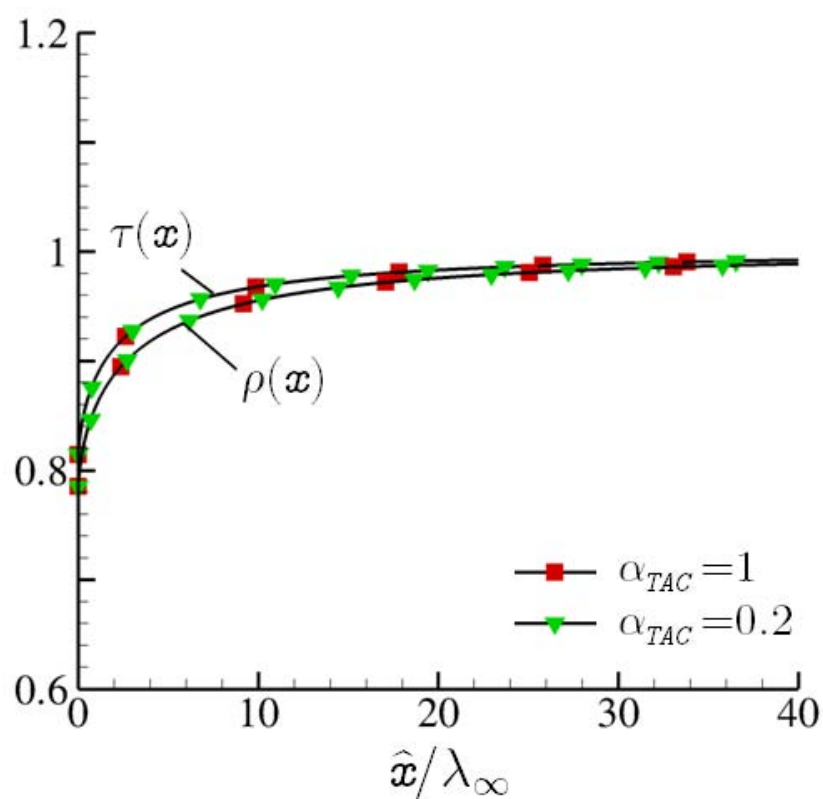
Figure 7.13: Dimensionless number density $\rho(x)$ and temperature $\tau(x)$ for temperature ratio $\tau_w = 0.05$ with sticking coefficient $\alpha_{SC} = 1$ and thermal accommodation coefficient $\alpha_{TAC} = [1, 0.2]$.
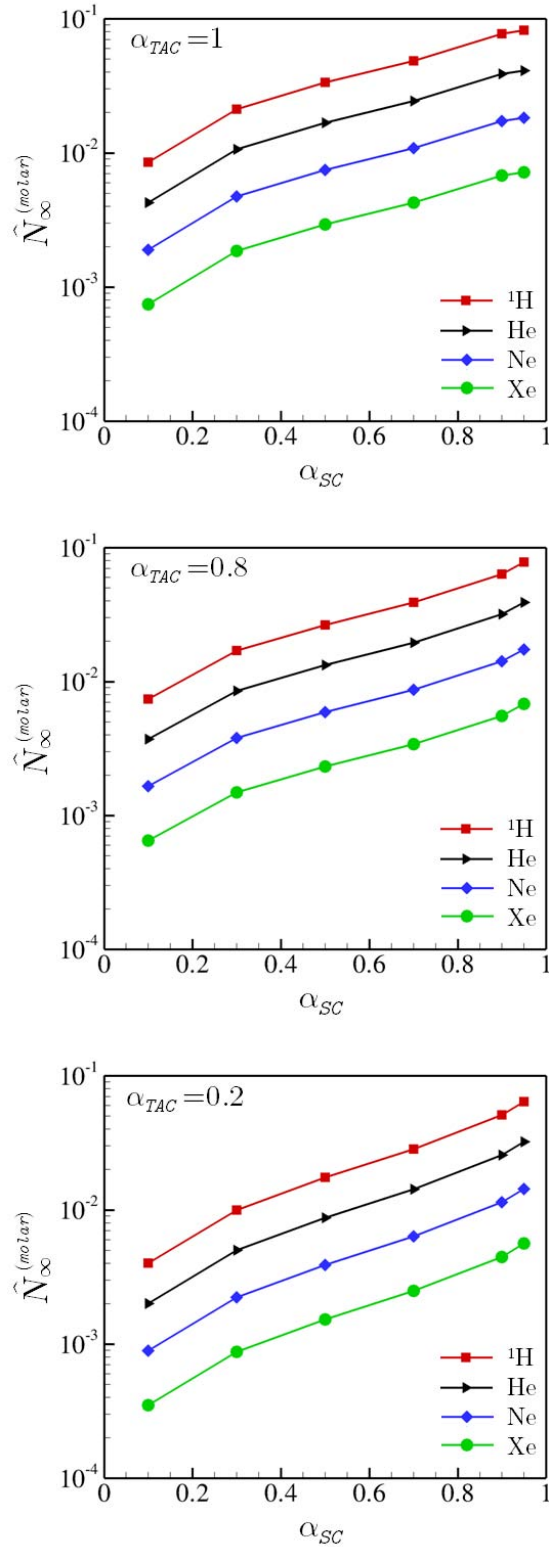
Figure 7.14: Net molar flux $\hat{N}_\infty^{(molar)}$ [mol/(m^2s)] of various gases as a function of the sticking coefficient α_{SC} for thermal accommodation coefficient $\alpha_{TAC} = [1, 0.8, 0.2]$ with $\hat{P}_\infty = 0.1$ Pa, $T_\infty = 300$ K and $\tau_w = 0.05$.

203
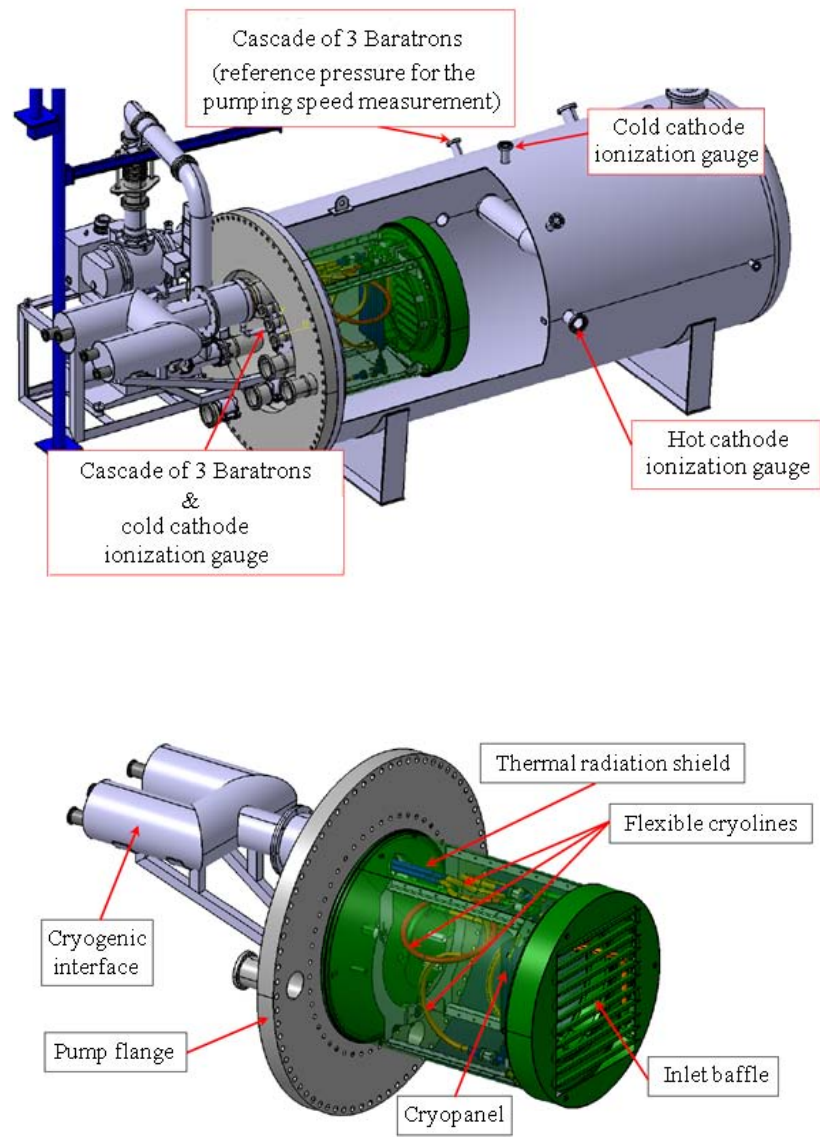
Figure 7.15: CAD views of the TIMO open panel pump and position of the pressure gauges.

204

Table 7.2: Simulation results for H_2 ($\omega = 0.67$) and adsorption surface temperature 18 K.

Sticking coefficient	$\alpha_{SC} = 0.7$	$\alpha_{SC} = 0.5$	$\alpha_{SC} = 0.1$	$\alpha_{SC} = 0.07$	$\alpha_{SC} = 0.05$	$\alpha_{SC} = 0.03$	$\alpha_{SC} = 0.01$
Rarefaction parameter	$\delta_0 = 2.69$	$\delta_0 = 2.91$	$\delta_0 = 4.96$	$\delta_0 = 5.88$	$\delta_0 = 7.07$	$\delta_0 = 10.01$	$\delta_0 = 18.9$
injected gas flow rate [sccm]	328	355	605	717	862	1222	2300
Net gas flow rate $\hat{N}$ [sccm]	200	202	203	201	199	207	178
Pressure at P_1 (Pa)	0.0136	0.0170	0.0511	0.0666	0.0863	0.134	0.280
Pumping speed S_R (m³/s) [Present work]	24.85	20.08	6.71	5.10	3.90	2.61	1.07
Pumping speed (m³/s) [TPMC]	28	21.3	4.95	3.51	2.52	1.53	0.51
Pumping speed (m³/s) [Experimental result]	$\simeq 2.61$ m³/s corresponding to panel temperature of 18 K						

Table 7.3: Simulation results for D_2 ($\omega = 0.67$) and adsorption surface temperature 18 K.

Sticking coefficient	$\alpha_{SC} = 0.09$	$\alpha_{SC} = 0.07$	$\alpha_{SC} = 0.05$	$\alpha_{SC} = 0.03$
Rarefaction parameter	$\delta_0 = 6.60$	$\delta_0 = 7.65$	$\delta_0 = 9.85$	$\delta_0 = 13.91$
injected gas flow rate [sccm]	570	660	850	1200
Net gas flow rate $\hat{N}$ [sccm]	190	194	208	211
Pressure at P_1 (Pa)	0.0692	0.0859	0.120	0.186
Pumping speed S_R (m³/s) [Present work]	4.64	3.82	2.93	1.92
Pumping speed (m³/s) [Experimental result]	$\simeq 3.54$ m³/s corresponding to panel temperature of 18 K			
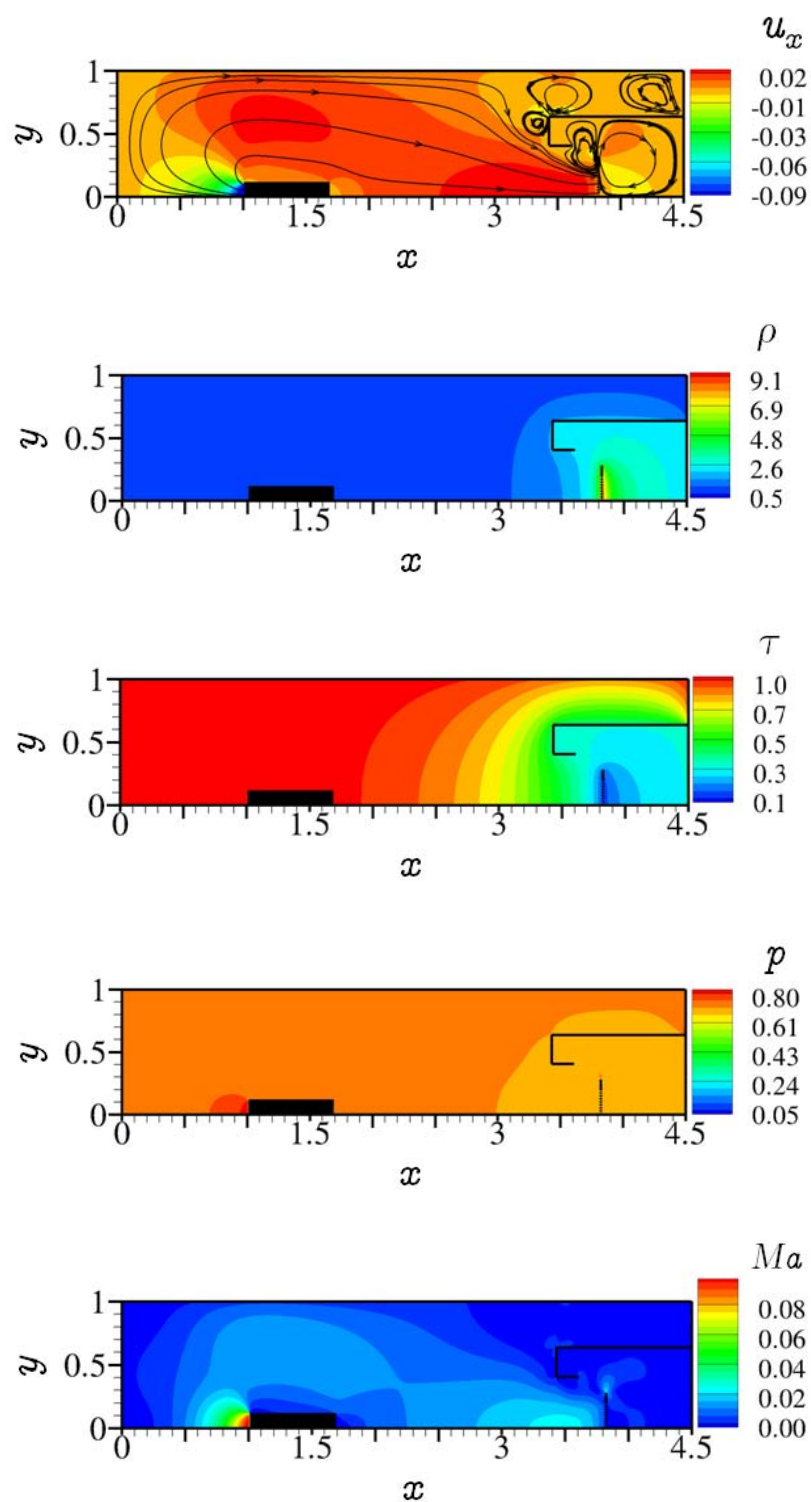
Figure 7.16: Dimensionless axial velocity, number density, temperature, pressure and Mach number isolines of H_2 ($\omega = 0.67$) for $\alpha_{SC} = 0.07$.
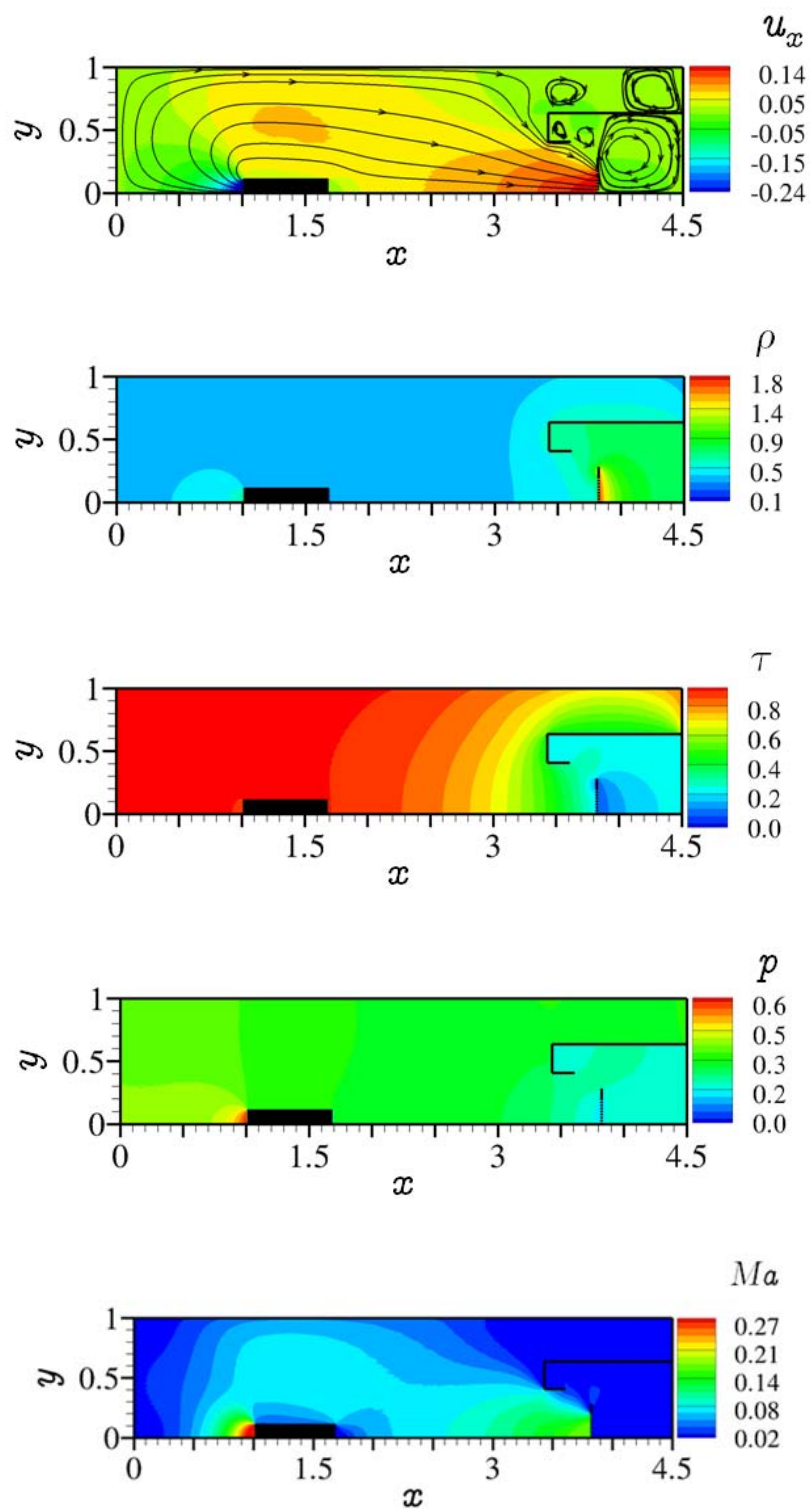
Figure 7.17: Dimensionless axial velocity, number density, temperature, pressure and Mach number isolines of H$_2$ ($\omega = 0.67$) for $\alpha_{SC} = 0.7$.

Chapter 8

Concluding remarks

The research work reported in this thesis is focused on the computational study of non-equilibrium transport phenomena in polyatomic gases in the whole range of the Knudsen number. More specifically, the effects of the rotational and vibrational degrees of freedom in polyatomic heat transfer, flow and adsorption processes based on the kinetic theory of gases are investigated. It is assumed that gas molecules possess both rotational and vibrational degrees of freedom, described by the rigid rotator and quantum harmonic oscillator models, respectively. Kinetic model equations have been computationally solved both deterministically and stochastically using the Discrete Velocity and the Direct Simulation Monte Carlo methods respectively. Results in terms of bulk quantities with practical interest, such as heat and mass flow rates, including comparisons between the kinetic models and the DSMC results as well as between simulations results and experimental data available in literature, are presented. A brief description of the investigated flow setups with the major contributions is outlined in Sections 8.1-8.3, while some future work perspectives are presented in Section 8.4. It is noted that the present work may be useful in the design and optimization of MEMS, vacuum sensors and other technological devices with polyatomic gases.

Overall, the theoretical/computational investigation performed in this thesis exhibits the importance of the rotational and vibrational degrees of freedom of polyatomic gases in non-equilibrium transport phenomena. It has been shown that ignoring the internal structure of the molecules may yield erroneous results and large deviations between measurements and

209

calculations. The work provides some useful insight in the design and optimization of processes and devices with polyatomic gases operating under rarefied conditions in a wide temperature range.

8.1 Polyatomic heat transfer

The problem of conductive heat transfer through rarefied non-polar polyatomic gases confined between infinite long parallel plates and coaxial cylinders maintained at different temperatures is investigated. The analysis is based on three kinetic models namely the ones proposed by Holway, Rykov and Andries as well as on the DSMC method supplemented by the Borgnakke-Larsen collision model. The quantitative behavior of the radial heat fluxes, temperatures and densities are examined in a wide range of the gas rarefaction parameter and for small, moderate and large normalized temperature differences at various radius ratios. The three kinetic models and the DSMC method provide very close values of the computed macroscopic quantities as well as very good agreement with corresponding experimental data available in the literature. In addition, the computational results perfectly match the analytical ones in the free molecular limit and tend to the analytical ones in the hydrodynamic regime.

The total heat fluxes of linear and non-linear polyatomic gases have been found to be higher about $30-50\%$ and $50-75\%$ respectively, than the corresponding monatomic ones, with the highest differences occurring in the free molecular limit. As the amount of elastic compared to inelastic collisions is increased, the translational heat fluxes are slightly increased and they tend to the monatomic ones, while always the rotational heat fluxes are about 50% and 75% of the translational ones for diatomic and polyatomic gases respectively. Concerning the effect of the vibrational degrees of freedom it is strongly depending on the number of vibrational degrees of freedom as well as on the activation vibrational temperature of the working gas. Therefore, different gases, namely N_2, O_2, CO_2, CH_4 and SF_6 representing diatomic as well as linear and nonlinear polyatomic molecules with 1 up to 15 vibrational modes are considered. In diatomic gases the vibrational heat flux varies from 5% up to 25% of the total one, while corresponding results in polyatomic gases with high number of vibrational modes show that even at low reference temperatures the contribution of the vibrational heat flux may be considerably

higher. For example, in the case of SF$_6$ at 300 K and 500 K the vibrational heat flux is computed to be 67% and 76% respectively of the total heat flux.

Moreover, the effect of the thermal accommodation at the boundaries has also been examined for various diffuse-specular reflection scenarios. In most cases as the thermal accommodation coefficient is increased, i.e. the gas-surface interaction becomes more diffusive, the dimensionless total heat flux is monotonically increased. The effective thermal conductivity approximation has been also studied finding out that it can be successfully applied in polyatomic gases to study non-equilibrium effects provided that the system Knudsen number is small.

8.2   Polyatomic flows

Polyatomic gas flows through short and long tubes have been studied. More specifically, the pressure driven rarefied polyatomic gas flow through short tubes into vacuum has been numerically investigated based on the Holway kinetic model subject to diffuse boundary conditions. Such flows are characterized by low Reynolds numbers and high viscous losses and therefore short circular micro-tubes may be used instead of typical micro-nozzles. The propulsion characteristics including the flow rate, the thrust, the impulse factor and the discharge coefficient as well as the distributions of the macroscopic quantities with practical interest have been obtained. It is found that the effect of the rotational degrees of freedom on the macroscopic quantities is small except in the case of temperature distributions. It may be concluded that the overall propulsion efficiency in the case of polyatomic gases compared to the one in monatomic gases is slightly improved. Also, it has been demonstrated that this type of flows, which have been simulated so far only based on the DSMC method, can be also tackled by kinetic modeling.

Also, the flow of a polyatomic rarefied gas in a capillary tube of infinite length driven by small pressure gradients (Poiseuille flow) or small temperature gradients (thermal creep flow) has been studied based on the Rykov model. Very good agreement with available numerical results and experimental data in literature for diatomic gases has been obtained. The effect of the rotational degrees of freedom on the mass flow rates due to pressure differences, as in the case of the short tubes, is almost negligible. On the contrary, there is a significant effect on the

thermal creep flow, where in diatomic and linear polyatomic gases the heat flow rate may be higher about $30-40\%$ than the corresponding monatomic one, while this difference can reach $50-65\%$ in the case of nonlinear polyatomic gases.

8.3 Polyatomic gas adsorption on solid surfaces

Gas adsorption flow has been investigated based on the Bhatnagar-Gross-Krook and Holway kinetic model equations for monatomic and polyatomic gases respectively. The one-dimensional half-space flow of a polyatomic gas in the presence of an absorbing planar wall has been considered. Overall the effect of the rotational degrees of freedom on the computed quantities is about 10%. Therefore, the dimensionless results of monatomic gases may be also used in the case of polyatomic gases. Furthermore, the influence of the partial thermal gas surface interaction on all flow quantities including the sticking coefficient has been studied. It has been found that as the gas thermal accommodation on the surface is reduced for prescribed adsorbing flux and temperature difference the sticking coefficient must be increased to sustain the prescribed flux or otherwise for the same sticking coefficient the adsorbing flux is reduced. This behavior is further enhanced as the difference, between the surface and the far upstream temperature is increased, which is commonly the case in cryogenic applications. Overall, the effect of the thermal accommodation coefficient is significant in all flow quantities and the type of thermal gas-surface interaction must be accordingly taken into consideration.

The study of the adsorption process is extended to the case of a two-dimensional configuration in order to simulate an open panel experiment, conducted at a test facility at the Karlsruhe Institute of Technology (KIT) in Germany. Combining computational results with experimental data, the values of the sticking coefficients of different gases have been estimated, supporting decision making related to the design of the cryogenic pumping system. Massive simulations have been performed for different sets of parameters following the experimental setup used at KIT. Simulations have been performed for different sets of parameters and numerical data have been recovered for H_2 and D_2. Following a comparison with experimental data, the sticking coefficient for both gases has been provided. In addition, the detailed flow structure in terms of all macroscopic quantities of practical interest is viewed and the effect of

the temperature of the adsorbing plate is reported. Most important a significant amount of back flow in the inlet slit is observed highly influencing the overall adsorption performance.

8.4   Future work

Continuation and further development of the present research may be performed in the following directions:

- Transport phenomena in rarefied binary gas mixtures consisting of polyatomic gases have not been investigated so far and it is a field where the knowledge and experience obtained in the present work could be very useful in the investigation of such processes. Particularly, simulating adsorption processes with such gases is very interesting both theoretically and technologically (e.g. cryopumps).

- Extending the present computational work by including dissociation and electronic excitation in polyatomic molecules using basic principles of the kinetic theory is also very promising. This will provide a more thorough understanding and lead to improved comparisons with experimental data for gases having low excitation energies.

- Estimation of the slip and jump coefficients in the case of polyatomic gases may be now performed in a relatively straightforward manner. Having these coefficients for polyatomic gases will allow the implementation of continuum mechanics equations with velocity slip and temperature jump boundary conditions for moderately small Knudsen number. This analysis is available in monatomic gases but very limited work has been done in polyatomic gases.

- The investigation of the feasibility of the three stage cryopump concept for the main vacuum pumping system of the Demonstration Power Plant (DEMO) fusion facility will be continued. More detailed comparisons with experimental data will be performed.

- Modification of the parallelized numerical codes developed here in order to be executed by GPUs with CUDA is an action which definitely must be seriously considered. This modification will result to high performance improvements and allow simulations of the real geometry without simplifications.

Appendices

Appendix A

Relaxation rates in a homogeneous gas

A.1   Rotational relaxation

Comparisons between the translational-rotational relaxation rates of the applied kinetic model equations and those of the DSMC method with the Borgnakke-Larsen collision model are performed. Consider a spatially homogeneous polyatomic gas at a constant equilibrium total temperature but different initial rotational and translational temperatures. Then, the rotational and translational temperatures will evolve and relax toward the constant equilibrium total temperature with a common rate determined by the collision frequency and rotational relaxation parameter Z. By operating accordingly on the kinetic model equations the time evolution of the translational-rotational temperatures may be obtained. Then, the parameter $Z^{(i)}$ is accordingly fixed to ensure equivalent translational and rotational relaxation rates in order to have a consistent comparison. The kinetic model equations Eq. (3.24) and Eq. (3.37) are rewritten for a time-dependent homogeneous system, i.e., by adding the time derivative term and omitting all space derivatives terms. Then, they are accordingly combined and the resulting equations are integrated over the velocity space to yield the following relaxation equations for each model:

- Holway

$$\frac{d\tau_{tr}}{dt} = \frac{8}{5\sqrt{\pi}} \Pr \frac{\sqrt{\tau_{tr}}}{Z^{(H)}} \left[\tau - \tau_{tr} \right], \quad \frac{d\tau_{rot}}{dt} = \frac{8}{5\sqrt{\pi}} \Pr \frac{\sqrt{\tau_{tr}}}{Z^{(H)}} \left[\tau - \tau_{rot} \right] \tag{A.1}$$

217

- Rykov

$$\frac{d\tau_{tr}}{dt} = \frac{8}{5\sqrt{\pi}} \frac{\sqrt{\tau_{tr}}}{Z^{(R)}} \left[\tau - \tau_{tr}\right], \quad \frac{d\tau_{rot}}{dt} = \frac{8}{5\sqrt{\pi}} \frac{\sqrt{\tau_{tr}}}{Z^{(R)}} \left[\tau - \tau_{rot}\right] \quad (A.2)$$

- Andries

$$\frac{d\tau_{tr}}{dt} = \frac{8}{5\sqrt{\pi}} \frac{\sqrt{\tau_{tr}}}{Z^{(A)}} \left[\tau - \tau_{tr}\right], \quad \frac{d\tau_{rot}}{dt} = \frac{8}{5\sqrt{\pi}} \frac{\sqrt{\tau_{tr}}}{Z^{(A)}} \left[\tau - \tau_{rot}\right] \quad (A.3)$$

All above equations have been deduced by introducing hard-sphere interactions ($\omega = 1/2$) and the dimensionless time $t = \hat{t}/\left(\lambda_0/\upsilon_0\right)$, with $\lambda_0 = 1/\left(\sqrt{2}\pi d^2 n_0\right)$ being the mean free path of hard sphere molecules and d denoting the molecular diameter, as well as the equation $\partial n/\partial t = 0$. It is also noted that in the relaxation equations of the Andries model $Z^{(A)} = \left(1 - \nu + \theta\nu\right)/\theta$ and $\mathrm{Pr} = \left(1 - \nu + \theta\nu\right)^{-1}$.

The relaxation rates of the kinetic model equations have been compared numerically with the corresponding ones of the DSMC method. It has been found that by setting

$$Z^{(DSMC)} = Z^{(A)}\left(\nu, \theta\right) = Z^{(R)}\left(\varpi_0, \varpi_1\right) = \frac{Z^{(H)}}{\mathrm{Pr}}, \quad (A.4)$$

where $Z^{(DSMC)}$ denotes the rotation collision parameter in the DSMC simulations, nearly identical translational-rotational relaxation rates are produced in all cases. The relations between the rotational collision numbers of the three kinetic models, shown in Eq. (A.4), are well justified by Eqs. (A.1)-(A.3), while their connection to $Z^{(DSMC)}$ is validated numerically. Some indicative results are demonstrated in Fig. A.1, where the time evolution of the translational and rotational temperatures towards the equilibrium temperature for a diatomic gas with $\mathrm{Pr} = 0.73$ and initial conditions $\tau_{tr}\left(0\right) = 3$ and $\tau_{rot}\left(0\right) = 1$, are shown. It is seen that for $Z^{(DSMC)} = Z^{(R)} = Z^{(A)} = 5$ and $Z^{(H)} = 3.65$ excellent agreement in the relaxation towards equilibrium between all models is obtained. The rotational collision number $Z^{(A)}$ has been obtained with $\nu = -0.5$ and $\theta = 0.273$, while $Z^{(H)} = Z^{(DSMC)}\,\mathrm{Pr}$. On the contrary for the Holway model presents a slower relaxation towards equilibrium. Eq. (A.4) is used in Section 3.5.2 to define the rotational collision number for the various kinetic models and the DSMC method in order to have a consistent comparison between the computed heat fluxes.

A.2 Vibrational relaxation

In the study of the heat transfer in polyatomic gases confined between parallel plates including the translational, rotational and vibrational degrees of freedom of the molecules in order to achieve a proper comparison between the Holway kinetic model and the DSMC method, it is necessary to match the rotational and vibrational relaxation rates of the two approaches by accordingly fixing the collision numbers $Z_r^{(i)}$ and $Z_v^{(i)}$, with the superscript i being (H) and $(DSMC)$ in the case of the Holway model and the DSMC method respectively. The corresponding analysis for the rotational relaxation rates has been done in Section A.1.

Consider a spatially homogeneous diatomic gas at a constant equilibrium total temperature and an initial vibrational temperature which is different than the initial translational and rotational temperatures which are set equal to each other. Then, all partial temperatures will evolve and relax toward the constant equilibrium total temperature with a common rate determined by the collision frequency and vibrational relaxation numbers $Z_r^{(i)}$ and $Z_v^{(i)}$. By operating accordingly on the kinetic model equations the time evolution of the temperatures may be obtained. Then, the parameters $Z_r^{(i)}$ and $Z_v^{(i)}$ are accordingly fixed to ensure equivalent translational, rotational and vibrational relaxation rates in order to have a consistent comparison.

The kinetic model Eqs. (5.15) are rewritten for a time-dependent homogeneous system, i.e., by adding the time derivative term and omitting all space derivatives terms. Then, they are accordingly combined and the resulting equations are integrated over the velocity and energy spaces to yield the following relaxation kinetic equations

$$\frac{dT_{tr}}{d\hat{t}} = \Pr \frac{T_{tr}^{1-\omega}\hat{P}_0}{T_0^{1-\omega}\mu\left(T_0\right)} \left[\frac{1}{Z_v^{(H)}} \left(T_{tot} - T_{tr}\right) + \frac{2}{5}\frac{1}{Z_r^{(H)}} \left(T_{rot} - T_{tr}\right) \right], \tag{A.5}$$

$$\frac{dT_{rot}}{d\hat{t}} = \Pr \frac{T_{tr}^{1-\omega}\hat{P}_0}{T_0^{1-\omega}\mu\left(T_0\right)} \left[\frac{1}{Z_v^{(H)}} \left(T_{tot} - T_{rot}\right) + \frac{3}{5}\frac{1}{Z_r^{(H)}} \left(T_{tr} - T_{rot}\right) \right], \tag{A.6}$$

$$\frac{d\left[T_{vib}\zeta_v\left(T_{vib}\right)\right]}{d\hat{t}} = \frac{\Pr}{Z_v^{(H)}} \frac{T_{tr}^{1-\omega}\hat{P}_0}{T_0^{1-\omega}\mu\left(T_0\right)} \left[T_{tot}\zeta_v\left(T_{tot}\right) - T_{vib}\zeta_v\left(T_{vib}\right)\right]. \tag{A.7}$$

All quantities are defined in Chapter 5. The number density remains constant in time $\partial n/\partial \hat{t} = 0$.

The relaxation rates of the kinetic model equations have been compared numerically with the corresponding ones of the DSMC method and it has been found that good agreement is observed by setting [172]

$$Z_i^{(H)} = \frac{\text{Pr}}{30} \left(6 - \frac{4}{\alpha} \right) \left(4 - \frac{4}{\alpha} \right) Z_i^{(DSMC)}, \qquad (A.8)$$

where $i = r$, v and $\alpha = 4/(2\omega - 1)$ is a parameter of the inverse power law potential which varies between the limits for Maxwell molecules ($\alpha = 4$) and hard sphere molecules ($\alpha \to \infty$).

Indicative results are demonstrated in Fig. A.2, where the time evolution of the translational, rotational and vibrational temperatures toward the equilibrium temperature for a diatomic gas (Pr = 0.764, $\omega = 0.74$, $\hat{P}_0 = 0.1$ Pa, $\mu(T_0) = 94.55$ μPa s) [145] with initial temperatures $T_{tr}^{(i)}(0) = T_{rot}^{(i)}(0) = 3371$ K and $T_{vib}^{(i)}(0) = 6742$ K, are shown. It is seen that for $Z_v^{(DSMC)} = 50$ and $Z_r^{(DSMC)} = 5$ there is very good agreement provided that using Eq. (A.8), $Z_v^{(H)} = 24.7$ and $Z_r^{(H)} = 2.47$. Eq. (A.8) is used in Subsection 5.4.1 to define the rotational and vibrational collision numbers for the Holway kinetic model and the DSMC method in order to have a consistent comparison between the computed heat fluxes and the other macroscopic quantities.
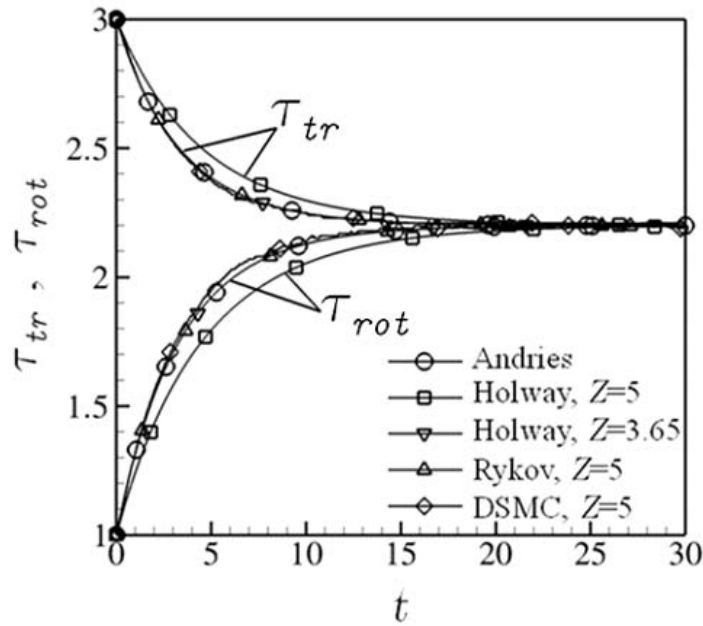
Figure A.1: Translational-rotational relaxation in a homogeneous gas.
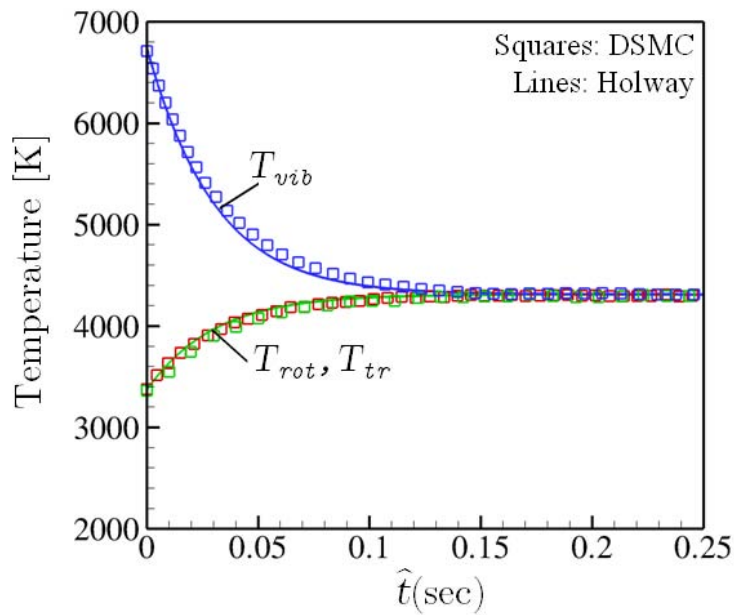
Figure A.2: Translational-rotational-vibrational relaxation in a homogeneous gas.

221

Appendix B

The H-Theorem for the Holway model

In classical statistical mechanics, the H-theorem, introduced by Ludwig Boltzmann in 1872, describes the tendency to decrease the quantity $\mathcal{H}$ (defined below) in a nearly-ideal gas of molecules [1]. As this quantity $\mathcal{H}$ was meant to represent the entropy of thermodynamics, the H-theorem was an early demonstration of the power of statistical mechanics as it claimed to derive the second law of thermodynamics. The H-theorem may be considered as more general than the second law of thermodynamics, which states that entropy cannot decrease, because it applies even far from equilibrium, while the entropy is defined only in equilibrium. However, the H-theorem has been proven only for dilute gases whereas the second law applies to any system in equilibrium. The H-theorem is formulated as [1]

$$\frac{\partial \mathcal{H}}{\partial \hat{t}} + \frac{\partial \mathcal{H}_i}{\partial \hat{x}_i} \leq 0, \quad i = \hat{x}, \hat{y}, \hat{z} \tag{B.1}$$

where

$$\mathcal{H} = \int\limits_{-\infty}^{\infty} \int\limits_{0}^{\infty} \hat{f} \ln \hat{f} \, d\hat{I} d\boldsymbol{v}, \quad \mathcal{H}_i = \int\limits_{-\infty}^{\infty} \int\limits_{0}^{\infty} v_i \hat{f} \ln \hat{f} \, d\hat{I} d\boldsymbol{v}. \tag{B.2}$$

223

Multiplying Eq. (2.5) by $\ln \hat{f}$ and integrating the resulting equation over $\hat{I}$ and $\boldsymbol{v}$ and after some routine manipulation is obtained

$$\frac{\partial}{\partial \hat{t}} \int\limits_{-\infty}^{\infty} \int\limits_{0}^{\infty} \hat{f} \ln \hat{f} \, d\hat{I} d\boldsymbol{v} + \frac{\partial}{\partial \hat{x}_i} \int\limits_{-\infty}^{\infty} \int\limits_{0}^{\infty} v_i \hat{f} \ln \hat{f} d\hat{I} d\boldsymbol{v} =$$

$$= \int\limits_{-\infty}^{\infty} \int\limits_{0}^{\infty} \left[\nu_{tr} \left(\hat{f}_{tr} - \hat{f} \right) + \nu_{rot} \left(\hat{f}_{rot} - \hat{f} \right) \right] \ln \hat{f} d\hat{I} d\boldsymbol{v}, \quad \text{(B.3)}$$

where v_{coll} is the collision frequency. In the derivation of Eq. (B.3) the collision invariant of mass has been used. Also, the following two equations can be easily proved for the Holway model

$$\int\limits_{-\infty}^{\infty} \int\limits_{0}^{\infty} \left(\hat{f}_{tr} - \hat{f} \right) \ln \hat{f}_{tr} d\hat{I} d\boldsymbol{v} = 0, \quad \int\limits_{-\infty}^{\infty} \int\limits_{0}^{\infty} \left(\hat{f}_{rot} - \hat{f} \right) \ln \hat{f}_{rot} d\hat{I} d\boldsymbol{v} = 0. \quad \text{(B.4)}$$

From the Eqs. (B.3)-(B.4) it is obtained

$$\frac{\partial}{\partial \hat{t}} \int\limits_{-\infty}^{\infty} \int\limits_{0}^{\infty} \hat{f} \ln \hat{f} \, d\hat{I} d\boldsymbol{v} + \frac{\partial}{\partial \hat{x}_i} \int\limits_{-\infty}^{\infty} \int\limits_{0}^{\infty} v_i \hat{f} \ln \hat{f} d\hat{I} d\boldsymbol{v} =$$

$$= \int\limits_{-\infty}^{\infty} \int\limits_{0}^{\infty} \left[\nu_{tr} \left(\hat{f}_{tr} - \hat{f} \right) \ln \left(\frac{\hat{f}}{\hat{f}_{tr}} \right) + \nu_{rot} \left(\hat{f}_{rot} - \hat{f} \right) \ln \left(\frac{\hat{f}}{\hat{f}_{rot}} \right) \right] d\hat{I} d\boldsymbol{v}. \quad \text{(B.5)}$$

The collision frequencies ν_{tr} and ν_{rot} are necessarily greater than 0 and the terms

$$\left(\hat{f}_{tr} - \hat{f} \right) \ln \left(\frac{\hat{f}}{\hat{f}_{tr}} \right), \quad \left(\hat{f}_{rot} - \hat{f} \right) \ln \left(\frac{\hat{f}}{\hat{f}_{rot}} \right), \quad \text{(B.6)}$$

are always lower than 0. We have therefore at the first order

$$\frac{\partial}{\partial \hat{t}} \int\limits_{-\infty}^{\infty} \int\limits_{0}^{\infty} \hat{f} \ln \hat{f} \, d\hat{I} d\boldsymbol{v} + \frac{\partial}{\partial \hat{x}_i} \int\limits_{-\infty}^{\infty} \int\limits_{0}^{\infty} v_i \hat{f} \ln \hat{f} d\hat{I} d\boldsymbol{v} \leq 0. \quad \text{(B.7)}$$

Consequently the H-theorem for the Holway model is proven.

Appendix C

Analytical solutions

In some cases, it is possible to derive analytical solutions in the two limits of the Knudsen number: the free molecular regime ($\delta_0 = 0$) and the hydrodynamic regime ($\delta_0 \to \infty$). Closed form expressions are provided here, used as benchmarking criteria for our numerical methods.

C.1 Free molecular regime

In the collisionless regime ($\delta_0 = 0$), the right hand side of the Boltzmann equation vanishes and the problem can be solved analytically by the method of characteristics.

- *Heat transfer between parallel plates*

  In the free molecular limit ($\delta_0 = 0$) the right hand side of the Eqs. (3.24) and (3.37) becomes zero and then based on the associated boundary conditions closed form expressions for the reduced distributions functions $\mathbf{\Psi}$ are readily deduced, which are substituted into the moment equations Eqs. (3.27)-(3.29) to yield analytical results for the macroscopic distributions. It is noted that in the free molecular limit all moments are independent of y and remain constant at any position between the plates. Following this procedure and using boundary conditions (3.45) and (3.46), the translational and rotational temperatures in terms of the thermal accommodation coefficient α and the normalized temperature

225

difference β are written as

$$\tau_{tr,fm}(\alpha,\beta) = \tau_{rot,fm}(\alpha,\beta) = \frac{\sqrt{\gamma^2-1}}{\gamma}, \tag{C.1}$$

while the translational and rotational heat fluxes are given by

$$q_{tr,fm}(\alpha,\beta) = \left(1+\frac{1}{\gamma}\right)^{3/2}\frac{\left(1-\gamma+\sqrt{\gamma^2-1}\right)}{\sqrt{\pi}} - \left(1-\frac{1}{\gamma}\right)^{3/2}\frac{\left(1+\gamma-\sqrt{\gamma^2-1}\right)}{\sqrt{\pi}}, \tag{C.2}$$

and

$$q_{rot,fm}(\alpha,\beta) = \frac{j}{4}q_{tr,fm}(\alpha,\beta) \tag{C.3}$$

respectively, where $\gamma = (2-\alpha)/(\alpha\beta)$. For the specific case of purely diffuse reflection ($\alpha = 1$ and $\gamma = 1/\beta$), Eqs. (C.1)-(C.3) are reduced to

$$\tau_{tr,fm}(\beta) = \tau_{rot,fm}(\beta) = \sqrt{1-\beta^2}, \tag{C.4}$$

$$q_{tr,fm}(\beta) = \frac{2}{\sqrt{\pi}}\left[(1+\beta)\sqrt{1-\beta} - (1-\beta)\sqrt{1+\beta}\right] \tag{C.5}$$

and

$$q_{rot,fm}(\beta) = \frac{j}{4}q_{tr,fm}(\beta). \tag{C.6}$$

The number density remains constant and equal to 1 ($\rho_{fm} = 1$). In the case of the study that includes vibrational degrees of freedom the vibrational temperature and heat flux may be included. Following the corresponding process which has been applied for the translational and rotational heat flux and using the boundary conditions (5.25) and (5.26) along with the moments (5.22) the vibrational heat flux is given as

$$q_{vib,fm} = \frac{1}{2\sqrt{\pi}}\frac{\sqrt{\tau_{w,C}\tau_{w,H}}}{\sqrt{\tau_{w,C}} + \sqrt{\tau_{w,H}}}\left[\tau_{w,H}\zeta_v(\tau_{w,H}) - \tau_{w,C}\zeta_v(\tau_{w,C})\right], \tag{C.7}$$

where $\tau_{w,H} = T_H/T_0$ and $\tau_{w,C} = T_C/T_0$, while ζ_v is the vibrational degrees of freedom as defined by Eq. (5.23). In the case of diatomic gases an analytical expression for the

226

vibrational temperature can be obtained as

$$\tau_{vib,fm} = \frac{\theta_v}{\ln\left[1 + 2\theta_v \dfrac{\sqrt{\tau_{w,C}} + \sqrt{\tau_{w,H}}}{\tau_{w,H}\sqrt{\tau_{w,C}}\zeta_v\left(\tau_{w,H}\right) + \tau_{w,C}\sqrt{\tau_{w,H}}\zeta_v\left(\tau_{w,C}\right)}\right]}, \qquad (C.8)$$

while the corresponding expression for polyatomic gases takes the form

$$\tau_{vib,fm} = \frac{\tau_{w,H}\sqrt{\tau_{w,C}}\zeta_v\left(\tau_{w,H}\right) + \tau_{w,C}\sqrt{\tau_{w,H}}\zeta_v\left(\tau_{w,C}\right)}{\zeta_v\left(\tau_{vib,fm}\right)\left(\sqrt{\tau_{w,C}} + \sqrt{\tau_{w,H}}\right)}. \qquad (C.9)$$

In Fig. C.1 the free molecular total heat flux $q_{fm} = q_{tr,fm} + q_{rot,fm}$ is plotted for a diatomic gas ($j = 2$) in terms of the parameters α and β. It is seen that at small β, q_{fm} is monotonically increased with the thermal accommodation coefficient α and the maximum q_{fm} occurs at $\alpha = 1$. However, at large β the corresponding behavior is non-monotonic and the maximum q_{fm} appears at some value of $\alpha < 1$. Similar results have also been obtained in Subsection 3.5.3 for $\delta_0 > 0$, provided that the temperature difference is adequately large and the gas rarefaction parameter remains low.
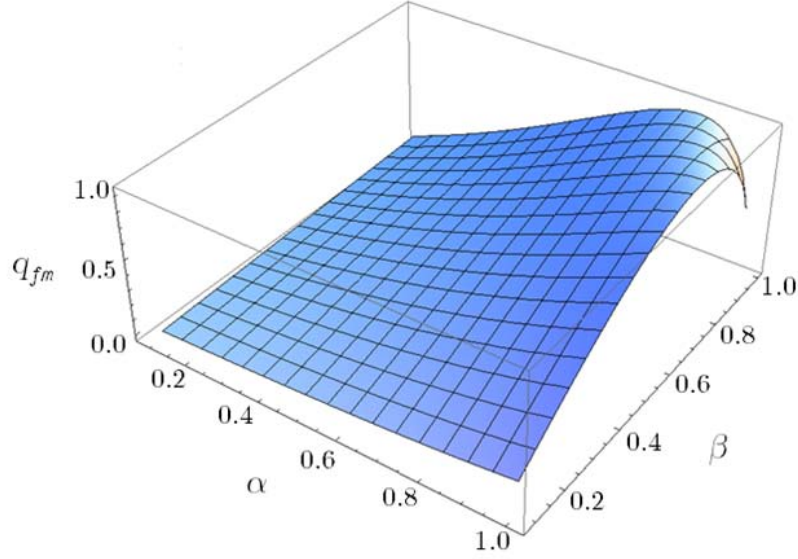
Figure C.1: The free molecular total heat flux q_{fm} in terms of the thermal accommodation coefficient α and the normalized temperature difference β.

- *Heat transfer between coaxial cylinders*

  The right hand side of Eq. (4.16) becomes zero and in the case of Maxwell diffuse boundary conditions the reduced distribution functions are given for $\theta \in [-\pi/2, \pi/2]$ by

$$F^+ = \frac{\rho_w}{\pi\,(1+\beta)}\exp\left(-\frac{\zeta^2}{1+\beta}\right), \quad G^+ = \frac{1}{2}(1+\beta)F^+, \quad S^+ = \frac{j}{2}(1+\beta)F^+ \qquad \text{(C.10)}$$

  and for $\theta \in [\pi/2, 3\pi/2]$ by

$$F^+ = \frac{1}{\pi}\exp\left(-\zeta^2\right), \quad G^+ = \frac{1}{2}F^+, \quad S^+ = \frac{j}{2}F^+. \qquad \text{(C.11)}$$

  where the impermeability parameter is found from the no penetration condition to be

$$\rho_w = \frac{1}{\sqrt{1+\beta}}. \qquad \text{(C.12)}$$

  Then, substituting Eqs. (C.10)-(C.12) into the moment Eqs. (4.19)-(4.21) and following a straightforward manipulation yields

$$\rho_{fm}(r,\beta) = \frac{1}{\pi}\left(\frac{\theta_1}{\sqrt{1+\beta}} - \theta_1 + \pi\right), \qquad \text{(C.13)}$$

228

$$\tau_{tr,fm}(r,\beta) = \tau_{rot,fm}(r,\beta) = \frac{1}{\rho_{fm}(r,\beta)\pi}\left[\theta_1\left(\sqrt{1+\beta}\right) + \pi - \theta_1\right], \qquad \text{(C.14)}$$

$$q_{tr,fm}(r,\beta) = \frac{\beta\gamma}{r\sqrt{\pi}}, \quad q_{rot,fm}(r,\beta) = \frac{j\beta\gamma}{4r\sqrt{\pi}}, \quad q_{fm}(r,\beta) = \left(1+\frac{j}{4}\right)\frac{\beta\gamma}{r\sqrt{\pi}}. \qquad \text{(C.15)}$$

In Eqs. (C.13) and (C.14) the discontinuity angle $\theta_1 = \sin^{-1}(\gamma/r)$ is displayed in Fig. (4.1). Obviously the results do not depend on the type of model and are exactly the same for the Holway and Rykov models. It is seen that in the free molecular limit for $j = 2$ and $j = 3$ the rotational heat flux is one half and three quarters respectively of the corresponding translational one, while in the case of a monatomic gas ($j = 0$) the rotational is equal to zero and the translational is equal to the total heat flux. It is noted that the numerical solution for $\delta_B = 0$ is in excellent agreement with the analytical results of Eqs. (C.13)-(C.15).

C.2   Hydrodynamic regime

In the continuum regime ($\delta_0 \to \infty$), we can apply the hydrodynamic equations.

- *Heat transfer between parallel plates*

  In the hydrodynamic limit ($\delta_0 \to \infty$) the Fourier law is introduced into the energy equation to yield the total heat flux

$$\frac{d\hat{q}}{d\hat{y}} = \frac{d}{d\hat{y}}\left(k\frac{dT}{d\hat{y}}\right) = 0, \qquad \text{(C.16)}$$

where k is the thermal conductivity. If Euler splitting of the internal modes of energy transfer is assumed, the polyatomic value of the thermal conductivity is [47]

$$k = \left(\frac{15}{4} + \frac{j}{2}\right)\mu R, \qquad \text{(C.17)}$$

where $j = 0, 2, 3$ is the number of the rotational degrees of freedom, μ is the viscosity and $R = k_B/m$ is the individual gas constant. Applying the same process of the non-dimensionalization mentioned in Subsection 3.3.1 and introducing the dependence of

viscosity on temperature according to Eq. (3.19) the dimensionless heat flux is written as

$$q\left(\delta_0 \to \infty\right) = \left(\frac{5}{4} + \frac{j}{6}\right) \frac{\left[(1+\beta)^{3/2} - (1-\beta)^{3/2}\right]}{\delta_0}. \tag{C.18}$$

The tabulated numerical results in Subsection 3.5.2 for $j = 0, 2, 3$ tend to the corresponding analytical results of Eq. (C.18) at large values of the gas rarefaction parameter.

- *Heat transfer between coaxial cylinders*

  Based on the Fourier law, the dimensionless heat flux for a monatomic gas with HS molecules confined between two cylinders has been obtained analytically in [89]. It is noted that the ratio of the thermal conductivity k of a polyatomic gas over its viscosity μ introducing the Eucken correction, can be written as [47]

$$\frac{k}{\mu} = \frac{9c_p - 5c_v}{4}, \tag{C.19}$$

  where c_p and c_v are the specific heats at constant pressure and temperature respectively given, in terms of the degrees of freedom $j = 0, 2, 3$, by

$$c_p = \frac{k_B}{m} \frac{5+j}{2}, \quad c_v = \frac{k_B}{m} \frac{3+j}{2}. \tag{C.20}$$

  Then, following the same procedure as in [89], it is readily deduced that

$$q(\delta_B \to \infty) = -\left(\frac{5}{4} + \frac{j}{6}\right) \frac{\left[(\beta+1)^{3/2} - 1\right]}{r\delta_B \ln \gamma}. \tag{C.21}$$

For $j = 0$, Eq. (C.21) is reduced to the monatomic heat flux in [89], while for $j = 2, 3$ the corresponding diatomic and polyatomic heat fluxes are obtained. The present numerical results for large values of the gas rarefaction parameter tend to the analytical results of Eq. (C.21).

230

Appendix D

Heat conduction at small temperature difference based on Rykov model

Here, the heat conduction in rarefied diatomic gases confined between two stationary coaxial cylinders at small temperature differences is investigated based on the Rykov model (R-model). The notation is kept the same as those presented in Chapter 4. When the temperature difference ΔT is small, the distribution functions can be linearized as follows [17]

$$\hat{g} = \hat{f}_0 \left(1 + L\beta \right), \quad \hat{h} = k_B T_B \hat{f}_0 \left(1 + H\beta \right), \quad \beta << 1 \tag{D.1}$$

where L and H are the unknown perturbation functions and $\hat{f}_0$ is the local Maxwellian in the equilibrium conditions

$$\hat{f}_0 = n_B \left(\frac{m}{2\pi k_B T_B} \right)^{3/2} \exp\left(\frac{-mv^2}{2k_B T_B} \right) \tag{D.2}$$

where n_B is the number density of the gas on the outer cylinder and T_B is the temperature of the outer cylinder.

Institutional Repository - Library & Information Centre - University of Thessaly
09/05/2024 09:47:55 EEST - 18.222.167.58

Introducing the following non-dimensional quantities

$$r = \frac{\hat{r}}{R_B}, \quad \zeta = \frac{\xi}{\upsilon_B}, \quad c_z = \frac{\xi_z}{\upsilon_B}, \quad \rho = \frac{n - n_B}{n_B}\frac{1}{\beta},$$

$$\tau_{tr} = \frac{T_{tr} - T_B}{T_B}\frac{1}{\beta}, \quad \tau_{rot} = \frac{T_{rot} - T_B}{T_B}\frac{1}{\beta}, \quad \tau = \frac{3\tau_{tr} + j\tau_{rot}}{3 + j}, \quad \text{(D.3)}$$

$$q_{tr} = \frac{Q_{tr}}{P_B\upsilon_B}\frac{1}{\beta}, \quad q_{rot} = \frac{Q_{rot}}{P_B\upsilon_B}\frac{1}{\beta}, \quad q = q_{tr} + q_{rot}$$

and Substituting Eqs. (D.1) into the kinetic equations Eqs. (4.11) and (4.12), the linearized R-model that in the cylindrical coordinates reads as

$$\zeta \cos\theta \frac{\partial L}{\partial r} - \frac{\zeta \sin\theta}{r}\frac{\partial L}{\partial \theta} = \delta_B \left(L_0 - L\right),$$

$$\zeta \cos\theta \frac{\partial H}{\partial r} - \frac{\zeta \sin\theta}{r}\frac{\partial H}{\partial \theta} = \delta_B \left(H_0 - H\right),$$

$$L_0 = \rho + \left[\frac{1}{Z}\tau + \left(1 - \frac{1}{Z}\right)\tau_{tr}\right]\left(\zeta^2 - \frac{3}{2}\right) + \left(\frac{\varpi_0 - 1}{Z} + 1\right)\frac{4}{15}q_{tr}\zeta \cos\theta \left(\zeta^2 - \frac{5}{2}\right), \quad \text{(D.4)}$$

$$H_0 = \rho + \frac{2}{5Z}\left(\tau_{rot} - \tau_{tr}\right)\left(\zeta^2 - 3\right) + \tau_{rot} + \tau_{tr}\left(\zeta^2 - \frac{3}{2}\right)$$

$$+ \left(\frac{\varpi_0 - 1}{Z} + 1\right)\frac{4}{15}q_{tr}\zeta \cos\theta \left(\zeta^2 - \frac{5}{2}\right) + 2\left(\frac{\varpi_1 - 1}{Z} + 1\right)(1 - \kappa)q_{rot}\zeta \cos\theta.$$

where δ_B is the rarefaction parameter defined in Eq. (4.3). The moments of the perturbation functions ρ, τ, τ_{tr}, τ_{rot}, q_{tr} and q_{rot} are given as

$$\rho = \frac{1}{\pi^{3/2}}\int\limits_0^{2\pi}\int\limits_0^{\infty}\int\limits_{-\infty}^{\infty} L \exp\left(-\zeta^2 - c_z^2\right)dc_z\zeta d\zeta d\theta, \quad \text{(D.5)}$$

$$\tau_{tr} = \frac{1}{\pi^{3/2}}\int\limits_0^{2\pi}\int\limits_0^{\infty}\int\limits_{-\infty}^{\infty} L \left(\frac{2}{3}\zeta^2 - 1\right)\exp\left(-\zeta^2 - c_z^2\right)dc_z\zeta d\zeta d\theta, \quad \text{(D.6)}$$

$$\tau_{rot} = \frac{1}{\pi^{3/2}}\int\limits_0^{2\pi}\int\limits_0^{\infty}\int\limits_{-\infty}^{\infty} (H - L)\exp\left(-\zeta^2 - c_z^2\right)dc_z\zeta d\zeta d\theta, \quad \text{(D.7)}$$

232

$$q_{tr} = \frac{1}{\pi^{3/2}} \int\limits_0^{2\pi} \int\limits_0^\infty \int\limits_{-\infty}^\infty L\zeta \cos\theta \left(\zeta^2 - \frac{5}{2} \right) \exp\left(-\zeta^2 - c_z^2 \right) dc_z \zeta d\zeta d\theta, \qquad (D.8)$$

$$q_{rot} = \frac{1}{\pi^{3/2}} \int\limits_0^{2\pi} \int\limits_0^\infty \int\limits_{-\infty}^\infty H\zeta \cos\theta \exp\left(-\zeta^2 - c_z^2 \right) dc_z \zeta d\zeta d\theta. \qquad (D.9)$$

To eliminate the velocity c_z the following three reduced functions are introduced

$$F = \frac{1}{\sqrt{\pi}} \int\limits_{-\infty}^\infty L \exp\left(-c_z^2 \right) dc_z,$$

$$G = \frac{1}{\sqrt{\pi}} \int\limits_{-\infty}^\infty L \left(c_z^2 - \frac{1}{2} \right) \exp\left(-c_z^2 \right) dc_z, \qquad (D.10)$$

$$S = \frac{1}{\sqrt{\pi}} \int\limits_{-\infty}^\infty H \exp\left(-c_z^2 \right) dc_z.$$

Then, Eqs. (D.4) are written in compact form as

$$\zeta \cos\theta \frac{\partial \boldsymbol{\Psi}}{\partial r} - \frac{\zeta \sin\theta}{r} \frac{\partial \Psi}{\partial \theta} = \delta_B \left(\boldsymbol{\Psi_0} - \boldsymbol{\Psi} \right), \qquad (D.11)$$

where $\boldsymbol{\Psi} = [F, G, S]^T$ is the vector of the unknown distribution functions, while the components of the vector $\boldsymbol{\Psi_0} = [F_0, G_0, S_0]^T$ are defined as follows

$$F_0 = \rho + \left[\frac{1}{Z}\tau + \left(1 - \frac{1}{Z} \right) \tau_{tr} \right] \left(\zeta^2 - 1 \right) + \left(\frac{\varpi_0 - 1}{Z} + 1 \right) \frac{4}{15} q_{tr} \zeta \cos\theta \left(\zeta^2 - 2 \right),$$

$$G_0 = \frac{\tau}{2Z} + \left(1 - \frac{1}{Z} \right) \frac{\tau_{tr}}{2} + \left(\frac{\varpi_0 - 1}{Z} + 1 \right) \frac{2}{15} q_{tr} \zeta \cos\theta,$$

$$S_0 = \rho + \frac{2}{5Z} \left(\tau_{rot} - \tau_{tr} \right) \left(\zeta^2 - \frac{5}{2} \right) + \tau_{rot} + \tau_{tr} \left(\zeta^2 - 1 \right)$$

$$+ \left(\frac{\varpi_0 - 1}{Z} + 1 \right) \frac{4}{15} q_{tr} \zeta \cos\theta \left(\zeta^2 - 2 \right) + 2 \left(\frac{\varpi_1 - 1}{Z} + 1 \right) q_{rot} \zeta \cos\theta (1 - \kappa).$$

$$(D.12)$$

233

The macroscopic quantities (Eqs. (D.5)-(D.9)) written in terms of the reduced distribution functions F, G and S as

$$\rho = \frac{1}{\pi} \int\limits_{0}^{2\pi} \int\limits_{0}^{\infty} F \exp\left(-\zeta^2\right) \zeta d\zeta d\theta, \tag{D.13}$$

$$\tau_{tr} = \frac{2}{3\pi} \int\limits_{0}^{2\pi} \int\limits_{0}^{\infty} \left[F(\zeta^2 - 1) - G\right] \exp\left(-\zeta^2\right) \zeta d\zeta d\theta, \tag{D.14}$$

$$\tau_{rot} = \frac{1}{\pi} \int\limits_{0}^{2\pi} \int\limits_{0}^{\infty} (S - F) \exp\left(-\zeta^2\right) \zeta d\zeta d\theta, \tag{D.15}$$

$$q_{tr} = \frac{1}{\pi} \int\limits_{0}^{2\pi} \int\limits_{0}^{\infty} \zeta \cos\theta \left[F(\zeta^2 - 2) - G\right] \exp\left(-\zeta^2\right) \zeta d\zeta d\theta, \tag{D.16}$$

$$q_{rot} = \frac{1}{\pi} \int\limits_{0}^{2\pi} \int\limits_{0}^{\infty} \zeta \cos\theta S \exp\left(-\zeta^2\right) \zeta d\zeta d\theta. \tag{D.17}$$

To close the formulation of the linearized Rykov model the boundary conditions have to be assigned. Although the numerical formulation would allow more general wall scattering models, purely diffuse type boundary conditions are considered. Applying, the same linearization (Eqs. (D.1)), dimensionalization (Eqs. (D.3)) and projection (Eqs. (D.10)) processes as for the governing equations, the linearized form of the outgoing distributions associated to Eqs. (D.11) are at the inner wall $(r = \gamma)$

$$F^+ = \rho_w + \left(\zeta^2 - 1\right), \quad G^+ = \frac{1}{2}, \quad S^+ = \rho_w + \zeta^2, \tag{D.18}$$

and at the outer wall $(r = 1)$

$$F^+ = G^+ = S^+ = 0. \tag{D.19}$$

The parameter ρ_w in Eqs. (D.18) is determined via the impermeability condition as

$$\rho_w = -\frac{2}{\sqrt{\pi}} \int\limits_{\pi/2}^{3\pi/2} \int\limits_{0}^{\infty} \zeta^2 \cos\theta F^- \exp\left(-\zeta^2\right) d\zeta d\theta - \frac{1}{2}. \tag{D.20}$$

The nonlinear vector Eqs. (D.11) along with the associated expressions (D.12), the moments (D.13-D.17) and the boundary conditions (D.18-D.20) provide a theoretically well-established closed kinetic formulation for the heat transfer problem under small temperature differences based on the R-model.

In Table D.1 a comparison between the heat fluxes obtained from the linear Rykov model with the corresponding results based on the nonlinear Rykov is performed. The dimensionless translational, rotational and total heat fluxes are given for various δ_B with $\gamma = 1/2$ and $\gamma = 1/10$. The enclosed gas is nitrogen (N_2) with $\omega = 0.74$, $\varpi_0 = 0.2354$, $\varpi_1 = 0.3049$, $\kappa = 0.645$ and $Z = 5$ [106]. Simulations based on the nonlinear Rykov model have been performed for $\beta = 0.01$. It is noted that in order to compare the results from the nonlinear Rykov model with the corresponding ones obtained from the linear Rykov they are divided by $\beta = 0.01$. The percentage error between the nonlinear (NL) and linear (L) heat flows, defined as $error = |(q_{NL} - q_L)/q_{NL}| \times 100$ is less that 1% for all δ_B and γ. So, the presented linear form of the Rykov model can be applied at small temperature differences, giving results very close to the corresponding results based on the nonlinear Rykov model.

Table D.1: Heat fluxes at the inner hot cylinder ($r = \gamma$) for N_2 ($j = 2$) based on the linear and nonlinear Rykov model ($Z = 5$, $\omega = 0.74$, $\varpi_o = 0.2354$, $\varpi_1 = 0.3049$, $\kappa = 0.645$).

γ	δ_B	q_{tr}		q_{rot}		q	
		Linear	Nonlinear	Linear	Nonlinear	Linear	Nonlinear
1/2	0.1	5.59(-1)	5.57(-1)	2.79(-1)	2.78(-1)	8.38(-1)	8.36(-1)
	0.5	5.37(-1)	5.35(-1)	2.67(-1)	2.67(-1)	8.04(-1)	8.02(-1)
	1	5.11(-1)	5.10(-1)	2.54(-1)	2.53(-1)	7.65(-1)	7.63(-1)
	5	3.70(-1)	3.68(-1)	1.76(-1)	1.76(-1)	5.46(-1)	5.44(-1)
	10	2.72(-1)	2.70(-1)	1.26(-1)	1.26(-1)	3.99(-1)	3.97(-1)
1/10	0.1	5.61(-1)	5.60(-1)	2.81(-1)	2.80(-1)	8.42(-1)	8.40(-1)
	0.5	5.49(-1)	5.48(-1)	2.74(-1)	2.74(-1)	8.24(-1)	8.22(-1)
	1	5.35(-1)	5.34(-1)	2.67(-1)	2.66(-1)	8.02(-1)	8.00(-1)
	5	4.36(-1)	4.35(-1)	2.13(-1)	2.13(-1)	6.50(-1)	6.47(-1)
	10	3.48(-1)	3.46(-1)	1.67(-1)	1.66(-1)	5.15(-1)	5.13(-1))

Bibliography

[1] C. Cercignani, *The Boltzmann equation and its applications*, Springer-Verlag, Berlin, 1988.

[2] C. M. Ho and Y. C. Tai, *Micro-electro-mechanical systems (MEMS) and fluid flows*, Annual Review of Fluid Mechanics, 30, 579612, 1998.

[3] Y. G. Sikharulidze, P. Moraes and A. N. Korchagin, *Analysis of accuracy at ballistic re-entry in the earth atmosphere*, In 14th Int. Symp. Space Flight Dynamics, 1999.

[4] J. C. Taylor, A. B. Carlson and H. A. Hassan, *Monte Carlo simulation of radiating re-entry flows*, Journal of Thermophysics and Heat Transfer, 8(3), 478-485, 1994.

[5] Z. Chavis and R. Wilmoth, *Plume Modeling and Application to Mars 2001 Odyssey Aerobraking*, Journal of Spacecraft and Rockets, 42, 450-456, 2005.

[6] M. A. Gallis, J. M. Reese and D. A. Lockerby, *New direction in fluid mechanics: non-equilibrium aerodynamic and microsystem flows*, Philosophical Transactions of the Royal Society of London A, 361(1813), 2967-2988, 2003.

[7] M. Gad-el-Hak, *The MEMS handbook*, CRC Press, Florida, USA, 2002.

[8] G. E. Karniadakis and A. Beskok, *Micro Flows: Fundamentals and simulation*, Spinger-Verlag, New York, 2002.

[9] G. Shi, C. S. Chan, W. J. Li, KS. Leung, Y. Zoo and Y. Jin, *Mobile Human Airbag System for Fall Protection Using MEMS Sensors and Embedded SVM Classifier*, Sensors Journal, 9(15), 495-503, 2009.

[10] S. Roy and C. K. Sarkar, *MEMS and Nanotechnology for Gas Sensors*, CRC Press, 2015.

[11] K. Jousten, *Handbook of Vacuum Technology*, Wiley-VCH Verlag, Weinheim, Germany, 2008.

[12] W. Umrath, *Fundamentals of Vacuum Technology*, Leybold, Cologne, 1998.

[13] C. Day and D. Murdoch, *The ITER Vacuum Systems*, Journal of Physics: Conference Series, 114, 2008.

[14] S. Naris, C. Tantos and D. Valougeorgis, *Kinetic modeling of a tapered Holweck pump*, Vacuum, 109, 341-348, 2014.

[15] P. J. Sun, J. Y. Wu, P. Zhang, L. Xu and M. L. Jiang, *Experimental study of the influences of degraded vacuum on multilayer insulation blankets*, Cryogenics, 49(12), 719-726, 2009.

[16] L. Boltzmann, *Weitere studien ber das wrmegleichgewicht unter gasmoleklen*, Sitzung Berichte Kaiserl. Akad. der Wissenschaften, 66(2), 275370, 1872.

[17] F. Sharipov and V. Seleznev, *Data on internal rarefied gas flows*, Journal of Physical and Chemical Reference Data, 27(3), 657-706, 1998.

[18] A. B. Huang and D.L. Hartley, *Nonlinear Rarefied Couette Flow with Heat Transfer*, Physics of Fluids, 11(6), 1321-1326, 1968.

[19] G. A. Bird, *Molecular Gas Dynamics and the Direct Simulation of Gas Flows*, Clarendon Press, Oxford, 1994.

[20] L. H. Holway, *New statistical models for kinetic theory: Methods of construction*, Physics of Fluids, 9(9), 1658-1673, 1966.

[21] V. A. Rykov, *A model kinetic equation for a gas with rotational degrees of freedom*, Fluid Dynamics, 10(6), 956-966, 1975.

[22] P. Andries, P. L. Tallec, J. P. Perlat and B. Perthame, *The Gaussian-BGK model of Boltzmann equation with small Prandtl number*, European Journal of Mechanics B/Fluids, 19(6), 813-830, 2000.

[23] C. Borgnakke and P. S. Larsen, *Statistical collision model for Monte Carlo simulation of polyatomic gas mixture*, Journal of Computational Physics, 18(4), 405-420, 1975.

[24] M. Knudsen, *Die Molekularstroemung der Gase durch Offnungen und die Effusion*, Annalen der Physik, 333(5), 999-1016, 1909.

[25] W. D. Niven, *Scientific Papers of James Clerk Maxwell*, Dover Publications, Inc., New York, 1965.

[26] L. Boltzmann, *Lectures on Gas Theory*, University of California Press, Berkeley, Translated by S.G. Brush, 1964.

[27] C. S. Wang-Chang and G. E. Uhlenbeck, *Transport phenomena in polyatomic gases*, University of Michigan Engineering, Research Report CM-681, 1951.

[28] N. Taxman, *Classical theory of transport phenomena in dilute polyatomic gases*, Physical Review, 110, 12351239, 1958.

[29] C. Shen, *Rarefied Gas Dynamics: Fundamentals, Simulations and Micro Flows*, Springer, 2005.

[30] I. Kuscer, *A model for rotational energy exchange in polyatomic gases*, Physica A, 158(3), 784-800, 1989.

[31] J. H. Ferziger and H. G. Kaper, *Mathematical Theory of Transport Processes in Gases*, North-Holland Publishing Company, Amsterdam, 1972.

[32] C. S. Wang-Chang and G. E. Uhlenbeck, *Transport phenomena in polyatomic gases*, University of Michigan Engineering, Research Report CM-681, 1951.

[33] E. P. Muntz, *Rarefied Gas Dynamics*, Annual Review of Fluid Mechanics, 21, 387-422, 1989.

[34] D. L. Morris, L. Hannon and A. L. Garcia, *Slip length in a dilute gas*, Physical Review A, 46(8), 5279-5281, 1992.

[35] T. F. Morse, *Kinetic model for gases with internal degrees of freedom*, Physics of Fluids, 7(2), 159-169, 1964.

[36] P. L. Bhatnagar, E. P. Gross and M. A. Krook, *A model for collision processes in gases. I. Small amplitude processes in charged and neutral one-component systems*, Physical Review, 94(3), 511-525, 1954.

[37] F. B. Hanson and T. F. Morse, *Kinetic models for a gas with internal structure*, Physics of Fluids, 10(2), 345-353, 1967.

[38] C. A. Brau, *Kinetic theory of polyatomic gasesmodels for collisions processes*, Physics of Fluids, 10(1), 48-55, 1967.

[39] W. P. Wood, *Kinetic theory analysis of light scattering in polyatomic gases*, Australian Journal of Physics, 24, 555567, 1971.

[40] F. J. McCormack, *Construction of linearized kinetic models for gaseous mixtures and molecular gases*, Physics of Fluids, 16(12), 2095-2105, 1973.

[41] W. Marques Jr., *Light scattering and sound propagation in polyatomic gases with classical degrees of freedom*, Continuum Mechanics and Thermodynamics, 16(6), 517528, 2004.

[42] A. S. Fernandes and W. Marques Jr., *Kinetic model analysis of time-dependent problems in polyatomic gases*, Phusica A, 373, 97-118, 2007.

[43] C. Cercignani, *Mathematical Methods in Kinetic Theory*, Plenum Publishing Corporation, New York, 1990.

[44] P. Andries, J. F. Bourgat, P. Tallec and B. Perthame, *Numerical comparison between the Boltzmann and ES-BGK models for rarefied gases*, Computer methods in Applied Mechanics and Engineering, 191(31), 3369-3390, 2002.

[45] I. N. Larina and V. A. Rykov, *Kinetic model of the Boltzmann equation for a diatomic gas with rotational degrees of freedom*, Computational Mathematics and Mathematical Physics, 50(12), 2118-2130, 2010.

[46] L. Wu, C. White, T. J. Scanlon, J. M. Reese and Y. Zhang, *A kinetic model of the Boltzmann equation for non-vibrating polyatomic gases*, Journal of Fluid Mechanics, 763, 24-50, 2015.

[47] E. A. Mason and L. Monchick, *Heat conductivity of polyatomic and polar gases*, The Journal of Chemical Physics, 36(6), 1622-1639, 1962.

[48] E. M. Shakhov, *Generalization of the Krook kinetic relaxation equation*, Fluid Dynamics, 3(5), 95-95, 1968.

[49] J. C. Maxwell, *On stress in rarefied gases arising from inequalities of temperature*, Philosophical Transactions of the Royal Society of London, 170, 231-256, 1879.

[50] I. N. Larina and V. A. Rykov, *Boundary conditions for gases on a body surface*, Fluid Dynamics, 21(5), 795 - 801, 1986.

[51] O. V. Sazhin, S. F. Borisov and F. Sharipov, *Accommodation coefficient of tangential momentum on atomically clean and contaminated surfaces*, Journal of Vacuum Science and Technology A, 19(5), 2499- 2503, 2001.

[52] C. Cercignani and M. Lampis, *Kinetic models for gas-surface interactions*, Transport theory and statistical physics, 1(2), 101-114, 1971.

[53] R. G. Lord, *Some extensions to the Cercignani-Lampis gas-surface scattering kernel*, Physics of Fluids A, 3(4), 706-710, 1991.

[54] C. Cercignani, *Theory and Application of the Boltzmann Equation*, Scottish Academic Press, Edinburgh, 1975.

[55] C. Cercignani and C. D. Pagani, *Variational approach to boundary value problems in kinetic theory*, Physics of Fluids, 9(10), 11671173, 1966.

[56] M. N. Kogan, *Rarefied Gas Dynamics*, Plenum, New York, 1969.

[57] S. Varoutis, D. Valougeorgis and F. Sharipov, *A study of the integro-moment method in multi-dimensional non-equilibrium flows subject to boundary induced discontinuities*, Journal of Computational Physics, 227(12), 6272-6287, 2008.

[58] T. Carleman, *Problemes Mathematiques dans la Theorie Cinetique des Gaz*, Almqvist and Wiksell, Uppsala, 1957.

[59] J. Broadwell, *Study of rarefied shear flow by the discrete velocity method*, Journal of Fluid Mechanics, 19(3), 401-414, 1964.

[60] A. B. Huang, P. F. Huang, D. P. Giddens, and R. Srinivasan, *High-speed leading edge problem*, Phys. Fluids, 16(6), 814-824, 1973.

[61] H. Cabannes, *The discrete Boltzmann equation (Theory and application)*, Lecture notes, University of California, Berkeley, 1980.

[62] S. K. Loyalka and K. A. Hickey, *Kinetic theory of thermal transpiration and the mechanocaloric effect: Planar flow of a rigid sphere gas with arbitrary accommodation at the surface*, Journal of Vacuum Science and Technology A, 9(1), 158163, 1991.

[63] M. Wakabayashi, T. Ohwada and F. Golse, *Numerical analysis of the shear and thermal creep flows of a rarefied gas over the plane wall of a Maxwell type boundary on the basis of the linearized Boltzmann equation for hard-sphere molecules*, European Journal of Mechanics and B/Fluids, 15(2), 175202, 1996.

[64] D. Valougeorgis, *Couette flow of a binary gas mixture*, Physics of Fluids, 31(3), 521524, 1988.

[65] C. Cercignani and F. Sharipov, *Gaseous mixture slit flow at intermediate Knudsen numbers*, Physics of Fluids A: Fluid Dynamics, 4(6), 12831289, 1992.

[66] V. Bobylev and C. Cercignani, *Discrete velocity models without nonphysical invariants*, Journal of Statistical Physics, 97(3), 677689, 1999.

[67] C. Cecignani and A. V. Bobylev, *Discrete velocity models: The case of mixtures*, Transport Theory and Statistical Physics, 29(1-2), 209216, 2000.

242

[68] B. Dubroca and L. Mieussens, *A conservative and entropic discrete-velocity model for rarefied polyatomic gases*, in: ESAIM Proceedings, EDP Sciences, 10, 127139, 2001.

[69] G. A. Bird, *Approach to translational equilibrium in a rigid sphere gas*, Physics of Fluids, 6(10), 1518-1519, 1963.

[70] W. Wagner, *A convergence proof for Birds direct simulation Monte Carlo method for the Boltzmann equation*, Journal of Statistical Physics, 66(3), 1011-1044, 1992.

[71] G. A. Bird, *Monte Carlo simulation of gas flows*, Annual Review of Fluid Mechanics, 10, 11-31, 1978.

[72] S. Varoutis, O. Sazhin, D. Valougeorgis and F. Sharipov, *Flow of a rarefied gas into vacuum through a tube of finite length*, Journal of Vacuum Science and Technology - A, 26(2), 228-238, 2008.

[73] S. Varoutis, D. Valougeorgis and F. Sharipov, *Gas flow through tubes of finite length over the whole range of rarefaction for various pressure drop ratios*, Journal of Vacuum Science and Technology A, 27(6), 1377-1391, 2009.

[74] K. Koura and H. Matsumoto, *Variable soft sphere molecular model for inversepowerlaw or LennardJones potential*, Physics of Fluids, 3(10), 2459-2465, 1991.

[75] F. Bergemann and I. D. Boyd, *New discrete vibrational energy model for the direct simulation Monte Carlo method*, Progress in Astronautics and Aeronautics, 158, 174-183, 1994.

[76] G. A. Bird, *The Q-K model for gas-phase chemical reaction rates*, Physics of Fluids, 23(10), 106101-106113, 2011.

[77] J. L. Strapasson and F. Sharipov, *Ab initio simulation of heat transfer through a mixture of rarefied gases*, International Journal of Heat and Mass Transfer, 71, 91-97, 2014.

[78] W. Jitschin and S. Ludwig, *Dynamical behavior of the Pirani sensor*, Vacuum, 75(2), 169-176, 2004.

[79] S. J. O'shea and R. E. Collins, *An experimental study of conduction heat transfer in rarefied polyatomic gases*, International Journal of Heat and Mass Transfer, 35(12), 3431-3440, 1992.

[80] H. Chalabi, O. Buchina, L. Saraceno, M. Lorenzini, D. Valougeorgis and G. L. Morini, *Experimental analysis of heat transfer between a heated wire and a rarefied gas in an annular gap with high diameter ratio*, Journal of Physics: Conference Series, 362, 012028, 2012.

[81] Y. Yang, I. Gerken, J. J. Brandner and G. L. Morini, *Design and experimental investigation of a gas-to-gas counter-flow micro heat exchanger*, Experimental Heat Transfer, 27(4), 340-359, 2014.

[82] S. C. Saxena, *Transport properties of gases and gaseous mixtures at high temperatures*, High temperature science, 3(2), 168-188, 1971.

[83] F. Sharipov and D. Kalempa, *Velocity slip and temperature jump coefficients for gaseous mixtures. IV. Temperature jump coefficient*, International Journal of Heat and Mass Transfer, 48(6), 1076-1083, 2005.

[84] Y. G. Semyonov, S. F. Borisov and P. E. Suetin, *Investigation of heat transfer in rarefied gases over a wide range of Knudsen number*, International Journal of Heat and Mass Transfer, 27(10), 1789-1799, 1984.

[85] W. M. Trott, J. N. Castaneda, J. R. Torczynski, M. A. Gallis and D. J. Rader, *An experimental assembly for precise measurement of thermal accommodation*, Review of Scientific Instruments, 82(3), 035120(1-12), 2011.

[86] H. Yamaguchi, K. Kanazawa, Y. Matsuda, T. Niimi, A. Polikarpov and I. Graur, *Investigation on heat transfer between two coaxial cylinders for measurement of thermal accommodation coefficient*, Physics of Fluids, 24(6), 062002(1-16), 2012.

[87] F. Sharipov and G. Bertoldo, *Heat transfer through a rarefied gas confined between two coaxial cylinders with high radius ratio*, International Journal of Vacuum Science and Technology, 24(6), 2087-2093, 2006.

[88] I. Graur and A. P. Polikarpov, *Comparison of different kinetic models for the heat transfer problem*, Heat Mass Transfer, 46(2), 237-244, 2009.

[89] S. Pantazis and D. Valougeorgis, *Non-linear heat transfer through rarefied gases between coaxial cylindrical surfaces at different temperatures*, European Journal of Mechanics B/Fluids, 29(6), 494-509, 2010.

[90] M. Vargas, S. Stefanov and V. Roussinov, *Transient heat transfer flow through a binary gaseous mixture confined between coaxial cylinders*, International Journal of Heat and Mass Transfer, 59, 302-315, 2013.

[91] J. W. Cipolla, *Heat transfer and temperature jump in a polyatomic gas*, International Journal of Heat and Mass Transfer, 14(10), 1599-1610, 1971.

[92] J. T. Lin and D. R. Willis, *Kinetic theory analysis of temperature jump in a polyatomic gas*, Physics of Fluids, 15(1), 31-38, 1972.

[93] S. K. Hsu and T. F. Morse, *Kinetic theory of parallel heat transfer in a polyatomic gas*, Physics of Fluids, 15(4), 584-591, 1972.

[94] P. Pazooki and S. K. Loyalka, *Heat transfer in a polyatomic gas - I. Plane parallel plates*, International Journal of Heat and Mass Transfer, 28(11), 2019-2027, 1985.

[95] B. Huang and P. F. Hwang, *Test of statistical models for gases with and without internal energy states*, Physics of Fluids, 16(4), 466-475, 1973.

[96] W. P. Teagan and G. S. Springer, *Heat transfer and density-distribution measurements between parallel plates in the transition regime*, Physics of Fluids, 11(3), 497-506, 1968.

[97] D. J. Alofs, R. C. Flagan and G. S. Springer, *Density distribution measurements in rarefied gases contained between parallel plates at high temperature differences*, Physics of Fluids, 14(3), 529-533, 1971.

[98] L. Lee and C. Y. Liu, *Kinetic-theory description of conductive heat transfer from a fine wire*, Physics of Fluids, 5(10), 1137-1148, 1962.

[99] J. W. Cipolla and T. F. Morse, *Kinetic description of cylindrical heat conduction in a polyatomic gas*, Physics of Fluids, 11(6), 1292-1300, 1968.

[100] S. Varoutis, O. Sazhin, D. Valougeorgis and F. Sharipov, *Flow of a rarefied gas into vacuum through a tube of finite length*, Journal of Vacuum Science and Technology A, 26(2), 228-238, 2008.

[101] S. Pantazis and D. Valougeorgis, *Rarefied gas flow through a cylindrical tube due to a small pressure difference*, European Journal of Mechanics B/Fluids, 38, 114-127, 2013.

[102] S. Misdanitis, S. Pantazis and D. Valougeorgis, *Pressure driven rarefied gas flow through a slit and an orifice*, Vacuum, 86(11), 1701-1708, 2012.

[103] S. S. Lo and S. K. Loyalka, *Flow of Rarefied Polyatomic Gas between Parallel Plates*, Journal of Vacuum Science and Technology A, 7(4), 2766-2773, 1989.

[104] S. K. Loyalka and T. S. Storvik, *Kinetic Theory of Thermal Transpiration and Mechanocaloric Effect. III. Flow of Polyatomic Gases between Parallel Plates*, Journal of Chemical Physics, 71(1), 339-350, 1979.

[105] S. K. Loyalka, T. S. Storvik, and S. S. Lo, *Thermal Transpiration and Mechanocaloric Effect. IV. Flow of Polyatomic Gases in a Cylindrical Tube*, Journal of Chemical Physics, 76(8), 4157-4170, 1982.

[106] V. A. Titarev and E. M. Shakhov, *Poiseuille Flow and Thermal Creep in a Capillary Tube on the Basis of the Kinetic R-Model*, Fluid Dynamics, 47(5), 661672, 2012.

[107] I. N. Larina and V. A. Rykov, *Computation of Rarefied Diatomic Gas Flows through a Plane Microchannel*, Computational Mathematics and Mathematical Physics, 52(4), 637-648, 2012.

[108] I. N. Larina and V. A. Rykov, *Numerical Investigation of Rarefied Diatomic Gas Flows through a Plane Channel into a Vacuum*, Fluid Dynamics, 48(3), 389-401, 2013.

[109] A. A. Alexeenko, S. F. Gimelshein, E. P. Muntz and A. D. Ketsdever, *Kinetic modeling of temperature driven flows in short microchannels*, 45(11), 1045-1051, 2006.

[110] B. T. Porodnov, P. E. Suetin, S. F. Borisov and V. D. Akinshin, *Experimental investigation of rarefied gas flow in different channels*, Journal of Fluid Mechanics, 64(3), 417-437, 1974.

[111] J. Balakrishnan, I. D. Boyd and D. G. Braun, *Monte Carlo simulation of vapor transport in physical vapor deposition of titanium*, Journal of Vacuum Science and Technology A: Vacuum Surfaces and Films, 18(3), 907-916, 2000.

[112] J. Lafferty , *Foundations of vacuum science and technology*, John Wiley and Sons, 1998.

[113] A. Frezzotti, G. P. Ghiroldi and L. Gibelli, *Rarefied gas mixtures flows driven by surface absorption*, Vacuum, 86(11), 1731-1738, 2012.

[114] A. Frezzotti, G. P. Ghiroldi and L. Gibelli, *DSMC Simulation of Rarefied Gas Mixtures Flows past Arrays of Absorbing Plates*, Vacuum, 103, 57-67, 2014.

[115] X. Luo, C. Day, H. Haas and S. Varoutis, *Experimental results and numerical modeling of a high-performancelarge-scale cryopump. I. Test particle Monte Carlo simulation*, Journal of Vacuum Science and Technology A, 29(4), 041601(1-7), 2011.

[116] S. Varoutis and C. Day, *Numerical modeling of an ITER type Cryopump*, Fusion Engineering and Design 87(7), 1395-1398, 2012.

[117] M. Kovari, R. Clarke and T. Shephard, *Compound cryopump for fusion reactors*, Fusion Engineering and Design, 88(12), 3293-3298, 2013.

[118] S. Liu, P. Yu, K. Xu and C. Zhong, *Unified gas-kinetic schemes for diatomic molecular simulations in all flow regimes*, Journal of Computational Physics, 259, 96-113, 2014.

[119] J. O. Hirschfelder, C. F. Curtiss and R. B. Bird, *Molecular Theory of Gases and Liquids*, Wiley, New York, 1954.

[120] J. Jean, *An Introduction to the Kinetic Theory of Gases*, Cambridge University Press, 1967.

[121] V. A. Rykov and V. N. Skobelkin, *Macroscopic description of the motions of a gas with rotational degrees of freedom*, Fluid Dynamics, 13(1), 144-147, 1978.

[122] J. C. Maxwell, *The Scientific Papers of James Clerk Maxwell*, Cambridge University Press, London, 1890.

[123] A. Frezzotti, *A numerical investigation of the steady evaporation of a polyatomic gas*, European Journal of Mechanics B/Fluids, 26(1), 93-104, 2007.

[124] C. Tantos, D. Valougeorgis and A. Frezzotti, *Conductive heat transfer in rarefied polyatomic gases confined between parallel plates via various kinetic models and the DSMC method*, International Journal of Heat Mass Transfer, 88, 636-651, 2015.

[125] I. A. Kostromin and V. A. Rykov, *Numerical Study of the Couette Flow of a Diatomic Rarefied Gas*, Computational Mathematics and Mathematical Physics, 53(11), 1684-1695, 2013.

[126] P. Feuer, *Theory of the thermal accommodation coefficients of a diatomic gas*, Journal of Chemical Physics, 39(5), 1311, 1963.

[127] D. J. Marsden, *Measurements of energy transfer in gas-solid surface interactions using electron beam excited emission of light*, Rarefied Gas Dynamics, 2, Academic Press, New York-London, 66-583, 1966.

[128] S. Chapman and T. G. Cowling, *The Mathematical Theory of Non-Uniform Gases*, Cambridge University Press, Cambridge UK, 1990.

[129] I. J. Wysong and D. C. Wadsworth, *Assessment of direct simulation Monte Carlo phenomenological rotational relaxation models*, Physics of Fluids, 10(11), 2983-2994, 1998.

[130] S. Pantazis and D. Valougeorgis, *Heat transfer between parallel plates via kinetic theory in the whole range of the Knudsen number*, Paper 407, 5th European Thermal-Sciences Conference, 19-22/5/2008, Eindhoven, Netherlands, 2008.

[131] J. A. Lordi and R. E. Mates, *Rotational Relaxation in nonpolar diatomic gases*, Physics of Fluids, 13(2), 291-308, 1970.

248

[132] C. Tantos, D. Valougeorgis, M. Pannuzzo, A. Frezzotti and G. L. Morini, *Conductive heat transfer in a rarefied polyatomic gas confined between coaxial cylinders*, International Journal of Heat Mass Transfer, 79, 378-389, 2014.

[133] G. E.Totten and M. A. H. Howes, *Steel Heat Treatment Handbook*, Marcel Dekker, USA, 1997.

[134] M. J. Assael, S. Mixafendi and W. A. Wakeham, *The Viscocity of Noraml Deuterium in the Limit of Zero Density*, Journal of Physical and Chemical Reference Data, 16(2), 1987.

[135] T. K. Bose, *High Temperature Gas Dynamics: An introduction for Physicists and Engineers*, Springer, 2014.

[136] A. La Porte and R. E. Putman, *The practical application of SF6 and helium for condenser tube and air Inleakage detection*, Condenser Technology Conference, Conco Services Corporation, Boston MA, August 1996.

[137] P. Chevrier, M. Barrault, C. Fievet, J. Maftoul and J. M. Fremillon, *Industrial applications of high-, medium- and low-voltage arc modelling*, Journal of Physics D: Applied Physics, 30(9), 1346-1355, 1997.

[138] M. Maiss and C. A. M. Brenninkmeijer, *Atmospheric SF6: Trends, Sources, and Prospects*, Environmental Science and Technology, 32(20), 3077-3086, 1998.

[139] S. Zhang and F.Yu, *Piezoelectric Materials for High Temperature Sensors*, Journal of the American Ceramic Society, 94, 3153-3170, 2011.

[140] I. Chakraborty, W. C. Tang, D. P. Bame and T. K. Tang, *MEMS micro-valve for space applications*, Sensors and Actuators A: Physical, 83(1-3), 188-193, 2000.

[141] F. J. Uribe, E. A. Mason and J. Kestin, *Thermal conductivity of nine polyatomic gases at low densities*, Journal of Physical and Chemical Reference Data, 19(5), 1123-1136, 1990.

[142] M. A. Gallis, J. R. Torczynski, D. J. Rader, M. Tij and A. Santos, *Normal solutions of the Boltzmann equation for highly nonequilibrium Fourier flow and Couette flow*, Physics of Fluids, 18(1), 017104(1-15), 2006.

[143] D. Bruno, A. Frezzotti and G. P. Ghiroldi, *Oxygen transport properties estimation by DSMC-CT simulations*, Proceedings of the 29th International Symposium on Rarefied Gas Dynamics, AIP Conference Proceedings 1628, 108, 2014.

[144] J. C. Haas, V. S. Arpaci and G. S. Springer, *Mass and heat transfer in a diatomic gas*, Journal of Plasma Physics, 6(3), 547-560, 1971.

[145] E. W. Lemmon and R. T Jacobsen, *Viscosity and Thermal Conductivity Equations for Nitrogen, Oxygen, Argon, and Air*, International Journal of Thermophysics, 25(1), 21-69, 2004.

[146] S. Varoutis, S. Naris, V. Hauer, C. Day and D. Valougeorgis, *Computational and experimental study of gas flows through long channels of various cross sections in the whole range of the Knudsen number*, Journal of Vacuum Science and Technology A, 27(1), 89-100, 2009.

[147] S. Pantazis, S. Varoutis, V. Hauer, C. Day and D. Valougeorgis, *Gas-surface scattering effect on vacuum gas flows through rectangular channels*, Vacuum, 85(12), 11611164, 2011.

[148] S. Naris and D. Valougeorgis, *Rarefied gas flow in a triangular duct based on a boundary fitted lattice*, European Journal of Mechanics - B/Fluids, 27, 810-822, 2008.

[149] S. F. Gimelshein, G. N. Markelov, T. C. Lilly, N. P. Selden, and A. D. Ketsdever, in Rarefied Gas Dynamics, edited by M. Capitelli (American Institute of Physics, Melville, NY), 437-443, 2004.

[150] T. Lilly, S. Gimelshein, A. Ketsdever, and G. N. Markelov, *Measurements and computations of mass flow and momentum flux through short tubes in rarefied gases*, Physics of Fluids, 18(9), 093601(1-11), 2006.

[151] F. Sharipov, *Rarefied Gas Dynamics: Fundamentals for Research and Practice*, Wiley-VCH, Berlin, 2016.

[152] G. D. Arney Jr. and A. B. Bailey, *Addendumtoanlnvestigation of the Equilibriwn Pressure Along Unequally Heated Tubes*, Tech. Doc. Report No. AEDC-TDR-62-188, 1962.

[153] A. Frezzotti and T. Ytrehus, *Kinetic theory study of steady condensation of a polyatomic gas*, Physics of Fluids, 18(2), 027101(1-12), 2006.

[154] T. A. Ward, *Aerospace Propulsion Systems*, John Wiley, 2010.

[155] S. Pantazis, S. Naris, C. Tantos, D. Valougeorgis, J. Andre, F. Millet and J. P. Perin, *Non-linear vacuum gas flow through a short tube due to to pressure and temperature gradients*, Fusion Engineering and Design, 88(9-10), 2384-2387, 2013.

[156] S. Pantazis and D. Valougeorgis, *Rarefied gas flow through a cylindrical tube due to a small pressure difference*, European Journal of Mechanics B/Fluids, 38, 114-127, 2013.

[157] F. Sharipov, *Rarefied gas flow through a long tube at any temperature ratio* , Journal of Vacuum Science and Technology A, 14(4), 2627-2635, 1996.

[158] M. Knudsen, *Thermischer Molekulardruck der Gase in Rhren*, Annalen der Physik, 338(16), 1435-1448, 1910.

[159] O. Reynolds, *On certain dimensional properties of matter in the gaseous state. Part I and Part II*, Royal Society Publishing, 170, 727, 1880.

[160] C. Day and A. Schwenk-Ferrero, *Sticking coefficients for helium and helium-containing mixtures at activated carbon under liquid helium cooling conditions*, Vacuum, 53(1-2), 253-256, 1999.

[161] C. Day, A. Antipenkov, M. Dremel, H. Haas, V. Hauer, A. Mack, D. K. Murdoch and M. Wykes, *R&D and design for the cryogenic and mechanical vacuum pumping systems of ITER*, Vacuum, 81(6), 738-747, 2007.

[162] S. Song S and M.M. Yovanovich, *Correlation of thermal accommodation coefficient for engineering surfaces*, ASME HTD-Vol. 69, 107-116, 1987.

[163] I. Graur, A. Ph. Polikarpov and F. Sharipov, *Numerical modeling of rarefied gas flow through a slit into vacuum based on the kinetic equation*, Computer and Fluids, 49(1), 87-92, 2011.

251

[164] F. Sharipov, *Benchmark problems in rarefied gas dynamics*, Vacuum, 86(11), 1697-1700, 2012.

[165] K Aoki, K. Nishino, Y. Sone and H. Sugimoto, *Numerical analysis of steady flows of a gas condensing on or evaporating from its plane condensed phase on the basis of kinetic theory: Effect of gas motion along the condensed phase*, Physics of Fluids A, 3(9), 2260-2275, 1991.

[166] I. J. Wysong and D. C. Wadsworth, *Assessment of direct simulation Monte Carlo phenomenological rotational relaxation models*, Physics of Fluids 10(11), 29832994, 1998.

[167] W. G. Baechler, *Cryopumps for research and industry*, Vacuum, 37(1-2), 21-29, 1987.

[168] H. Haas, C. Day, D. Valougeorgis, S. Naris and C. Tantos, *Design Assessment Studies DAS05-T02: Further examination of isotope separation in a cryopump*, Report for TAWP13-DAS05-D02, 2013.

[169] M. Dremel, R. Pearce, H. Strobel, V. Hauer, C. Day and P. Wikus, *The new build to print design of the ITER torus cryopump*, Fusion Engineering and Design, 88(6-8), 760-763, 2013.

[170] M. Scannapiego and X. Luo, Final Report on *Evaluation of the initial TIMO open panel experiment*, IDM reference EFDA_D_2LMBRT, 2015.

[171] Minutes of meeting TFV-V-CRP Project Meeting 1 (April 2015).

[172] B. L. Haas, D. B. Hash, G. A. Bird, F. E. Lumpkin, III and H. A. Hassan, *Rates of thermal relaxation in direct simulation Monte Carlo methods*, Physics of Fluids 6(6), 2191-2201, 1994.

[173] C. Tantos, D. Valougeorgis, G. P. Ghiroldi and A. Frezzotti, *Effect of vibrational degrees of freedom on the heat transfer in polyatomic gases confined between parallel plate*, submitted in International Journal of Heat and Mass Transfer.